University of Southampton

FACULTY OF NATURAL AND ENVIRONMENTAL SCIENCES

Ocean and Earth Sciences

Development of Numerical Simulation Methods to Support Emerging Rapid and Automated Radioanalytical Techniques

Frances Mary Burrell

Thesis for the degree of Doctor of Philosophy

August 2017

UNIVERSITY OF SOUTHAMPTON

ABSTRACT

FACULTY OF NATURAL AND ENVIRONMENTAL SCIENCES

Ocean and Earth Sciences

Doctor of Philosophy

DEVELOPMENT OF NUMERICAL SIMULATION METHODS TO SUPPORT EMERGING RAPID AND AUTOMATED RADIOANALYTICAL TECHNIQUES

By Frances Mary Burrell

The global demand for radiological characterisation of a vast range of sample matrices as well as the pressure to improve emergency preparedness has led to the emergence of novel rapid and automated techniques. For radioanalytical procedures involving the separation and isolation of difficult to measure nuclides, a particular focus has been on the use of pumps or pressure gradients to accelerate the flow of solutions through a chromatographic column. The introduction of elevated flow rates as well as changing procedural specifications due to advances in detection method, shifts in nuclide detection levels required for dose assessments and growing interest in unusual matrices has contributed to the need for new or modified radioanalytical methods. The development and validation of methods can involve a large volume of experimental work and is often hindered by a lack of certified reference materials and isotopic tracers. The development of software to simulate chromatographic breakthrough and elution profiles would therefore be a useful tool in method development and validation as well as in support of routine radiological analysis using automated separation techniques.

This thesis details the development of a numerical simulation method for modelling chromatographic breakthrough. A mechanistic and modular approach has been followed based on the numerical solution of ordinary differential equations to describe concentration change with respect to time. The method was first developed to describe the batch sorption and desorption of analytes and then applied to a packed bed geometry under a range of operating conditions. The proposed numerical simulation method shows great potential for the prediction of elution profiles from any chromatographic system provided the correct input parameters are defined.

List of Contents

List of Tables

List of Figures

Note: Both figures from Chapter 1 (Introduction) are repeated in the relevant data chapters (Chapters 4-6) for ease of reference.

Declaration of Authorship

Academic Thesis: Declaration Of Authorship

I, **Frances Burrell**

declare that this thesis and the work presented in it are my own and has been generated by me as the result of my own original research.

Title of thesis: **Development of Numerical Simulation Methods to Support Emerging Rapid and Automated Radioanalytical Techniques**

I confirm that:

1. This work was done wholly or mainly while in candidature for a research degree at this University;
2. Where any part of this thesis has previously been submitted for a degree or any other qualification at this University or any other institution, this has been clearly stated;
3. Where I have consulted the published work of others, this is always clearly attributed;
4. Where I have quoted from the work of others, the source is always given. With the exception of such quotations, this thesis is entirely my own work;
5. I have acknowledged all main sources of help;
6. Where the thesis is based on work done by myself jointly with others, I have made clear exactly what was done by others and what I have contributed myself;
7. None of this work has been published before submission.

Signed: ……

Date: ……

Acknowledgements

Firstly, I would like to thank the Nuclear Decommissioning Authority and GAU Radioanalytical for funding this project. Huge thanks go to my academic supervisors, Ian Croudace and Phil Warwick, for introducing me to the fascinating field of radiochemistry during my MChem placement and guiding and encouraging me on my journey from placement student to PhD candidate. My confidence has grown due to their belief in my scientific ability and the challenges they have helped me to face. I would also like to thank Steve Walters, my industrial supervisor, who has always been approachable and willing to impact his expert knowledge. I am also very grateful for the opportunities provided through my NNL supervision to attend scientific conferences and meetings, go on industry visits and seek valuable advice from the Modelling and Simulation team at NNL Risley.

Thank you to the GAU team who have welcomed me from the start. I would particularly like to thank Pawel, Mark and Maddie for sharing their lab-based expertise and practical tips with me. I have learnt so much from them. I would also like to thank Zivi for his time and patience in helping me to analyse a large amount of samples by ICP-MS. Further to that, thanks go to all the PhD students in the radiochemistry research group, past and present. I have had some excellent role models.

I am also thankful for the fantastic group of fellow students I lived with. I could not have asked to share the PhD journey with a better group of people. Thank you also to James, who has supported me, encouraged me, lifted my spirits and helped me to see the way forward. Finally, thanks go to my parents and sister, who are always at the end of the phone line (or a long drive) with a listening ear and words of encouragement.

List of Abbreviations

BDST	Bed depth service time model
cFI	Continuous flow injection
CPU	Central processing unit
CSA	Cross-sectional area
CSV	Comma-separated values (file)
DAAP	Diamyl amylphosphonate
DTM	Difficult to measure
ETM	Easy to measure
FIA	Flow injection analysis
HDEHP	Di(2-ethylhexyl) orthophosphoric acid
HETP	Height equivalent of a theoretical plate
HPGe	High purity germanium (gamma detector)
HPLC	High performance liquid chromatography
HSDM	Homogeneous surface diffusion model
ICP-MS	Inductively coupled plasma mass spectrometry
ICP-QQQ	Triple quadrupole inductively coupled plasma mass spectrometry
ITM	Impossible to measure
IUPAC	International Union of Pure and Applied Chemistry
LDF	Linear driving force
LLE	Liquid-liquid extraction
LOV	Lab-on-valve
MC	Mixing cells
MCFIA	Multicommutated flow injection analysis
MPFS	Multi-pumping flow systems
MQ	Milli-Q2
MSFIA	Multisyringe flow injection analysis
NaI	Sodium iodide (gamma detector)
NDA	Nuclear Decommissioning Authority
NNL	National Nuclear Laboratory
NORM	Naturally occurring radioactive materials
ODE	Ordinary differential equation

PDE	Partial differential equation
PDM	Pore diffusion model
PDSM	Pore and surface diffusion model
PD	Plug flow plus dispersion
PF	Plug flow
PFO	Pseudo-first-order
ppb	Parts per billion
ppm	Parts per million
PSO	Pseudo-second-order
PTFE	Polytetrafluoroethylene
Re	Reynolds number
rFIA	Reverse flow injection analysis
Sc	Schmidt number
SEM	Scanning electron microscopy
SFA	Segmented flow analysis
Sh	Sherwood number
SI	Sequential injection
SIXEP	Sellafield Ion Exchange Effluent Plant
SPE	Solid phase extraction
SRT	Statistical rate theory
TDMS	Technical Data Management Streaming (file)
TRU	Transuranic (resin)
UPLC	Ultra performance liquid chromatography
VI	Virtual instrument
WAC	Waste acceptance criteria
WENO	Weighted essentially non-oscillatory method

Chapter 1: Introduction

1.1. Rationale

1.1.1. Radioanalytical characterisation of waste arising from nuclear decommissioning

This project was sponsored by the Nuclear Decommissioning Authority (NDA) and GAU-Radioanalytical and came under the characterisation theme within the NDA Bursary Scheme. A statement in the NDA's most recent strategy document[1] (effective from April 2016) presented to the UK and Scottish Parliaments under Schedule 2 of the Energy Act 2004 highlighted the importance of characterisation at all stages of decommissioning operations from baseline evidence through to clean-up quality assessment:

> "Characterisation plays an important role in the decommissioning of nuclear facilities. It is the basis for planning, identification of the extent and nature of contamination, assessment of potential risk impacts, cost estimation, implementation of decommissioning and waste management, radiation protection, protection of the environment, as well as supporting decisions to release the site and buildings."

Non-radiological characterisation can be used to assess the chemical environment and guiding decontamination strategies as well as identify chemically toxic materials which may present a processing hazard or fall below landfill waste acceptance criteria (WAC)[2]. The requirement to accurately quantify non-radiological risk is expected to become increasingly important for the UK nuclear industry[3]. The quantification of the nature and amount of radioactive contamination is, however, well-established and is the driving factor in nuclear waste classification and management. Radiological characterisation is essential both in minimising the amount of material requiring costly processing and storage and in ensuring public safety.

International guidance on calculation of total radioactivity recommends using a combination of historical records, on-site non-destructive analysis and sampling of materials for laboratory-based destructive analysis. Historical records can include details of building materials, reactor operating conditions, accidental releases or leaks and waste processing and management[2,4]. The comprehensiveness of these records dictates the subsequent *in-situ* characterisation and sampling strategy. In the case of well-documented sites, computational modelling of neutron activation of materials in the reactor can be used to predict the radionuclide distribution[2] whereas historical wastes with low traceability require more extensive initial characterisation[5]. The principal non-destructive, *in-situ* methods are gamma imaging, gross alpha/beta measurements, gamma spectrometry, neutron counting methods and calorimetry[2,5]. These methods can only

quantify easy to measure (ETM) nuclides so must be used in combination with destructive methods to build a full radiological inventory. Destructive methods involve sampling the material and conducting laboratory-based radiochemical analysis. This is required to obtain activity measurements of 'difficult to measure' (DTM) alpha and beta emitting radionuclides as well as in the case of very heterogenic or penetrative contamination where depth profiles are required. These two measurement techniques are combined to produce a complete waste inventory through the use of scaling factors (also known as radionuclide fingerprints or nuclide vectors). This technique is recognised as the ISO21238:2007 international standard and is based on the correlations between key easy to measure nuclides such as such as Co-60, Cs-137, Ce-144 and Sb-125 and difficult or impossible to measure (ITM) nuclides[6,7]. These correlations are material and site specific and are generated from destructive analysis characterisation. The correlation between the nuclides may be based on chemical similarity or an empirically observed relationship. If chemical decontamination is carried out on a material, the scaling factors associated with the material may also significantly change[2,4]. In addition, scaling factors are used for stable and homogeneous waste streams generated during the operation of a power plant; it should be noted, however, that destructive analysis would be required to reassess these factors if changes were made to the reactor operation or waste processing routes[4,7].

In-situ development needs have been identified for the Sellafield site; these include methods for the location of radiological hot spots, imaging techniques and faster activity measurements in hard to access and highly active areas via remotely operated robotic devices[8]. This research challenge has also been recognised by the UK government which is planning to invest £93 million towards robotics and AI in extreme environments (including nuclear energy, deep mining, space and off-shore energy) under the Industrial Strategy Challenge Fund[9]. This fund was created to provide funding and support to UK businesses and researchers and is part of the government's £4.7 billion increase in research and development over 4 years, starting in 2017.

Destructive measurements are more costly than *in-situ* measurements with the full procedure of sample extraction, transportation to external laboratories and radiochemical analysis following a representative sampling plan contributing significantly to the UK's decommissioning budget. There is, therefore, a considerable need to develop faster and cheaper radiochemical analysis methods.

1.1.2. Development of rapid radioanalytical methods

Destructive radiochemical analysis of alpha and beta emitting radionuclides requires isolation of the analyte(s) from the bulk matrix and other interferents. Interfering species vary depending on detection method employed; radiometric techniques such as liquid scintillation counting or alpha spectrometry can exhibit problematic spectral overlap between radionuclides whereas mass spectrometry suffers from isobaric or polyatomic interferents (e.g. measurement of ^{239}Pu requires considerable decontamination from the more abundant uranium isotopes due to the formation of $^{238}U^{1}H^{+}$ in the plasma)[10]. Separation of analytes can be time consuming and requires significant analyst input.

In addition to supporting the decommissioning phase, characterisation is required in all other phases of the life cycle of a nuclear facility from baseline measurements during construction to monitoring of wastes and health physics during operation to final surveys for site license termination[4]. Radiochemical laboratories may receive samples from a variety of nuclear power plants at different stages of their life cycle and from multiple locations both nationally and internationally. These facilities may also be equipped to receive and analyse samples from research reactors, radioisotope production sites, the radiopharmaceutical industry, naturally occurring radioactive materials (NORM) producing industries such as the oil and gas sector and environmental monitoring surveys. Reliable analytical techniques must therefore be available for measuring radionuclide content in a wide range of sample matrices in a cost-effective and efficient manner.

An additional motivation to improve turnaround times for the quantification of radionuclides is emergency preparedness. In the event of a nuclear accident, nuclear attack or detonation of a radiological dispersal device, reliable and rapid information regarding the radionuclides present, their quantity and spatial distribution is essential in informing dose estimates and making crucial decisions on the guidance issued to the public including the appropriate use of costly evacuation procedures. After this initial demand, the focus would move to more extensive characterisation to assist in the decontamination process, followed by further analysis of the wider radiochemical composition including longer-lived nuclides to ensure the safety of the existing/returned population.

Radioanalytical procedures for the isolation of alpha and beta emitting radionuclides often involve multiple steps including sample dissolution, precipitation, evaporation, column chromatography and preparation of the correct matrix for detection. Active research is being undertaken to improve these procedures in terms of reducing the amount of sample required, minimising the

cost, volume and toxicity of reagents used and waste generated and improving the separation of species in the chromatographic step through tailored elution sequences or through the development of new sorptive materials with greater selectivity. Advances are also being made to detection methods. This includes the development of novel scintillators[11] or improved understanding of factors affecting shape of spectra[12] in liquid scintillation counting; better source preparation methods or software based techniques for deconvolution of spectra in alpha spectrometry[13]; and more sensitive mass spectrometry instrumentation such as triple quadrupole inductively coupled plasma mass spectrometry[14]. These advances also change the requirements of the radioanalytical separation procedure in terms of the matrix, analyte yield and accepted levels of interferent in the final solution. Another driving factor for research into new radioanalytical procedures is an emerging interest in measurement of an isotope of an element that was previously insignificant for dose assessments; for example, the long-lived fission product, Se-79 ($t_{1/2}$ ~3 x 10^5 years)[15,16] and Zr-93 ($t_{1/2}$ ~1.5 x 10^6 years) which can be present in irradiated fuel cladding, formed by the activation of stable zirconium[17]. This growing interest could be due to changes in reactor building materials or waste processing techniques, better understanding of migration in the environment or a desire to better assess the activity remaining after extended time periods. New methods can be validated by testing the entire procedure using certified reference materials and the continued quality of results maintained using proficiency tests and intercomparison exercises[18]. In the UK, however, the limited range of certified reference materials and certified isotopic tracers available hinders the validation of new methods for the complete range of sample matrices encountered.

Due to its many advantages, radioanalytical procedures that have been newly developed or improved for the reasons listed above usually include at least one column chromatography step. Optimisation of column chromatography to achieve the desired analyte yield and decontamination factors can require a large number of experimental tests due to multiple variables including the volume and composition of the loading sample, wash solution and eluting reagent(s) as well as the length and diameter of the packed bed. Software capable of simulating the chromatographic column output in the form of concentration against volume would therefore be a useful tool for method development or sample specific optimisation of elution sequences. If based on robust scientific knowledge, simulation software could also be used in conjunction with certified reference materials as evidence for the validation of new radiochemical procedures for a wide range of sample matrices.

Another emerging area of research to improve radioanalytical turnaround times is automation of column chromatography. The use of pumps or air pressure gradients to control the flow of

solutions through the column adds an additional variable to the chromatographic step; velocity. This could also be incorporated into column output simulation software to aid in the optimisation of chromatographic operating conditions to minimise total sample analysis time whilst meeting additional specifications such as cost and interferent decontamination. In order to include flow rate into simulation software, knowledge of the kinetics of the interaction of analytes with the packed bed is needed. Unfortunately, the current availability of kinetic information for radioanalytical chromatographic separations is limited.

The aims of this project were therefore to investigate the kinetics and thermodynamics of the interaction of dissolved species with sorptive materials and to use this information to develop a method for simulating the concentration output from a chromatographic column using a wide range of adjustable variables. This simulation method could be used to support and validate the development of rapid and automated radioanalytical techniques.

1.2. Modelling of chromatographic breakthrough profiles in radiochemistry

As summarised in the literature review (Chapter 2), the flow rate through the column controls the width of the breakthrough or elution profiles of the analyte(s) and interfering species. This can lead to changes in recovery within set volume fractions between different experiments where flow rate is varied. Other column operating conditions such as bed length and diameter, particle size, packing geometry, temperature, loading volume/concentration/matrix as well as rinsing and elution volume/matrix can also impact the shape of the column output concentration profile. Quantification or modelling of these output profiles within the field of radiochemistry has been limited.

1.2.1. Quantification of breakthrough profiles

Prior to the commercialisation of extraction chromatographic resins by Eichrom, the effect of various column parameters on the height equivalent of a theoretical plate (HETP) were investigated for HDEHP on an inert diatomaceous earth support[19,20]; this material was later commercialised as Ln resin. The concept of theoretical plates originates from the processes of distillation[21] and countercurrent extraction[22,23] and was first applied to chromatography by Martin and Synge[24] who defined the theoretical plate as a layer where the concentration in the solution issuing from it is in equilibrium with the mean concentration of solute in the stationary phase throughout the layer. In effect, the chromatographic column is hypothetically divided up into equal length sections within which the average partitioning between the mobile and stationary phases is equal to that at equilibrium. This concept is commonly used in high performance liquid

chromatography (HPLC) or gas chromatography to assess column performance under different conditions. In the characterisation of Ln resin, Horwitz et al. used an equation given by Glueckauf[25] (Equation 1.1.) to calculate the number of plates (N) for a column of a set length (L) from the retention volume, i.e. the cumulative volume at which the peak concentration occurs (V_R, referred to as V_{max} by the authors), and the volumetric width at 1/e of the peak height (W).

$$N = \frac{8V_R^2}{W^2} = \frac{L}{HETP} \qquad \text{Equation 1.1.}$$

This method assumes Gaussian shaped peaks[26] and is determined experimentally by addition of a discrete volume (~0.1 mL in the two publications being discussed) to the top of the column followed by elution using the same matrix; this is known as isocratic elution. In this thesis, the column output from this type of experiment is referred to as a breakthrough profile. This term is used to distinguish isocratic elution profiles from elution profiles generated by separation procedures consisting of sample loading followed by step changes in reagent to selectively elute interferent and analyte species. Breakthrough experiments can be conducted with discrete or continuous sample loading conditions; the latter leads to complete breakthrough whereby the concentration entering the column equals the concentration at the output and dynamic equilibrium in the system has been reached.

The first of the two publications by Horwitz et al.[19] investigated the effects of particle size, HDEHP loading, flow rate and temperature on HETP while the second[20] also looked at the effects of packing method (dry or slurry), column diameter and bed length. In both studies, plots of HETP against interstitial fluid velocity (u_e) were made. In the earlier study, the data showed a positive linear relationship and could therefore be described by the Van Deemter equation (Equation 1.2.) as being within the flow rate range where aqueous phase diffusion (the second term) is negligible (Figure 1.1.). By contrast, the latter study found that HETP started to level off at fast flow rates indicating that applying the Van Deemter equation to this system would be an oversimplification. The authors measured the diffusion coefficients for the analyte (Eu^{3+}) in the mobile and stationary phases and used these values to calculate expected plate heights through more complex equations. The agreement between the calculated and experimental HETP values is within a factor of ~2. This study also quantified the asymmetry of the peaks finding that even at the larger plate heights (0.08 – 0.15 cm), asymmetry factors only reached as high as 1.2.

$$HETP = A + \frac{B}{u_e} + Cu_e \qquad \text{Equation 1.2.}$$

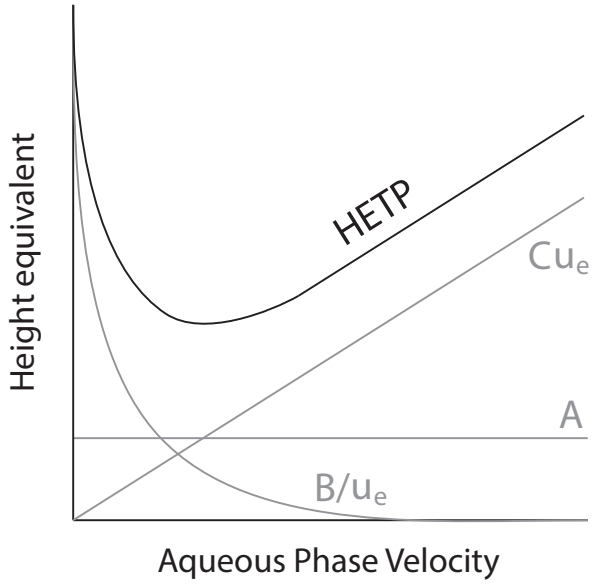

Figure 1.1.
Diagram depicting the contributions to HETP at different aqueous phase velocities.
This includes eddy dispersion (A), molecular diffusion (B) and aqueous-solid transfer kinetics (C).

These two publications also defined the number of free column volumes to peak maximum parameter (k') which is subsequently used in the majority of studies evaluating the interaction of dissolved species with extraction chromatography resins for radioanalytical separations. This parameter is calculated from the volume of the mobile phase (v_m) and V_R (Equation 1.3.) and is converted to the volume distribution ratio (D) by multiplying by the ratio of the volumes of the stationary (v_s) and mobile phases (Equation 1.4.). The volume distribution ratio (D) is a measure of the partitioning of species between the aqueous phase and the immobilised organic phase and is usually calculated from the weight distribution ratio (D_w) which is a measure of the uptake per gram of sorptive material (including the inert support).

$$k' = \frac{V_R - v_m}{v_m} \qquad \text{Equation 1.3.}$$

$$D = k' \frac{v_m}{v_s} \qquad \text{Equation 1.4.}$$

It should be noted that the terminology concerning partitioning of species varies between publications; for example, the term volume distribution ratio (D) is used in the current Eichrom/TrisKem literature but is previously referred to as the distribution coefficient (k_D). The IUPAC recommendations for nomenclature for chromatography[27] prefers the term distribution constant over distribution coefficient as it conforms more closely to the general usage in science. This guidance document also refers to the k' parameter as the retention factor and states that there is no need to include the prime sign. As sorptive materials with both liquid and solid

stationary phases are investigated in this thesis, the distribution constant (k_D) will henceforth refer to the ratio of analyte concentration on the solid material ($[aq]_0$-$[aq]_{eq}$) per solid mass (W_s) to that in the aqueous phase ($[aq]_{eq}$) per volume (V_{aq}) at equilibrium (Equation 1.5.).

$$k_D = \frac{([aq]_0 - [aq]_{eq}) \times V_{aq}}{[aq]_{eq} \times W_s} \qquad \text{Equation 1.5.}$$

HETP values were not as thoroughly investigated in further publications by Horwitz et al. but a value of 0.11 cm is quoted for a reference system using TRU resin (flow velocity = 1-2 mL/cm^2 min) and stated to be the same for Sr elution from Sr resin using the same particle size (50 – 100 µm)[28]. This publication also presents an agreement of k' values obtained via batch and column methods.

Miyamoto et al. used measurements of the HETP to optimise the conditions for a sequential separation procedure of ultra-trace U, Th, Pb, and lanthanides using two different particle size anion exchange resins[29]. As the flow rates used in this experiment were much slower (0.019 - 0.140 mL/min), all three terms in the Van Deemter equation (Equation 1.2.) impact over this velocity range creating a flow rate vs HETP plot with a minima for each particle size (Figure 1.1.).

Although quantification of breakthrough profiles in terms of HETP can be a useful tool in assessing and optimising column performance, the relationship between theoretical plate height and the predicted shape of the column output concentration profile depends on the chosen chromatographic model.

1.2.2. Chromatographic modelling

In order to predict how radioanalytical chromatographic separation procedures will perform under different column operating conditions, a mathematical or computational method for calculating the concentration of analyte and interferent species in the column output solution with respect to time and/or volume is needed. Conversely, this method can be applied to calculate an unknown sample concentration from knowledge of the loading volume, flow rate and output or on-column measurements. This relies on reproducible column operating conditions and robust descriptions of kinetic and thermodynamic parameters including the sorption isotherm.

Calculation of sample loading concentration using mathematical methods has been applied to the on-column detection of α or β emitting radionuclides using scintillating minicolumns using two approaches. In the first approach, detailed by Egorov et al.[30], a small volume sample is loaded

followed by a rinse step to remove interferents; these are seen as transient signals on the detector trace. The analyte is retained on the column and the activity is measured over a specified integration time during either the rinse step or by stopping the flow once interfering radionuclides have been removed. This approach relies on avoiding any breakthrough of the analyte to ensure quantitative retention on the column (< 0.3 % analyte loss). A mathematical formula has been used to calculate the maximum sample loading volume that can be used to ensure this condition is met. This formula includes column dimensions, the HETP and the retention factor (k') and has been solved using an estimated HETP of 0.11 cm. The retention factor in this publication is assumed to be a constant under a given acid concentration meaning that the system is modelled using a linear isotherm. The relationship between flow rate and HETP has not been explored.

The second approach is based on equilibrium being obtained following complete breakthrough of large volume samples. Under continuous sample loading conditions, the concentration retained on the column increases until equilibrium is reached at which point the on-column activity reaches a plateau and the column input concentration is equal to the column output concentration. Egorov et al.[31] compared two mathematical models for describing the column output concentration profile and the on-column activity under continuous loading conditions. These are referred to as the Gaussian model and the low plate number model.

An equation for the total on-column activity as a function of column output volume (A_V) was given in order to calculate the loading volume required to reach equilibrium. A_v was obtained by deducting the integral of the activity concentration breakthrough function from the total activity input (Equation 1.6.). The total activity input was calculated from the activity concentration in the loading sample (C_{in}) and the volume loaded (V_{in}). The Gaussian model function for the continuous loading condition was based on the integral of a Gaussian distribution. This can be expressed using the error function (erf) in terms of the retention volume and the number of plates (Equation 1.7.). The low plate number model was developed by Lövkvist et al.[32] and can be expressed using the complimentary error function (erfc) in terms of the retention volume and the number of plates (Equation 1.8.).

$$A_V = C_{in}V_{in} - C_{in}\int_0^V f(V)dV \qquad \text{Equation 1.6.}$$

$$f(V) = \frac{1}{2} + \frac{1}{2}erf\left(\left(\frac{V}{V_R} - 1\right)\sqrt{\frac{N}{2}}\right) \qquad \text{Equation 1.7.}$$

$$f(V) = \frac{1}{2} erfc\left(\left(1 - \frac{V}{V_R}\right)\sqrt{\frac{NV_R}{2V}}\right) + \frac{1}{2} e^{2N} erfc\left(\left(1 + \frac{V}{V_R}\right)\sqrt{\frac{NV_R}{2V}}\right) \qquad \text{Equation 1.8.}$$

Both models were found to fit the experimental data well for the longer length column tested (2.9 cm) whereas the Gaussian model was less reliable for a shorter column (0.6 cm); it was therefore concluded that the low plate number model was needed if the number of theoretical plates was low ($N \leq 5$).

A more complex method for modelling chromatographic breakthrough profiles was employed in the development of a separation procedure for the recovery of neptunium from spent nuclear fuel[33]. Scaled-down experiments with an organic anion exchange resin (DOWEX MSA-1) column were conducted using Th(IV) as a proxy for Np(IV). The column output concentration profiles were simulated computationally using Fortran 95 text-based programming language. Partial differential equations and boundary conditions describing the chromatographic column as well as a squared-pulse sample loading were input and breakthrough data was generated. Unfortunately, further details of the numerical solving method were not provided. The equations used for describing the system included aqueous phase diffusion and the kinetics of transfer between the aqueous and solid phases. Hydrodynamic assumptions included a uniform diffusion constant and an incompressible fluid. Sorption/desorption kinetics assumed a second-order reaction based on a Langmuir isotherm. A series of five experiments were conducted with varying concentration of Th(IV) in the loading solution whilst maintaining the other column operating conditions such as bed dimensions and flow rate. Increasing the loading concentration caused the breakthrough profile to become more asymmetrical with an earlier peak position and a higher degree of tailing. This was explained by the non-linearity of the sorption isotherm. Values for the maximum solid concentration of Th(IV), the magnitude of sorption and desorption rate constants (ratio kept constant) and apparent diffusion constant were fitted by minimising the sum of the squared deviations between the calculated and experimental profiles. The contributions of sorption/desorption kinetics and aqueous phase diffusion could not be separated so the maximum values for these parameters were assessed instead.

Another example of the use of computational simulation for describing the movement of species through a packed bed in the nuclear industry is modelling of ion exchange at the Sellafield Ion Exchange Effluent Plant (SIXEP) in Cumbria, UK [34]. This plant is responsible for decontamination of storage pond effluents prior to authorised discharge. The final step in the process is retention of

dissolved species (most importantly the conservative ions, Cs^{+} and Sr^{2+}) on an inorganic ion exchanger (clinoptilolite). A dual bed system is used whereby observation of activity breakthrough from the lead bed onto the lag bed is followed by removal of the lead bed, promotion of the lag bed to the lead position and installation of fresh material in the lag position. The SIXEP facility has led to a large decrease in the levels of radioactivity discharged into the Irish Sea.

The cation exchange step has been simulated using gPROMS modelling code through the input of differential equations. These equations include a description of turbulence within the aqueous phase due to the packed bed geometry, diffusion of species across the stagnant layer surrounding the solid particles (film diffusion), ion exchange kinetics and diffusion within the solid particles. Mass balance control is maintained with both the dissolved cation entering the active site and the species released being accounted for. For simplicity it is assumed that one of these species is the sodium cation which is initially sorbed onto the ion exchanger as well as being the major cationic species in the feed solution. Modelling of intraparticle diffusion by Fickian diffusion was found to be an over-simplification due to the added requirement for charge balancing within the pores of the material. Further work involving molecular dynamics showed that intraparticle diffusion is very slow and penetration of species during usual column residence times is only to a depth of a few microns. Using a lumped solid simplification rather than radial discretisation, was therefore an effective way to reduce the computational demand without significantly affecting simulation output. It was noted, however, that intraparticle diffusion would become important when investigating the potential for leaching of retained radionuclides during long-term storage.

1.3. Simulation of chromatographic separations in the wider scientific literature

Whilst there are few examples of simulation being applied for chromatographic radioanalytical separations, guidance can be sought from literature relating to other scientific disciplines such as HPLC and preparative chromatography where simulation methods are better established.

In high performance liquid chromatography (HPLC) the goal is to detect and quantify the different species present in an aqueous sample based on differences in time taken to pass through a chromatographic column and the integrated peak areas. The peaks must therefore be sufficiently resolved and are characterised using calibration standards. The typical HPLC operation sequence involves loading the sample solution in a small discrete volume (μL) and eluting the analytes using a constant mobile phase composition (isocratic elution) or a varying mobile phase composition (gradient elution) using either gradual or step changes. The particle size used for HPLC has decreased since the early 1970s (50 – 100 μm) to a few microns[35] and even more recently < 2 μm

using techniques referred to as ultra performance liquid chromatography (UPLC)[36]. The flow rate through the column is usually optimised to achieve the highest number of plates (N); for example, using a particle diameter of ~5 µm and a bed length of 10 cm, a value for N in excess of 5000 can be easily achieved[35]. Under these conditions and provided analyte concentrations in the loading sample are sufficiently low (within the linear part of the sorption isotherm), the chromatogram peaks are assumed to be Gaussian in shape (Figure 1.2). This is based on the theoretical assumption that the rate of progress down the column for a population of molecules of the same species follows a normal distribution. This produces a symmetrical elution peak with a standard deviation (σ) proportional to the mean retention volume (V_R) or retention time (t_R).

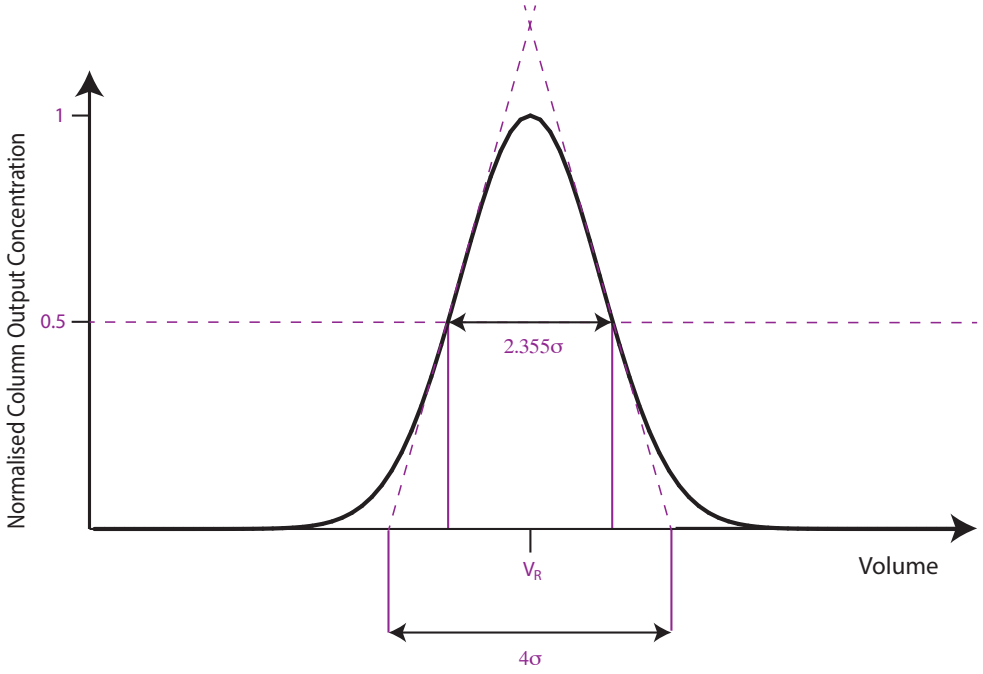

Figure 1.2.
Diagram depicting the Gaussian distribution.

In the case of discrete sample loading, the column output concentration function in terms of volume (Equation 1.9.) using the Gaussian model can be expressed using either the standard deviation (Equation 1.10.) or the number of plates (Equation 1.11.) where $N = (V_R/\sigma)^2$.

$$C_{out,V} = C_{in} V_{in} f(V) \qquad \text{Equation 1.9.}$$

$$f(V) = \frac{1}{\sigma\sqrt{2\pi}} e^{-\left(\frac{V-V_R}{\sigma\sqrt{2}}\right)^2} \qquad \text{Equation 1.10.}$$

$$f(V) = \frac{1}{V_R}\sqrt{\frac{N}{2\pi}} e^{-\frac{N}{2}\left(\frac{V}{V_R}-1\right)^2} \qquad \text{Equation 1.11.}$$

Gaussian shaped peaks have been assumed in the development of software for simulating HPLC[37]. This software (named HPLC Simulator) was written in Java and is available for free on the internet and as a downloadable app for the android operating system. It has been developed for use as an educational tool due to a lack of free or low cost HPLC simulation software with a suitable level of sophistication and ability to run on modern operating systems. The software includes a large number of user input controls including isocratic or gradient elution using mixtures of water and methanol or acetonitrile, temperature, injection volume and flow rate as well as column diameters, particle size and porosity (column and particle). The reduced Van Deemter terms (A, B and C) can also be set. The software includes 22 preloaded organic compounds which may be found in the sample loading solution as well as the option to include custom compounds for which the concentration in the loading solution can be chosen along with thermodynamic parameters. These thermodynamic parameters are the slope and intercept values for the log isocratic retention factor in water vs temperature and solvent sensitivity factor vs temperature plots. These values can be determined experimentally by measuring the retention factor of the species under varying eluent compositions and temperatures.

As the relationship between HETP and column operating parameters such as particle size, extractant loading, flow rate and temperature[19] as well as packing method (dry or slurry), column diameter and bed length[20] has been explored for extraction chromatographic resins (Section 1.2.1.), it is plausible that modelling of breakthrough profiles using the Gaussian distribution for discrete sample loading could be applied to these materials. In fact, the Gaussian model has already been used by Egorov et al.[31] in the case of continuous sample loading although the low number of plates restricted the application of this model for shorter bed lengths (Section 1.2.2.).

Outside of HPLC, chromatographic separations are carried out on columns operated under a much wider range of conditions for a variety of purposes. The field of preparative chromatography, for example, is interested in the use of columns for the isolation of products for further processing or commercial purposes. The operating parameters are therefore chosen to achieve a high level of purity at minimal cost. The loading of large sample volumes with potentially high concentrations of the desired product is common in order to increase production rate[38,39]. This can cause overloading of the column. Operating under these conditions is referred to as non-linear chromatography as the assumption of analyte concentrations remaining within the linear part of the sorption isotherm is not valid. The characteristic retention time for a species is no longer a constant but a function of concentration; i.e. the sorption isotherm. Overloading also increases the asymmetry of elution peaks meaning that a Gaussian distribution can no longer be assumed. In addition to non-linear conditions, chromatographic separations beyond HPLC may take place

under much larger dimensions (industrial scale processes), with larger, irregular or highly porous particles, over a large range of flow rates and taking advantage of a variety of analyte retention mechanisms. The significance of the competing chemical and physical processes can therefore alter greatly over the range of column operating conditions. Robust knowledge of chromatographic processes and use of modelling and simulation techniques is extremely useful for optimisation and quality control.

There is a large volume of literature describing the movement of dissolved species within a packed bed via mass-transfer and/or sorption mechanisms as mathematical functions. Fortunately, there have been a number of comparison or review papers and books written to collate this research and provide guidance on the different approaches available for modelling and simulation of both linear and non-linear chromatography[39–43]. Researchers will often specify a series of differential and/or partial differential equations describing the change in concentration with time and/or position (usually axial column position or radial particle position) for their chromatographic system of interest. By inputting observed or hypothetical conditions, these equations can be used to extract quantitative parameters or simulate experimental datasets. Assumptions and simplifications are commonly used to allow an algebraic solution to be reached or reduce the computing power needed to derive a numerical solution.

Due to parallel development of ideas and changes in the popularity of particular phases and terms over the years, chromatographic terminology can be confusing and classification of approaches to modelling can vary. Focussing on two resources giving extensive summaries of chromatographic modelling and simulation[39,42], a brief introduction to the different approaches will be given. Nicoud[42] has also suggested a unified naming convention based on a *hydro-kinetics* format. The *hydro* refers to hydrodynamics and can either be mixing cells (*MC*), plug flow (*PF*) or plug flow plus dispersion (*PD*). The *kinetics* can either be based on Fickian intraparticle diffusion (*Fick*), a Linear Driving Force approximation (*LDF*) or not included (*Equil*). Indication of whether the model averages analyte concentration over the entire solid particle encompassing the framework and pores (lumped solid – single line above *kinetics*) or distinguishes between concentration in these two locations (pore and solid phases - double line above *kinetics*) was also given. For the most part, this naming convention can be translated into the more traditional terms used by Guiochon[39] (Table 1.1.).

Table 1.1.
Translation between naming convention detailed by Nicoud[42] and more traditional terminology given by Guiochon[39].

Nicoud	Guiochon
$PF - \overline{Equil}$	Ideal model (Equilibrium model)
$MC - \overline{Equil}\ or\ PD - \overline{Equil}$	Equilibrium dispersive model
$MC - \overline{LDF}\ or\ PD - \overline{LDF}$	Lumped kinetic model
$MC - \overline{\overline{LDF}}\ or\ PD - \overline{\overline{LDF}}$	(Lumped) pore model
$MC - \overline{\overline{Fick}}\ or\ PD - \overline{\overline{Fick}}$	General rate model

The ideal model is the simplest approach and does not include any aqueous phase dispersion or sorption/desorption kinetics contributions. If given in terms of theoretical plates, N would be infinite as this model assumes perfect column efficiency. The breakthrough profile generated by this model is a function of the sample loaded, the column dimensions and the sorption isotherm. If the analyte concentration is sufficiently small (within the linear part of the sorption isotherm), the breakthrough profile has the same shape as the injection profile whereas under non-linear conditions tailing or fronting is seen. Tailing is seen for favourable sorption isotherms such as the Langmuir isotherm whereas fronting is seen for unfavourable isotherms. A wide range of sorption isotherms have been developed for single analyte and multi-analyte solutions[40,44]. The applicable isotherm for the chromatographic system under investigation can be determined empirically by measuring the concentration of analyte remaining in solution after contact with the sorptive material under batch conditions using a range of initial aqueous analyte concentrations.

The most complete and complex approach to chromatographic simulation is known as the general rate model. This involves describing the system as a series of partial differential equations covering the four main steps of column-based sorption/desorption[40,43]: (1) fluid flow and aqueous phase dispersion; (2) diffusion across the stagnant layer surrounding the solid particles (film diffusion); (3) diffusion within the sorptive material (intraparticle diffusion); and (4) the chemical reaction (e.g. ion exchange or complexation). The general rate model also distinguishes between the analyte concentration within the pores of the sorptive material and the concentration sorbed on to the active sites. Nicoud[42] assumes that diffusive processes are modelled using Fickian diffusion but also states that this is not always the case and that other models of diffusion are possible. There are multiple different equations for modelling each of these steps; in fact Guiochon[39] remarks that there are almost as many versions of the general rate model as there are specific cases of chromatography and that each author tends to write their own. The description of the chromatographic system must also include boundary conditions and the applicable sorption isotherm. Due to the complexity of this approach, solution of the partial differential

equations in order to simulate the chromatographic process is not obtainable by algebraic methods; a numerical solution using computational software is therefore required.

The remaining approaches are simplifications of the general rate model. The lumped kinetic and lumped pore simplifications model the mass transfer kinetics (film diffusion and/or intraparticle diffusion) as a single differential equation with respect to time. This is referred to as the linear driving force (LDF) approximation. The former does not distinguish between the analyte concentration in the pore solution and the concentration sorbed onto the solid, while the latter applies the LDF approximation to the transfer of species between the aqueous phase and the pore solution[45]. The concentration sorbed onto the solid framework is then proportional to the concentration in the pore solution. The equilibrium dispersive simplification does not describe the sorption/desorption reaction in detail but combines the effects of aqueous phase dispersion and the rate of the overall interaction with the sorptive material in a single parameter. The Gaussian function is shown to be a solution of the equilibrium dispersive model under the restricted assumptions of a linear sorption isotherm, an infinitely narrow loading volume and sufficiently fast sorption/desorption kinetics.

The mixing cell and plug flow plus dispersion approaches are analogous to the Eulerian and Lagrangian models for air or fluid flow. The mixing cell approach defines a series of column divisions of set volume in which the analyte concentration can change due to the addition and removal of molecules whereas the plug flow plus dispersion approach maps the movement of the injected volume. In the latter approach, the volume modelled is not set. Plug flow plus dispersion models therefore include partial differential equations whilst mixing cell models can be represented by ordinary differential equations and algebraic equations only. Simplification to ordinary differential equations via the mixing cell model also removes the need for boundary conditions and reduces the computing power required for numerical solution.

Some of the models using equilibrium or linear driving force approximations can be solved algebraically if the chromatographic system description is not too complex. The Laplace transform has been shown to be a useful tool in converting differential equations into algebraic equations that can be more readily solved[42]. In these cases, the chromatographic breakthrough profiles can be simulated using a single mathematical function. Examples of single equation models included in recent reviews[40,43] are the Thomas model, the Bohart-Adams model, the bed depth service time (BDST) model, the Yoon-Nelson model, the Dose-Response model and the Wang model. Some confusion has arisen over the use of the first three equations in this list leading to a clarification by Chu[46]. Chu demonstrates that an equation which has often been

referred to as the Thomas model in the literature is equivalent to the Bohart-Adams model and that the BDST model is also a rearrangement of the Bohart-Adams model. The actual Thomas model assumes a Langmuir isotherm and a pseudo-second-order rate equation. In the case of continuous sample loading and if axial dispersion is neglected, the algebraic solution for the analyte concentration at the column output can be expressed (Equation 1.12.) where J is a function involving a zero-order Bessel function of the first kind, r and n are constants and T is a function of time (t). This solution is not easily applied although an approximation can be used to simplify the calculation of J under certain conditions.

$$C_{out,t} = \frac{C_{in} \times J\big((n/r), nT\big)}{J\big((n/r), nT\big) + \big[1 - J\big(n, (nT/r)\big)\big] exp\big[\big(1 - (1/r)\big)(n - nT)\big]} \qquad \text{Equation 1.12.}$$

The Bohart-Adams model assumes a (highly favourable) rectangular isotherm and a quasi-chemical rate equation. The algebraic solution in the case of continuous sample loading and with axial dispersion neglected is significantly more manageable than the Thomas equation. The column output concentration function can be expressed in terms of volume (Equation 1.13.) using the Bohart-Adams rate constant (k_{BA}), the flow rate (u) and the analyte concentration on the solid phase at equilibrium (q_e). The value of q_e is a constant due to the rectangular nature of the sorption isotherm. Chu[46] showed that it is possible to replace this constant value with an equation for the Langmuir isotherm (Equation 1.14.) which expresses q_e in terms of the maximum analyte concentration on the solid phase (q_{max}), the analyte concentration in the aqueous phase at equilibrium (C_e) and a constant (b). The calculated breakthrough profiles from the Bohart-Adams model using the Langmuir isotherm correction and the Thomas model were identical indicating that the Bohart-Adams model is a limiting case of the Thomas model for a highly favourable isotherm.

$$C_{out,V} = C_{in} f(V) = \frac{C_{in}}{e^{\frac{k_{BA}}{u}(q_e v_s - C_{in} V)} + 1} \qquad \text{Equation 1.13.}$$

$$q_e = \frac{q_{max} b C_e}{1 + b C_e} \qquad \text{Equation 1.14.}$$

More complex models of chromatographic processes must be solved numerically using computational tools such as ordinary differential equation (ODE) solvers or partial differential equation (PDE) solvers. These tools solve systems of differential equations using a method of initial estimation followed by iterative comparison and readjustment of values at either set or

variable time (and/or spatial) steps until all equations are met to a defined level of accuracy. Different methods for solving systems of ordinary differential equations are available such as Runge-Kutta or Euler's method[42]. ODE solvers can only be used if axial and/or radial positions are discretised. PDE solvers are commonly based on finite difference or weighted residual methods such as orthogonal collocation[42,43,47,48] although research into more advanced methods such as the weighted essentially non-oscillatory (WENO) method is ongoing[49,50]. Commercially available software capable of simulating diffusion and sorption/desorption processes in a chromatographic column include multi-purpose coding environments (MATLAB, COMSOL Multiphysics, LabVIEW), dynamic process simulation tools (AspenONE engineering suite, gPROMS) and geochemical speciation and transport tools (Geochemists Workbench). Some software has also been made freely available over the internet including Orchestra which can be used for simulating chemical speciation and reactive transport processes, PHREECQ which can be used for simulating speciation, batch-reaction, one-dimensional transport, and inverse geochemical calculations and Chromulator which is free for academic users and can be used to simulate various chromatographic systems through a range of executable packages. The available software tools offer a range of capabilities for the simulation of radioanalytical separations. Unfortunately, they also have some disadvantages; more restrictive software with pre-programmed sorptive or diffusive equations may not allow for a sufficiently detailed description of the chromatographic system to be modelled, while more flexible software would require the analyst to have knowledge of the coding language and to build their own description.

Bespoke software may also be written from scratch using any of the available text-based or visual coding languages. This is the approach that has been taken in the PhD project described in this thesis. The advantage of writing bespoke software is that the chromatographic radioanalytical separation system can be described using appropriate mathematical equations in order to strike a balance between simulation accuracy and computational demand. The developed software can then be published with a user friendly interface allowing the analyst to input the experimental parameters and view the results in an accessible format. LabVIEW visual programming language has been used in the development of the bespoke software as it is easy to learn and can also be used for hardware control. In fact, several examples of the use of LabVIEW to control automated radioanalytical separation systems have already been seen[29,51–54]. LabVIEW includes two ODE solvers based on either a cluster of formula strings and variable strings or a strictly typed reference to a virtual instrument (VI) for implementing the right-hand side of an ordinary differential equation. Templates are available to assist in using the ODE solvers. A PDE solver is also available but can only be used for a limited range of predefined equation types (Helmholtz,

heat and wave equations). In order to develop a numerical simulation method for describing radioanalytical separations an assessment of the significance of both aqueous phase dispersion processes (step 1) and sorption/desorption kinetics (steps 2-4) will be made and suitable equations chosen. A successful numerical simulation method should use a suitable amount of complexity to generate accurate descriptions of the experimental breakthrough and elution profiles whilst minimising computation time.

1.3.1. Aqueous phase dispersion

When describing chromatographic processes using the ideal model, it is possible for the breakthrough or elution profile of a species to have the same shape and width as the injected sample. As previously mentioned, this hypothetical scenario is based on linear chromatography using an infinitely efficient column[39] and is not seen experimentally. The observed increase in width from an injected sample to the breakthrough profile is due to both interaction with the solid particles and axial dispersion. Axial dispersion (D_{ax}) is usually described as consisting of a molecular diffusion term and an eddy dispersion term combined in an additive manner (Equation 1.15.).

$$D_{ax} = \gamma_{diff} D_{diff} + \gamma_{eddy} D_{eddy} \qquad \text{Equation 1.15.}$$

$$\gamma_{diff} = 0.45 + 0.55\varepsilon \qquad \text{Equation 1.16.}$$

$$\frac{d[A]_x}{dt} = \frac{\gamma_{diff} D_{diff}}{\delta} \left([A]_y - [A]_x\right) \qquad \text{Equation 1.17.}$$

The molecular diffusion term is a product of the molecular diffusion coefficient (D_{diff}) and a correction factor (γ_{diff}) which is related to the tortuosity of the column. Diffusion coefficients vary according to the size of the molecule and the viscosity of the solution but are typically of the order of 10^{-5} cm^2/s. For example, the value for $½UO_2^{2+}$ in a dilute aqueous solution at 25°C is quoted as 0.426×10^{-5} cm^2/s[55]. A range of different values suggested for the correction factor are listed in Perry's chemical engineers handbook[47] with one highlighted example of an equation for calculating the correction factor according to the porosity (ε) of the column (Equation 1.16). Some authors[26,35], however, suggest that molecular diffusion is more complex as it can occur in the stationary phase as well as the mobile phase. The diffusion coefficient for an inorganic species in the stationary phase of an extraction chromatographic resin can be measured using a capillary-based method[20]. The value determined for Eu(III) in the organic solvent HDEHP (stationary phase for Ln resin) at 25°C is ~2×10^{-7} cm^2/s.

According to the Fick model of diffusion, molecules move from high to low concentration in proportion to the concentration gradient. The rate of concentration change in a discretised volume (x) is therefore a function of the difference in concentration between the defined volume and the neighbouring volume (y) divided by the distance (δ) between them (Equation 1.17.). Using the assumption that a discrete sample volume is delivered to the top of a column with a uniform distribution across the column radius, molecular diffusion causes a vertical (or axial) broadening of the injected sample as it travels down the column. The magnitude of the broadening is proportional to the time spent in the column. The contribution of the molecular diffusion term to the width of the breakthrough profile is therefore inversely proportional to flow rate and can be quantified using plots of HETP change with flow rate focussing on the slope for flow rates less than the HETP minima (Figure 1.1.). Mobile phase diffusion is represented by the second term of the Van Deemter equation (Equation 1.2.).

The other factor contributing to axial broadening of a discrete injected sample as it moves down the column is due to different pathways through the packed bed. The presence of the solid particles in the column means that the flowing solution stream splits and recombines as it progresses down the column. As the pathways are of different lengths and widths, this creates a range of possible flow velocities for a population of dissolved species. This process, known as eddy dispersion (D_{eddy}), can be calculated (Equation 1.18.) by multiplying the aqueous phase velocity (u_e in m/s – often referred to as the interstitial fluid velocity) by the average diameter of the solid particles (d_p in m). As with the molecular diffusion term, a range of different values and equations have been suggested for the correction factor (γ_{eddy}), with some commonly used examples being listed in Perry's chemical engineers handbook[47]. The simplest description of the correction factor listed is a constant value of 0.5 with more complex equations involving column parameters such as porosity and the Reynolds (Re) and Schmidt (Sc) numbers (Equations 1.19. and 1.20.) where u is the fluid velocity (not correcting for porosity) and v is the kinematic viscosity. The equation for calculating HETP includes the overall axial dispersion term divided by the interstitial flow velocity (Equation 1.21.). This means that when γ_{eddy} is a constant, the contribution of the eddy dispersion term to the width of the breakthrough profile is independent of flow rate as represented by the first term of the Van Deemter equation (Equation 1.2.).

$$D_{eddy} = u_e d_p \qquad \text{Equation 1.18.}$$

$$Re = \frac{d_p u}{\nu} \qquad \text{Equation 1.19.}$$

$$Sc = \frac{\nu}{D_{diff}}$$ Equation 1.20.

$$HETP = \frac{2D_{ax}}{u_e} + Cu_e$$ Equation 1.21.

1.3.2. Sorption/desorption kinetics

The rate of transfer between the aqueous and solid phases also contributes to the width of the breakthrough or elution profile. The overall rate is controlled by either the rate of diffusion across the stagnant layer surrounding the solid particles (film diffusion), the rate of diffusion within the solid particles (intraparticle diffusion), the rate of the chemical reaction (for example ion exchange or complexation) or a combination of these processes. Even for species that do not preferentially concentrate on the sorptive material, their passage down the column can be slowed by entering the pores of the solid particles; for example, the difference in accessibility of pores between species is exploited in size exclusion chromatography.

The rate of sorption can be investigated in the column geometry by varying the flow rate and measuring the effect on the breakthrough or elution profiles. The relationship can be quantified using plots of HETP change with flow rate focussing on the slope for flow rates greater than the HETP minima (Figure 1.1.). Alternatively, kinetic rate parameters can be extracted by curve fitting through comparison of calculated and experimental profiles. An example of curve fitting by Yamamura[33] has already been discussed. Investigating the sorption/desorption rate via this method can be quite labour and resource intensive as analysis of multiple breakthrough fractions from many chromatography separations are needed.

An alternative way to measure sorption/desorption kinetics is via closed batch experiments. This technique involves contacting a known mass of sorptive material with an aqueous solution containing the analyte species and measuring the concentration either in solution or transferred onto the solid after a set amount of time. Thermodynamic properties of a material are also often investigated using batch experiments; for example, the effect of acid concentration, pH or temperature on the distribution constant (at equilibrium) can be readily determined. Investigating the effect of different initial aqueous concentrations on the position of equilibrium can also be used to determine the sorption isotherm. The most common isotherm used in the characterisation of sorptive materials is the Langmuir isotherm. The Langmuir isotherm is classified as a favourable isotherm and assumes homogeneous monolayer adsorption. Multiple other isotherms have been developed and are summarised in a number of review papers[43,44,56].

Batch experiments can also be used to separate the different contributions to the rate of sorption/desorption. Quantification of intraparticle diffusion can be achieved by varying the particle size whereas film diffusion can be quantified by varying the mixing speed. These kinetic parameters can then be input into equations describing the chromatographic processes. The approach that has been chosen in this project is to use a numerical simulation method to accurately describe the sorption/desorption systems studied under the batch conditions and then apply the optimised equations to the column geometry.

Due to the popularity of batch experiments for characterisation of sorptive materials, a number of rate equations have been developed for describing sorption/desorption under these conditions. Two of the most popular equations for modelling kinetics assuming that the chemical reaction is the rate-controlling step are the pseudo-first-order[57] (PFO) and pseudo-second-order[58,59] (PSO) rate equations (Equations 1.22. and 1.23. respectively). Both of these equations describe the rate of change of an adsorbed species (q_t) as a function of the effective available sorption sites ($q_e - q_t$), where q_e is the concentration of adsorbed species at equilibrium (mg/g). These two rate equations have been widely applied in the characterisation of novel sorptive systems although there has been some debate on the validity of assigning a PFO or PSO classification based on indicators of goodness of fit due to a mathematical bias towards the PSO equation. In addition there is a lack of agreement on the theoretical derivation of the two equations. Further detail on the application of the PFO and PSO rate equations to sorptive systems will be given later in this thesis and a comparison to the numerical simulation method made (Chapter 3).

$$\frac{dq_t}{dt} = k_1(q_e - q_t) \qquad \text{Equation 1.22.}$$

$$\frac{dq_t}{dt} = k_2(q_e - q_t)^2 \qquad \text{Equation 1.23.}$$

Another group of equations modelling the rate of sorption/desorption assume that intraparticle diffusion is the rate-controlling step. The Fick model of diffusion can be applied to a porous solid to produce a partial differential equation describing the change in analyte concentration with respect to both time and radial position within the solid particle. The terms included in the partial differential equation depend on whether diffusion is assumed to occur mainly within the pores (pore diffusion model – PDM), between active sites located on the walls of the pores (homogeneous surface diffusion model – HSDM) or a combination of both (pore and surface diffusion model – PSDM)[43,47]. This theory can also be extended to include a bidispersed pore structure involving both macro- and micro-pores either in series or in parallel by defining two

partial differential equations. Another variation of the pore diffusion model is the shrinking core model which defines a mass transfer zone that begins on the outer region of the particle and progresses inwards at a set velocity. Amongst the terms included in the partial differential equations there will be either an effective pore diffusion coefficient or a surface diffusion coefficient (or both). The pore diffusion coefficient is usually calculated from the molecular diffusion coefficient for the analyte divided by a tortuosity factor (τ) for which several predictions based on particle porosity have been made[42,47]. Solid diffusion coefficients are usually smaller and less well understood although some values have been suggested.

A few solutions to the differential equations for describing intraparticle diffusion have been published in order to predict the average analyte concentration on the lumped solid phase at time (t)[60,61]. One of these solutions is the Crank equation (Equation 1.24.) which has been further simplified to model either short or long times only. This model assumes surface diffusion only as indicated by the surface diffusion coefficient ($D_{diff,s}$). The long times simplification is also commonly known as the Boyd equation. Another popular equation is the Weber-Morris equation (Equation 1.25.) which uses a simplified diffusion rate coefficient (k).

$$\frac{q_t}{q_e} = 1 - \frac{6}{\pi^2}\sum_{n=1}^{\infty}\frac{1}{n^2}e^{-\frac{D_{diff,s}n^2\pi^2 t}{(0.5d_p)^2}} \qquad \text{Equation 1.24.}$$

$$q_t = k\sqrt{t} \qquad \text{Equation 1.25.}$$

The Crank model of intraparticle diffusion was applied to the sorption of the uranyl ion onto a novel solid-phase extractive scintillating resin[62]. An estimated surface diffusion coefficient of 2 x 10^{-12} cm^2/s was determined by comparing the time taken to achieve a set ratio of loading/output concentration for two columns of different particle size that had previously been contacted with analyte and stored for either 18 or 190 hours. Input of this diffusion coefficient value into the Crank model allowed for prediction of radial concentration plots at different time intervals for two different size particles. Full radial equilibrium was determined to be reached after 4000 hours for particles with a radius of 63 µm and after 25000 hours for particles with a radius of 192 µm. This slow rate of intraparticle diffusion was suggested to be due to the gel-type structure of the polymer based material developed.

Film diffusion (or external mass transfer) is harder to quantify under batch conditions so is often minimised by maintaining a well-stirred solution. One example where film diffusion for radionuclide sorption on an anion exchange resin has been measured uses a single bead and an

acoustic streaming method to control the mixing rate[63] (see Section 1.4. for more details). Film diffusion is also usually assumed to follow the Fick model of diffusion. The change in analyte concentration with respect to time for the average solid particle ($[A]_s$) can therefore be expressed (Equation 1.26.) as a function of the concentration gradient between the bulk aqueous solution ($[A]_{aq}$) and the surface of the lumped solid particle ($[A]_{s,surface}$) where SA_s refers to the surface area of the solid and δ is the thickness of the stagnant layer. The value of δ is calculated (Equation 1.27.) from the diameter of the solid particles (d_p) and the Sherwood number (Sh). Multiple equations for the calculation of the Sherwood number are given in the literature with recommended correlations listed in modelling and simulation guides[42,43,47]. In general, these correlations include the dimensionless Reynolds and Schmidt numbers (Equations 1.19 and 1.20.).

$$\frac{d[A]_s}{dt} = \frac{D_{diff} SA_s}{\delta V_s}\left([A]_{aq} - [A]_{s,surface}\right) \qquad \text{Equation 1.26.}$$

$$\delta = \frac{d_p}{Sh} \qquad \text{Equation 1.27.}$$

Numerical simulation of chromatographic systems using the general rate model is based on combining equations describing the sorptive interaction and the extent of axial dispersion. The suitable level of complexity is often based on empirical measurements made under either batch or column conditions to determine parameters such as the nature of the sorption isotherm and the rate controlling sorption step for the system under investigation. As previously mentioned, diffusion is usually modelled using Fickian characteristics. Nicoud[42], however, suggests that there may be situations where the Fick model of diffusion may be inadequate and other models such as the Maxwell-Stefan model of diffusion may be needed due to interactions between dissolved species. This adds further complexity to the numerical simulation method.

Conversely, the contribution of mass transfer (film diffusion and/or intraparticle diffusion) can be simplified using the linear driving force (LDF) approximation. This approximation can be thought of as a first order rate equation based on the local deviation from equilibrium[39]. The driving force is for the concentration in two neighbouring regions to be equal[42,43,47]. If kinetics is determined to be controlled by film diffusion only then the LDF approximation for the change in concentration in the lumped solid phase is equal to Fickian diffusion across the stagnant layer (Equation 1.26.). If intraparticle diffusion is determined to be significant, then the change in concentration in the lumped solid phase is a function of the analyte concentration gradient between the surface of the particle and the average of the entire lumped solid volume (Equation 1.28.). This function includes a rate coefficient (k). If film diffusion is assumed to be instantaneous, the concentration

at the surface of the particle is equal to the bulk aqueous phase concentration and k can be calculated from either the pore diffusion coefficient or the surface diffusion coefficient or both. If film diffusion is included, the concentration gradient between the bulk solution and the particle surface are incorporated into the differential equation along with the thickness of the stagnant layer. It has been shown that in many situations the LDF approximation produces comparable simulated datasets to more complex models using Fickian diffusion[64].

$$\frac{d[A]_s}{dt} = k\left([A]_{s,surface} - [A]_s\right) \qquad \text{Equation 1.28.}$$

1.3.3. Other contributions to the shape of breakthrough profiles

Besides the sorption isotherm, sorption/desorption kinetics and aqueous phase dispersion, a few other experimental variables that can impact upon the shape of the breakthrough profile are worth mentioning. Firstly, the temperature at which the separation procedure is operated can have an impact on the sorption/desorption kinetics and distribution constant at equilibrium. For radioanalytical separations, temperature is not usually a variable that is controlled as separation procedures are carried out at room temperature. It should, however, be considered if a rapid or automated technique is developed involving a heat assisted volume reduction or dissolution step directly prior to a column-based separation.

Another variable to consider is the packing density and structure of the sorptive material bed. This is a variable that has the potential to alter over the course of the chromatographic procedure. For example, application of high pressures to achieve fast flow rates could compact the bed, leading to lower porosity and shorter bed length whereas sudden drops in pressure could cause a movement of particles in the opposing direction. Allowing the column to dry out can also impact the structure observed upon resuming the delivery of solution as pockets of air may remain causing a reduction in the accessible volume of the column. The packing density and bed length can also change due to shrinking or swelling of the solid particles in response to changes in the solution matrix such as pH. The magnitude of all these changes depends on the sorptive material chosen, the initial column packing method and whether a preconditioning step using the same matrix and flow rate as the sample loading step is included. Horwitz et al.[19,20] found that both temperature and packing method (dry or slurry) had an effect on measured HETP values.

Although the effect of eddy dispersion and molecular diffusion processes on the width of breakthrough profiles has been discussed (Section 1.3.1.), both of these processes are concerned

with the vertical distribution of a species population in the column. The sample is assumed to be loaded evenly across the column radius and not show any variation in progress down the column with radius. In reality, this is not always a valid assumption. Evidence of a non-uniform radial distribution of an injected solution has been achieved using computed tomography[65]. In this study, the progress of a potassium iodide solution was monitored by taking a cross-sectional image at four different positions down the column length. The chromatographic front was shown to arrive earlier in the centre of the column than at the edges. It was concluded that the radial difference in flow rate was due to denser packing near the column walls as a product of frictional forces during the slurry packing method. Another possible cause for non-uniform radial distributions is temperature induced viscosity gradients[42]. The radial and vertical distributions can be combined into a single eddy dispersion parameter. Alternatively, if the column radius for the chromatographic system being modelled is sufficiently large, the radial component can be neglected as a flow rate gradient will only occur over a small fraction of the cross-sectional area in the vicinity of the column walls.

The final variable to consider is the impact of other dissolved species. If the selectivity of the sorptive material is low, other species can compete for the same active sites. When the concentration of competing species is sufficiently high, the distribution constant of the analyte on the sorptive material may decrease due to saturation of the active sites causing breakthrough or elution profiles to shift to a lower retention volume. It is also possible that whilst the distribution constant at equilibrium may be unaffected by high concentrations of other dissolved species, the kinetics of sorption/desorption may alter. This was observed in a comparison of the interaction of barium and radium with MnO_2 resin under conditions of varying salinity[66]. It was suggested that Ca^{2+} ions in the saline solution can be taken up by sorptive sites but that this reaction is less favourable than the uptake of Ba^{2+} ions. This means that the final position of equilibrium is independent of calcium concentration but the time taken to reach equilibrium decreases at higher concentrations due to the kinetics of ion exchange. The interaction between different dissolved species on analyte distribution constants on DGA resin and UTEVA resin was investigated in detail by Roman[67]. In addition to competition between species, formation of co-complexes may occur. The co-complex will exhibit a different distribution constant to that of the individual analytes; the addition of a dissolved species causing an increase in affinity is described as having a synergistic effect whereas a species causing a decrease is described as antagonistic. Zirconium was seen to have a synergistic effect on americium sorption on DGA resin as did technetium under hydrochloric matrices. Sometimes the formation of a co-complex or a change in acidity can cause a change in solubility of an analyte. For example, $Al(NO_3)_3$ is reported to

cause a salting-out effect on Th(IV)[68]. The formation of a precipitate can extend the time taken for a species to travel down the column as well as having an effect on the pressure needed to maintain the flow rate. Likewise, the solubility of certain sorptive materials may also be dependent on the solution matrix with loss of solid phase volume via dissolution causing a change in column packing and affecting sorption/desorption kinetics. The amount of organic phase immobilised on extraction chromatography resins can also reduce over the course of a chromatographic sequence (or multiple sequences if the column is reused). Fortunately, there are methods to reduce this leaching process; for example, the extraction potential of Sr resin can be stabilised by addition of the organic solvent (octan-1-ol) to the aqueous reagent solutions[69].

1.4. Sorptive materials studied

The three materials investigated in this study are UTEVA resin, anion exchange resin and zirconium phosphate. The interaction of dissolved inorganic species with these three sorptive materials is investigated under both batch and column conditions and is expected to vary due to the different solid structures and uptake mechanisms.

UTEVA resin is an extraction chromatography resin manufactured by Eichrom (distributed in Europe by TrisKem) and was first characterised in 1992[70]. The solvent extractant is diamyl amylphosphonate (DAAP) which was selected for its high retention of uranium in 1-3 M HNO_3, difference in selectivity between uranium and thorium and minimal solubility in aqueous solutions. UTEVA resin is prepared by impregnating an inert polymeric support material with the undiluted extractant at a loading ratio of 40 %. In the batch and column breakthrough experiments detailed in this thesis, a particle size of 100 – 150 µm was used with 8M HNO_3 as the aqueous phase. The retention factors (k') for Pu (IV), Np(IV), U (VI), Th (IV) and Am (III) under these conditions are approximately 1000, 400, 300, 200, 0.07 respectively. The analytes investigated in this thesis were uranium and thorium which are retained as the neutral nitrate species $UO_2(NO_3)_2$ and $Th(NO_3)_4$ by complexation with DAAP under sufficient nitric acid concentration. In the column elution experiment (see Chapter 6), uranium and thorium were also loaded in 8M HNO_3. Thorium was then eluted using 6M HCl followed by uranium elution in 2% HNO_3. The retention factor (k') for U (VI) is ~200 in 6M HCl but drops to ~20 in 2% HNO_3, whereas k' for Th (IV) in 6M HCl is ~0.9. The quoted retention factor values are taken from the characterisation publication by Horwitz et al.[70] and were calculated from measurements taken from batch experiments using an equilibrium time of 2 hours and a conversion factor (D_w/k') of 1.665. An agreement was noted, however, between the k' values for uranium and thorium calculated using the batch method and those calculated from the peak position in a

chromatographic breakthrough experiment using 2M HNO_3. A description of sorption/desorption kinetics under batch conditions was not given but it was suggested that equilibrium was reached in less than 15 minutes (although the solid/aqueous ratio was varied between experiments).

A later publication[71], showed the kinetics of sorption for U (VI) onto UTEVA resin to be even faster with equilibrium being obtained in less than 10 minutes using a solid/aqueous ratio of 0.01 g / 1 mL and a particle size of 50 – 100 µm. This was comparable to similar experiments using other extraction chromatographic resins such as TEVA resin and TRU resin[71] as well as the sorption of Eu (III) on DGA resin[72]. Slower kinetics were noted, however, for the sorption of Ta on DGA resin under similar conditions with equilibrium taking ~1 hour under batch conditions and a broader breakthrough peak seen in the chromatographic column experiment in comparison to other analytes[73]. The cause of the slower interaction is unknown. A slower rate of uptake was also seen for uranium on UTEVA-2 resin (not currently commercially available) with equilibrium taking between 20 – 30 minutes to be obtained[74]. This difference is attributed to the higher viscosity of the solvent extractant on this material in comparison with UTEVA resin; the stationary phase for UTEVA-2 comprises of an equimolar mixture of DAAP and Cyanex 923. A lower solid/aqueous ratio can also increase the time taken to reach equilibrium; ~2 hours was needed for U(VI) and Th(IV) to equilibrate with a material using carminic acid as the immobilised extractant and a mixing ratio of 0.06 g / 100 mL[75]. It was observed that the rate of sorption/desorption under batch conditions was proportional to agitation speed which would indicate that film diffusion is the rate controlling step. This process was not quantified, however, and further investigations used a high agitation speed in order to remove the contribution of film diffusion and compare the fit of the kinetic data to either complexation reaction controlled models (PFO, PSO and Elovich) or intraparticle diffusion models (Bangham or Weber-Morris). The best fit was obtained by either of the intraparticle diffusion models. This is not an unexpected result as the Bangham model can be understood as the generalization of the Weber-Morris model[60]. This connection was not acknowledged in the publication and the Weber-Morris model was referred to as the intraparticle diffusion model highlighting the confusion that exists around algebraic solutions of differential equations for sorptive processes.

The anion exchange resin used in the experiments detailed in this thesis is also supplied by TrisKem. This material consists of quaternary amine functional groups on styrene divinyl benzene polymeric beads with a cross linkage of 8 % and a dry mesh size of 100 – 200 (74 – 149 µm). The resin is preloaded with chloride ions which can then be exchanged with anionic species with a greater affinity for the active sites. The system studied under both batch and column conditions was the interaction of uranium and thorium with this resin from an 8M HNO_3 aqueous phase.

Under these conditions Th (IV) is retained as the stable $[Th(NO_3)_6]^{2-}$ anion with a weight distribution constant of ~300 whereas U (VI) is less strongly retained with a weight distribution constant between 10 and 20[76,77]. This is due to the lower equilibrium concentration of $[UO_2(NO_3)_4]^{2-}$ anions[78].

Data on the kinetics of batch sorption/desorption for organic ion exchange resins indicates that this process is slower than for extraction chromatographic resins. Equilibrium between Th (IV) in 6M HNO_3 and DOWEX MSA-1 (macroporous type, 200 – 400 mesh) was obtained by 0.84 days (solid/aqueous ratio not stated)[33]. Another publication[78] found that Pu (IV) sorption from 7M HNO_3 onto DOWEX 1x4 (50 – 100 mesh) took 6 hours to reach equilibrium whereas sorption onto Tulsion A-PSL resins was complete in 4 hours (using a ratio of 0.25 g solid / 3 mL aqueous phase). A factor suggested to reduce the time taken for organic cation exchange resin systems to reach equilibrium (from days to minutes) is the presence of hydrophilic sulfonic acid functional groups[79]. The rate of ion exchange in these materials is suggested to be controlled by diffusion; either external or intraparticle[63,80,81]. The extent of film diffusion was investigated by comparing the kinetics of Pu (IV) sorption onto a single AG 1x4 bead (~760 µm diameter) under stationary conditions and using acoustic mixing (0.02 mL of 7.5 M HNO3 as the aqueous phase)[63]. Under the well-mixed conditions, equilibrium was reached in ~4 hours and the calculated rate constant was 3.1 – 5.8 times faster than when no mixing was applied. This was equated to a drop in the thickness of the stagnant layer from 153 µm to 16 µm. Comparison between different intraparticle diffusion models for the sorption of Cu^{2+} on IONAC SR-5 (470 – 530 µm particle size) indicated linear Fickian behaviour as described by the Crank model at low analyte concentrations and shrinking core behaviour at high analyte concentration[81]. This radially diffusive behaviour was visible on an imaging microscope. The shrinking core model also gave the best description for the kinetics of sorption of Cr(III) onto Diphonix cation exchange resin (particle size = 150-300 µm) even though the initial concentration was kept low in this study[80].

The behaviour of an inorganic ion exchanger was also studied in this thesis. The material chosen was a zirconium phosphate supplied by a commercial-in-confidence source. Characterisation of particle size by sieving revealed a distribution of 125 – 1000 µm with 57 % of the particles (by mass) falling within the 710 – 1000 µm range. XRF analysis indicated that the material was supplied in the sodium form. No information on the amorphous or crystalline nature of the material studied or its porosity was obtained. Literature for α-zirconium phosphate states that cations with a diameter over 2.61 Å may not enter the pores unless a base is added[82] whereas amorphous materials exhibit a larger pore size of 10 – 30 Å and may also have a slight mesoporous structure[83].

Within the nuclear industry, zirconium phosphates have been suggested for use in the industrial scale removal of radionuclides from aqueous wastes[84] and even as ceramic waste forms for nuclear waste immobilization[85,86]. Advantageous properties include high thermal and acid stability, high capacity and the ability to retain a large variety of species; one material showed potential for the incorporation of almost all 42 nuclides present in a typical commercial nuclear waste[86]. Although these applications often use zirconium phosphate for irreversible ion exchange purposes, reversible reactions have been published for amorphous zirconium phosphate[82,87,88]. The kinetics of ion exchange is expected to be controlled by intraparticle diffusion[89]. Using a solid/aqueous ratio of 0.1 g / 10 mL, equilibrium was not reached after up to 150 minutes for Pb(II), Bi(III) or Th(IV) on amorphous zirconium phosphate (30 – 60 mesh)[87]. The authors of that publication fitted rate constants using a simple first-order kinetic model. Another study found fast initial kinetics due to outer-surface sorption followed by a slower diffusion dominated phase for an amorphous sample (0.05 g / 100 mL, 1 – 20 μm). Equilibrium was observed to be reached in less than an hour which could be due to the small particle size and large surface area ratio. This two-step process was also suggested in early kinetic analysis of ion exchange in very fine crystalline particles[90]. More recent investigations have indicated that once diffusion control has been established, the rate of hydrogen-sodium exchange within α-zirconium phosphate is determined by the concentration and mobility of defects[91]. The kinetics and thermodynamics of batch and column interactions of barium with zirconium phosphate are investigated in this thesis. The aqueous phase used was seawater at a pH of ~8. If the rate of sorption/desorption is dominated by intraparticle diffusion, the time taken to reach equilibrium is expected to be relatively long due to the large average particle size.

1.5. Thesis outline

This thesis details a novel approach for the development of a numerical simulation method for describing and predicting chromatographic profiles in radioanalytical separation procedures using LabVIEW visual programming language (National Instruments). This approach starts by simulating the interaction of dissolved species with sorptive materials in a closed system and then applies the optimised equations to a packed bed geometry via the addition of appropriate flow dynamics. This demonstrates that kinetic and thermodynamic parameters can be measured under batch conditions and input into simulation software to predict chromatographic elution profiles. This method has been tested using three contrasting sorptive materials and a range of column operating conditions.

Chapter 2 is a review of emerging rapid and automated radioanalytical techniques with a focus on methods for increasing the flow rate through chromatographic columns. The range of flow rates tested and the impact that increasing the flow velocity has on analyte recovery and decontamination factors is discussed.

Chapter 3 describes the overall methodology used in the collection and interpretation of data.

Chapter 4 describes the development of a numerical simulation method for modelling the kinetics of sorption/desorption under batch conditions. The use of an ordinary differential equation solver is explained along with the required LabVIEW coding and differential equations for both porous and non-porous materials. The effect of external mass transfer is assessed by comparing experiments conducted under constant tumbling or stationary conditions. The impact of analyte and interferent concentration is also investigated. The numerical simulation method is compared to the pseudo-first-order and pseudo-second-order equations as well as the Langmuir isotherm.

Chapter 5 describes the adaptation of the method developed in chapter 3 for describing closed systems into a numerical simulation method for modelling chromatographic column breakthrough in experiments conducted under controlled flow conditions. The interaction between kinetic and hydrodynamic processes has been investigated and recommendations for further investigations to improve the accuracy of the method have been made. The tolerance of the method to errors in input parameters has been assessed along with the effect of physical phenomena such as backpressure and extractant leaching.

Chapter 6 extends the numerical simulation method to describe the chromatographic breakthrough of two species from an extraction chromatographic resin simultaneously under a range of sample loading concentrations and volumes. The numerical simulation method is also compared to the Gaussian and Bohart-Adams single equation models. Finally, the potential for implementation of numerical simulation as a radioanalytical method development tool is discussed using an example elution sequence.

Chapter 7 describes the overall conclusions drawn from the project and the possible future applications.

Chapter 2: Review of Emerging Rapid and Automated Techniques in Radiochemistry

2.1. Chromatographic techniques

As part of the radioanalytical procedure, separation of analytes from the bulk matrix and each other was historically achieved by either precipitation followed by centrifuging/evaporation or by liquid-liquid extraction (LLE). While the former technique is still widely used for preconcentration of the analyte and the removal of some bulk matrix elements, LLE has been largely replaced by extraction chromatography. The immobilisation of analyte-specific solvent extractants onto polymer beads allows for easier and more efficient separations; producing less waste and leading to higher decontamination factors. The need to prepare batches of resin prior to analysis, however, meant that the use of this method was limited until the revolutionary work of Horwitz et al. to develop a wide range of commercially available extraction chromatographic resins; these have been manufactured and distributed by Eichrom since its foundation in 1990 (distributed in Europe by TrisKem).

Another company that has been developing highly selective materials for column-based separation of metals and anions for several decades (since 1988) is IBC. These solid phase extraction (SPE) materials are based on molecular recognition technology and comprise of a macrocyclic ligand chemically bonded to a solid support[92]. The range of materials branded SuperLig have industrial scale nuclear applications whilst the range branded AnaLig are designed for analytical use. A comparison between solvent extraction and SPE for the isolation of Sr-90 from fish bone ash samples indicated that in a nitric acid solution, the selectivity of the solvent based extraction chromatographic Sr-resin for strontium was superior than that of AnaLig Sr-01[93]. An advantage of AnaLig Tc-02 over TEVA resin for the isolation of Tc-99 is that elution is achieved using hot deionised water meaning that it can be directly mixed with the scintillant for liquid scintillation counting without any additional matrix adjustment steps[94].

An alternative type of chromatography used in radioanalytical procedures is ion exchange chromatography. Both anion and cation exchange materials are often used in columns as a preconcentration step or in separation sequences where the charge on a metal ion is altered by control of the pH of the eluting reagent. These resins come preloaded with a weakly bound ion; this is then replaced by competing dissolved species with a greater affinity for the active sites.

In addition to isolation of analytes for radiometric or mass spectrometric detection via selective retention and elution sequences, species may be preferentially concentrated on a column containing a dual functionality scintillating extractant or composite column (extraction chromatographic resin or ion exchange resin plus scintillating particles)[95]. The light output is detected on line by photomultiplier tubes positioned in close proximity to the preconcentrating column. In addition to the linear column geometry, this analysis method has been applied to a disc-shaped bed.

The flow rate through columns containing a sorptive material can be controlled using automated or semi-automated systems. Although a controlled increase in flow rate through the column can be achieved by the attachment of a pump or vacuum box, the linear packed bed geometry also lends itself to more complex fluid handling systems using a computer controlled instrumental set-up of connected tubes, pumps, valves and possible online analyte detection. As most chromatographic sequences were originally developed using gravity-driven flow rates, changes to the expected analyte yields and decontamination from interferents could be observed at elevated flow rates. Some examples of flow rate controlled chromatographic separations in the field of radiochemistry and the effects on the eluted fractions arising from the increase in solution velocity will therefore be discussed. The sorptive material, analytes measured, flow rate control method and range of flow rates tested have been tabulated for direct comparison (Table 2.1.). Although the flow rate (u) is usually quoted in mL/min, the linear interstitial velocity (u_e) is dependent on the internal column diameter (d_{col}) and column porosity (ε) which is a measure of the packing density (Equation 2.1.).

$$u_e = \frac{u}{\pi \times (0.5 \times d_{col})^2 \times \varepsilon} \qquad \text{Equation 2.1.}$$

2.1.1. Vacuum box

Vacuum based systems are yet to be applied to fully-integrated automated systems where samples and reagents are programmatically introduced; however, the simplicity of the equipment and versatility to use either columns or stackable resin cartridges has led to this system gaining popularity over recent years by reducing the time taken to elute solutions from batches of up to 24 samples. Some authors did not test a range of flow rates but kept to the 0.5 - 1 mL/min recommendation from Eichrom for use with their 2 mL volume cartridges[73,96] although in one of these examples, studies of the kinetics of sorption were made under batch conditions[73]. Other authors did not specify their reasoning but often chose a slower flow rate for loading and elution

steps than for rinsing[97–99]. It was also noted that if a constant vacuum pressure was maintained over the course of the chromatographic separation, this could lead to different flow rates depending on the solution flowing through the column[100]. Where a range of flow rates were tested, the method efficiency did not change within the range tested[100] or only began to be effected at very high flow rates[101]. The latter study quoted flow rate in mL/s and did not specify the range of flow rates tested but suggested an upper limit for desorption flow rate above which the normalized percentage of extraction decreased to 94 %.

2.1.2. Pressurised injection

Another method for increasing flow rate is the use of nitrogen gas to apply a positive pressure to drive sample and reagent solutions from their containers and through the column. One study[68] compared the relationship between applied pressure and flow rate for different reagent solutions and either a single or tandem column set-up and found quite a large range (9.7 - 30.0 mL/min from +20 PSI) as well as deviations between repeated experiments under the same conditions indicating that this method has a low level of flow rate control. They did, however, highlight some advantages of the technique; it is capable of achieving high velocities, is relatively low cost and could be useful for separations where viscous liquids are present or where reactions produce large volumes of gas. The level of automation in the procedures using pressurised gas driven flow varied with some authors stating the use of multi-position valves to select the sample/reagent and deliver it to the column[68,102,103]; some authors making use of automated fraction collectors[68,104,105]; and one example using Chromeleon 7 software to control the operation of these components in a timed sequence[68]. An optimum flow rate was determined in two studies[29,103]; Sommers et al.[103] found that above 0.1 mL/min the amount of Ba in the loading and wash fractions increased (this data was not presented) whereas Miyamoto et al.[29] investigated in more detail, varying particle size, applied pressure and column length to optimise the resolution of analyte peaks. They used theoretical plate theory to determine the conditions needed to minimise the height equivalent of a theoretical plate (HETP – see Section 1.3.). Some kinetic considerations were also made in the automated system for actinide separation[68]; the elution of U(IV) was suggested to be more challenging due to the increased contact time with the resin bed, the retention of Th(IV) was found to be lower than previous experiments run at half the flow rate, and a pause of at least 7 minutes was needed to allow for the reduction of Np(IV) to Np(III) to occur. The authors acknowledged that further investigations could help in the understanding of these phenomena.

2.1.3. Flow injection and sequential injection

The most widespread method for controlling the rate of solution flow through a column is the use of a fluid pump. These techniques are based on flow injection analysis (FIA) which was developed by Ruzicka in the 1970s[106] as an alternative to segmented flow analysis (SFA). Initial FIA techniques were based on sample injection into a laminar flow stream and the subsequent measurement of a transient rather than a steady state signal[107,108]. Detection challenges and flow rate inconsistencies associated with the air bubbles separating reaction solutions in SFA systems were also eliminated[109,110]. Continuous flow injection (cFI) in the context of radiochemical separations involves a peristaltic pump coupled to an injection valve to achieve a continuous flow of sample solution followed by a sequence of wash volumes, valence adjustment solutions and eluents though a resin bed (Figure 2.1). A second generation of flow injection analysis was developed in 1990 to take advantage of increased computer based control of components therefore offering greater versatility and lower reagent consumption. In sequential injection (SI) methods, samples and reagents are sequentially aspirated into a holding coil via a multi-position valve (Figure 2.1). The flow is then reversed and the solutions are pumped through the column in the opposite order (last aspirated enters column first). This method commonly uses a syringe pump, although it was noted that a peristaltic pump could also be used[111].

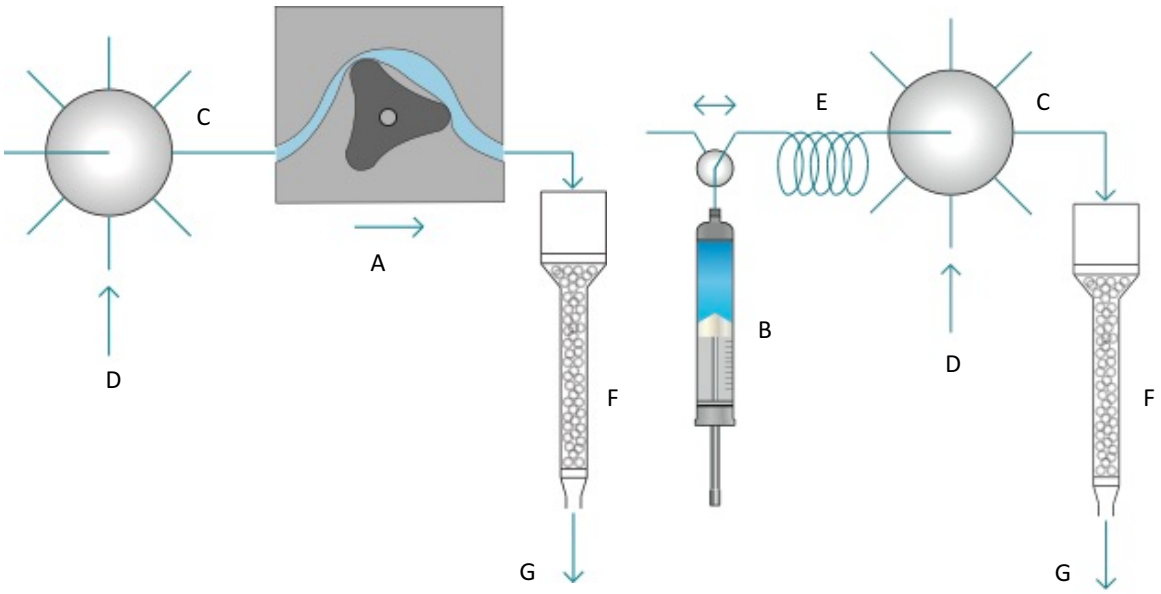

Figure 2.1.
Illustration of flow injection (left) and sequential injection (right).
Diagrams show a peristaltic (A) or syringe (B) pump, a multi-position valve (C) with a highlighted sample or reagent entry port (D), a holding coil (E) and the separation column (F) with an outlet (G) where the resulting eluent is collected, detected online or diverted to waste.

In more recent years a larger variety of fluid handling methods such as reverse flow injection analysis (rFIA), multisyringe flow injection analysis (MSFIA), multicommutated flow injection analysis with multi-channel pump (MCFIA), multi-pumping flow systems (MPFS) and lab-on-valve (LOV) systems with bead injection as well as miniaturised and microfluidic devices have been developed[108]. A few reviews[112,113,107,114,115] have been published summarising the use of automated fluid handling techniques in chromatographic radiochemical analysis detailing the level of automation, choice of components and the subsequent detection method; this could be either off-line or online including ICP-MS, flow-through or on-column scintillation and spectrophotometric flow cell. Another comprehensive review of the literature will not be made here, instead a description of the different methods for controlling flow rate and the kinetic considerations made will be given.

2.1.4. Peristaltic pump

Flow rate is controlled using a peristaltic pump in a large number of publications. This technology uses rollers to compress tubing, pushing the contained solution in the direction specified. The flow rate is determined by the speed of rotation as well as the size of the tubing. Over time, the flow rate produced by a particular rotation speed can decrease due to wear of the tubing; the extent of this effect depends on the choice of tubing material and the pressure applied. Regular recalibration is required to maintain flow rate accuracy. Additionally, the accuracy of aspirating volumes smaller than one pump head revolution is low due to the random starting position of the rollers[111]. Nevertheless, a large range of flow rates are possible. Over half of the publications listed did not give an explanation of the flow rate(s) chosen or any evidence of testing other flow rates during method development. Four of these publications used a single flow rate whereas six used different flow rates depending on the step within the chromatographic separation procedure. Within the publications which listed a range of flow rates tested, four of these found no significant effect on the analyte yield within the expected elution fraction for the range tested[54,116–118] although a small degree of peak broadening at faster fluid velocities was observed by one research group[117,118]. A broadening of the elution peak was also observed by Chung et al.[52,53] The flow rate for the elution step was therefore chosen to optimise both analysis time and reagent volume. The earlier study states that the maximum flow rate through four columns in parallel is 5 mL/min using their automated system[52]. The second study also suggested reducing the flow rate in the rinsing step to avoid early stripping of the analyte[53]. A slower flow rate for elution in comparison to loading was also required in the chromatographic procedure developed by Hosseini et al.[119] for the concentration of uranium and thorium from a large sample volume (3 L to 10 mL). They tested the removal efficiency in the loading step over a large range of flow rates

and found a difference in the flow rate at which a decrease from 100 % occurred between the two analytes. The largest range of flow rates tested was by Moon et al.[66] who stated an upper limit of the pumping rate as 300 mL/min. In this experiment radium and barium were concentrated from a large sample volume (1 L) and recovered by dissolving the extractant off the resin substrate, meaning that the flow rate range only applied to a loading phase. No decrease in method efficiency was seen across the entire range for both analytes when loaded in deionised water, however, if the loading sample was of a higher salinity (35 ‰), a decrease in extraction was seen even at moderately elevated flow rates (above gravity flow rate). Kinetic sorption data was also conducted under batch conditions and showed a decrease in the rate of sorption with increasing salinity. This study supports the direct link between data gathered under batch conditions and the movement of species through a packed bed.

2.1.5. Linear motion pump

Greater control over flow rate and solution volume can be achieved using a linear motion pump. Within the scientific literature, there are examples of radiochemical separations using digitally controlled single syringe pumps[30,31,51,69,120–127], plunger or piston pumps[33,98,128], multisyringe burettes[129–141] and solenoid micropumps[142,143]. A large amount of research was conducted at Pacific Northwest National Laboratory (USA) in the late 1990s – early 2000s in adapting the techniques used in sequential injection analysis for radioanalytical chromatography. This included using wider bore tubing for the holding coil to speed up the aspiration step and increase throughput. As this change could lead to greater mixing between reagents, two procedures were developed; either the introduction of air segments between stacked solutions or a sequence of aspiration into the holding coil followed by immediate delivery to the column for each solution in turn. During the last decade, this research has been taken forward by a group at the University of the Balearic Islands who have applied their technique of multisyringe flow injection analysis (MSFIA)[109,110] to radiochemical separations. This technique centres around a multisyringe burette (most often containing four syringes) with individually controlled three-way solenoid multi-commutation valves on each syringe line. This allows for more versatile and advanced flow networks such as lab-on-valve (LOV) systems. Combination of a multisyringe burette and solenoid micropumps in a hyphenated MSFIA-MPFS system allows for controlled separation sequences from large sample loading volumes due to the continuous dispensing provided by the solenoid micropumps.

Amongst the publications using linear motion pumps, approximately half did not test the effect of flow rate on the separation procedure with one publication making reference to earlier work[131].

In some cases, the flow rate required for aspirating solutions into the holding coil or loading the slurry of sorptive material into the column channel was optimised; although the geometry of the packed bed may have an effect on chromatographic kinetics, this factor will not be included in this discussion regarding operating flow rates. For a couple of systems, the upper limit on flow rate through the column was determined by backpressure limitations,[98,138,141] although some band spreading at faster flow rates was also depicted in one example[138]. Band width was also mentioned by another author but not demonstrated[124]. A few studies observed no significant variation in method efficiency over the flow rate range tested[30,69,139,141] whereas six selected a flow rate for one or more steps in the procedure based solely on analyte recovery[120,129,130,133,135,137]. One study observed a combination of physical and chemical factors determining optimum flow rate[134]. This experimental procedure involved loading the organic extractant onto the support material as part of the operating sequence; it was therefore less strongly retained as required a flow rate of less than 1 mL/min through the column to avoid being washed off. The elution stage, however, required a slower flow rate than the loading stage to achieve the optimum analyte recovery.

Only one publication attempted to quantify chromatographic kinetics[33]. Although flow rate through the column was not varied in this study, calculated elution curves generated by different concentrations of thorium(IV) loaded onto anion exchange resin were compared to experimental data in order to fit thermodynamic and kinetic parameters. Comparisons between calculated and experimental breakthrough profiles were also made in the development of an equilibration-based preconcentrating minicolumn sensor[31]. Although kinetics was not quantified, the overall column efficiency in terms of the number of theoretical plates (N) was assessed for two different bed lengths by fitting the experimental data to either a Gaussian or low plate number model.

2.2. Other automated systems and concluding remarks

The flexibility of fluid handling has led to other radiochemical separation methods being automated. This includes sample pre-treatment steps prior to column-based separation such as the microwave-assisted digestion of caustic aged nuclear waste samples for Tc-99 analysis[144]. This method involved controlled delivery of the sample to the closed reaction vessel followed by acidifying and oxidising reagents. After the reaction had been allowed to complete, the digested sample was automatically transferred to the chromatographic column.

Liquid-liquid extraction separations can also be improved via automated miniaturised devices[145]. Examples used for the analysis of radionuclides include lab-in-syringe methods[146,147] and microfluidic techniques[148–151]. In-syringe procedures involve magnetic stirring followed by phase

separation and controlled dispensing of the extractant phase for analysis. Microfluidic techniques involve introducing the organic and aqueous phases into the microchannel either in parallel producing laminar flow[148,149] or as droplets to generate a slug flow pattern[150]. Using both these methods, a much higher relative interfacial area is achieved which allows for a more efficient species transfer between the two phases. Control over flow rate using microsyringe pumps permits calculation of contact times and optimisation of experimental conditions according to extraction kinetics. Microfluidic liquid-liquid extraction of radionuclides has been numerically simulated using the COMSOL Multiphysics direct solver SPOOLES[152]. In comparison to a method involving the analytical solution of differential equations, the numerical simulation method gave a superior description of the experimental results.

Throughout the literature, the benefits of automated or semi-automated techniques have been highlighted. The time taken to carry out radioanalytical separations is reduced and throughput can be further increased by parallel separations or by fully-automated systems that allow for continuous operation. Due to the potentially high levels of radioactivity in samples arising from nuclear decommissioning, automated procedures also lower the dose received by analysts. The reduced manual input also reduces the analytical cost and chance of human error. These benefits can be obtained from systems using automatic sample and reagent dispensing and fraction collection without elevating the flow rate through the column[153,154]. Gaining precise control over the volume of solutions and rate at which they flow through the packed bed, adds the additional benefit of reproducibility and consistency between samples allowing for a higher quality of results. Existing rapid or automated procedures have been optimised for known matrices and exhibit reliable behaviour within the defined operating envelopes. Flow rate decisions have been largely guided by basic empirical findings such as the recovery of analytes within a pre-defined elution sequence or on practical considerations such as pressure limitations. A greater understanding of the movement of different species through a sorptive bed would allow for a more accurate selection of column operating conditions and elution sequences based on target decontamination factors as well as economic considerations.

Table 2.1.
Summary of literature describing radioanalytical separations using controlled solution flow rates through a chromatographic column.

Sorptive material(s)	Analyte(s)	Flow rate control	Internal column diameter (cm)	Flow rate range (mL/min)	Optimal flow rate (mL/min)	Reference
TEVA resin UTEVA resin	Rf homologs (Zr, Hf)	Vacuum box	0.8 (2 mL cartridge)	1	Effect of flow rate not tested, Flow rate based on Eichrom recommendation	Alfonso et al.[96]
DGA resin	Db homologs (Ta, Nb, Pa)	Vacuum box	0.8 (2 mL cartridge)	0.5 - 1	Effect of flow rate not tested, Flow rate based on Eichrom recommendation	Despotopulos et al.[73]
TRU resin DGA resin TEVA resin	Am, Pu, U	Vacuum box	0.8 (2 mL cartridge)	1 - 10	Method efficiency not affected by flow rate	Gostic[100]
TEVA resin DGA resin	Pu	Vacuum box	0.8 (2 mL cartridge)	~1	Effect of flow rate not tested, Basis of flow rates chosen unknown	Grate et al.[155]
TRU resin TEVA resin UTEVA resin DGA resin DIPHONIX resin	Cm, Pu, U, Am	Vacuum box	0.8 (2 mL cartridge)	Not specified (usual flow rate set to 1 drop per second)	Desorption flow rates <90 for Am on TRU resin, <34.2 for Am on DGA resin and <48 for Pu on TEVA/UTEVA resin	Janda et al.[101]
DGA resin LN resin (Plus both in tandem)	Ca, Lu, Hf, U, Th, Yb	Vacuum box	0.8 (2 mL cartridge)	<2 for loading and elution 3 for rinsing	Effect of flow rate not tested, Basis of flow rates chosen unknown	Pourmand et al.[97]
DGA resin UTEVA resin (Plus both in tandem)	Am, Cm, Pu, U	Vacuum box	0.8 (2 mL cartridge)	~2 for loading ~5 for elution and rinsing	Effect of flow rate not tested, Flow rates based on work by Gostic[100]	Roman[67]
Sr resin	Sr	Vacuum box	0.5 (2 mL column)	~1	Effect of flow rate not tested, Basis of flow rates chosen unknown	Russell et al.[14]
Sr resin	Sr, Ra	Vacuum box	0.8 (2 mL cartridge)	1 for loading and elution 1 – 2 for rinsing	Effect of flow rate not tested, Basis of flow rates chosen unknown	Sadi et al.[98]

Sorptive material(s)	Analyte(s)	Flow rate control	Internal column diameter (cm)	Flow rate range (mL/min)	Optimal flow rate (mL/min)	Reference
TRU resin UTEVA/DGA resin in tandem	Am	Vacuum box	Cartridge size not specified	1 for loading and elution 2 for rinsing	Effect of flow rate not tested, Basis of flow rates chosen unknown	Wang et al.[99]
TEVA resin UTEVA resin Sr resin (Plus all 3 in tandem)	Pu, U, Sr	Vacuum box	Not specified	Not specified	Not specified	Zapata-García et al.[156]
TEVA/DGA resin in tandem	Np	Nitrogen pressure	0.8 (2 mL cartridge)	Not specified	Applied pressure of +10 PSI	Guérin et al.[102]
TEVA/DGA resin in multi-dimensional sequence	Th, U, Np, Pu, Am	Nitrogen pressure	0.8 (2 mL cartridge)	10 - 20	Applied pressure not specified	Guérin et al.[157]
TEVA/DGA resin in multi-dimensional sequence	Th, U, Np, Pu, Am	Nitrogen pressure	0.8 (2 mL cartridge)	9.7 - 30.0 (± 0.1)	Applied pressure of +20 PSI creates range of flow rates	Guérin et al.[68]
Anion exchange resin	U, Th, Pb, lanthanides	Nitrogen pressure	1.5	0.019 - 0.140	0.035 Varied applied pressure, particle size and column length	Miyamoto et al.[29]
Anion exchange resin	U, Pu, Th, Pb, lanthanides	Argon pressure	0.2	Not specified	Applied pressure of 0.45 MPa	Miyamoto et al.[158]
Sr resin	Ba, Cs	Nitrogen pressure	0.0762	Not specified	0.1	Sommers et al.[103]
Proprietary material	Sr	Nitrogen pressure	1	1	Effect of flow rate not tested, Basis of flow rate chosen unknown	Zhang et al.[104]
Proprietary materials	Sr, Cs	Nitrogen pressure	1	1	Effect of flow rate not tested, Basis of flow rate chosen unknown	Zhang et al.[105]
TRU resin	Eu (proxy for Am), Pu, Th, U	Peristaltic pump	0.3 and 0.5	0.33 – 3.2	No impact of flow rate on recovery, Flow rate set at 1.6 for compatibility with the sample delivery requirements of the ICP-MS	Aldstadt et al.[116]
TEVA resin	Tc	Peristaltic pump	1	1 - 7	5 for conditioning, loading and rinsing 1.5 for elution	Chung et al.[52]

Sorptive material(s)	Analyte(s)	Flow rate control	Internal column diameter (cm)	Flow rate range (mL/min)	Optimal flow rate (mL/min)	Reference
Sr resin	Sr	Peristaltic pump	1	1 - 5	5 for conditioning and clean-up, 3 for loading, 2 for rinsing and elution	Chung et al.[53]
Cation/anion exchange resin in tandem	Se	Peristaltic pump	Not specified	1	Effect of flow rate not tested, Basis of flow rate chosen unknown	Comte et al.[16]
Proprietary material	U	Peristaltic pump	0.16	1.5	Effect of flow rate not tested, Basis of flow rate chosen unknown	Duval et al.[159]
TRU resin	Am, Pu	Peristaltic pump	0.46	1 - 3	Peak broadening at higher flow rates, Analytes remain separated	Egorov et al.[117]
Levextrel resins (HDEHP and TBP) Aluminum oxide Activated carbon	Ga	Peristaltic pump	0.89	2 for conditioning 1 for loading, rinsing and elution	Effect of flow rate not tested, Basis of flow rates chosen unknown	Fan et al.[160]
Sr resin	Sr	Peristaltic pump	0.21	0.5 for loading and elution 1 for rinsing	Effect of flow rate not tested, Basis of flow rate chosen unknown	Grate et al.[161]
TRU resin	Am, Pu	Peristaltic pump	0.3 and 0.46	1 for 0.3 cm ID 1 - 3 for 0.46 ID	Peak broadening at higher flow rates, Analytes remain separated	Grate et al.[118]
Sr resin TEVA resin TRU resin	U, Th, Pu, Np, Am, Sr	Peristaltic pump	0.7	1	Effect of flow rate not tested, Basis of flow rate chosen unknown	Habibi et al.[162]
TEVA resin TRU resin	Tc, Th, U	Peristaltic pump	Not specified	2.2 for loading 3.5 for rinsing 2 for elution	Effect of flow rate not tested, Basis of flow rates chosen unknown	Hollenbach et al.[163]
Proprietary material	U, Th	Peristaltic pump	0.4	1 - 18 for loading 1 - 5 for elution	10 for loading 2 for elution	Hosseini et al.[119]
2 x TEVA resin	Tc	Peristaltic pump	0.66 and 0.3	0.8 for 8M HNO_3 2.3 for other solutions	Effect of flow rate not tested, Basis of flow rates chosen unknown	Kim et al.[164]

Sorptive material(s)	Analyte(s)	Flow rate control	Internal column diameter (cm)	Flow rate range (mL/min)	Optimal flow rate (mL/min)	Reference
TEVA resin	Np, Pu	Peristaltic pump	0.3	0.83 for HCl solutions 1.6 for HNO_3 solutions	Effect of flow rate not tested, Basis of flow rates chosen unknown	Kim et al.[165]
MnO_2 resin	Ra, Ba	Peristaltic pump	0.9	1 - 300 (plus gravity flow)	Effect of flow rate dependant on salinity	Moon et al.[66]
Cation exchange resin	Sr, Ra	Peristaltic pump	Not specified	3.8	Effect of flow rate not tested, Basis of flow rate chosen unknown	St-Amant et al.[166]
TEVA resin UTEVA resin Anion exchange resin	Tc, Np, Pu, U	Peristaltic pump	Not specified	Not specified	Not specified	Qiao et al.[167]
TEVA resin TRU resin Sr resin	Pu, Am, Sr	Peristaltic pump	1	1 - 5	Chemical recovery insignificantly affected by flow rate	Yoon et al.[54]
Cation exchange resin / Sr resin in tandem	Sr	Peristaltic pump	1.6 and 0.7	5 for loading 1 for rinsing	Effect of flow rate not tested, Basis of flow rates chosen unknown	Zhang et al.[168]
Sr resin	Sr	Syringe pump	0.32	1	Effect of flow rate not tested, Basis of flow rate chosen unknown	Barbesi et al.[51]
TRU resin	U, Th, Np, Pu, Am	Syringe pump	Not specified	1 - 10 for loading 1 - 12 for rinsing 1 - 10 for elution	2.5 for loading 6 for rinsing 2 for elution	Charlton et al.[120]
SuperLig 620	Sr, Ba	Syringe pump	Not specified	1	Effect of flow rate not tested, Basis of flow rate chosen unknown	DeVol et al.[121]
TEVA resin	Tc	Syringe pump	0.46	1.5 for conditioning, loading and rinsing 0.5 for elution	Effect of flow rate not tested, Basis of flow rates chosen unknown	Egorov et al.[122]
Scintillating microspheres (proprietary)	Tc	Syringe pump	0.3	1 - 7	Equilibrium concentration on column unaffected by flow rate	Egorov et al.[30]

Sorptive material(s)	Analyte(s)	Flow rate control	Internal column diameter (cm)	Flow rate range (mL/min)	Optimal flow rate (mL/min)	Reference
Sr resin TEVA resin TRU resin	Sr, Am, Tc	Syringe pump	0.212 and 0.2	0.5 - 1 depending on resin/analyte	Effect of flow rate not tested, Basis of flow rates chosen unknown	Egorov et al.[123]
TRU resin	Am, Pu, Np	Syringe pump	0.4	1.5 for conditioning and rinsing 1 for elution if dilution line not used 0.5 for elution if dilution line used	Narrower Np elution peaks and improved Th elution recovery at slower flow rate	Egorov et al.[124]
Anion exchange resin SuperLig 620	Tc, Sr	Syringe pump	0.4	0.3 for Sr 2 for Tc (plus stops = 1.63 average)	Effect of flow rate not tested, Basis of flow rates chosen unknown	Egorov et al.[31]
Anion exchange resin	Tc	Syringe pump	0.46	1.5 for reversed-flow elution	Effect of flow rate not tested, Basis of flow rate chosen unknown	Egorov et al.[125]
TRU resin	Am, Cm, Pu	Syringe pump	0.4	3 for conditioning 2 for loading, rinsing and elution	Effect of flow rate not tested, Basis of flow rates chosen unknown	Grate et al.[126]
Sr resin	Sr	Syringe pump	0.46	0.5 - 5	Method efficiency not affected by flow rate	Grate et al.[69]
TEVA/UTEVA resin in tandem	U, Np, Pu	Syringe pump	0.5	3 for conditioning 1.2 for loading, rinsing and elution (2.4 for rinsing TEVA)	Effect of flow rate not tested, Basis of flow rates chosen unknown	Qiao et al.[127]
Dionex HPIC: Cation concentrator Cation chromatography (guard and analytical columns)	Sr, Ra	Piston pumps	0.4 (pre-concentration column) 0.3 (analytical and guard columns)	0.25 - 1	Flow rate no higher than 0.25 when using the preconcentration column to avoid backpressure problems	Sadi et al.[98]

Sorptive material(s)	Analyte(s)	Flow rate control	Internal column diameter (cm)	Flow rate range (mL/min)	Optimal flow rate (mL/min)	Reference
TEVA/UTEVA resin in tandem	Np	Double plunger pumps	0.46	Not specified	Not specified	Taguchi et al.[128]
Anion exchange resin	Th (Np proxy)	Plunger pump	1	0.5	Effect of flow rate not tested, Basis of flow rate chosen unknown	Yamamura et al.[33]
UTEVA resin	U	Multisyringe burette	0.32	2 for conditioning and rinsing 0.8 for loading and elution	0.8 determined as optimum flow rate for loading and elution Range tested not stated	Avivar et al.[129]
UTEVA resin	U, Th	Multisyringe burette	0.32	2 for conditioning and rinsing 0.8 for loading and elution	0.8 determined as optimum flow rate for loading and elution Range tested not stated	Avivar et al.[130]
UTEVA resin	U, Th	Multisyringe burette	0.32	2 for conditioning and rinsing 0.8 for loading and elution	Effect of flow rate not tested, Flow rates based on previous work[129,130]	Avivar et al.[131]
Macroporous bead cellulose coated with MnO_2	Ra	Multisyringe burette	0.32	1.5	Effect of flow rate not tested, Basis of flow rate chosen unknown Note: flow rate for lixiviation of sample tested	Ceballos et al.[132]
Sr resin	Sr	Multisyringe burette	0.35	5 for conditioning 1 - 10 for loading 3 for rinsing 2 for elution	1 for loading Recovery linearly decreases when increasing the flow rate for loading	Fajardo et al.[133]
Proprietary material (HDEHP)	Y	Multisyringe burette	0.3	0.3 - 1	0.4 for loading 0.5 for rinsing 0.3 for elution Organic phase swept away at flow rate of 1	Fajardo et al.[134]

Sorptive material(s)	Analyte(s)	Flow rate control	Internal column diameter (cm)	Flow rate range (mL/min)	Optimal flow rate (mL/min)	Reference
Cation exchange resin Sr resin	Sr	Multisyringe burette	0.16	2 - 10 for loading onto cation exchange resin 0.6 for loading onto Sr resin 2 for conditioning, rinsing and elution	2 for loading onto cation exchange resin Lower recovery at faster flow rate of 10	Kołacińska et al.[135]
Sr resin	Sr, Pb	Multisyringe burette	0.15	2 for conditioning and rinsing 0.6 for loading 1 for elution	Effect of flow rate not tested, Basis of flow rates chosen unknown	Mola et al.[136]
UTEVA resin	U, Th	Multisyringe burette	0.55	2 for conditioning and rinsing 0.8 for loading 0.5 – 3 for elution	0.8 for elution Recovery decreases at higher flow rates	Mola et al.[137]
TEVA resin	Pu	Multisyringe burette	0.5	1 for loading and elution 0.6 – 2 for rinsing	1 for rinsing Back pressure increased exponentially with the increase of flow rate	Qiao et al.[138]
Sr resin	Sr	Multisyringe burette	0.32	0.6 for loading 2 for conditioning and rinsing 0.6 – 2 for elution	Multivariate analysis screening study using flow rate range of 0.6 – 2 for elution Elution flow rate not significant so set as 2	Rodríguez et al.[139]
TEVA resin	Tc	Multisyringe burette	0.32	0.6 for loading 2 for conditioning, rinsing and elution	Effect of flow rate not tested, Basis of flow rates chosen unknown	Rodríguez et al.[140]
TEVA resin	Tc	Multisyringe burette	0.32	2 for conditioning 0.6 – 2 for loading and elution	Multivariate analysis screening study using flow rate range of 0.6 – 2 for loading and elution Flow rate not significant so set as 2 Flow rates above 2 = backpressure problems	Villar et al.[141]

Sorptive material(s)	Analyte(s)	Flow rate control	Internal column diameter (cm)	Flow rate range (mL/min)	Optimal flow rate (mL/min)	Reference
TRU resin	U	Multisyringe burette, Solenoid micropumps	0.35	3 for conditioning and rinsing 1.5 for loading and elution	Effect of flow rate not tested, Basis of flow rates chosen unknown	Avivar et al.[142]
TRU resin	Am, Pu	Multisyringe burette, Solenoid micropumps	0.35	0.5 for loading 3 for rinsing 1 for elution	Effect of flow rate not tested, Basis of flow rates chosen unknown	Fajardo et al.[143]

Chapter 3: Methodology

3.1. Reagents and materials

Low concentration uranium and thorium solutions were prepared from 1000 mg/L elemental stock solutions (Inorganic Ventures, Virginia, USA). High concentrations of uranium and thorium were prepared by dissolution of solid nitrate salts (BDH chemicals, no longer licensed). Radiotracers (H-3 and Ba-133) were supplied from Amersham plc, Buckinghamshire, UK and all other reagents were from Fisher Scientific, Loughborough, UK unless otherwise specified. Acids were prepared from Analar grade concentrated solutions and high purity water (18.2 MΩ) from a Milli-Q2 system (Merck, York, UK). The use of tritium as a radiotracer was in the form of tritiated water.

Atlantic seawater was supplied by OSIL, Hampshire, UK. This solution was prepared by filtration of natural open-ocean water collected from the surface waters of the mid-Atlantic and has a salinity of 35. The composition is expected to be similar to published data with Cl^- (19,354 ppm), Na^+ (10,770 ppm), Mg^{2+} (1,290 ppm), sulphate species (904 ppm), Ca^{2+} (412 ppm) and K^+ (399 ppm) comprising the major ionic species. After addition of acidic radiotracer solutions, the sorption solutions were titrated back to the pH of the seawater matrix (8 ± 0.05) using NH_4OH. Seawater was used for experiments investigating the sorption/desorption/breakthrough profiles of Ba^{2+} with zirconium phosphate. Although Ba-133 was used as a radiometric tracer, the total barium spike concentration was insignificant, therefore the Ba^{2+} concentration was estimated to be that of the average concentration in seawater (14 ppb). A high salinity matrix was used for these experiments as zirconium phosphate is soluble in non-saline water as evidenced by the presence of zirconium in the aqueous phase after contact with MQ water (measured by ICP-MS).

Anion exchange resin (100-200 mesh / 74-149 µm, 1x8, chloride form) and UTEVA resin (100-150 µm) were obtained from TrisKem International, Bruz, FRANCE. The inorganic ion exchanger was a zirconium phosphate (125–1000 µm, sodium form) and was supplied by a commercial-in-confidence source.

3.2. Procedures

3.2.1. Batch experiments

Batch experiments were carried out to investigate the interactions of: uranium and thorium in 8M HNO_3 with UTEVA resin; uranium and thorium in 8M HNO_3 with anion exchange resin; and barium in seawater with zirconium phosphate. The experimental conditions varied were solid/aqueous ratio, constant tumbling or stationary, particle size (zirconium phosphate only), concentration of interferents and analyte concentration (UTEVA resin only).

The experimental procedure for batch sorption comprised of weighing a set mass (0.01 g – 1 g) of the solid sorbent material into a plastic scintillation vial (22 mL; 2.4 cm internal diameter) before adding a set volume of the analyte solution (10 mL), recording the new mass and start time. The mixture was allowed to equilibrate for a set amount of time in either a stationary upright position or constantly tumbling on a roller mixer. The solution was then filtered through a PTFE syringe filter (0.45 µm) and the concentration or activity remaining measured.

The experimental procedure for batch desorption comprised of a scaled up sorption step with filtering by vacuum in order to recover the solid phase; this was left to air dry. The desorption experiment was then carried out following a similar procedure to sorption, mixing analyte-free solution with the dried solid material.

3.2.2. Column experiments

Fresh chromatographic columns were prepared for each experiment by loading either a slurry of the solid material in deionised water (UTEVA resin and anion exchange resin) or the dry solid (zirconium phosphate) into a polypropylene column (0.7 cm average internal diameter) on top of the preinstalled glass frit. Once the bed had settled and the excess solution drained, another glass frit was positioned on the top to secure the bed. The column was then preconditioned to the same matrix as the subsequent loading solution by pumping the solution through at a moderate flow rate (~2 mL/min) for 5 minutes. Although care was taken to avoid the column drying out, trapped air bubbles could sometimes be observed.

The flow rate through the column was controlled by either a Masterflex 7550-62 (Cole-Palmer UK, London, UK) or a Minipuls3 (Gilson Scientific UK, Bedfordshire, UK) peristaltic pump with Nalgene tubing (2 mm ID). The tubing was attached to the column by a customised lid using Luer fittings.

Introduction of small volume (25 µL or 500 µL) loading solutions was made by removing the lid and pipetting the solution directly on to the top frit and reconnecting the lid before commencing

pumping of the wash solution. Introduction of larger volume (1 mL +) loading solutions or continuous loading was achieved by inserting the peristaltic pump tubing input into the loading solution and commencing pumping; once the container was emptied the tubing was quickly moved into the wash solution producing a small air bubble between the two solutions. Collection of breakthrough fractions was achieved using a 2112 Redirac automated fraction collector (LKB Bromma, no longer licensed) or manually by timed exchange of collection vessels. Vessels were weighed before and after collection of fractions to determine the collected mass and hence flow rate.

3.2.3. Other procedures

An estimation of the particle size distribution for the inorganic ion exchanger was achieved by sieving a known mass of solid (~5 g) through a series of stainless steel / brass sieve shakers of decreasing mesh sizes (1000 μm, 710 μm, 500 μm, 250 μm, 125 μm).

The density of the sorptive materials was measured by filling a measuring cylinder to a known volume (10 mL) and recording the mass. The void ratio was then calculated by added MQ water up to a known volume (15 mL) and recording the increase in mass.

3.3. Instrumentation

3.3.1. ICP-MS

Stable uranium, thorium and zirconium concentration measurements were performed on a Thermo Scientific X-series II quadrupole ICP-MS (Thermo Fisher Scientific, Waltham, MA USA) and an Agilent 8800 triple quadrupole ICP-MS (Agilent, Santa Clara, CA, USA). The aqueous solutions were diluted to ppb level and introduced to the instrument in a 2% HNO_3 matrix. Six calibration standards (including a 0 ppb solution) were prepared from single element ICP-MS standards (Inorganic Ventures, Virginia, USA). This set was run prior to each batch of samples spanning the expected concentration range of the samples. All calibration standards and samples were spiked with a mixture of In/Re to give a final concentration of 5 ppb for use as internal standards.

3.3.2. Gamma spectrometry

Barium-133 activity concentration was measured on well-type HPGe gamma detectors (Canberra Industries, Harwell, UK) and the Cobra II Automated NaI Gamma Counter model 5003 (Packard Instrument Company, no longer licensed). Analysis of the HPGe energy spectra and calculation of radionuclide activity was performed using Fitzpeaks software (JF Computing, Stanford in the Vale, UK). A background spectrum for the HPGe detectors was collected on a weekly basis and

deducted from the measured spectrum for each sample/standard. A height correction was applied in the case of partially-full sample vials. A single value in Bq/g was obtained from the Cobra II Automated NaI Gamma Counter for each sample.

3.3.3. Liquid scintillation counting

Tritium activity concentration was measured by liquid scintillation counting on Wallac 1440 Quantulus ultra low-level spectrometers (Perkin Elmer, Waltham, MA, USA). Gold Star (Meridian Biotechnologies Ltd, Epsom, UK) liquid scintillation cocktail was used for these measurements. A matrix-matched instrument blank and instrument standard was run with each batch of samples to determine background counts and instrument efficiency.

3.3.4. Other instrumentation

Scanning electron microscopy images were collected using a Leo 1450VP SEM (Zeiss, Oberkochen, Germany) and an Oxford Instruments X-Act 10 mm^2 area SDD EDS Detector, utilising the AZtec Energy software system (Oxford Instruments, Oxfordshire, UK).

Stable magnesium and calcium concentration measurements were performed on a Metrohm 861 Advanced Compact IC with the Metrosep C 4 - 150/4.0 column, utilising the IC net software (Metrohm AG, Herisau, Switzerland). The aqueous solutions were diluted to ppm level and introduced to the instrument in a 0.002M HNO_3 matrix. Four calibration standards were run prior to each batch of samples spanning the expected concentration range of the samples.

3.4. Conversion of raw experimental data to graphical plots

For each set of batch experiment solutions measured by ICP-MS, gamma spectrometry, liquid scintillation counting or ion chromatography, an aliquot of the solution contacted with the solid material was also measured and the data corrected to this reference value. Corrections were also applied for differences in dilution (or evaporation and dilution) factors. The sorption value was then determined from the initial mass of solid and solution as well as the density of the solution. The propagated uncertainty on this final value is composed of the calibration uncertainty, the statistical counting uncertainty on the raw data, the uncertainty on the initial analyte concentration in solution and weighing uncertainties associated with the mass of the initial solid and solution as well as the masses recorded for calculation of dilution factors. The data is plotted against the duration of batch mixing time (sorption/desorption plots) or initial aqueous concentration (isotherm plots).

For each set of column experiment fractions measured by ICP-MS, gamma spectrometry or liquid scintillation counting, the data was simply corrected to the column output concentration by accounting for the different dilution (or evaporation and dilution) factors. The propagated uncertainty on this final value is composed of the calibration uncertainty, the statistical counting uncertainty on the raw data and weighing uncertainties associated with the masses recorded for calculation of dilution factors. The data is plotted against the midpoint of the collected fraction (mL).

3.5. Numerical simulation

Numerical simulation has been developed using LabVIEW 2015 (National Instruments UK, Newbury, Berkshire). LabVIEW is a visual programming language capable of interfacing with and controlling hardware as well as manipulating multidimensional data arrays. Numerical simulation of sorption kinetics has been achieved using the pre-programmed *ODE solver VI* to solve sets of ordinary differential equations with respect to time (Figure 3.1.). The final concentration values are fed through a *while loop shift register* to become the *ODE solver input variables* with the loop iteration value added to the time outputs. The *while loop* has been coded to operate either until stopped by the user, when the change in lumped solid concentration between simulations is less than a defined order of magnitude; i.e. "equilibrium" has been achieved or after 1000 iterations (equivalent to 1000 seconds). The total data stored is then reduced to every 100th value and written to a .CSV file. As this is also contained within a *while loop* the 1000 iterations of the inner loop begins again unless equilibrium has been reached. For simulations producing more than 1 x 10^6 seconds the length of an excel spreadsheet is exceeded so a binary TDMS format is used and the data saved to a series of files. This also increases the amount of significant figures saved. The basic *ODE solver* equation inputs and subsequent modifications are explained in further detail in the following results and discussion section.

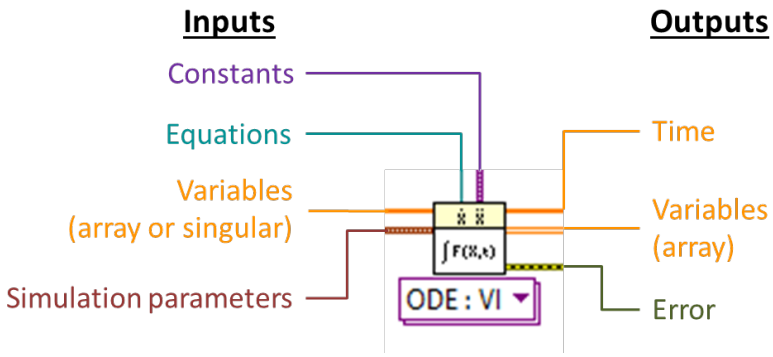

Figure 3.1.
ODE solver as it appears within the LabVIEW graphical development interface.
Constants are input as variant data and differential equations are input as a strictly typed reference to the VI that implements the right-hand side of an ordinary differential equation dX/dt=F(X,t).

The type of solver used for these simulations is *Runge-Kutta 45 (variable*); this choice, the absolute and relative tolerances and time steps are programmatically set (Table 3.1.) and remain constant for all simulations carried out in this project. The final time is set to 1 (time basis for the simulation is seconds) and a *wait* of 10 milliseconds added in order to reduce CPU and memory usage.

Table 3.1.
List of simulation parameters programmatically input into ODE solver.

Parameter	Value
Initial Time	0
Final Time	1
Time Step	0 (only used if a fixed step-size solver is chosen)
Absolute Tolerance	1E-8
Relative Tolerance	1E-8
Continuous Solver	Runge-Kutta 45 (variable)
Discrete Time Step	Final time / 1000
Minimum Time Step	Final time / 1E9
Maximum Time Step	Final time / 100
Initial Time Step	Final time / 1000

The 10 ms wait function, an ODE solver in a while loop and the write delimited spreadsheet VI were also used to simulate chromatographic column breakthrough. The LabVIEW coding was, however, modified to include an array of input and output variables. Due to the larger amount of data generated, only the final temporal values from each iteration of the *ODE solver* are fed through the *while loop shift register*. To achieve a consistent level of detail between different simulations, however, iterations adding up to a total of 0.1 mL (0.01 mL for tritium based hydrodynamic experiments) were collated and averaged; this value was then output to the .CSV file and also displayed on an onscreen *XY graph*. This graph allows the operator to monitor progress and determine when to stop the simulation.

Chapter 4: A Numerical Simulation Method for Modelling the Kinetics of Batch Sorption and Desorption of Inorganic Species on Three Contrasting Materials

Abstract

A numerical simulation method has been developed to describe the transfer of analytes between solid and aqueous phases. The method employs an ordinary differential equation solver within the LabVIEW visual programming language to plot the change in concentration in both phases with respect to time. The method has been assessed using a range of experimental data for three contrasting sorptive materials (UTEVA resin, anion exchange resin and zirconium phosphate). Internal and external mass transfer effects have also been evaluated by conducting experiments under either stirred or stationary conditions. In addition, the impact of analyte and interferent concentrations on thermodynamic and kinetics was investigated for UTEVA resin. Finally, the numerical simulation approach has been compared to two commonly used kinetic equations (pseudo-first-order and pseudo-second-order). The mechanistic nature of simulation can provide an insight into the conditions under which these equations are valid and explain mathematical biases observed.

4.1. Introduction

A range of microscopic imaging, speciation studies and sorption quantification experiments are often employed in the characterisation of novel sorptive materials for water treatment or analytical chemistry. These techniques are useful for determining the structure of the synthesised material as well as the physical and thermodynamic behaviour under variable pH, temperature and aqueous matrices. Another important measure of the performance of the material is the sorption kinetics which can have a significant impact on the suitability of a material designed for use under fast flowing systems. Although aqueous sorption onto solid materials usually occurs in fixed-bed or column configurations, closed-system (batch) experiments are employed as a simpler method to generate information on the temporal progress of sorption and the time taken to reach equilibrium.

Interpretation of kinetic batch sorption data frequently involves regression analysis to classify the kinetic relationship between the analyte and sorptive material and to generate rate constants which can be used to compare the performance of different systems. The most commonly

applied classifications are the pseudo-first-order[57] (PFO) and pseudo-second-order[58,59] (PSO) rate equations (Equations 4.1 and 4.2. respectively). Both of these equations describe the rate of change of an adsorbed species (q_t) as a function of the effective available sorption sites ($q_e - q_t$), where q_e is the concentration of adsorbed species at equilibrium (mg/g).

$$\frac{\mathrm{d}q_t}{\mathrm{d}t} = k_1(q_e - q_t) \qquad \text{Equation 4.1.}$$

$$\frac{\mathrm{d}q_t}{\mathrm{d}t} = k_2(q_e - q_t)^2 \qquad \text{Equation 4.2.}$$

The equations can be rearranged into several different linear or non-linear forms with corresponding plots from which a rate constant is derived. Recently, however, several authors have disputed the validity of assigning one of these equations to a sorptive system based on direct comparisons of statistical measures. Lin et al.[169] used the example of methylene blue adsorption on activated carbon to question the use of the correlation coefficient (R^2) value in determining the best fit as this measure favoured an equation format which had a lower degree of accuracy in predicting the equilibrium position. They instead preferred to compare fit using the normalised standard deviation Δq(%). They also noted that the magnitude of uncertainties may alter significantly when converting from non-linear to linear equation formats and that prior knowledge of the equilibrium position is not required for data fitting when using non-linear formats. These observations indicate that inherent mathematical bias in the choice of plotting axes and equation format may hinder the correct assignment of rate orders.

Ascertaining whether the reaction has proceeded long enough for equilibrium to be obtained is another issue faced in the interpretation of kinetic data. This problem is raised by Gupta et al.[61] in their review of metal ion adsorption on inorganic materials. They suggest that the PFO equation is often valid for initial sorption but fails to accurately predict the position of equilibrium. The non-requirement for prior estimation of parameters is also given as the main advantage of the PSO equation in the review of second-order models by Ho[170].

Lack of agreement on the theoretical derivation of PFO and PSO equations is another factor undermining their assignment based purely on statistical fitting measures. Azizian[171] developed a general equation for adsorption and desorption which was based on Langmuir kinetics and included an initial solute concentration term (C_0). This equation was shown to simplify to the PFO under high C_0 or to the PSO when C_0 was low. Azizian's derivation also stated a relationship between k_1 and C_0 which could be exploited to distinguish the separate rate constants of

adsorption (k_a) and desorption (k_d). The relationship between k_2 and C_0 is suggested to be more complex involving two fitting parameters and without the ability to separate out the values for k_a and k_d.

Azizian's method, however, has been critiqued by Liu et al.[56,172] who propose that, rather than assuming a pre-set reaction order of either 1 or 2, the kinetics of sorption obeys the universal rate laws for chemical reactions whereby the reaction order is based on the rate-determining step and must be determined experimentally. They therefore suggest a general rate law where the reaction order for the effective concentration of sorption sites can be either an integral or a rational non-integral number. Both the PFO and PSO are therefore special cases of the general rate equation. It should be noted, however; that their theory is based on biosorption processes which are likely to be more complex than the sorption of metal ions.

Several review papers[56,61,170,173] also describe another popular kinetic model which was developed by Roginsky and Zeldovich in 1934 and is referred to as the Elovich equation. This model is limited to the description of the initial rate of sorption and is equivalent to the pseudo-second-order equation under circumstances where fractional surface coverage is less than 0.7.

All of the models discussed thus far focus on situations where the surface reaction is assumed to be the rate-controlling step. In reality, the total sorptive process consists of four steps[40,173,174]: aqueous diffusion of the analyte from the bulk solution; diffusion of the analyte across the stagnant layer surrounding the solid particles; intraparticle diffusion within the pores of the solid material and the chemical sorption/desorption step which can occur both on the surface of the particle or after penetration into the pores. For non- or macroporous materials under well stirred conditions the exclusion of mass transfer processes can be a valid simplification, however, this does not apply to every sorptive system investigated.

For batch experiments consisting of suspended particles in a rapidly-moving solution, the concentration of analyte in the aqueous phase is spatially constant. In slow-moving solutions, however, a stagnant layer can build up around the solid particle and inhibit the rate of transfer of the analyte from the bulk solution to the surface of the particle. In this process, known as film diffusion, the bulk solution is still spatially constant but a concentration gradient exists around the particles where analyte has been depleted from the solution near the surface due to the sorption reaction. In stationary solutions, the bulk solution may also begin to exhibit concentration gradients depending on the difference between the rate of sorption and the rate of diffusion. Particles with porous structures also exhibit intraparticle diffusion through the liquid contained within their pores.

The general rate of diffusion for an analyte (A) is expressed by a mass transfer constant (k_A) which is a function of the diffusion coefficient (D_{diff}) and the distance travelled (δ) (Equation 4.3.). This equation is based on the Fick model of diffusion and assumes no interaction between dissolved species. The diffusion coefficient is dependent on the analyte being studied and the properties of the solution such as viscosity and other species present[42]. The mass transfer constant can be used to calculate the temporal change in concentration for a defined volume in the system if the concentration gradient and dimensions of the volume are known.

$$Mass\ transfer\ constant\ (k_A) = \frac{D_{diff}}{\delta} \qquad \text{Equation 4.3.}$$

$$\frac{d[A]_s}{dt} = k_A \frac{SA_s}{V_s}\left([A]_{aq} - [A]_{s,surface}\right) \qquad \text{Equation 4.4.}$$

In the case of film diffusion, δ refers to the thickness of the stagnant layer and the rate of concentration change in the solid particle is a function of the surface area of the particle (SA_s), the volume of the particle (V_s) and the difference in concentration between the particle surface and the bulk aqueous solution (Equation 4.4.). Several equations have been developed to estimate the film thickness based on the dimensionless Sherwood (Sh), Reynolds (Re) and Schmidt (Sc) numbers (Equations 4.5. – 4.7.) where u = fluid velocity, ν = kinematic viscosity and d_p is the diameter of the (spherical) particle[42,47]. Although these equations are generally applied to fixed-bed configurations with a constant solution flow rate, some definitions of the minimum value of the Sherwood number under the limiting conditions of a stationary solution have been suggested ranging from 0 to 3.89[175]. A Sherwood number of 0 would imply an infinitely thick stagnant layer meaning that transfer of analyte molecules to the surface of the particle is impossible, this is therefore physically unrealistic[42]. In addition, at very low Sherwood numbers the stagnant layer extends far into the bulk solution and the processes of diffusion across this film and diffusion in the bulk solution become blurred.

$$Re = \frac{d_p u}{\nu} \qquad \text{Equation 4.5.}$$

$$Sc = \frac{\nu}{D_{diff}} \qquad \text{Equation 4.6.}$$

$$Sh = \frac{d_p}{\delta} \qquad \text{Equation 4.7.}$$

Intraparticle diffusion is a more complex process as the pore diameter, geometry and chemical environment can alter the importance of the competing diffusion processes: surface diffusion (along the walls of the pore), pore diffusion (through the liquid contained within the pores) and Knudsen diffusion (diffusion involving frequent collisions with the pore walls)[43]. Two popular equations for expressing intraparticle diffusion are the Weber-Morris equation and the Crank equation whereas a more complex description is given by the shrinking core model[40,56,61].

An alternative approach to sorption kinetics was developed from the work of Ward et al. which initially began by examining the rate of gas absorption at a liquid interface[176] and later expanded to include other interfaces[177]. This approach is known as the statistical rate theory (SRT) and is based on the chemical potentials of analyte and sorptive material. SRT has been applied to sorption/desorption rate-controlled systems by Rudzinski et al[178] as well as including the effects of competing species[179] and multiple diffusion processes[174]. The flexibility of this approach means that different equations can be included depending on the system being studied. For the modelling of competitive sorption, Langmuir-Freundlich kinetics were employed[180] and a stochastic simulation method (CKS software package, later renamed Kinetiscope) used for determination of the rate constants for the two competing species.

Rather than fitting equations that describe sorption/desorption curves, sets of differential equations describing the competing processes can be solved numerically by iterative adjustment of concentrations at either set or variable time steps until all equations are met to a defined level of accuracy across the specified time period. Several free (PHREEQC, Orchestra, CHEAQS) or licensed (COMSOL Multiphysics, MATLAB, The Geochemist's Workbench, gPROMS) software packages are capable of simulating the kinetics of batch sorption by this method. Simulation control can vary from constrained input of constants and initial conditions to a blank coding environment in which the user can specify all conditions and processes using a glossary of programmed keywords. The former may lack the flexibility to account for both sorption and mass transfer processes or accurately describe complex relationships between sorptive materials and solutions containing multiple analytes.

An alternative approach to coding is offered by National Instruments LabVIEW; this software provides a blank coding environment where conditions and processes are added by inserting, positioning and connecting graphically represented structures and functions. Although LabVIEW is most commonly used in the control of hardware and acquisition of data, the extensive data manipulation capability makes it a suitable option for simulation of sorptive kinetics.

This chapter explains the development of a numerical simulation method to describe sorption and desorption processes under batch conditions using LabVIEW visual programming software. A multi-dimensional interpretation of kinetics is given and explores the connections between solid/aqueous ratios, analyte and interferent concentrations, sorption and desorption rates and diffusion. The method has been demonstrated and validated using three contrasting sorptive materials which find use within the radioanalytical and nuclear decommissioning industries.

4.2. Results and discussion

4.2.1. Batch experiments

The kinetic and thermodynamic behaviour of three sorptive materials was investigated using sorption and desorption experiments with external mass transfer controlled by conducting the experiments either under constant tumbling using a roller mixer or in stationary vials. The time taken to reach equilibrium was observed to be dependent on both solid/aqueous ratio and mixing speed (stationary or well-mixed).

Under constant tumbling and equivalent solid/aqueous ratios, the equilibrium between UTEVA resin and both analytes (uranium and thorium) in 8M HNO_3 was reached faster than the other systems investigated. Both analytes showed high uptake on UTEVA resin with average distribution constant (k_D) values of 459 and 592 for uranium and thorium respectively. These values are of a similar order of magnitude to the values quoted in the literature[70] but in a different order regarding the affinity of UTEVA resin for the two analytes (quoted k' for U(VI) in 8 M HNO_3 ~300; quoted k' for Th(IV) in 8 M HNO_3 ~200; assuming $k_D/k' = 1.7$). Equilibrium for the anion exchange resin system took longer to be reached under equivalent conditions with a high uptake for thorium (average $k_D = 280$) and a low uptake for uranium (average $k_D = 12$); this is also in line with previously established thermodynamic data[76,77] (quoted k_D for U(VI) in 8 M HNO_3 ~10-20; quoted k_D for Th(IV) in 8 M HNO_3 ~300). The zirconium phosphate showed very slow kinetics for barium sorption. The k_D value, however, was found to be larger for higher ionic strength matrices with an average distribution constant of 1800 reached in a seawater matrix. This phenomenon was attributed to dissolution of the solid material in water as evidenced by the presence of zirconium in the aqueous phase after contact of MQ water with the solid material. To simplify the numerical simulation, zirconium phosphate dissolution is minimised by introducing the barium radiotracer in an Atlantic seawater matrix (adjusted to ~pH 8).

The introduction of external mass transfer limitations altered the kinetics of sorption for all three materials with the effect greatest for UTEVA resin. After a similar initial uptake, the rate of sorption slowed down and the expected equilibrium position took longer to be reached.

The presence of high concentrations of Mg and Ca was determined to have no effect on the kinetics and thermodynamics of U and Th sorption for UTEVA and anion exchange resins implying that these species do not compete for complexant/exchange sites. The relationship between two competing species was investigated for UTEVA resin only. It was found that increasing the concentration of uranium above the linear section of the sorption isotherm reduced the equilibrium position for both uranium and thorium in a combined solution.

The complete range of experimental data collected was simulated using LabVIEW. A "Lego® approach" to numerical simulation was taken whereby a basic model based on a simplified description of processes is expanded upon to introduce levels of complexity[42].

4.2.1.1. Numerical simulation – Basic sorption and desorption

The basic simulation does not include any mass transfer kinetics and was developed using data for the three materials collected via kinetic sorption and desorption experiments under constant tumbling conditions.

The *ODE solver* is operated as described in the methodology section (Chapter 3). The model constants are the forward rate constant ($\vec{k}$), the reverse rate constant ($\overleftarrow{k}$), the volume fraction of the solid phase (V_s) and the volume fraction of the aqueous phase (V_{aq}). The variables are singular values for initial analyte concentration in the aqueous phase $[aq]$ and initial analyte concentration in the solid phase $[s]$. This basic simulation does not take into account intraparticle diffusion. The analyte concentration at different locations within the sorptive material and associated internal concentration profiles are not specified; instead the concentration is averaged over the entire volume. This approach is referred to as the lumped solid simplification or lumped kinetic model[39,42]. For UTEVA resin this lumped solid encompasses the inert polymeric bead and the immobilised organic phase containing the complexant. For the ion exchange materials it comprises of the analyte concentration in the solid pores as well as the analyte absorbed onto the active sites. An advantage of this simplification is that it avoids the need to estimate pore volume.

The *ODE solver* inputs the initial variables and the model constants into two differential equations based on Langmuir kinetics (Equations 4.8. and 4.9.) and calculates the temporal change in

concentration by solving the two equations simultaneously according to the chosen simulation parameters (Table 3.1.). This generates an array of output variables in the form of analyte concentration in both the solid and aqueous phases along with the corresponding time intervals.

$$\frac{d[s]}{dt} = \vec{k}[aq] - \overleftarrow{k}[s] \qquad \text{Equation 4.8.}$$

$$\frac{d[aq]}{dt} = \left(\overleftarrow{k}[s] - \vec{k}[aq]\right) \times \left(\frac{V_s}{V_{aq}}\right) \qquad \text{Equation 4.9.}$$

As these equations are based on the difference in concentration between two adjacent volumes (lumped solid or aqueous), all analyte quantities are converted into mol/dm^3 for use as input variables. For uranium and thorium solutions, this is a simple conversion from ppb; for the barium-133 in seawater solution, a concentration of 14 ppb (1.02 x 10^{-7} mol/dm^3) is assumed based on data provided for the composition of the Atlantic seawater used. Additionally, the mass of solid material is converted into a volume by taking into account the density of the material. Densities were empirically estimated using a gravimetric liquid displacement technique and determined to be 1.7 g/cm^3 for zirconium phosphate and 1.1 g/cm^3 for both UTEVA and anion exchange resins. The latter value is in agreement with the reference density of UTEVA resin (1.10 g/cm^3)[70] and the calculated density of anion exchange resin (1.12 g/cm^3 from a reference bed density of 0.7 g/cm^3 and an assumed free column volume of 0.375 mL/mL).

For simulation of sorption, the initial lumped solid analyte concentration was set to zero whereas desorption simulations were initialised with the final lumped solid analyte concentration and an aqueous analyte concentration of zero. Desorption experiments were conducted in the same matrix as the sorption experiments; i.e. 8M HNO_3 for UTEVA and anion exchange resins and seawater for zirconium phosphate. As the concentration of barium in seawater is a positive value, the activity of Ba-133 was used instead (assumed to be 0 Bq/L in seawater). A density correction had to be applied for UTEVA resin (factor of 2.7) and anion exchange resin (factor of 1.5) under desorption conditions as the equilibrated materials were heavier than prior to sorption due to some acid retention.

For sorption experiments, the forward rate constant ($\vec{k}$) for each analyte-solid sorption system was calculated from the initial slope of concentration change in the solid phase divided by the initial concentration in the aqueous phase. This produced positive values with units of s^{-1}. The reverse rate constant ($\overleftarrow{k}$) was calculated by dividing the concentration ratio (solid/aqueous) at equilibrium by the forward rate constant. For desorption experiments, $\overleftarrow{k}$ was calculated from the

initial slope; this was then divided into the concentration ratio at equilibrium to obtain $\vec{k}$. The equilibrium value was estimated to be the concentration ratio after the longest duration of mixing undertaken for each solid material.

The $\vec{k}$ and $\overleftarrow{k}$ values were input and the numerical simulation run for each analyte-solid sorption system in turn. The simulated datasets for analyte concentration in the solid and aqueous phases have been combined into a single value taking into account the density (ρ) of the solid for ease of comparison with the experimental data across the range of conditions tested (Equation 4.10.). Once the system has reached equilibrium this ratio is equivalent to the distribution constant (Equation 4.11.) which is usually defined as the ratio of analyte concentration on the solid material ($[aq]_0$-$[aq]_{eq}$) per solid mass (W_s) to that in the aqueous phase ($[aq]_{eq}$) per volume (V_{aq}).

$$sorption\ value = \frac{[s]}{[aq]\times\rho_s} \qquad \text{Equation 4.10.}$$

$$k_D = \frac{([aq]_0 - [aq]_{eq})\times V_{aq}}{[aq]_{eq}\times W_s} \qquad \text{Equation 4.11.}$$

Starting with an experimental solid/aqueous ratio of 0.1 g / 10 mL, this approach was able to simulate the thermodynamic position of equilibrium for all three materials but didn't fully describe the kinetics observed. In the case of UTEVA resin, the basic simulation using the chosen model constants underestimated the initial rate of sorption/desorption. The rate constant values can be better estimated by either conducting experiments using shorter mixing times or by reducing the mass of solid material (keeping the aqueous volume constant at 10 mL). Due to the practical difficulties of short mixing times (<30 seconds), the latter option was chosen. Additionally, the investigation of an alternative solid/aqueous ratio can be used to further validate the presence of V_s/V_{aq} in the differential equations (Equation 4.9.). The initial slope of sorption/desorption is expected to increase with increasing V_s/V_{aq} due to a higher proportion of either complexant molecules or exchange sites. Sorption experiments using a solid/aqueous ratio of 0.01 g / 10 mL were therefore conducted for UTEVA and anion exchange resins whereas a ratio of 1 g / 10 mL was chosen for zirconium phosphate as this material exhibited much slower kinetics.

Using these three datasets a single sorption value at equilibrium for each resin-analyte system was chosen based on an average of all the k_D values collected discounting negative or zero values for uranium sorption on anion exchange resin. This single sorption value sets the ratio of $\vec{k}$ and $\overleftarrow{k}$ however the magnitude of the two constants depends of which dataset is chosen. For both

uranium and thorium sorption on UTEVA resin the simulation is optimised using $\vec{k}$ determined from the 0.01 g sorption dataset; for uranium sorption on anion exchange resin $\overleftarrow{k}$ determined from the desorption dataset is used due to large uncertainties on both sets of sorption data and for barium sorption on zirconium phosphate as well as thorium sorption on anion exchange resin $\vec{k}$ determined from the 0.1 g sorption dataset is chosen.

The goodness of fit between the experimental and simulated data (Table 4.1.) has been assessed using normalised standard deviation analysis (Equation 4.12.) where n is the number of data points (negative or zero experimental sorption values are excluded). This analysis indicated that the basic numerical simulation gave an adequate description of the interaction of uranium and thorium with UTEVA resin in 8M HNO_3 provided that the rate constants set are based on the 0.01 g resin dataset (Figures 4.1. and 4.2.). This basic simulation did not however, fully describe sorption and desorption mechanisms for the two ion exchange materials.

$$\Delta q(\%) = 100\times\sqrt{\frac{\sum[(exp-sim)/exp]^2}{(n-1)}} \qquad \text{Equation 4.12.}$$

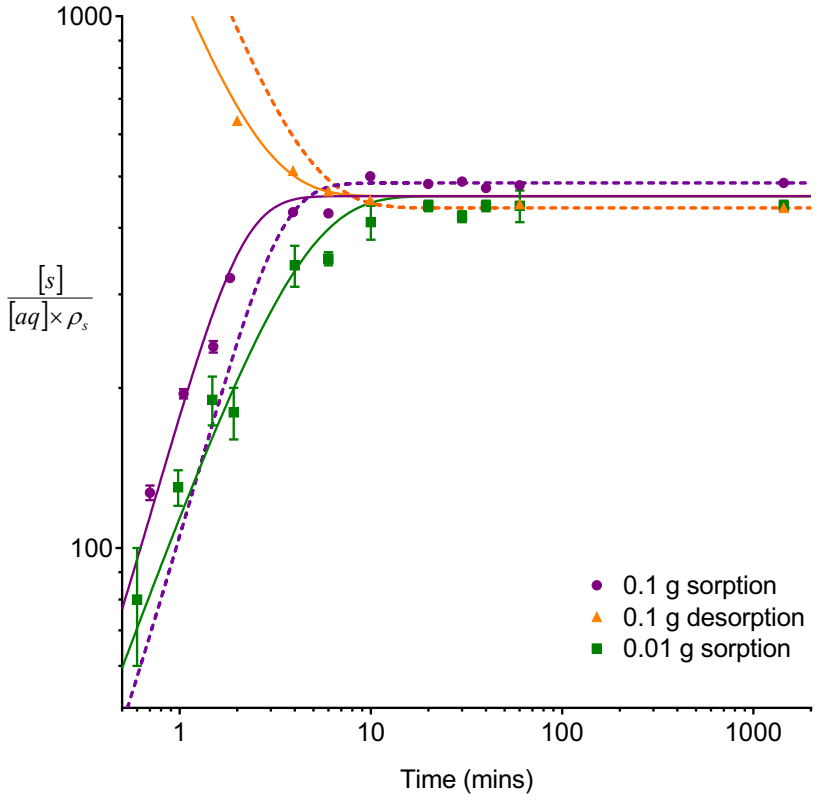

Figure 4.1.
Comparison between experimental data and numerical simulation of sorption/desorption of uranium between 8M HNO_3 and UTEVA resin.
The basic simulation was used (Equations 4.8. and 4.9.).
The solid lines represent simulations using shared input parameters ($\vec{k}$ = 2.263 and $\overleftarrow{k}$ = 4.483 x 10^{-3}) for the three experimental conditions depicted.
The dashed lines represent input parameters based on the initial and final data points obtained under a particular experimental condition (0.1 g sorption or 0.1 g desorption).
The numerical simulation method used input parameters based on an aqueous volume of 10 mL for each experiment. No external mass transfer was included.

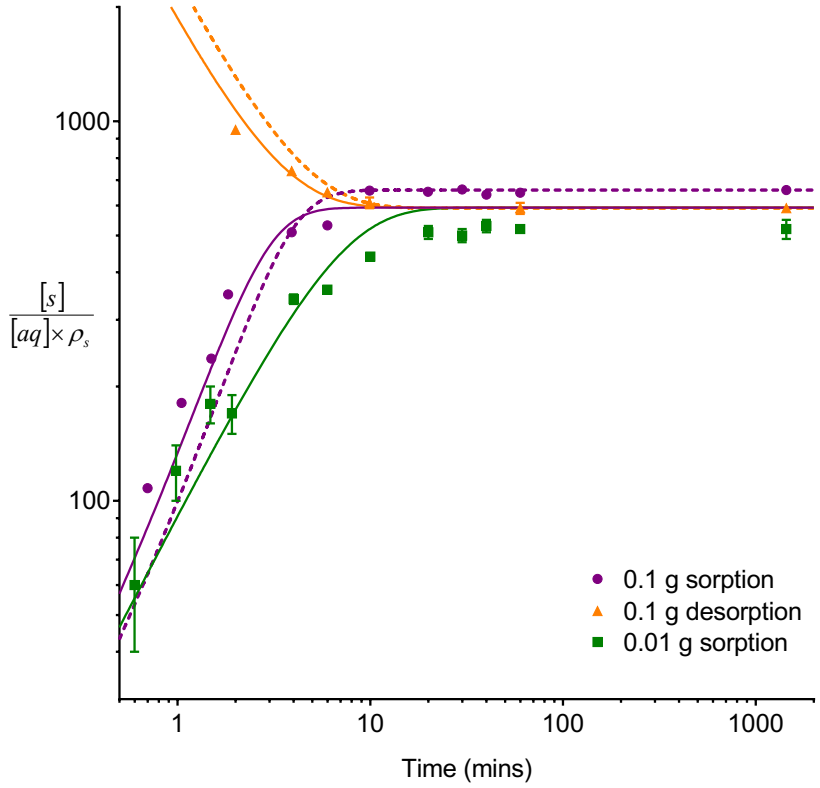

Figure 4.2.
Comparison between experimental data and numerical simulation of sorption/desorption of thorium between 8M HNO_3 and UTEVA resin.
The basic simulation was used (Equations 4.8. and 4.9.).
The solid lines represent simulations using shared input parameters ($\vec{k}$ = 1.730 and $\overleftarrow{k}$ = 2.656 x 10^{-3}) for the three experimental conditions depicted.
The dashed lines represent input parameters based on the initial and final data points obtained under a particular experimental condition (0.1 g sorption or 0.1 g desorption).
The numerical simulation method used input parameters based on an aqueous volume of 10 mL for each experiment. No external mass transfer was included.

4.2.1.2. Numerical simulation – Introduction of internal mass transfer

The initial sorption/desorption slopes for anion exchange resin and zirconium phosphate could be simulated by the basic model, however, this did not account for the observed slowing of kinetics before equilibrium was reached (see difference between experimental data points and dashed lines in Figures 4.5.-4.7.). This phenomenon was largest for zirconium phosphate and is due to slow intraparticle diffusion of the analyte. Ion exchange materials often have porous structures within which species can migrate internally. The speed of this internal transfer can depend on a number of variables such as the viscosity within the pores, the availability of active sites, the pore diameter and the radius and diffusivity of the ionic species. For the numerical simulation of intraparticle diffusion, surface diffusion has been assumed with sorbed species being transferred between active sites located on the internal pore surfaces[43,47]. In addition, the Fick model of diffusion has been applied whereby an analyte moves according to its own concentration gradient with no influence from other species[42].

The basic numerical simulation coding was therefore modified to include internal mass transfer. This involves splitting the lumped solid fraction up into two or more sections. For a two section split, the *ODE solver* would have three input and output variables and henceforth three differential equations (Equations 4.13.-4.15.) as well as three fraction constants and an additional rate constant (k_{int}). The initial concentrations for the outer and inner fractions were both set to zero.

$$\frac{d[s]_{inner}}{dt} = k_{int}[s]_{outer} - k_{int}[s]_{inner} \qquad \text{Equation 4.13.}$$

$$\frac{d[s]_{outer}}{dt} = \vec{k}[aq] - \overleftarrow{k}[s]_{outer} - \left[(k_{int}[s]_{outer} - k_{int}[s]_{inner}) \times \left(\frac{V_{s,inner}}{V_{s,outer}}\right)\right] \qquad \text{Equation 4.14.}$$

$$\frac{d[aq]}{dt} = \left(\overleftarrow{k}[s]_{outer} - \vec{k}[aq]\right) \times \left(\frac{V_{s,outer}}{V_{aq}}\right) \qquad \text{Equation 4.15.}$$

To determine the magnitude of internal mass transfer as well as appropriate solid fractionation, different size zirconium phosphate particles were investigated. The raw material was analysed by sieving to have a particle size distribution of 57 % 710-1000 µm, 31 % 500-710 µm, 11 % 250-500 µm and <1 % 125-250 µm. This range of sizes is due to the fragility of the material and its tendency to break into smaller pieces; this was observed via scanning electron microscopy (Figure

4.3.) and utilised to obtain smaller particle size ranges by grinding the material using a pestle and mortar followed by separation into a 125-250 µm sample and a 250-500 µm sample.

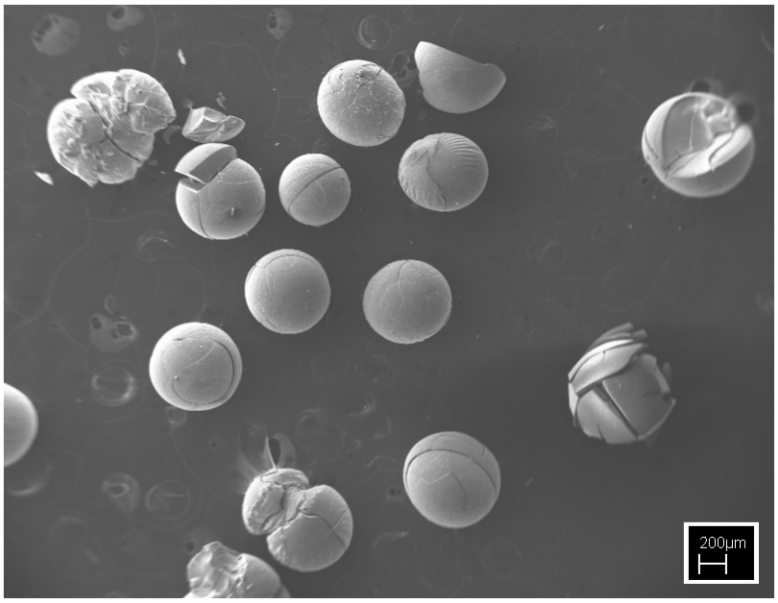

Figure 4.3.
Scanning electron microscopy image of the zirconium phosphate material as supplied.
Some breakage of the spherical solid particles has occurred upon adhesion to the backing material.

Sorption of barium-133 from 10 mL of seawater was compared for both the particle sizes as well as the raw material (0.1 g of solid in each experiment). As there were no data for pore size available and no pores were visible under electron microscopy, the additional model constants were determined by trial and error. By assuming an initial penetration of the analyte into the outermost 5 µm of the particle and average radii for each of the size ranges of 93.75 µm, 187.5 µm and 375 µm, the outer and inner fractions were set. As the diffusion length and diffusivity are constant, the change in k_{int} between each particle size is related to the area of the division between the two sections and the volume of the inner section. As the inner section is a sphere; area/volume can be simplified to ¾ radius and a simple formula for determining the ratio between two internal rate constants employed (Equation 4.16.).

$$\frac{k_{int,a}}{k_{int,b}} = \frac{A_a}{A_b} \times \frac{V_{inner,b}}{V_{inner,a}} = \frac{r_{inner,b}}{r_{inner,a}} \qquad \text{Equation 4.16.}$$

The rate constants have been increased to account for the reduction in the volume of the solid phase which can exchange directly with the aqueous solution. The new constants are based on sorption of barium into the outer fraction of the 125-250 µm sample (0.1 g experiment) and applied to the other two particle sizes.

Setting k_{int} for the smallest particle size to 1.0 x 10^{-5} allowed the modified numerical simulation method to give an adequate description of the dataset with a Δq(%) of 40 % (Table 4.1.). Unfortunately, calculating the associated internal mass transfer constants for the other two particle sizes did not fully simulate the observed data. In comparison to the basic simulation for the original 125-1000 µm sample, however, the simulation using two internal fractions was an improvement with a reduction in Δq(%) from 217 % to 123 %. This implies that internal mass transfer does impact sorption kinetics but that a two fraction division is an oversimplification.

Table 4.1.
Goodness of fit between experimental data and results of numerical simulation method with and without the inclusion of intraparticle diffusion.
Comparison has been made using normalised standard deviation (Δq(%)) analysis (Equation 4.12.).
The numerical simulation method used input parameters based on an aqueous volume of 10 mL for each experiment. No external mass transfer was included.

Sorptive material	Analyte	Solid mass (g)	Notes	Δq(%)		
				Basic simulation	2 internal fractions	3 internal fractions
UTEVA resin	Uranium	0.1	Sorption	8	N/A	N/A
		0.1	Desorption	4		
		0.01	Sorption	10		
	Thorium	0.1	Sorption	13	N/A	N/A
		0.1	Desorption	6		
		0.01	Sorption	17		
Anion exchange resin	Uranium	0.1	Sorption	104*	64*	N/A
		0.1	Desorption	49	633	
		0.01	Sorption	43*	78*	
	Thorium	0.1	Sorption	84	20	N/A
		0.1	Desorption	42	28	
		0.01	Sorption	104*	45*	
Zirconium phosphate	Barium	0.1	Sorption (125-250 µm)	N/A	40	27
		0.1	Sorption (250-500 µm)		68	21
		0.1	Sorption (125-1000 µm)	217*	123*	52*
		0.1	Desorption (125-1000 µm)	53*	36*	34*
		1	Sorption (125-1000 µm)	259*	226*	38*

*Large uncertainties on experimental data (average for dataset > 20%)

Each particle size was therefore split into three sections based on an initial 5 µm penetration followed by an additional 25 µm. The numerical simulation coding was modified to include four input variables including an additional differential equation, volume fraction and internal mass transfer constant. Increased k_{int} values for exchange between the outer and mid sections were calculated to reflect the decrease in volume and k_{int} values for exchange between the mid and inner sections were also calculated based on the same fitted value. This three-internal section

modification generated good simulated data for all three particle sizes as well as desorption from the 125-1000 µm sample (Figures 4.4. and 4.5.).

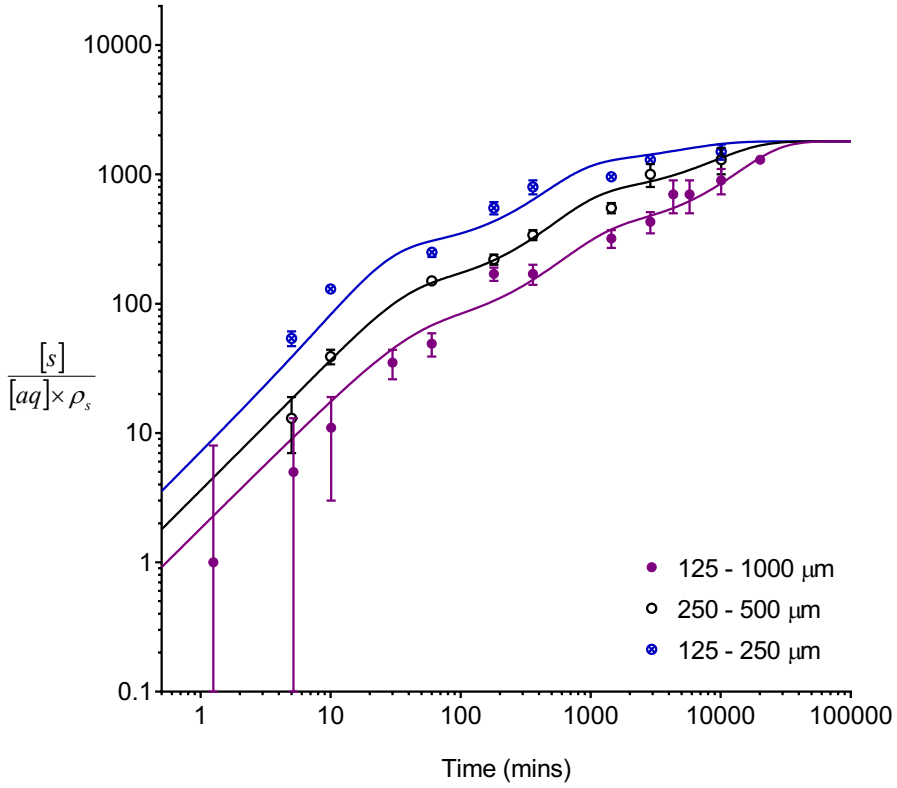

Figure 4.4.
Comparison between experimental data and numerical simulation of sorption of barium between seawater and zirconium phosphate for three particle sizes.
Three internal fractions based on radial penetrations of 5 µm and 30 µm were assumed.
The solid lines represent simulations using shared input parameters ($\vec{k}$ = 1.311 and $\overleftarrow{k}$ = 4.283 x 10^{-4}) for the three particle sizes depicted.
The numerical simulation method used input parameters based on an aqueous volume of 10 mL and a solid mass of 0.1 g for each experiment. No external mass transfer was included.

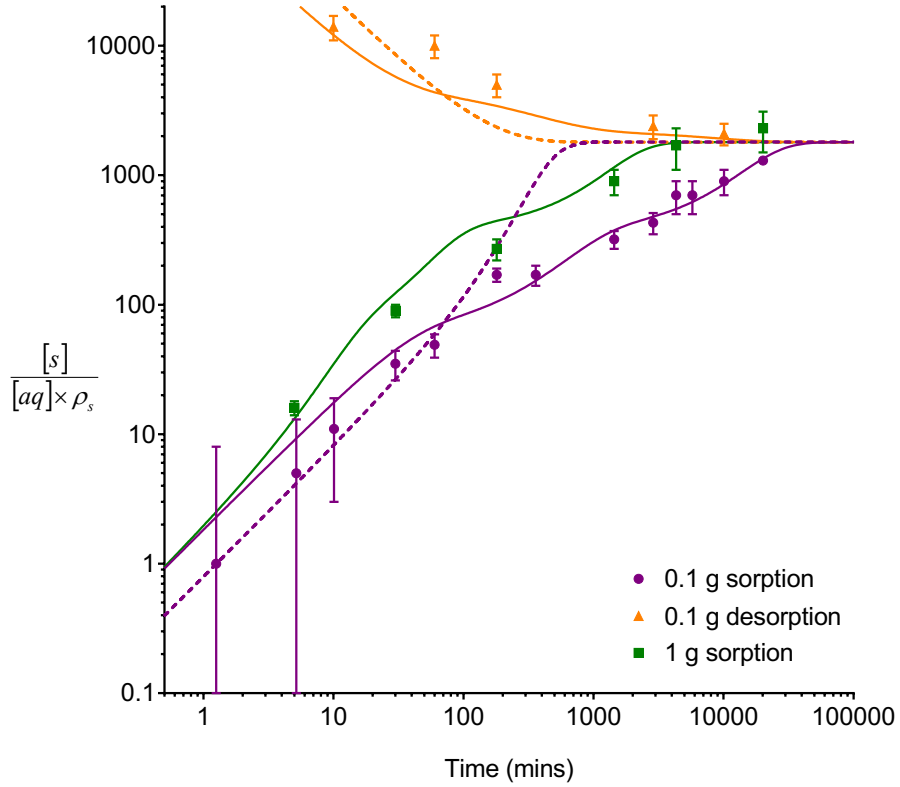

Figure 4.5.
Comparison between experimental data and numerical simulation of sorption/desorption of barium between seawater and zirconium phosphate for a single particle size.
The solid lines represent simulations using three internal fractions based on radial penetrations of 5 µm and 30 µm and modified rate constants ($\vec{k}$ = 1.311 and $\overleftarrow{k}$ = 4.283 x 10^{-4}).
The dashed lines represent simulations based on no internal mass transfer and without any modification to the rate constants ($\vec{k}$ = 2.244 x 10^{-2} and $\overleftarrow{k}$ = 7.334 x 10^{-6}).
The numerical simulation method used input parameters based on an aqueous volume of 10 mL for each experiment. No external mass transfer was included.

The experimental dataset generated using the greater mass of solid (1 g) was also simulated using the two- and three-internal section approaches. The k_{int} values were modified by multiplying the 0.1 g values by the ratio of the two solid volume fractions (Equation 4.17.). Although this modification to the k_{int} values generated simulated datasets that better described the experimental data, there is not enough evidence whether a linear relationship between the solid/aqueous ratio and the rate of intraparticle diffusion exists (see Chapter 5 for further discussion).

$$\frac{k_{int,a}}{k_{int,b}} = \frac{V_{s,a}}{V_{s,b}} \qquad \text{Equation 4.17.}$$

The internal fractionation approach was also applied to the experiments conducted using anion exchange resin. Although only a single particle size was investigated an estimation of the rate of diffusion within the particle was made. As with the zirconium phosphate simulation, an initial penetration of 5 µm was assumed and the particle was split into inner and outer sections. Using these fractions and a k_{int} value of 2.0 x 10^{-4} for the 0.1 g experiments and 2.0 x 10^{-5} for the 0.01 g experiments Δq(%), statistics of <45 % were produced for thorium (Table 4.1.). It was therefore concluded that the two-internal fraction simplification was suitable for the simulation of analyte interaction with anion exchange resin from 8M HNO_3 (Figures 4.6. and 4.7.).

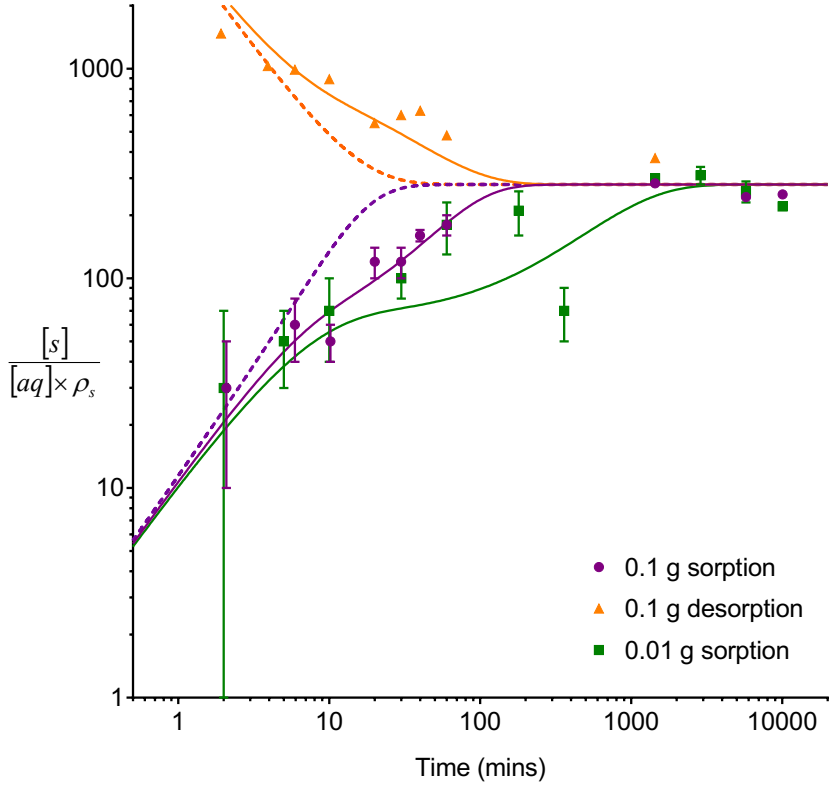

Figure 4.6.
Comparison between experimental data and numerical simulation of sorption/desorption of thorium between 8M HNO_3 and anion exchange resin.
The solid lines represent simulations using two internal fractions based on a radial penetration of 5 µm and modified rate constants ($\vec{k}$ = 0.8267 and $\overleftarrow{k}$ = 2.684 x 10^{-3}).
The dashed lines represent simulations based on no internal mass transfer and without any modification to the rate constants ($\vec{k}$ = 0.2031 and $\overleftarrow{k}$ = 6.593 x 10^{-4}).
The numerical simulation method used input parameters based on an aqueous volume of 10 mL for each experiment. No external mass transfer was included.

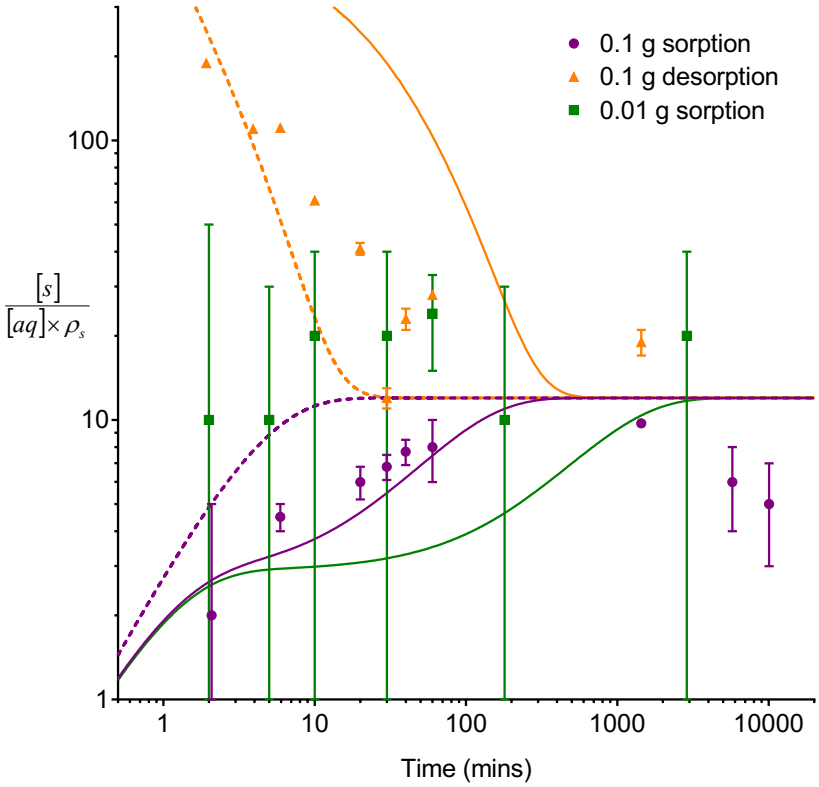

Figure 4.7.
Comparison between experimental data and numerical simulation of sorption/desorption of uranium between 8M HNO_3 and anion exchange resin.
The solid lines represent simulations using two internal fractions based on a radial penetration of 5 µm and modified rate constants ($\vec{k}$ = 0.2274 and $\overleftarrow{k}$ = 1.723 x 10^{-2}).
The dashed lines represent simulations based on no internal mass transfer and without any modification to the rate constants ($\vec{k}$ = 5.586 x 10^{-2} and $\overleftarrow{k}$ = 4.232 x 10^{-3}).
The numerical simulation method used input parameters based on an aqueous volume of 10 mL for each experiment. No external mass transfer was included.

Although it has been shown to be an adequate method of simulating ion exchange processes under the experimental conditions investigated, splitting the solid particle into separate internal fractions to represent intraparticle diffusion is still a simplified model. The physical process of surface diffusion is a continuous movement of analyte molecules between all active sites within the particle. It is therefore hypothesised that the accuracy of the numerical simulation method in describing the kinetics of sorption/desorption in porous materials could be improved by increasing the number of internal fractions or by using a PDE solver to numerically solve the concentration change in the solid particle in terms of both time and radial position. In addition, the mechanism of intraparticle diffusion may be more complex than homogeneous surface diffusion. Diffusion within the pore solution may also take place with a different associated rate constant. The structure of the pores may also not be homogeneous; a bidispersed structure may be present with macro- and micro-pores either in series or parallel[43,47]. Finally, interactions

between dissolved and/or sorbed species may occur; therefore intraparticle diffusion may be better described using the Maxwell-Stefan model of diffusion[42].

4.2.1.3. Numerical simulation – Effect of external mass transfer

The experiments already described were conducted under constant tumbling conditions to avoid external mass transfer effects. Under stationary conditions, however, a stagnant layer builds up around the surface of the particles. The impact of this process on experimentally determined sorption datasets was assessed and the numerical simulation method modified to include aqueous phase diffusion.

As with internal mass transfer where the solid particle was divided into multiple fractions, external mass transfer can be represented by splitting the aqueous volume into a bulk fraction and a surface fraction. Aqueous diffusion occurs between the bulk and surface whereas sorption and desorption occurs between the surface and solid (or outer solid if internal fractionation is also applied). The numerical simulation coding is therefore modified to include an additional input/output variable and consequent differential equations (Equations 4.18. and 4.19.), amended aqueous volume fractions and an external mass transfer constant. The initial concentrations for the bulk and surface fractions were both set to the same value as previously used in the basic simulation for the combined aqueous fraction.

$$\frac{d[aq]_{surface}}{dt} = k_{ext}[aq]_{bulk} - k_{ext}[aq]_{surface} + \left[\left(\overleftarrow{k}[s]_{(outer)} - \vec{k}[aq]_{surface}\right)\times\left(\frac{V_{s,(outer)}}{V_{aq,surface}}\right)\right] \quad \text{Equation 4.18.}$$

$$\frac{d[aq]_{bulk}}{dt} = \left(k_{ext}[aq]_{surface} - k_{ext}[aq]_{bulk}\right)\times\left(\frac{V_{aq,surface}}{V_{aq,bulk}}\right) \quad \text{Equation 4.19.}$$

Comparison of batch experimental data between well-mixed and stationary conditions was used by Paxton at al.[63] to calculate the thickness of the stagnant layer surrounding a single anion exchange bead. For the material investigated (AG 1x4 bead, ~760 µm diameter) this was determined to be 153 µm in the stationary solution, falling to 16 µm under acoustic mixing conditions. In the current study, a set mass (0.1 g) was used as opposed to a single particle. The solid particles therefore settled down onto the base of the vial to form a thin bed consisting of more than one layer. Trial and error manipulation of aqueous volume fractions and k_{ext} values to achieve a good fit to the experimental data indicated that in the case of a settled bed of particles,

the thickness of the stagnant layer is dependent on the bed volume. This is, in turn, dependent on the density of the particles and the packing geometry. Packing volumes were calculated by volumetric displacement measurements. For both ion exchange materials, close random packing with a packing density of 0.625 was determined; a 0.1 g bed of anion exchange resin would therefore fill a volume of 0.145 mL whereas a 0.1 g bed of zirconium phosphate would fill a volume of 0.094 mL. For UTEVA resin a packing density of 0.345 was determined; this looser structure could be due to repulsive hydrophobic forces between the organically coated particles. A 0.1 g bed of UTEVA would fill a volume of 0.264 mL.

Taking into account these differences in packing it was discovered that the size of the surface fraction could be calculated by multiplying the bed volume by 23. The significance of this factor is not known but it is thought to be related to the dimensions of the vial used in the experiments. In addition, agreement has not yet been reached regarding the maximum thickness of the stagnant layer in the process of film diffusion. It is therefore unclear whether the differential equations used (Equations 4.18. and 4.19.) describe diffusion in the bulk solution or diffusion over a thick film layer. Further investigations using a range of aqueous volumes and mixing containers of different geometries would help improve understanding of the formation of stagnant zones. As film diffusion was not quantified under the constant tumbling conditions, it can be assumed to be incorporated into the forward and reverse rate constants describing transfer between the aqueous phase and the lumped (outer) solid phase. This is similar to the linear driving force approximation commonly used in the simulation of chromatographic processes[42,64].

The calculated surface and bulk volume fractions for each of the three materials were used to set k_{ext} values for each analyte/resin system by taking into account the cross-sectional area of the vial (CSA), the dimensions of the total volume occupied (solid and aqueous phases combined) and the diffusion coefficient for the analyte being simulated (Equation 4.20.). Estimated D_{diff} values were taken from literature values for diffusion in water at 25°C[55] (0.426 x 10^{-5} cm^2/s for ½UO_2^{2+}; 0.620 x 10^{-5} cm^2/s for $^1/_3Ce^{3+}$ - as a proxy for Th^{3+}; 0.847 x 10^{-5} cm^2/s for ½Ba^{2+}).

$$k_{ext} = \frac{CSA}{V_{surface}} \times \frac{D_{diff}}{L_{bulk}} \qquad \text{Equation 4.20.}$$

Simulation of sorption under external mass transfer limited conditions was run for the five datasets collected. The modified LabVIEW coding was tailored for each material; no internal fractionation was introduced for UTEVA resin, 2 internal fractions were used in the simulation of anion exchange resin systems and zirconium phosphate was split into 3 internal fractions.

This approach gave a good description of the processes occurring (Figures 4.8.-4.10.) with low Δq(%) statistics (Table 4.2.).

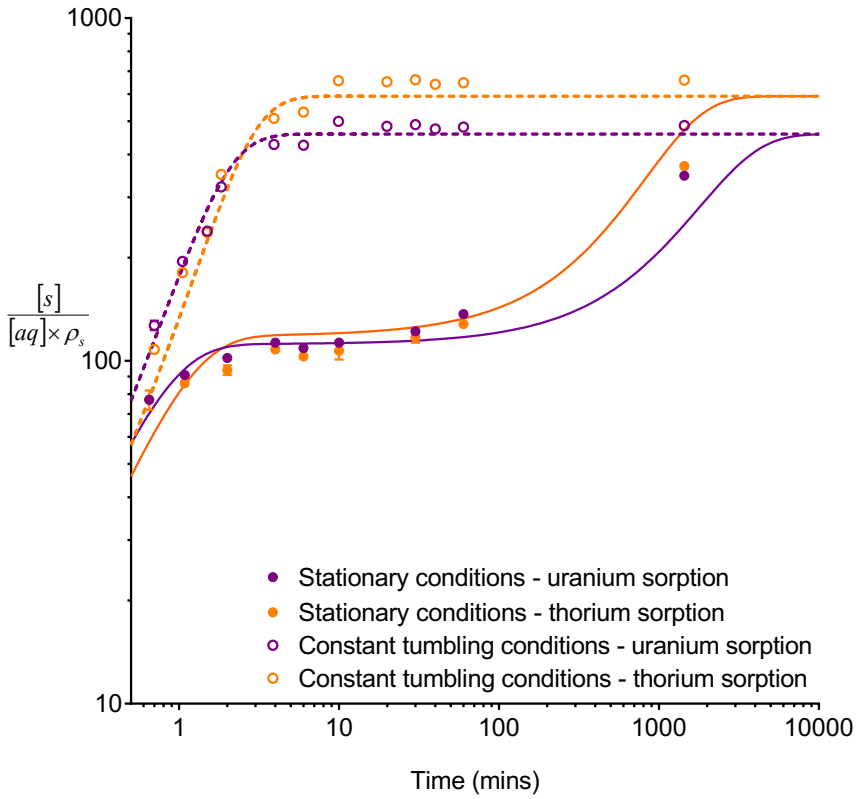

Figure 4.8.
Comparison between experimental data and numerical simulation of sorption for UTEVA resin under stationary and constant tumbling conditions.
The solid lines represent simulations using two aqueous fractions based on the settled resin bed.
The dashed lines represent simulations based on no external mass transfer.
No internal fractions have been included for the simulations.
The numerical simulation method used input parameters based on an aqueous volume of 10 mL for each experiment and an internal diameter of the reaction vessel of 2.4 cm.

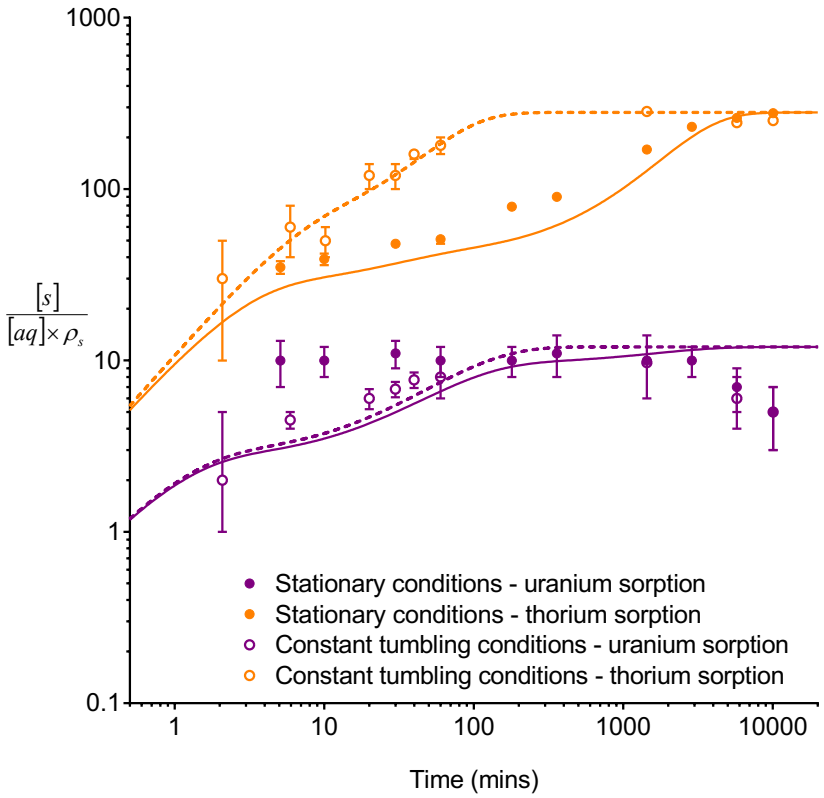

Figure 4.9.
Comparison between experimental data and numerical simulation of sorption for anion exchange resin under stationary and constant tumbling conditions.
The solid lines represent simulations using two aqueous fractions based on the settled resin bed.
The dashed lines represent simulations based on no external mass transfer.
Two internal fractions have been included for the simulations.
The numerical simulation method used input parameters based on an aqueous volume of 10 mL for each experiment and an internal diameter of the reaction vessel of 2.4 cm.

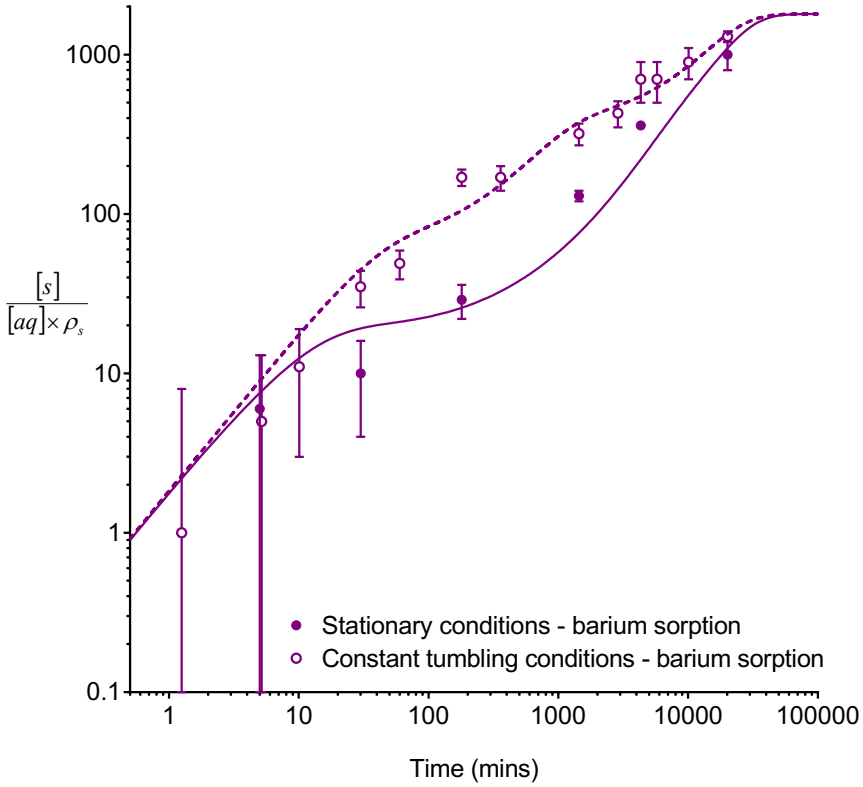

Figure 4.10.
Comparison between experimental data and numerical simulation of sorption for zirconium phosphate under stationary and constant tumbling conditions.
The solid lines represent simulations using two aqueous fractions based on the settled resin bed.
The dashed lines represent simulations based on no external mass transfer.
Three internal fractions have been included for the simulations.
The numerical simulation method used input parameters based on an aqueous volume of 10 mL for each experiment and an internal diameter of the reaction vessel of 2.4 cm.

Table 4.2.
Goodness of fit between experimental data and results of numerical simulation method with the inclusion of aqueous phase diffusion.
Comparison has been made using normalised standard deviation (Δq(%)) analysis (Equation 4.12.).
The numerical simulation method used input parameters based on an aqueous volume of 10 mL for each experiment. Sorption was carried out under stationary conditions.

Sorptive material	Analyte	Solid mass (g)	Δq(%)
			Simulation including external mass transfer
UTEVA resin	Uranium	0.1	12
	Thorium	0.1	17
Anion exchange resin	Uranium	0.1	65*
	Thorium	0.1	24
Zirconium phosphate	Barium	0.1	50*

*Large uncertainties on experimental data (average = 25% for uranium sorption on anion exchange resin and 39% for barium sorption on zirconium phosphate)

4.2.1.4. Numerical simulation – Effect of analyte and interferent concentration

The three sorptive materials investigated can be used to separate or concentrate analytes from aqueous or dissolved samples. In this real-life scenario, both interacting and non-interacting species will be present alongside the analyte being isolated. Depending on their concentration and speciation interferents can have various effects including synergistic sorption, competitive sorption or competitive complex formation[66,67].

As previously mentioned, a significant reduction in k_D for barium sorption on zirconium phosphate was observed when deionised water (adjusted to ~pH 8) was used as the matrix rather than seawater. Additionally, the magnitude of the reduction was linked to the amount of NaOH used in the titration. Furthermore, ICP-MS measurement of the concentration of zirconium present in the aqueous phase after contact with the solid particles indicated a dissolution process. The rate of zirconium leaching was calculated to be ~1.7×10^{-9} g/s per gram of solid material. Due to the added complexity of solid dissolution and the need to control pH, no further investigations into the effect of analyte and interferent concentrations were conducted for zirconium phosphate in this study.

The presence of a high concentration of both magnesium and calcium was investigated for both UTEVA and anion exchange resins. An 8M HNO_3 solution containing 440 ppm Mg, 440 ppm Ca, 230 ppb U and 230 ppb Th (all values given to 2sf) was prepared. Using a solid/aqueous ratio of 0.1 g / 10 mL, sorption values of uranium and thorium on both materials were unaffected by the presence of these interferents with negligible difference in Δq(%) statistics between the experimental data points and the numerical simulation (including internal mass transfer for anion exchange resin) when comparing sorption with and without Mg/Ca (Table 4.3. and Figures 4.11. and 4.12.). In addition, measurement of the level of sorption of magnesium and calcium by ion chromatography indicated little interaction with either UTEVA resin or anion exchange resin (k_D <5). Both of these species are therefore non-competing interferents.

Table 4.3.
Goodness of fit between experimental data and results of numerical simulation method with or without the presence of interferents.
Comparison has been made using normalised standard deviation (Δq(%)) analysis (Equation 4.12.).
The numerical simulation method used input parameters based on an aqueous volume of 10 mL for each experiment.

Sorptive material	Analyte	Solid mass (g)	Δq(%)	
			No interferent	Mg/Ca interferents
UTEVA resin	Uranium	0.1	8	12
	Thorium	0.1	13	18
Anion exchange resin	Uranium	0.1	64*	47*
	Thorium	0.1	20	21

*Large uncertainties on experimental data (average = 33 % for no interferent and 21 % for Mg/Ca interferents)

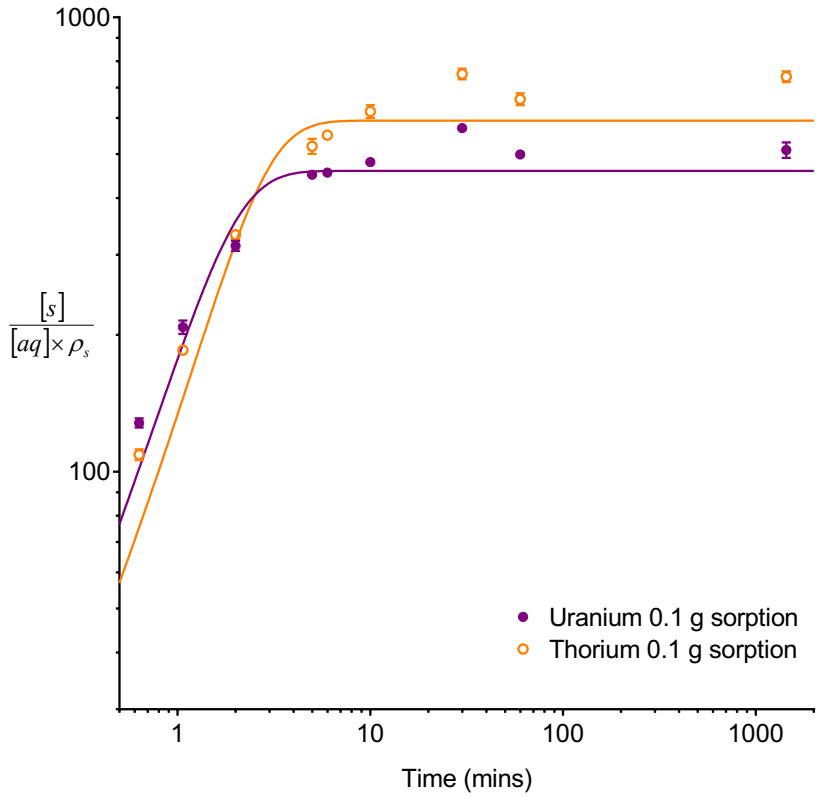

Figure 4.11.
Comparison between experimental data and numerical simulation of sorption of uranium and thorium between 8M HNO_3 and UTEVA resin in the presence of Mg/Ca interferents.
The experimental data relates to sorption of uranium and thorium from a solution containing 440 ppm Mg and 440 ppm Ca.
The numerical simulation method used input parameters based on the optimised rate constants as well as an aqueous volume of 10 mL and a solid mass of 0.1 g for each experiment. No internal or external mass transfer was included.

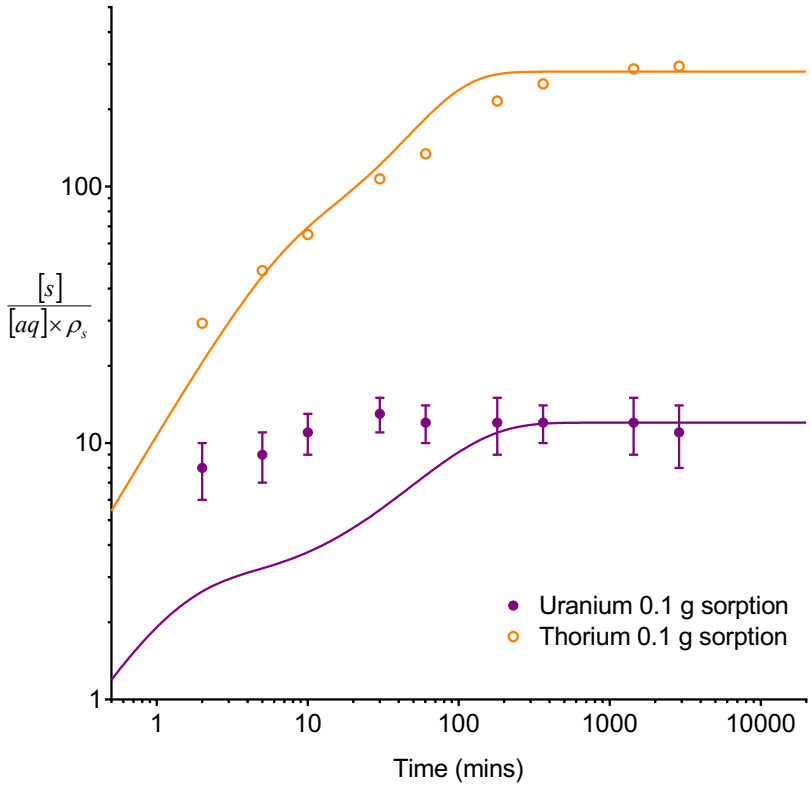

Figure 4.12.
Comparison between experimental data and numerical simulation of sorption of uranium and thorium between 8M HNO_3 and anion exchange resin in the presence of Mg/Ca interferents.
The experimental data relates to sorption of uranium and thorium from a solution containing 440 ppm Mg and 440 ppm Ca.
The numerical simulation method used input parameters based on the optimised rate constants as well as an aqueous volume of 10 mL and a solid mass of 0.1 g for each experiment. Two internal fractions based on a radial penetration of 5 µm were included. No external mass transfer was included.

As UTEVA resin showed favourable sorption of both uranium and thorium, conducting kinetic experiments from a solution containing a high concentration of one of the species and a low concentration of the other could provide simultaneous kinetic information on the effect of high analyte concentration and the effect of a competing interferent. A solution of 8M HNO_3 containing 470 ppm U and 240 ppb Th (2sf) was hence prepared and mixed with UTEVA resin using a solid/aqueous ratio of 0.1 g / 10 mL. The high concentration of uranium caused a decrease in the k_D values of both uranium and thorium.

In order to modify the LabVIEW coding to simulate the sorption of uranium and thorium simultaneously, information on the concentration of complexant molecules and their stoichiometric relationship with the analytes must be obtained. This was achieved by conducting a series of experiments using 8M HNO_3 solutions containing only a single interacting species at varying concentrations. At high initial aqueous concentrations (>1000 ppm) the concentration on

the lumped solid phase at equilibrium tended towards a constant value indicating saturation of the complexant molecules. The value for uranium was approximately double that of thorium although large uncertainties were present when measuring concentration changes after sorption equilibrium had been obtained at high initial aqueous concentrations. As it has been suggested that the uranyl nitrate species present in 8M HNO_3 undergoes a 1:2 stoichiometric reaction with the extractant[70] (Equation 4.21.) it is therefore proposed that thorium nitrate undergoes a 1:4 stoichiometric reaction with the extractant (Equation 4.22.); this is a theoretically valid assumption as there are twice as many nitrate ligands surrounding the metal ion.

$$UO_2(NO_3)_2 + 2E \leftrightarrow UO_2(NO_3)_2E_2 \qquad \text{Equation 4.21.}$$

$$Th(NO_3)_4 + 4E \leftrightarrow Th(NO_3)_4E_4 \qquad \text{Equation 4.22.}$$

The numerical simulation coding was modified to include a lumped solid extractant concentration model constant ($[s]_E$) of 1.5 mol/dm^3, rate constants for uranium and thorium and the solid and aqueous concentration input variables for both species along with four associated differential equations (Equations 4.23.–4.26.). Assuming the proposed reaction mechanisms are single step reactions with no intermediate products (i.e. Equations 4.21 and 4.22. are the rate determining steps) the rate order with respect to the extractant is 2 in the case of uranium sorption and 4 in the case of thorium sorption. For the modified numerical simulation method, the forward rate constants used in the basic simulation were divided by $[s]_E^n$ where n = 2 (uranium) or 4 (thorium). From the lumped solid extractant concentration model constant ($[s]_E$) of 1.5 mol/dm^3, it follows that if UTEVA resin was fully saturated with a single analyte, the lumped solid concentration would be 162 mg/g (uranium) or 79.1 mg/g (thorium). These values are similar to the reference capacity for uranium on UTEVA resin (96 mg/g) as calculated from the original characterisation data by Horwitz et al[70]. The deviation from this quoted value could be due to the difference in experimental methods of determination. The quoted capacity was determined by measuring the amount of sorbed analyte after saturating the column; as the loading concentration of uranyl nitrate used in this measurement has not been specified, it cannot be known whether true saturation or equilibrium was achieved.

$$\frac{d[s]_U}{dt} = \vec{k}_U[aq]_U([s]_E - 4[s]_{Th} - 2[s]_U)^2 - \overleftarrow{k}_U[s]_U \qquad \text{Equation 4.23.}$$

$$\frac{d[aq]_U}{dt} = \left[\overleftarrow{k}_U[s]_U - \vec{k}_U[aq]_U([s]_E - 4[s]_{Th} - 2[s]_U)^2\right] \times \left(\frac{V_s}{V_{aq}}\right) \qquad \text{Equation 4.24.}$$

$$\frac{d[s]_{Th}}{dt} = \vec{k}_{Th}[aq]_{Th}([s]_E - 4[s]_{Th} - 2[s]_U)^4 - \overleftarrow{k}_{Th}[s]_{Th} \qquad \text{Equation 4.25.}$$

$$\frac{d[aq]_{Th}}{dt} = [\overleftarrow{k}_{Th}[s]_{Th} - \vec{k}_{Th}[aq]_{Th}([s]_E - 4[s]_{Th} - 2[s]_U)^4] \times \left(\frac{V_s}{V_{aq}}\right) \qquad \text{Equation 4.26.}$$

The simulation was run for each analyte at a range of aqueous concentration inputs whilst constraining the other species inputs to zero. The sorption value once equilibrium had been achieved was then plotted against initial aqueous concentration and compared to the experimental data (Figure 4.13.). A good fit was observed for both uranium (Δq(%) = 15 %) and thorium (Δq(%) = 27 %).

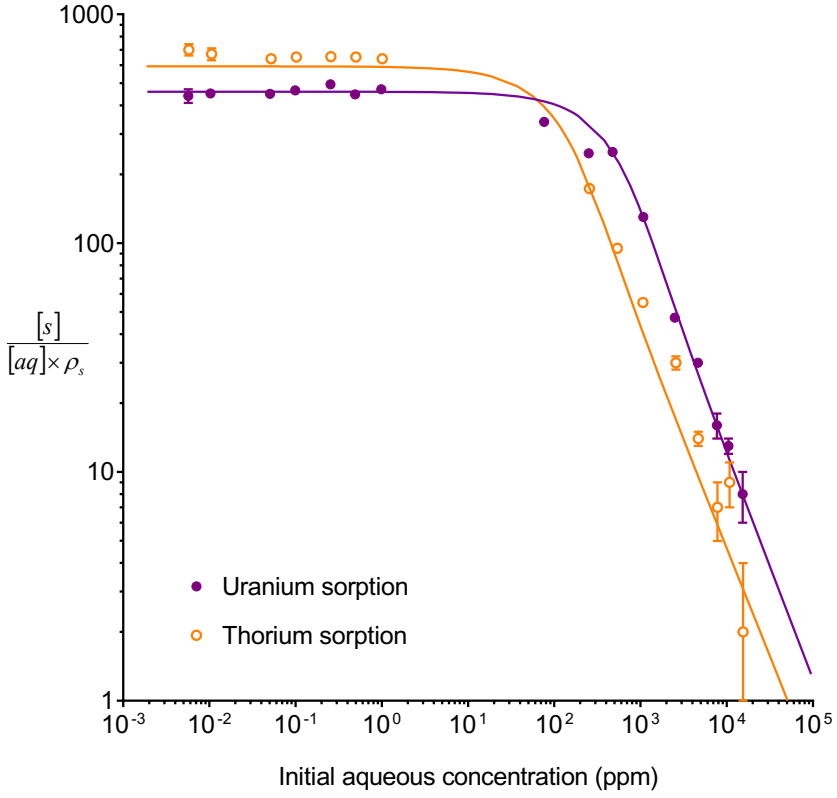

Figure 4.13.
Comparison between experimental data and numerical simulation of uranium and thorium sorption equilibrium positions between 8M HNO_3 and UTEVA resin at a range of initial aqueous concentrations.
The solid lines represent the final values obtained from simulations using differential equations including both species as well as a lumped solid extractant concentration model constant of 1.5 mol/dm^3 (Equations 4.23.–4.26.).
The numerical simulation method used input parameters based on an aqueous volume of 10 mL and a solid mass of 0.1 g for each experiment. The initial aqueous concentration of the species not being simulated was constrained to zero. No external mass transfer was included.

Returning to the mixed analyte solution (470 ppm U and 240 ppb Th), the simultaneous simulation approach accurately predicted the reduction in k_D value for both analytes in

comparison to a mixed solution containing low concentrations (250 ppb U and 260 ppb Th). The kinetics of sorption were also accurately captured (Figure 4.14.) with Δq(%) values for the high uranium solution of 11 % (uranium) and 6 % (thorium).

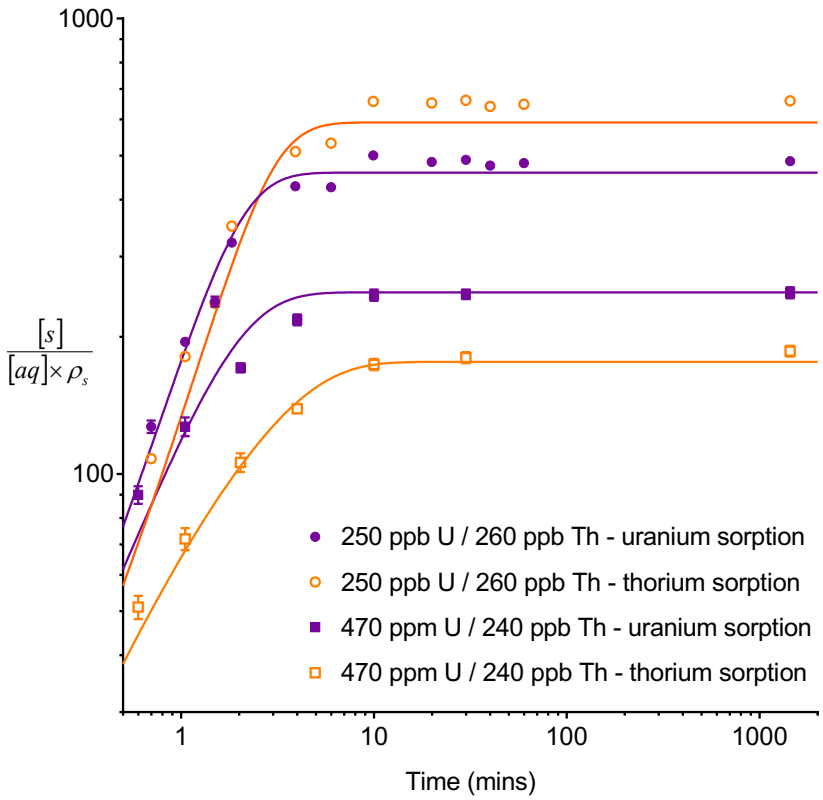

Figure 4.14.
Comparison between experimental data and numerical simulation of sorption of uranium and thorium between 8M HNO_3 and UTEVA resin using different initial uranium concentrations.
The solid lines represent simulations using differential equations including both species as well as a lumped solid extractant concentration model constant of 1.5 mol/dm^3 (Equations 4.23.–4.26.).
The numerical simulation method used input parameters based on an aqueous volume of 10 mL and a solid mass of 0.1 g for each experiment. No external mass transfer was included.

4.2.2. Comparison to commonly used kinetic and thermodynamic classifications

The numerical simulation approach to sorption modelling describes the rate of uptake via a combination of processes including both external and intraparticle diffusion and sorption kinetics. The concentration of both analytes and interferents and their stoichiometric relationship with the complexant or active sites is also taken into account. Examples of simulated datasets produced by this method were assessed under the commonly applied pseudo-first-order/pseudo-second-order classification system.

Although several linear and non-linear forms of the PFO and PSO equations exist, this assessment is based on two of the most commonly used linear forms (Equations 4.27. and 4.28.). Using these

equations, labelling of a sorptive system as either PFO or PSO is determined by plotting $\ln(q_e-q_t)$ against time (PFO) or t/q_t against time (PSO) and applying linear regression to assess the goodness of fit. This method has been carried out on a selection of the simulated sorption curves (Table 4.4.). A subset of the simulation values produced has been taken as the size of the datasets produced can be very large. Although the size of these subsets vary (33 – 103 data points), in each case they encompass the whole sorption process up to equilibrium ($q_e-q_t = 0$) and contain evenly time spaced data points.

$$ln(q_e - q_t) = ln(q_e) - k_1 t \qquad \text{Equation 4.27.}$$

$$\frac{t}{q_t} = \frac{1}{k_2 q_e^2} + \frac{1}{q_e} t \qquad \text{Equation 4.28.}$$

As multiple rate constants were used in the simulation, the two examples including internal diffusion and the example including external diffusion were hypothesised to fit neither of the simplified rate equations. All three examples, however, were approximately linear over the temporal subset selected for both the PFO and the PSO with R^2 values greater than 0.994. The pseudo-second-order rate equation fitted the data better with R^2 values greater than 0.9998 and much more accurate estimations of the position of equilibrium (predicted q_e) despite this value being integral to the PFO plot (y-intercept). This observation is due to an initial faster rate indicating a period of complexation or exchange controlled uptake before diffusion processes begin reducing the effective concentration of either analyte molecules (external mass transfer) or sorption sites (internal mass transfer). The presence of a faster rate can be observed as a deviation from linearity by selecting an alternative subset of the simulation data (Figures 4.15. and 4.16. inset plots). This trend was also observed when a recently developed combined surface reaction and diffusion-controlled kinetic equation was plotted under the usual PSO parameters[181]. In the three examples described in this chapter, it was found that the deviation from linearity was more severe for the PFO plots (Figure 4.15.). This accounts for the inaccuracy of the predicted q_e values as this form of the PFO equation relies on the y-intercept for determination of q_e. On the other hand, the PSO equation uses the gradient of the slope meaning that linear regression analysis of PSO plots is a more reliable method for q_e determination. It is important, however, that the correct time period has been sampled. For example, taking a different simulation data subset (Figure 4.16.), gives a less accurate predicted q_e value of 1.164×10^{-3} for barium sorption on zirconium phosphate.

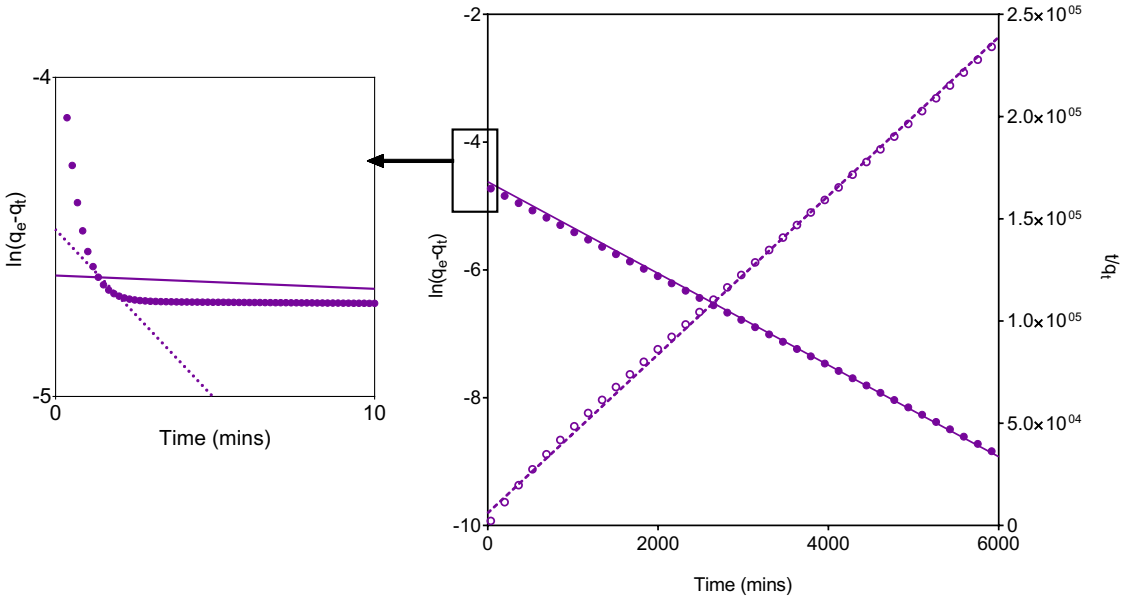

Figure 4.15.

Comparison between simulated datasets and the pseudo-first-order and pseudo-second-order equations using the single analyte numerical simulation method for uranium sorption from a non-stirred 8M HNO_3 solution (10 mL) onto UTEVA resin (0.1 g).

PFO equations are plotted as $\ln(q_e - q_t)$ on the left hand axis, simulated data points are given as closed symbols and linear regression is given as a solid line.

PSO equations are plotted as t/q_t on the right hand axis, simulated data points are given as open symbols and linear regression is given as a dashed line.

The larger plot shows the numerically simulated dataset until equilibrium has been reached whilst the inset plot shows the initial 10 minutes only. Two external fractions have been used in the simulation. The dotted line represents linear regression analysis for the PFO equation for the initial 10 minutes only.

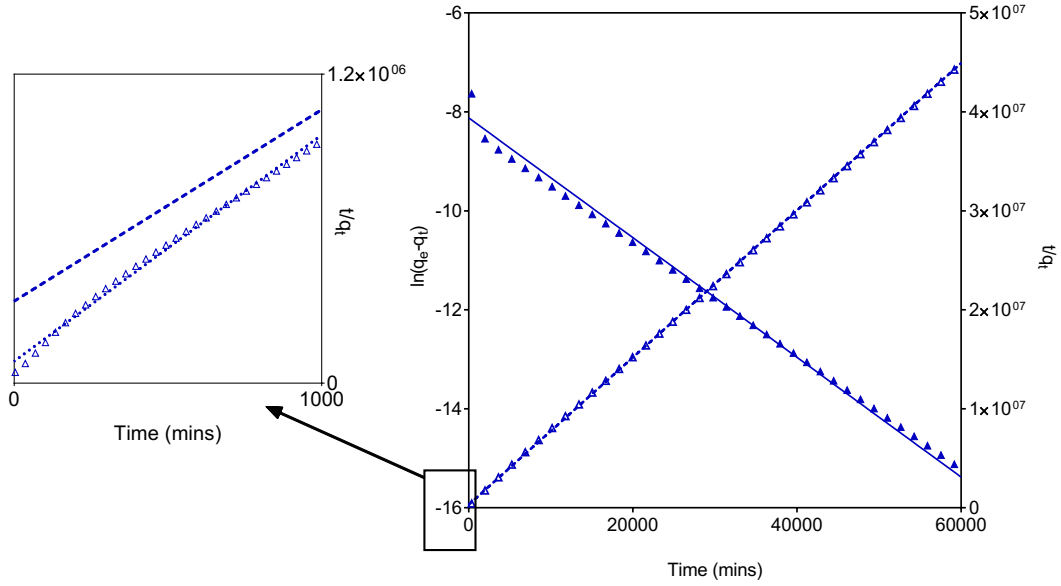

Figure 4.16.
Comparison between simulated datasets and the pseudo-first-order and pseudo-second-order equations using the single analyte numerical simulation method for barium sorption from a stirred seawater solution (10 mL) onto zirconium phosphate (0.1 g).
PFO equations are plotted as $\ln(q_e - q_t)$ on the left hand axis, simulated data points are given as closed symbols and linear regression is given as a solid line.
PSO equations are plotted as t/q_t on the right hand axis, simulated data points are given as open symbols and linear regression is given as a dashed line.
The larger plot shows the numerically simulated dataset until equilibrium has been whilst the inset plot shows the initial 1000 minutes only. Three internal fractions have been used in the simulation. The dotted line represents linear regression analysis for the PSO equation for the initial 1000 minutes only.

Data produced using the modified numerical simulation method including rate orders for both analytes and extractant molecules (based on stoichiometry) was also analysed for correlation with PFO and PSO equations. As with the diffusion based examples, simulated sorption data using a high initial aqueous concentration of (one of) the analyte(s) showed a faster initial rate in both plots although high R^2 values were obtained (>0.990) when selecting a subset encompassing the entire sorption process. The non-exact description of the simulated datasets to either of the PFO or PSO equations reflects the added complexity to the sorption process once the analyte concentration becomes significant and the extractant is no longer in excess. The R^2 values obtained for the simultaneous simulation of both uranium and thorium on UTEVA resin are lower indicating a more complex rate equation due to the competition between analytes. Conversely, the simulated datasets for sorption at low initial aqueous concentrations showed a good fit to the PFO equation (Figure 4.17.) independently of the temporal subset chosen, the stoichiometry and corresponding rate order and whether competing analytes were included. This suggests that the pseudo-first-order equation can be used to describe sorption when the analyte concentration(s) is/are significantly lower than the extractant concentration; this conclusion contradicts the

theoretical derivation of the PFO and PSO equations by Azizian et al[171]. The analyte concentration is determined to be significantly low when the sorption value at equilibrium is at the maximum (Figure 4.13.).

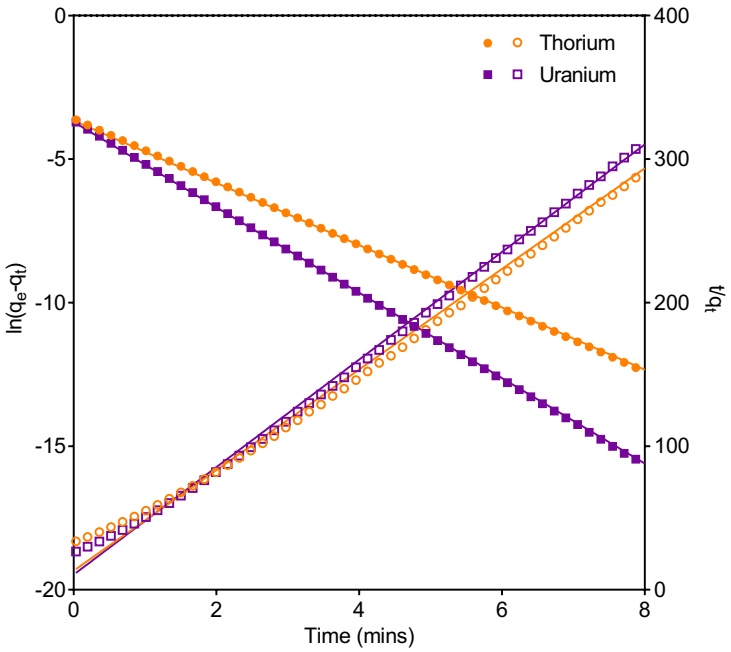

Figure 4.17.
Comparison between simulated datasets and the pseudo-first-order and pseudo-second-order equations using the multiple analyte numerical simulation method.
Uranium and thorium sorption from a stirred 8M HNO_3 solution (10 mL) onto UTEVA resin (0.1 g) is simulated. Both analytes were simulated simultaneously using rate orders based on stoichiometric ratios of 1U:2E and 1Th:4E and initial aqueous analyte concentrations of 250 ppb U and 260 ppb Th.
PFO equations are plotted as $\ln(q_e - q_t)$ on the left hand axis, simulated data points are given as closed symbols and linear regression is given as a solid line.
PSO equations are plotted as t/q_t on the right hand axis, simulated data points are given as open symbols and linear regression is given as a dashed line.

Based on this analysis of numerically simulated datasets, it is suggested that the classification of experimentally determined sorption data to either PFO or PSO kinetics relies greatly on the times sampled and the initial aqueous analyte concentration. Whether equilibrium has been obtained or not is particularly important for the PFO equation as an estimation of q_e is needed to produce the plot. As the difference between the goodness of fit between the two equations is often marginal, the magnitude of uncertainties on the experimental measurements can also be important. In general, the PSO equation provides a better estimation of q_e and has the added benefit of not requiring prior knowledge of this value.

Table 4.4.

Goodness of fit of simulated datasets to pseudo-first-order and pseudo-second-order equations.

Plots of $\ln(q_e - q_t)$ vs t (PFO) and t/q_t vs t (PSO) have been generated using the same set of evenly time spaced data points covering the whole sorption process to equilibrium (equilibrium obtained when $q_e - q_t = 0$). These plots have been analysed using linear regression and R^2 values quoted. The predicted solid concentration at equilibrium (predicted q_e) has also been calculated from either the intercept (PFO, Equation 4.27.) or slope (PSO, Equation4.28.) for comparison with the final simulated solid concentration (simulated q_e).

Sorptive material	Analyte	Solid fractions	Aqueous fractions	> 1 analyte simulated simultaneously?	Initial [aq]	Rate order*	Simulated q_e (mg/g)	PFO		PSO	
								R^2	Predicted q_e (mg/g)	R^2	Predicted q_e (mg/g)
UTEVA resin	Uranium	1	2	No	N/A	N/A	2.543E-02	0.9990	9.843E-03	0.9999	2.578E-02
Anion exchange resin	Thorium	2	1	No	N/A	N/A	1.882E-02	0.9996	1.088E-02	0.9998	1.914E-02
Zirconium phosphate	Barium	3	1	No	N/A	N/A	1.338E-03	0.9947	2.972E-04	1.000	1.345E-03
UTEVA resin	Uranium	1	1	Yes	250 ppb U and 260 ppb Th	1U:2E	2.562E-02	0.9997	2.453E-02	0.9984	2.670E-02
	Thorium	1	1			1Th:4E	2.741E-02	0.9995	2.571E-02	0.9984	2.853E-02
UTEVA resin	Uranium	1	1	No	250 ppb U	1U:1E	2.562E-02	0.9997	2.594E-02	0.9975	2.719E-02
UTEVA resin	Uranium	1	1	Yes	470 ppb U and 240 ppb Th	1U:2E	4.239E+01	0.9908	4.231E+01	0.9993	4.352E+01
	Thorium	1	1			1Th:4E	1.881E-02	0.9974	9.873E-03	0.9997	1.957E-02
UTEVA resin	Uranium	1	1	No	470 ppb U	1U:2E	4.239E+01	0.9998	3.150E+01	0.9996	4.312E+01
UTEVA resin	Uranium	1	1	No	470 ppb U	1U:1E	4.553E+01	0.9998	3.878E+01	0.9994	4.645E+01

*Rate order is assumed to be equivalent to stoichiometry.

The numerical simulation method for UTEVA resin including stoichiometry based rate orders was also compared to the thermodynamic Langmuir isotherm (Equation 4.29.). Simulating a single analyte solution, the solid (q_e) and aqueous (C_e) concentrations at equilibrium for a range of initial aqueous concentrations were generated and the resulting plots (Figures 4.18. and 4.19.) analysed using linear regression.

$$\frac{C_e}{q_e} = \frac{1}{bq_{max}} + \frac{1}{q_{max}} C_e \qquad \text{Equation 4.29.}$$

Simulations using a 1:1 stoichiometry (analyte:extractant) fitted the Langmuir isotherm exactly (R^2 = 1.000) whereas sorptive systems where the analyte reacts with a greater ratio of extractant molecules show a deviation from linearity. This deviation increases when moving from a 1:2 stoichiometry (R^2 = 0.9997) to a 1:4 stoichiometry (R^2 = 0.9990). This subtle difference can be observed at the low end of the concentration range (Figures 4.18. and 4.19. inset plots).

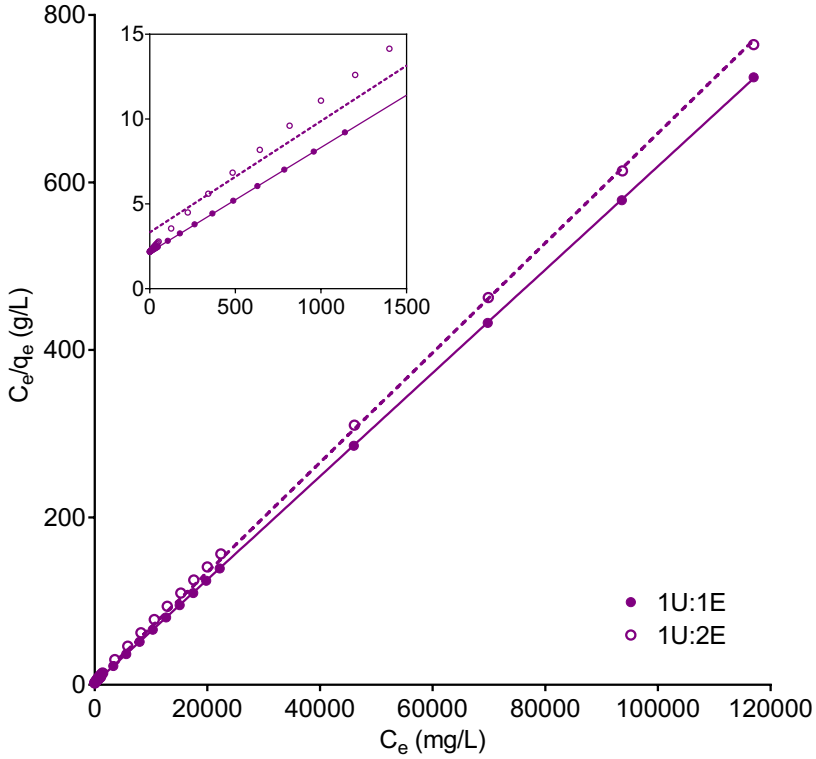

Figure 4.18.
Comparison between simulated equilibrium values and the Langmuir isotherm for uranium sorption.
Uranium sorption from a stirred 8M HNO_3 solution (10 mL) onto UTEVA resin (0.1 g) is simulated.
Rate orders were based on stoichiometric ratios of 1U:2E and 1U:1E. The lumped solid extractant concentration model constant was set to 1.5 mol/dm^3 for 1U:2E and 0.75 mol/dm^3 for 1U:1E.
Linear regression has been applied to both datasets across the entire concentration range simulated.
The inset plot shows a zoomed in view of the low end of the concentration range.

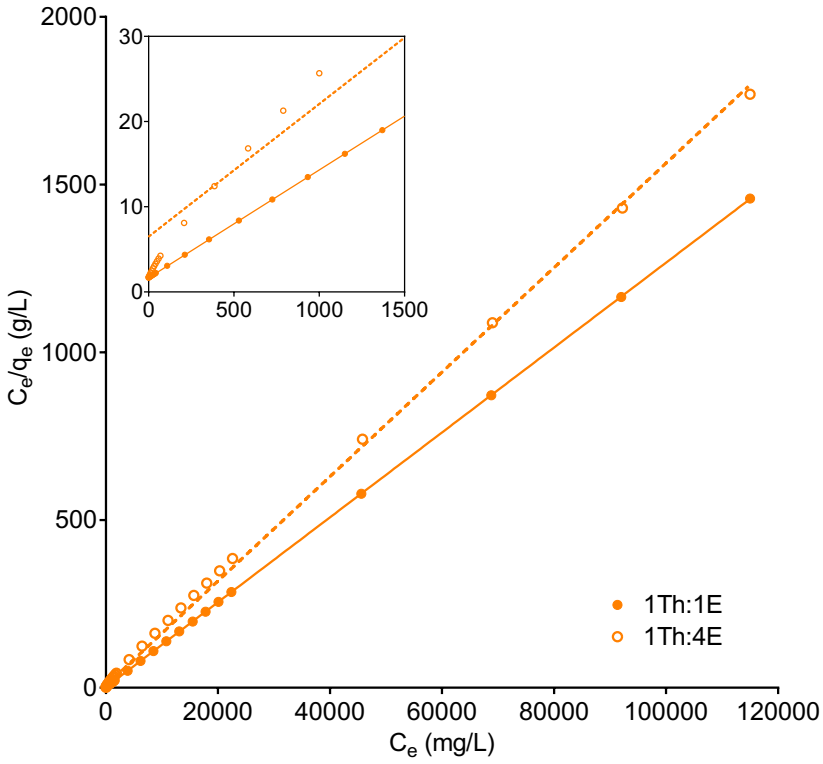

Figure 4.19.
Comparison between simulated equilibrium values and the Langmuir isotherm for thorium sorption.
Thorium sorption from a stirred 8M HNO_3 solution (10 mL) onto UTEVA resin (0.1 g) is simulated. Rate orders were based on stoichiometric ratios of 1Th:2E and 1Th:4E. The lumped solid extractant concentration model constant was set to 1.5 mol/dm^{-3} for 1Th:4E and 0.375 mol/dm^{-3} for 1Th:1E. Linear regression has been applied to both datasets across the entire concentration range simulated. The inset plot shows a zoomed in view of the low end of the concentration range.

Other models describing sorption isotherms have been developed[44,56], including the Freundlich, Sips and the Redlich-Peterson isotherms; the latter two both include the Langmuir isotherm as a special case. None of these models, however, fully describe the data produced by the numerical simulation method.

4.3. Conclusions

A numerical simulation method has been developed using LabVIEW visual programming. This method has been applied to three contrasting sorptive materials under a range of experimental conditions. Internal diffusion must be included to describe sorption for the porous ion exchangers investigated; the accuracy of the simulation can be improved by increasing the number of fractions the solid material is divided up into. The impact of external diffusion was explored by simulating stationary batch experiments and found to impact upon the settled particle bed. The relationship that solid and aqueous volumes and experimental geometry has on external diffusion related simulation parameters is an area for future research. The effect of analyte and competing species concentrations was also successfully simulated for UTEVA resin. Extending the simulation to include exchange site concentration parameters for anion exchange resin and zirconium phosphate could be more complex due to the lower selectivity of these materials meaning more competition between species. In addition, there is a competing dissolution process occurring for zirconium phosphate. The numerical simulation approach developed fitted a Langmuir isotherm if a 1:1 stoichiometry and elementary reaction kinetics between the analyte and extractant was assumed. It was also proposed that under all stoichiometric ratios and at low initial aqueous concentrations, sorption of an analyte could be described by pseudo-first-order kinetics providing rate was not diffusion controlled. At high initial aqueous concentrations and if diffusion was included, the simulated sorption process did not fit either pseudo-first-order or pseudo-second-order equations. This is in contradiction to predicted behaviour based on theoretical derivations of the PFO and PSO equations by Azizian et al[171].

Development of the numerical simulation method in LabVIEW benefitted from the graphical nature of the programming environment. Modification of the basic simulation by extending arrays, adding connections and duplicating and editing VIs was relatively simple. The ODE solver, however, required the differential equations to be in certain formats to avoid mass balance errors. For example; $k_{int}[s]_{outer} - k_{int}[s]_{inner}$ was acceptable whereas $k_{int}([s]_{outer} - [s]_{inner})$ generated incorrect concentrations. Another limitation of this numerical simulation method was the length of time taken to generate data, this could be reduced by lowering the amount of data passed between each iteration of the while loop or selecting a shorter wait time although the latter could increase the CPU loading of the simulation and effect the execution of other software. As described, this method was developed using an ODE solver; it is possible that diffusion processes could be better simulated using a partial differential equation (PDE) solver whereby concentration change is solved both temporally and spatially. Currently, there are limited options for PDE

solvers within the LabVIEW development system; these are based on Helmholtz, heat, and wave equations in one or two dimensions and are expected to further add to simulation run times.

The numerical simulation method could be easily adapted from suspended particles in a contained solution to other geometries such as a thin film of particles on the container wall or inserted probe or a fixed-bed or column through which an aqueous solution can flow. It is hypothesised that the same processes will apply under these geometries although the aqueous mass transfer component may be more complex in flow through systems as flow rate will impact upon the magnitude of processes such as molecular diffusion and eddy dispersion.

Chapter 5: A Numerical Simulation Method for Modelling Chromatographic Column Breakthrough of Inorganic Species on Three Contrasting Materials

Abstract

A numerical method for simulating the transfer of inorganic species between an aqueous solution and a sorptive solid under batch conditions has previously been developed for three contrasting materials (UTEVA resin, anion exchange resin and zirconium phosphate) using LabVIEW visual programming software (Chapter 4). This chapter proposes an adaptation of this numerical simulation method to describe chromatographic breakthrough profiles. The differential equations and kinetic rate constants determined for the three sorptive materials in a closed batch system were directly applied to a simulated flow-through column by considering the resin bed as a series of discrete vertically stacked sections. Analyte transfer between the solid and aqueous phases was simulated within each section to produce an array of solid and aqueous concentration values; this was followed by advancement of the aqueous phase values by one array position. This process was repeated in an iterative manner with the aqueous concentration value in the final array position generating the simulation of column output. The simulated breakthrough profiles were compared to experimental data for a range of flow rates and bed lengths. Observed inconsistencies between the simulated and experimental datasets have been evaluated by taking into consideration solid and aqueous phase diffusion, eddy dispersion, errors in the simulation input parameters and additional physical phenomena associated with the experimental column set-up.

5.1. Introduction

Column-based liquid chromatography is a widely used technique for analysis of complex samples via separation of the individual components or for purification of products for commercial purposes. In the field of radioanalytical chemistry, chromatographic separations are used to isolate analytes from the bulk matrix and interfering species to facilitate quantification by radiometric or mass spectrometric detection techniques. Modelling and simulation of chromatographic processes can therefore be a very useful tool in optimising column operating parameters to reduce analysis time, improve separation factors or maximise profit.

Mathematical equations have hence been developed to describe the movement of dissolved species in a packed bed. These equations often describe the concentration change with respect

to time and can be solved to predict the concentration either on the column or in the column output solution at any given time. Depending on the complexity of the equations chosen and any assumptions made, the solution can be obtained using either algebraic or numerical methods[39,42]. The most complete approach to chromatographic simulation is known as the general rate model. This approach employs a series of partial differential equations describing concentration change in terms of both time and location whilst distinguishing between the aqueous and solid phases (pore concentration and sorbed concentration), axial position on the column and radial position within the solid particles. Concentration change can occur via any of the four main chromatographic processes[40,43]: (1) fluid flow and aqueous phase dispersion; (2) diffusion across the stagnant layer surrounding the solid particles (film diffusion); (3) diffusion within the sorptive material (intraparticle diffusion); and (4) the chemical reaction (e.g. ion exchange or complexation). Due to its complexity, the general rate model can only be solved using a computational partial differential equation solver.

Simplifications can, however, be applied to reduce the description of chromatographic processes to a series of ordinary differential equations. It has already been shown (Chapter 4) that numerical simulation methods employing an ordinary differential equation solver can be used to describe the kinetic transfer of species between solid and aqueous phases for porous and non-porous materials. This method uses a lumped solid simplification and was successfully applied to a closed system under either well mixed or stationary conditions; however, it is hypothesised that the same equations can also be applied to flow-through column geometry. In this chapter, this hypothesis is tested using the materials, analytes and matrices that were previously modelled under batch sorption/desorption conditions. Initially, a discrete volume containing the analyte(s) was added to the top of the sorptive bed and washed through using the same matrix as the loading solution. The position, width and symmetry of the resulting breakthrough peak(s) was shown to be dependent upon the bed length and flow rate through the column. The numerical simulation method was applied using the rate constants and differential equations developed under batch conditions along with adaptations to include the column dimensions, packing density and flow of the aqueous phase.

Column breakthrough is a more complex system to simulate than batch sorption/desorption due to the increased input parameters and uncertainties in their definition. Inaccurate input or over simplification of one of these parameters may have a significant impact on the breakthrough simulation. Combined parameter errors may also have either an additive or opposing effect depending on the operating conditions; it is therefore difficult to isolate input errors. In addition, the rate of movement of a species down a column is not only determined by interaction with the

solid phase but by molecular diffusion within the aqueous phase and the velocity range of the solution due to different paths through the packed bed. The combination of the latter two factors is known as axial dispersion and is dependent on the molecular diffusivity of the species, the column packing density, the linear flow velocity and the particle size[35,42,47].

An assessment of the magnitude of aqueous phase diffusion as well as physical diffusion in the pores of the lumped solid phase was made by investigating the breakthrough of a discrete volume of tritiated water from each of the sorptive materials. The relationship between the two axial dispersion processes was also examined for the non-porous material at the slowest flow rate.

The numerical simulation method for describing sorption/desorption under batch conditions had indicated that internal diffusion in the two porous materials could be simulated by assuming that surface diffusion was the dominant mechanism and that the rate of this was proportional to the solid-aqueous ratio. These assumptions are re-evaluated in this chapter. An analysis of the sensitivity of the numerical simulation method to errors in input parameters was also conducted to discuss the difference in breakthrough profiles obtained under repeated conditions. Additional physical processes such as backpressure and leaching of the extractant are also considered.

5.2. Results and discussion

5.2.1. Modification of numerical simulation method to describe column conditions

A numerical simulation method has previously been developed to successfully describe batch sorption/desorption for three contrasting sorptive materials (see Chapter 4). A "Lego® approach" was taken whereby a basic model was modified in order to describe more complex processes[42]. The basic model is built upon the lumped kinetic model whereby concentration is averaged over the solid phase with no internal concentration gradients. Aqueous concentration gradients are also neglected and an averaged value is again assumed.

For the kinetic transfer of low concentrations of uranium and thorium between 8M HNO_3 and UTEVA resin under constant tumbling conditions, the basic model was found to be sufficient. This method involved the simultaneous solution of just two differential equations (Equations 4.8. and 4.9. – reproduced below for clarity) requiring 4 model constants; the forward rate constant ($\vec{k}$), the reverse rate constant ($\overleftarrow{k}$), the volume fraction of the lumped solid phase (V_s) and the volume fraction of the aqueous phase (V_{aq}) as well as two input variables; the initial analyte concentration in the aqueous phase $[aq]$ and the initial analyte concentration in the lumped solid phase $[s]$. The two rate constants were determined from the experimental data and the other inputs from knowledge of the experimental set-up.

$$\frac{d[s]}{dt} = \vec{k}[aq] - \overleftarrow{k}[s] \qquad \text{Equation 4.8.}$$

$$\frac{d[aq]}{dt} = \left(\overleftarrow{k}[s] - \vec{k}[aq]\right) \times \left(\frac{V_s}{V_{aq}}\right) \qquad \text{Equation 4.9.}$$

Due to the porous nature of the material, it was necessary to modify the model for describing transfer of uranium and thorium between 8M HNO_3 and anion exchange resin (under constant tumbling conditions) was modified to include internal mass transfer. This was achieved by division of the lumped solid into two fractions and the introduction of an internal rate constant (k_{int}). In this modification, three differential equations are used (Equations 4.13.-4.15. - reproduced below for clarity), requiring 6 model constants and three input variables.

$$\frac{d[s]_{inner}}{dt} = k_{int}[s]_{outer} - k_{int}[s]_{inner} \qquad \text{Equation 4.13.}$$

$$\frac{d[s]_{outer}}{dt} = \vec{k}[aq] - \overleftarrow{k}[s]_{outer} - \left[\left(k_{int}[s]_{outer} - k_{int}[s]_{inner}\right) \times \left(\frac{V_{s,inner}}{V_{s,outer}}\right)\right] \qquad \text{Equation 4.14.}$$

$$\frac{d[aq]}{dt} = \left(\overleftarrow{k}[s]_{outer} - \vec{k}[aq]\right) \times \left(\frac{V_{s,outer}}{V_{aq}}\right) \qquad \text{Equation 4.15.}$$

In the case of kinetic transfer of barium between seawater and zirconium phosphate (under constant tumbling conditions), two solid fractions was found to be insufficient in simulating internal diffusion processes. For this material, three solid fractions were employed although it was suggested that this simplification would lack accuracy when simulating batch experiments with higher solid/aqueous ratios. The fractionation of the two porous materials was based on an assumption of an initial penetration of 5 µm. Rate constants were determined from the experimental data and calculated for different particle sizes, fractionation choices and solid/aqueous ratios based on a constant rate of diffusion throughout the material and the observation that flux was proportional to the solid/aqueous ratio.

The magnitude of external diffusion was also investigated by conducting batch experiments under stationary conditions. Two processes can occur; the diffusion of species through the bulk aqueous solution to a settled resin bed and diffusion across a stagnant layer surrounding each solid particle (film diffusion). The magnitude of film diffusion depends on the tumbling speed with the length of the stagnant layer shorter in faster mixing conditions. The length of the

stagnant layer under stationary conditions, however, has not reached consensus[42,47] with some authors arguing a maximum is reached[175] and others suggesting an infinite length, blurring the line between the two diffusive processes. It was found that bulk aqueous diffusion / thick film diffusion had a significant kinetic impact under these conditions, particularly for UTEVA resin as this material exhibited the fastest sorption/desorption kinetics under constant tumbling conditions. The kinetics of film diffusion under constant tumbling conditions was not empirically quantified; instead this process was incorporated in the forward and reverse rate constants describing transfer between the aqueous phase and the lumped (outer) solid phase.

In this chapter, the numerical simulation method detailed above has been modified to describe chromatographic column breakthrough. A packed bed of sorptive material interacts with the species in solution in much the same way as in a closed batch experiment, however, in this open system, the aqueous phase is mobile meaning that the concentration in contact with the stationary solid phase can change. As a consequence, the probability of a molecule in the solid phase to either remain or transfer back into the aqueous phase can also change. This dynamic system can be approximated by representing the column as a set of axially distributed closed systems (Figure 5.1.). Within each closed system, species may transfer between the two phases as well as between the radial fractions of the solid in the case of porous materials in an attempt to reach equilibrium. The concentration in each phase/solid radius of a closed system is given as an average value and changes over time as a product of the competing rate equations. As the solution flows through the column, the aqueous phase moves into the next axial division and a new closed system is initiated.

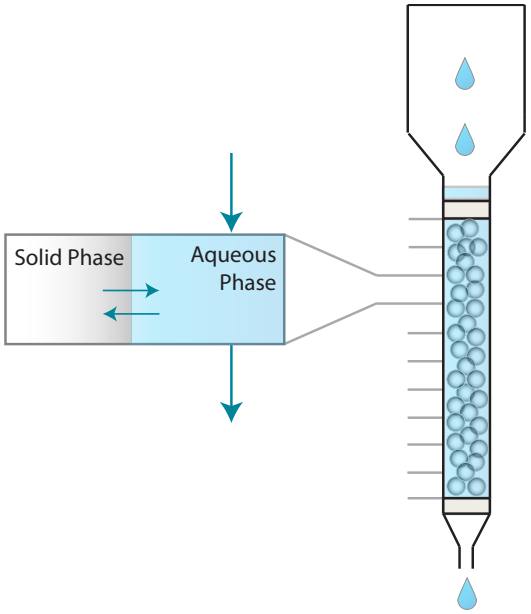

Figure 5.1.
Graphical depiction of numerical simulation method for chromatographic breakthrough.
Note: Not to scale.

This simplified model of sorption/desorption within a column can be numerically simulated in LabVIEW by modification of the batch simulation method. Rather than single value *ODE solver* input variables, a 2D array is used representing the concentrations in each volume fraction for each axial division. The final time *simulation parameter* for the *ODE solver* is equal to the duration of solution residence time within each axial division; this is programmatically calculated by dividing the volume (mL) of the aqueous phase in each division by the flow rate (mL/min) and converting this to seconds. After each iteration, an array of final values is extracted from the temporal concentration output of the *ODE solver*. From this array the aqueous concentration values are passed along one array position and a new value is input into the top array position representative of the concentration in the solution being delivered to the top of the column. The aqueous concentration value in the bottom array position is extracted and becomes the column output. The new 2D array is passed through the *while loop shift register* to become the new input variables for the next iteration.

This numerical simulation method for chromatographic column breakthrough was operated using the relevant equations and rate constants for each material as determined under the batch conditions. The simulated datasets were compared to experimental datasets under a range of flow rates and bed lengths.

5.2.2. Comparison of numerical simulation method with experimental data

In order to simulate a chromatographic column breakthrough, the experimental conditions must be known or estimated. The final time *simulation parameter* that controls how many seconds the *ODE solver* simulates on each iteration is equivalent to the duration of solution residence time in each axial division (Equation 5.1.).

$$duration\ (s) = \frac{V_{aq} \times \pi \times r^2 \times 60 \times L_{col}}{u \times n} \qquad \text{Equation 5.1.}$$

This is calculated programmatically by dividing the volume of the aqueous phase in each axial division by the flow rate (u - converted to mL/s). This volume is calculated from the effective cross-sectional area and length of each division; knowledge of the internal radius of the column (r) and volume fraction of the aqueous phase (V_{aq}) are needed as well as a suitable number of divisions (n) for the bed length (L_{col}). For all the experiments conducted in this study, the same design of chromatographic column was used and r was set to 0.35 cm. The volume fraction of the aqueous phase depends on the packing density of the sorptive material; this was calculated by volumetric displacement measurements. For anion exchange resin and zirconium phosphate close random packing was observed whereas UTEVA resin exhibited a looser structure, possibly due to repulsive hydrophobic forces. From these measurements, V_{aq} was set to 0.375 for anion exchange resin and zirconium phosphate simulations and to 0.655 for UTEVA resin simulations. Additional inputs are flow rate (mL/min), loading concentration, loading volume (mL) and bed length (cm). These all vary according to the experiment conducted. As the differential equations used in this chapter do not include a lumped solid extractant constant, the concentration magnitude and units do not have an impact on the simulated profile.

To simulate breakthrough experiments, the initial concentration in all phases was set to zero and the loading concentration was introduced into the top aqueous phase array position for the amount of iterations equivalent to the loading volume divided by the volume of the aqueous phase in each axial division (a correction to the loading concentration in the last iteration was made if this value was not an integer to ensure an overall mass balance), following which the loading concentration was programmatically set to zero.

An assessment was carried out to determine the lowest number of axial divisions needed to achieve an accurate simulation without unnecessarily increasing the computational load and simulation execution time (Figure 5.2.). From this test an axial division length of 0.1 cm was

chosen; the number of divisions (n) therefore alters according to bed length. As n must be an integer, when column lengths are given to the nearest 0.05 cm, the number of divisions is rounded up and the length of the axial divisions is slightly less than 0.1 cm.

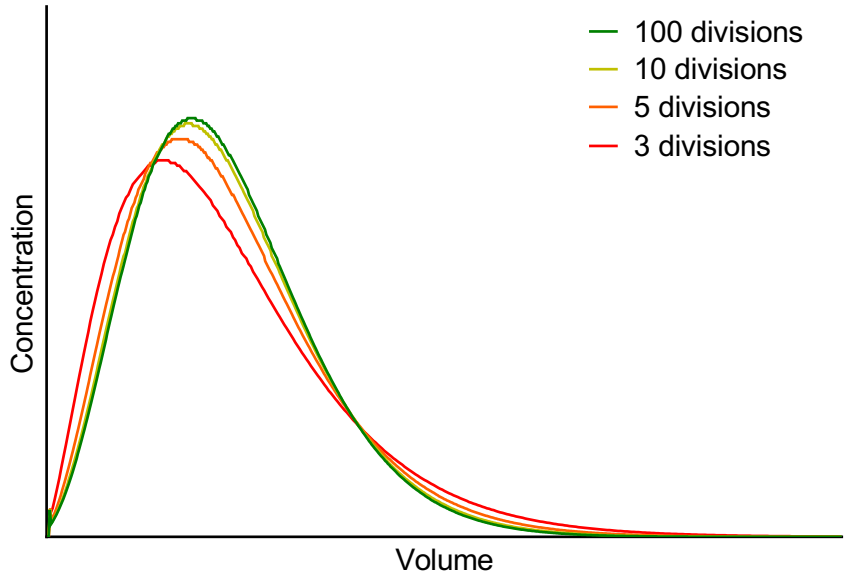

Figure 5.2.
Comparison between numerical simulations of breakthrough profiles using different numbers of axial divisions.
The following hypothetical parameters were kept constant: bed length = 1 cm; column radius = 0.35; flow rate = 1 mL/min; loading volume = 0.025 mL; V_{aq} = 0.655; V_s = 0.345; $\vec{k}$ = 1; $\overleftarrow{k}$ = 0.01. Aqueous phase diffusion has not been included in the simulations.

5.2.2.1. Simulation using parameters determined under batch conditions

As previously mentioned, the numerical simulation method for describing batch sorption/desorption was successfully applied to three sorptive materials providing accurate rate constants and solid volume fractions were input. The values determined under the batch conditions were tested for suitability as inputs for the adapted numerical simulation method for chromatographic breakthrough. The internal rate constants and solid volume fractions for the two porous materials were corrected for the larger solid fraction in the packed bed (compared to the batch conditions); anion exchange resin was modelled using two solid fractions and one internal rate constant whereas zirconium phosphate was modelled using three solid fractions and two internal rate constants.

Simulations were initially run to describe a series of discrete loading breakthrough experiments for the three sorptive materials using a range of bed lengths and flow rates (Table 5.1.). These experiments involved the loading of a small volume followed by a wash step using the same matrix as the loading solution (8M HNO_3 for UTEVA resin and anion exchange resin experiments

and seawater for zirconium phosphate experiments). As the loading and wash solutions were identical, no changes to the rate constants were made between the two steps.

The simulated profiles were compared to the experimental results by plotting the simulated value (y axis) against the experimental value (x axis) for the closest possible breakthrough fraction (mL). A linear trendline was applied to the resulting plot and forced through the origin. Regression analysis of the trendline generated a slope value and an R^2 value. The slope value gives information on the agreement between the peaks of the two datasets; an exact match between the two datasets would give a slope value of 1 whereas an overestimation in the time taken for the breakthrough profile to peak would give a slope value <1. The R^2 value gives information on agreement between the shapes (width and symmetry) of the simulated and experimental datasets. It should be noted, however, that the experimental concentration values are given for the mid-point of a collected volume so are averaged over a larger volume than the concentration values (averaged over 0.1 mL) in the simulated data. Additionally, some experimental datasets do not cover the whole breakthrough profile although a peak in concentration is always reached.

Table 5.1.
Linear regression analysis for comparison of experimental data to simulated breakthrough profiles without the inclusion of aqueous phase diffusion.
Experimental data (x-axis) is plotted against simulated data (y-axis) to generate R^2 and slope values.
The numerical simulation method uses rate constant and solid volume fractions calculated from batch sorption/desorption experimental data.
In addition to the variable input parameters listed for each experiment, a column radius of 0.35 cm is assumed with V_{aq} = 0.655 for UTEVA resin and V_{aq} = 0.375 for anion exchange resin and zirconium phosphate. The axial division length is set to 0.1 cm except for experiment 8 where it is 0.95/10 cm.

Expt.	Sorptive material	Bed length (cm)	Flow rate (mL/min)	Loading volume (mL)	Analyte	Slope	R^2
1	UTEVA resin	1	2.12	0.025	Uranium	0.7813	0.9725
					Thorium	0.7784	0.9685
2	UTEVA resin	1.1	3.60	0.025	Uranium	0.8915	0.8754
					Thorium	0.8964	0.3169
3	UTEVA resin	2	1.89	0.025	Uranium	0.8374	0.7746
					Thorium	0.8160	0.9640
4	UTEVA resin	2	1.89	0.025	Uranium	0.9791	0.9985
					Thorium	1.1003	0.9782
5	UTEVA resin	1	5.48	0.025	Uranium	0.9274	0.6450
					Thorium	0.8915	0.1869
6	UTEVA resin	3.9	28.8	0.025	Uranium	0.7498	0.7745
					Thorium	0.7535	0.7181
7	UTEVA resin	2	0.230	0.025	Uranium	0.8235	0.9155
					Thorium	0.9691	0.9537
8	Anion exchange resin	0.95	1.70	0.025	Uranium	0.2282	0.9016
					Thorium	0.2080	-0.6483
9	Anion exchange resin	2	1.07	0.025	Uranium	0.5548	-0.0110
					Thorium	0.1583	-2.0435
10	Anion exchange resin	1.9	0.475	0.025	Uranium	0.8160	0.4924
					Thorium	0.0546	0.5348
11	Anion exchange resin	3.8	1.14	0.025	Uranium	0.8038	0.5264
					Thorium	0.0835	0.7173
12	Anion exchange resin	3.8	3.46	0.025	Uranium	0.5326	0.5430
					Thorium	0.3961	-4.9171
13	Anion exchange resin	3.7	10.2	0.025	Uranium	0.1426	0.8790
					Thorium	0.1834	-1.2835
14	Anion exchange resin	3.8	0.236	0.025	Uranium	1.0715	0.9040
					Thorium	1.4777	0.3451
15	Anion exchange resin	3.7	3.52	0.988	Uranium	2.4847	0.4161
					Thorium	0.2525	-0.1738
16	Zirconium phosphate	2	1.82	1.0015	Barium	2.1677	0.5707
17	Zirconium phosphate	4	1.82	1.0138	Barium	1.0424	0.4666
18	Zirconium phosphate	4	0.931	0.5	Barium	0.1372	0.8567
19	Zirconium phosphate	5	0.142	0.5	Barium	2×10^{-5}	-0.3328
20	Zirconium phosphate*	3	0.125	0.5	Barium	3×10^{-7}	-0.0896

*This experiment was based on a particle size of 125-250 µm. All other zirconium phosphate experiments used a particle size of 125-1000 µm.

In general, both the slope and R^2 values show a better fit for UTEVA resin than for anion exchange resin and zirconium phosphate. The best fit was observed for UTEVA resin experiment 4 as characterised by slope and R^2 values close to 1 and verified through visual comparison of the two datasets for both uranium and thorium (Figure 5.3.). The ability of the numerical simulation method to describe the breakthrough profile on UTEVA resin shows similar trends for uranium and thorium. This could be due to the similar chemical behaviour with this material; equilibrium had been reached in less than 10 minutes for both analytes under batch conditions (Chapter 4) using a relatively low solid/aqueous ratio (0.1 g / 10 mL). The strong retention and fast kinetics generated approximately Gaussian shaped experimental and simulated profiles at slow flow rates (<2 mL/min) although the tailing slope was slightly longer than the leading one. Faster flow rates and shorter columns produced a higher degree of tailing in the experimental datasets with less wash solution required to reach peak breakthrough concentration. Although these results were reflected in the simulated data, an initial spike was also generated which was not seen in the experimental data even if corrections were made for the difference in resolution. The size of this spike increased with flow rate. In addition, the simulations of breakthrough profiles at the fastest flow rates (>5 mL/min) significantly misrepresented the shape of the leading slope.

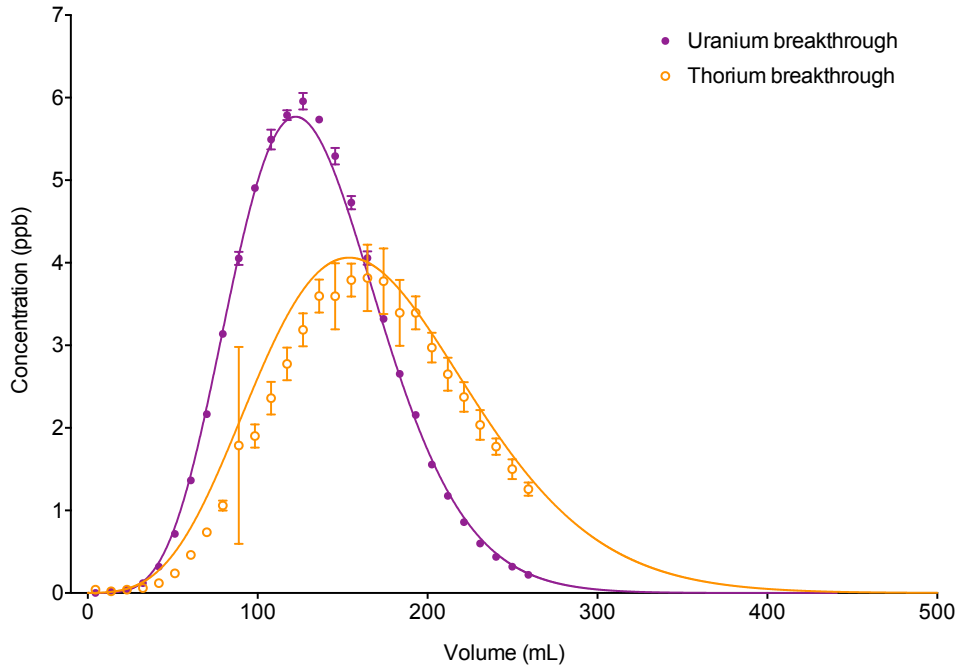

Figure 5.3.
Comparison between experimental data and numerical simulation of uranium and thorium breakthrough profiles from UTEVA resin in 8M HNO_3 under conditions corresponding to experiment 4 (Table 5.1.).
The two analytes have been simulated separately. Axial division length = 0.1 cm. Aqueous phase diffusion has not been included in the simulations.

Thorium also showed a strong interaction with anion exchange resin in 8M HNO_3 under batch conditions. The rate of transfer was slower than for UTEVA resin, however, and showed some dependence on the rate of diffusion within the solid particles. This behaviour appeared to generate highly asymmetrical profiles with significant tailing although the tailing region of the chromatogram was only covered in a few experimental datasets (8, 13 and 15 and to a lesser extent in experiment 12). The numerical simulation method failed to describe either the position of the peak or shape of the breakthrough profile for this analyte. At the slowest flow rate (0.236 mL/min), a more gradual leading slope was observed and a better estimation of the position of peak breakthrough was made. The interaction of uranium with anion exchange resin in 8M HNO_3 is much less favourable. This is reflected in the experimental and simulated datasets by a sharp initial breakthrough, the exact position of this peak and shape of the tailing slope are, however, not correctly described by the numerical simulation method particularly at faster flow rates. The magnitude of this interaction has been estimated under batch conditions but has a larger associated uncertainty due to the small difference between initial and final aqueous concentrations. A more accurate estimation of the distribution constant (sorption value at equilibrium) could be made by using a larger solid/aqueous ratio in the batch sorption experiments. This would improve the numerical simulation of the position of the uranium breakthrough peak.

Barium sorption/desorption between zirconium phosphate and seawater was shown to have the slowest kinetics under batch conditions with considerable dependence upon internal diffusion rate. The experimental data for chromatographic breakthrough showed the highest degree of asymmetry. At the faster flow rates tested (>0.9 mL/min) the majority of the barium passed through the column in the first 10 mL of washing. There was, however, still a measureable activity of Ba-133 in fractions collected after 100 mL of washing indicating a slow release from the solid pores. For example, mass balance calculations for experiment 18 suggested that approximately 65% of the activity added remained on the column after 339 mL of (loading plus wash) solution had been collected. Broader peaks were seen for slower flowing experiments (<0.2 mL/min) and a more gradual leading slope was seen for a chromatographic column loaded with a ground up sample of zirconium phosphate (125-250 µm). This could be due to the higher surface area and lower average particle diameter increasing the kinetics of sorption. The numerical simulation method described above predicted the early breakthrough profiles and low levels of breakthrough after longer washing at the faster flow rates but failed to accurately describe the tailing slope. At slower flow rates, simulated profiles were much more symmetrical and had later peaks than those observed experimentally.

The lack of agreement between experimental and simulated datasets could be due to incorrect description of sorption/desorption/diffusion kinetics, errors in input parameters describing the experimental conditions or the presence of hydrodynamic/physical processes that have not yet been included in the numerical simulation method.

5.2.2.2. Investigation into hydrodynamic processes

The numerical simulation method described thus far models the chromatographic column as a series of closed systems, however, this simplification does not accurately quantify the impact of hydrodynamic processes. In addition to sorption onto the solid phase and incorporation in the downwards flow of the aqueous phase, species can transfer between the aqueous phases in two adjacent divisions by molecular diffusion. This can lead to a broadening of the breakthrough profile. Another contribution to broadening is eddy dispersion; this term refers to the non-linear flow of dissolved species travelling down the column. In a packed bed, the presence of the solid particles force the fluid stream to separate and recombine as it travels downwards[35,42,47]. The multiple different paths available are not equal in length meaning that although an average residence time within each axial division can be assumed from the flow rate, column dimensions and packing density, the actual residence time for any given molecule will sit in a range determined by the fastest and slowest routes through the bed. The contributions from molecular diffusion (D_{diff}) and eddy dispersion (D_{eddy}) are usually combined additively (Equation 5.2.) into a single axial dispersion term (D_{ax}).

$$D_{ax} = \gamma_{diff} D_{diff} + \gamma_{eddy} D_{eddy} \qquad \text{Equation 5.2.}$$

The molecular diffusion contribution is a product of the molecular diffusion coefficient (m^2/s) and a correction factor (γ_{diff}). Several different empirical estimations of γ_{diff} have been suggested with values typically close to 0.7[42,47]. As this factor is thought to be related to tortuosity, other equations have been proposed for calculating γ_{diff} based on column porosity[47]. The rate of diffusion is dependent on molecular radius and viscosity; hence the molecular diffusion coefficient is specific to each dissolved species and the solution through which it is diffusing. A more thorough description of molecular diffusion can also include the contribution of diffusion within the stationary phase although this is usually of a much smaller magnitude to aqueous phase diffusion[26,35].

The eddy dispersion term also has an associated correction factor (γ_{eddy}) which can be estimated by a range of different equations[47]. Some of the commonly used equations include column parameters such as porosity and the dimensionless Reynolds and Schmidt numbers. Eddy dispersion can be calculated (Equation 5.3.) from the aqueous phase velocity (u_e in m/s – often referred to as the interstitial fluid velocity) multiplied by the average diameter of the solid particles (d_p in m).

$$D_{eddy} = u_e d_p \qquad \text{Equation 5.3.}$$

As axial dispersion is acting concurrently to the downwards flow through the column, it can be useful to define the column Péclet number (Equation 5.4.). The larger this number is, the less contribution axial dispersion has to the shape of the breakthrough profile. The Péclet number can be included in the Van Deemter equation (Equations 5.5. and 5.6.). This equation is used to quantify the efficiency of chromatographic columns by defining a measure known as the height equivalent of a theoretical plate (HETP). For columns of the same bed length, a lower HETP value would mean better separation of analyte breakthrough peaks.

$$Pe = \frac{u_e L_{col}}{D_{ax}} \qquad \text{Equation 5.4.}$$

$$HETP = \frac{2L_{col}}{Pe} + Cu_e \qquad \text{Equation 5.5.}$$

$$HETP = 2\gamma_{eddy} d_p + \frac{2\gamma_{diff} D_{diff}}{u_e} + Cu_e = A + \frac{B}{u_e} + Cu_e \qquad \text{Equation 5.6.}$$

The three terms that make up the HETP value are: eddy dispersion (A) which is independent of aqueous phase velocity; molecular diffusion (B/u_e) which is inversely proportional to aqueous phase velocity and the kinetics of interaction with the solid phase (Cu_e) which is proportional to aqueous phase velocity. This last term encompasses external film diffusion, internal diffusion within the solid phase and sorption/desorption. The three plate terms can be combined to calculate the flow rate at which the column exhibits the lowest HETP / highest efficiency (Figure 5.4.).

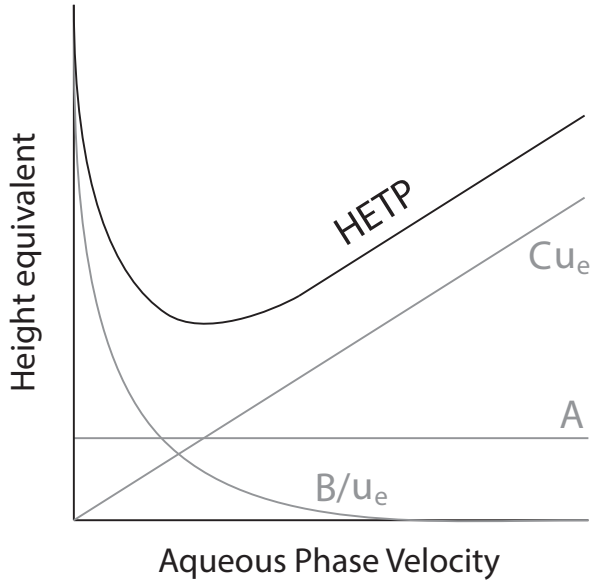

Figure 5.4. (Reproduction of Figure 1.1.)
Diagram depicting the contributions to HETP at different aqueous phase velocities.
This includes eddy dispersion (A), molecular diffusion (B) and aqueous-solid transfer kinetics (C).

The numerical simulation method developed thus far simulates solid phase interaction (Cu_e). This is reflected in the simulated datasets by a broadening and increase in asymmetry with flow rate due to the shorter time allowed for transfer between the aqueous and solid phases in each iteration. The molecular diffusion term (B/u_e) can also be included in the LabVIEW coding by modifying the differential equation for the change in concentration in the aqueous phase with respect to time (Equation 5.7.). With this modification, species in the aqueous phase in axial division z can either pass into the solid phase in axial division z or into the aqueous phase in neighbouring divisions (z-1 and z+1). The proportion following each transfer route depends on the difference in concentration between the phases/divisions and the rate constant associated with transfer. The magnitude of the aqueous diffusion rate constant (k_{diff}) is dependent on the diffusion coefficient for the analyte (A) in the solution matrix (D_A) and the length (L_{ax}) of the axial divisions selected (Equation 5.8.).

$$\frac{d[aq]_z}{dt} = \left[\left(\overleftarrow{k}[s] - \vec{k}[aq]\right)\times\left(\frac{V_s}{V_{aq}}\right)\right] + k_{diff}[([aq]_{z+1} - [aq]_z) + ([aq]_{z-1} - [aq]_z)] \quad \text{Equation 5.7.}$$

$$k_{diff} = \frac{D_A}{L_{ax}}\times\frac{V_{aq}\times\pi\times r^2}{V_{aq}\times\pi\times r^2\times L_{ax}} = \frac{D_A}{{L_{ax}}^2} \quad \text{Equation 5.8.}$$

The axial division length was previously set to 0.1 cm as a compromise between accuracy and computation time. This length, however, is a direct representation of the eddy dispersion term (B) as it represents the range associated with the average aqueous phase velocity. A short axial division length would indicate little difference between the slowest and fastest routes through the packed bed whereas a larger length represents a greater range of paths. This length acts as a constant baseline upon which the other two terms are added; their relative importance varying with flow rate. A better understanding of the aqueous phase diffusion and aqueous-solid interaction terms would allow for a more informed choice of axial division length.

An attempt to probe the complex interaction of diffusive and dispersive forces was made by examining the experimental breakthrough profiles of a discrete volume of tritiated water from each of the three sorptive materials (Figure 5.5.). Tritium (as HTO) is assumed to not undergo chemical uptake by any of the sorptive materials; this was verified by batch equilibrium measurements which showed no sorption with the drop in aqueous concentration being less than measurement uncertainty (values before and after sorption within 5.0 ± 0.1 Bq/g). The removal of sorption/desorption kinetics leaves aqueous phase diffusion, film diffusion, solid phase pore diffusion and eddy dispersion as the main breakthrough profile contributors.

For each sorptive material, three hypothetical scenarios were simulated. Firstly, no diffusion and minimal eddy dispersion was simulated (solid line). This assumes that the solid phase is impenetrable to tritium, that the range of flow rates is very small and that there is no molecular diffusion up/down the column. This was simulated by setting all rate constants ($\vec{k}$, $\overleftarrow{k}$, k_{int} and k_{diff}) to zero and the length of the axial divisions to 0.01 cm. This generated a sharp breakthrough profile with the same width as the input volume (0.025 mL). The position of the simulated peak was slightly later for UTEVA resin due to the greater aqueous phase volume fraction (V_{aq}) in each axial division.

The second simulated scenario (dashed line) again assumes no interaction with the solid phase ($\vec{k}$, $\overleftarrow{k}$, $k_{int} = 0$) and minimal eddy dispersion but introduces aqueous phase diffusion. Keeping the length of the axial divisions to 0.01 cm, k_{diff} was set to 230 s^{-1}. This corresponds (via Equation 5.8.) to a diffusion coefficient (D_A) of 2.3 x 10^{-6} m^2/s which is 3 orders of magnitude faster than values found in the literature for the self-diffusion coefficient of water at 25°C[182]. Setting k_{diff} to the more realistic value of 0.23 s^{-1} produced little deviation from the no diffusion scenario at the experimental flow rates. Neither of the values of k_{diff} chosen included any correction for tortuosity. The hypothetically large diffusion has been included to illustrate the broadening effect

of including diffusion in the numerical simulation; this broadening is both forwards and backwards from the breakthrough peak with greater effect on the tailing slope.

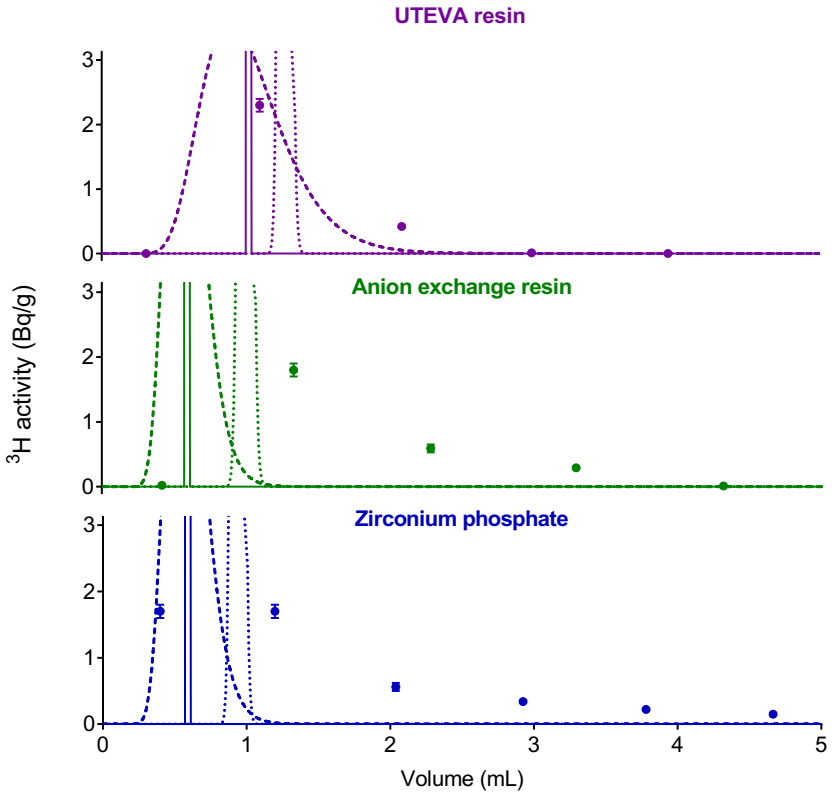

Figure 5.5.
Comparison between experimental data and numerical simulation of breakthrough profiles of tritium in MQ water.
Common parameters for all three materials: bed length = 4 cm; column radius = 0.35; loading volume = 0.025 mL
For UTEVA resin: flow rate = 1.86 mL/min; V_{aq} = 0.655
For anion exchange resin: flow rate = 1.86 mL/min; V_{aq} = 0.375
For zirconium phosphate: flow rate = 1.74 mL/min; V_{aq} = 0.375
Details of the three simulated scenarios (solid, dashed and dotted lines) are given in the main body of text.

The final scenario (dotted line) assumes a physical transfer between the aqueous and solid phases but no aqueous phase diffusion and minimal eddy dispersion. Fast film and internal diffusion kinetics have been simulated (axial division length = 0.01 cm, k_{diff} = 0) based on estimations of the pore volume fraction of each of the solid materials. As the process of diffusion is the movement of species towards a uniform concentration and the solid materials are only partially accessible to dissolved species, the lumped solid (solid framework plus pores) concentration at equilibrium would be lower than the aqueous concentration at equilibrium. The porosity of UTEVA resin was calculated as 48 % from literature data[70], porosity of 42 % for anion exchange resin was taken from product information[183] and a value of 36 % was estimated for zirconium phosphate based on

gravimetric water exclusion tests. The forwards, reverse and internal rate constants were set to fast enough values to ensure that equilibrium between the aqueous and solid phases was reached in each iteration. As the solid phase is fixed and the aqueous phase mobile a new equilibrium is established after each iteration. This produced characteristic Gaussian shaped profiles with the peak position related to the non-interacting scenario peak and the available pore volume.

None of these three hypothetical scenarios matched the experimental data. The experimental breakthrough datasets exhibited broad, asymmetrical profiles with the asymmetry more pronounced for the ion exchange materials and largest for zirconium phosphate. For UTEVA resin, the experimental data indicated that tritium can diffuse into the immobilised organic solvent and that this process is not instantaneous, i.e. there is a rate constant associated with this process. At the flow rate investigated, it appears that this process is the greatest contributor to the shape of the breakthrough profile. Similar experiments investigating breakthrough of a discrete volume of tritium at different flow rates could help quantify diffusion rates. Slower flow rates would help obtain a better estimation of aqueous phase diffusion, whereas faster flow rates may help identify whether the rate of transfer between the two phases is dominated by diffusion within the organic solvent or by film diffusion. The latter process is related to flow rate as fluid dynamics alter the thickness of the stagnant layer surrounding the solid particles. Better estimations of diffusion rates would then help quantify the eddy dispersion length.

The greater retention associated with the two ion exchange materials indicates that internal diffusion is a rate limiting factor at the flow rates investigated. Previous description of internal diffusion for interacting species was based on surface diffusion within the pores; movement within the solid phase was modelled as being due to hopping of species between exchange sites[43,47]. As tritium has been shown to diffuse into/out of the solid material without a chemical interaction, this suggests that surface diffusion is not the only process. Tritium diffusion is slower for zirconium phosphate, indicating pore diffusion with a kinetic dependence on pore diameter. More detailed experimental data regarding tritium breakthrough could help better quantify the rate of pore diffusion for these materials as well as the rate of film diffusion. It should be noted, however, that dissolution of zirconium phosphate was observed in low ionic strength solutions as evidenced by the presence of zirconium in the aqueous phase after contact with MQ water. This could complicate attempts to quantify pore diffusion using tritiated water. The amount of solid fractions used in the numerical simulation method to describe intraparticle diffusion may need to be increased and possibly a better description of the pore structure given. Separate rate constants for the two diffusion mechanisms may be needed and/or a bidispersed pore

description. The pore structure may also be non-homogeneous; for example, a dendritic structure would give narrower pores and lower porosity towards the centre of the particle.

For the numerical simulation of batch sorption/desorption of chemically interacting species on UTEVA resin; film diffusion, organic phase diffusion and complexation kinetics were expressed by a single pair of forward and reverse rate constants. This simpler system transferred much more straightforwardly to the numerical simulation of chromatographic column breakthrough and could also be used to investigate diffusion and eddy dispersion effects. Simulation of the UTEVA resin chromatographic experiment conducted at the slowest flow rate (Experiment 7 - Table 5.1.), gave a significantly worse fit to the experimental data if an axial division length of 0.01 cm was chosen instead of the previous 0.1 cm (Figures 5.6. and 5.7. and Table 5.2.). This observation suggests that sorption/desorption kinetics is not the only contributor to breakthrough profile shape at this slow flow rate.

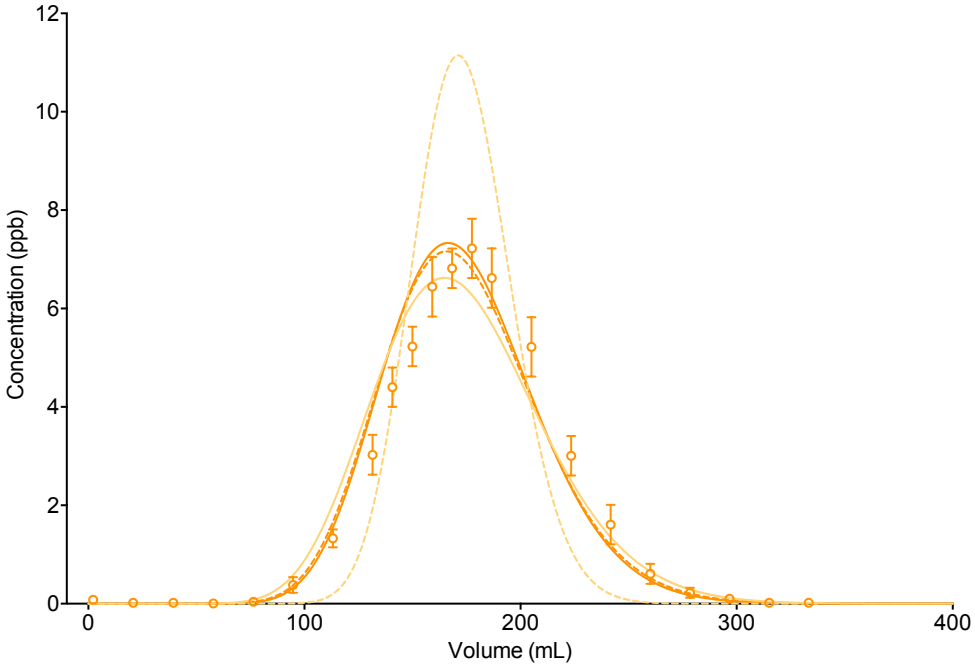

Figure 5.6.
Comparison between experimental data and numerical simulation of thorium breakthrough profiles from UTEVA resin in 8M HNO_3 under conditions corresponding to experiment 7 (Table 5.1.).
The two analytes (uranium and thorium) have been simulated separately.
See Table 5.2. for information on the simulation conditions.

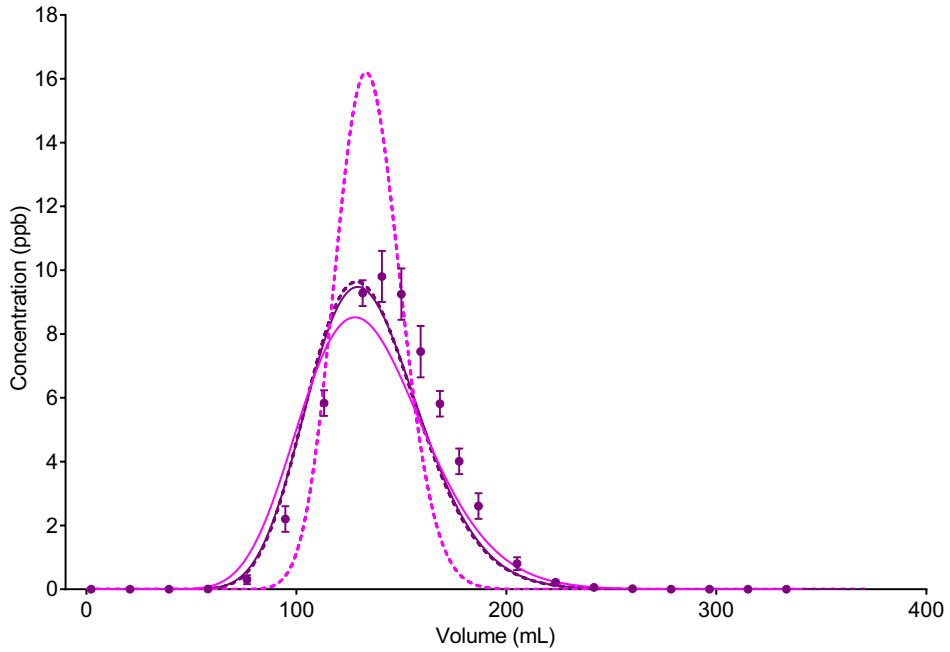

Figure 5.7.
Comparison between experimental data and numerical simulation of uranium breakthrough profiles from UTEVA resin in 8M HNO_3 under conditions corresponding to experiment 7 (Table 5.1.).
The two analytes (uranium and thorium) have been simulated separately.
See Table 5.2. for information on the simulation conditions.

Table 5.2.
Linear regression analysis for comparison of experimental data to simulated breakthrough profiles using various axial division lengths and k_{diff} values.
Experimental data (x-axis) is plotted against simulated data (y-axis) to generate R^2 and slope values.
The numerical simulation method uses rate constant and solid volume fractions calculated from batch sorption/desorption experimental data.
The experimental data and numerical simulation method input parameters correspond to experiment 7 (Table 5.1.).

Axial division length (cm)	k_{diff} (s^{-1})	Analyte	Figure	Plot	Slope	R^2
0.1	0	Uranium	5.7.		0.8235	0.9155
		Thorium	5.6.		0.9691	0.9537
0.01	0	Uranium	5.7.		1.0992	0.7692
		Thorium	5.6.		1.2762	0.8897
0.08	0	Uranium	5.7.		0.8756	0.9259
		Thorium	5.6.		1.0341	0.9673
0.01	4	Uranium	5.7.		0.8768	0.9177
		Thorium	5.6.		1.0184	0.9640

A better fit to the experimental data was obtained when either setting the axial division length to 0.08 cm (k_{diff} = 0) or by setting the axial division length to 0.01 cm and introducing aqueous phase division (k_{diff} = 4). This aqueous diffusion rate constant corresponds to a diffusion coefficient of 4 x 10^{-4} cm^2/s which is two orders of magnitude faster than the quoted values of 0.620 x 10^{-5} cm^2/s for $^1/_3Ce^{3+}$ (proxy for Th^{4+}) and 0.426 x 10^{-5} cm^2/s for $½UO_2^{2+}$ in water at 25°C[55]. In addition, the composition of the 8M HNO_3 matrix and the geometry of the packed bed could lower the expected diffusion rate due to the higher viscosity and tortuosity. The fit obtained by a 0.01 cm axial division length and k_{diff} of 4 is therefore not a realistic estimation of these two parameters. Multiple axial division length (between 0.01 and 0.1 cm) and aqueous diffusion rate constant (between 0 and 4) combinations are possible to generate almost identical simulated datasets. Further chromatographic breakthrough experiments using UTEVA resin and the same column dimensions at a range of slow (<0.5 mL/min) flow rates could be used to obtain better estimations for axial division length and aqueous diffusion rate constants for both species. The separation of the two axial dispersion processes may be further complicated by film diffusion which may contribute to broadening of breakthrough profiles at slower flow rates due to an increase in the thickness of the stagnant layer surrounding the solid particles.

Although the preliminary investigations into the contributions of diffusion (aqueous phase, film and pore) and eddy dispersion to chromatographic breakthrough profiles suggest that further similar experiments could lead to an estimation of numerical simulation input parameters to describe these processes, there are some additional considerations that have not yet been discussed.

Firstly, the axial division length has been thus-far assumed to be independent of flow rate; however, equations for estimating the coefficient term (γ_{eddy}) that feature the Reynolds number have a linear flow velocity dependency[47]. A variation on the Van Deemter equation (Equation 4.11.) proposes $Au_e^{1/3}$ as the eddy dispersion term; this is known as the Knox equation[35]. The relationship between flow rate and eddy dispersion could be due to or in addition to higher fluid pressures causing compression or distortion of the packed bed. The packed bed may also not consist of evenly packed spheres but may include irregular particle shapes, broken particles or a large particle size distribution range. Depending on the column packing method this could cause a non-homogeneous bed structure due to different settling rates. In addition to vertical eddy dispersion, flow rate variations across the column radius can be encountered due to temperature induced viscosity gradients or non-uniformities in packing structure[42]. For example, faster fluid progression in the centre of a chromatographic column as observed using computed tomography was suggested to be due to denser packing at the column walls as a product of frictional forces

during slurry packing[65]. This imaging technique could also be used in further investigations into the structure of packed beds of the three contrasting sorptive materials to quantify the relationship between of column radius and eddy dispersion and hence improve the estimation of axial division length.

Some thought should also be given to the inclusion of the aqueous volume contained within the frits securing the top and bottom of the packed bed in the chosen experimental set up as well as the droplet that collects in the outlet of the column before dripping into the collection vessel. These volumes are estimated to contain a maximum of 200 µL of fluid. It should be noted, however, that mixing could take place in the solution below the lower frit prior to collecting in the vessel below and that diffusion could take place into and out of the frits.

Small volume loading solutions (0.025 mL) in discrete chromatographic experiments were pipetted on to the top of the upper frit before the lid was re-connected and pumping commenced; this delay could allow for either slow flow or diffusion onto the top axial division of the packed bed. It was also observed that the columns used in this study did not have a constant radius (tapering slightly from top to bottom) meaning that aqueous phase velocity could be faster at the bottom than at the top of the packed bed.

5.2.2.3. Intraparticle diffusion in porous ion exchange materials

As discussed earlier, the numerical simulation method showed poor accuracy in describing chromatographic breakthrough profiles for anion exchange resin and zirconium phosphate using forward and reverse rate constants as well as solid fractionation and internal rate constants determined from batch sorption/desorption experiments. Previous investigations into the change in kinetics between different solid/aqueous ratios under batch conditions showed a decrease in the time taken to reach equilibrium for zirconium phosphate experiments with 1 g of solid in comparison to 0.1 g of solid (aqueous volume = 10 mL in each case). From this evidence it was suggested that the rate of internal diffusion was dominated by surface diffusion (species hop between exchange sites) and that the $k_{internal}$ values had a linear relationship with the solid/aqueous ratio. It was also suggested that the numerical simulation method required more internal fractions to accurately describe the experimental dataset obtained under the higher solid/aqueous ratio conditions.

The investigation into breakthrough profiles of tritiated water indicated that pore diffusion is also possible for both anion exchange resin and zirconium phosphate and that this is likely to be a faster process than internal surface diffusion. A better understanding of different internal

diffusion processes and the level of detail required to describe them at higher solid/aqueous ratios as present in packed bed geometries could help improve the accuracy of the numerical simulation method in describing chromatographic breakthrough from porous ion exchange materials. Zirconium phosphate showed particularly slow kinetics with equilibrium between barium in seawater and the solid material taking over 2 weeks to be achieved under batch conditions (0.1 g solid / 10 mL aqueous solution). Evidence of slow release from the pores of this material was also seen in the chromatographic experiments.

A further investigation into the rate of internal diffusion in a packed bed geometry was undertaken over the course of 16 days. This experiment involved pumping a large volume of seawater containing Ba-133 through a packed bed of zirconium phosphate (4 cm bed length) for ~8 hours a day and collecting outlet fractions. The pump operated at a speed of around 1.7 mL/min but this fluctuated slightly with a decrease in speed daily and over the course of the experiment due to distortion of the peristaltic tubing. The pump was switched off over night and over the weekend and the column capped to prevent it drying out. After 6 days of loading (plus one final night), the column inlet was switched to seawater without additional barium. This solution was then run through the column for ~8 hours a day for 6 days (Figure 5.8.).

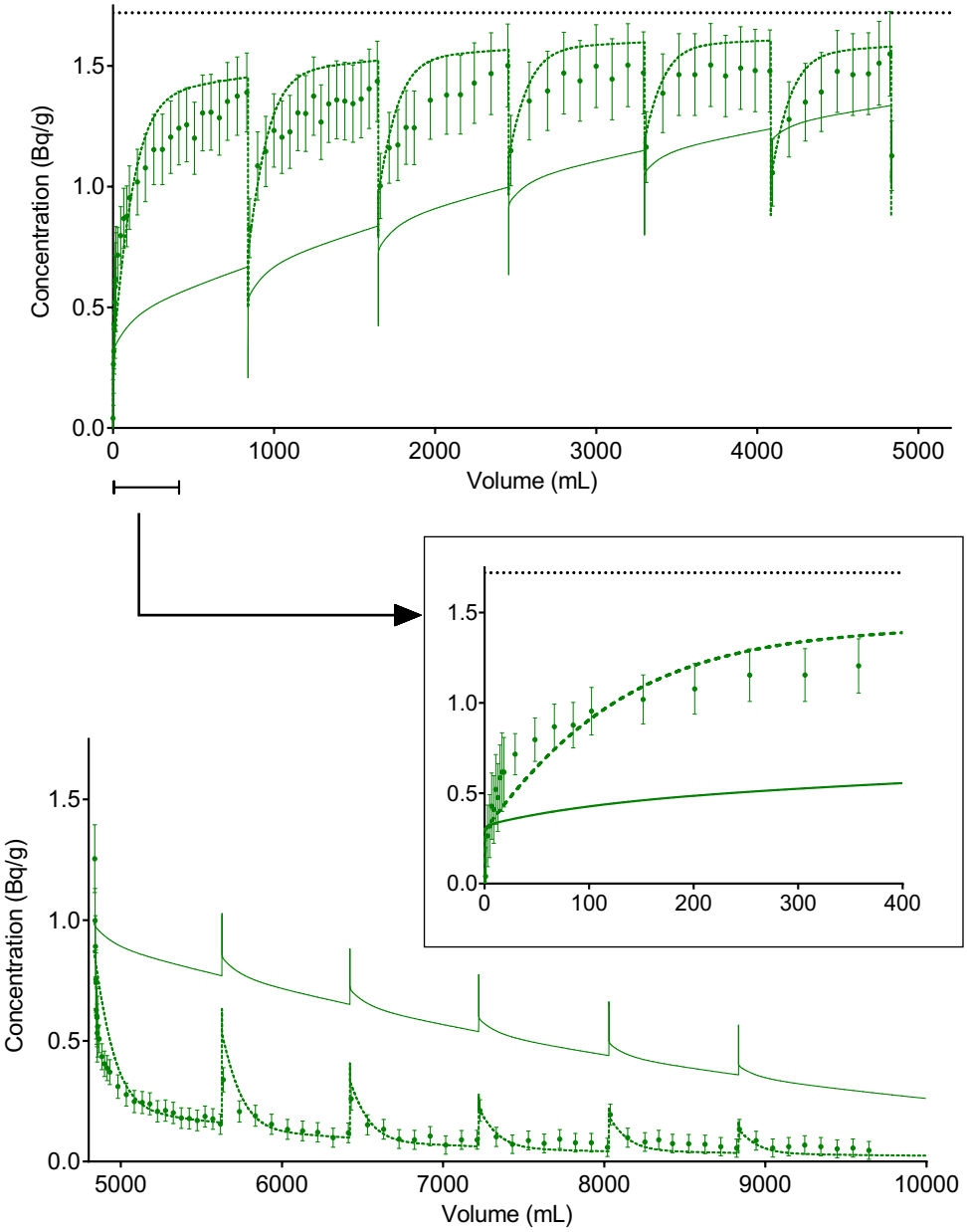

Figure 5.8.
Comparison between experimental data and numerical simulation of barium breakthrough profiles from zirconium phosphate in seawater for an extended loading and wash experiment.
The plot is split into the 6 days during which the solution of seawater plus Ba-133 was loaded (top) and the 6 days during which non-active seawater solution was loaded (bottom). The first ~4 hours of the experiment is highlighted (inset).
The value for the internal rate constant is either equal to (dashed line) or calculated from (solid line) that determined from 0.1 g solid batch sorption/desorption experiments.
Common simulation parameters: bed length = 4 cm; column radius = 0.35; V_{aq} = 0.375; loading concentration = 1.72 Bq/g (horizontal dotted line); axial division length = 0.1 cm. Aqueous phase diffusion has not been included in the simulations.
Average flow rates for each day and stationary periods set programmatically.

The experimental data showed that after 192 hours of interaction with the loading solution (flowing and stationary) there was ongoing net transfer of Ba-133 towards the solid phase. This is evidenced by the outlet concentration not being equal to the inlet concentration at the end of the 6th day loading. There was also a reduction in concentration in the collected fractions following a stationary period indicating slow internal diffusion over the course of ~16 hours (overnight) which also reduced in the outer solid concentration meaning that a greater rate of uptake from the aqueous phase was seen for several hours before returning to the internal diffusion controlled rate. This reduction in outlet concentration was greater after the fifth day of loading when the aqueous phase was stationary for ~64 hours over the weekend. An opposite trend was seen when the column inlet was switched to the wash solution (seawater without Ba-133 spike) with increased concentration in fractions collected after a stationary period and activity still measureable after 176 hours of contact with the wash solution (flowing and stationary).

Numerical simulation of this extended experiment was achieved by addition of a *case structure* to the LabVIEW coding. This additional coding allowed for simulation of the entire experiment in a continuous, programmatically determined sequence. A case was written for each flowing and stationary period with the appropriate flow rate input value (mL/min) for that period. The numerical input was selected according to the *while loop* iteration (via a *subVI*). The flow rate for each ~8 hour flowing period was calculated from the total volume collected divided by the total running time for that day whereas the flow rate for a stationary period was selected such that a single iteration lasted for the total time the pump was stopped. The numerical simulation method used a single loading concentration of 1.72 Bq/g although five different stock solutions were used with an average concentration of 1.718(4) Bq/g. Additionally, the average flow rate for each day is a simplification as a decrease in flow rate was observed over the ~8 hour pumping period.

Using the forward and reverse rate constants for zirconium phosphate determined under batch conditions with three solid phase fractions and internal rate constants scaled up for the higher solid/aqueous ratio in a packed bed (same values as selected in Table 5.1.), the numerical simulation method did not describe the experimental data. Using the same $\vec{k}$ and $\overleftarrow{k}$ values and solid phase fractions but selecting lower internal rate constants equal to those that were used in the numerical simulation of batch sorption/desorption between 10 mL of aqueous solution and 0.1 g of solid material, however, the numerical simulation method generated a better description of the experimental data. This observation suggests that either the assumption made from the batch investigations that internal rate constants are linearly proportional to the solid/aqueous

ratio is incorrect or that the rate of diffusion within porous materials is more complex; it may not be a constant value with internal radius and/or may consist of both pore diffusion and surface diffusion contributions.

A comparison between the two models of internal diffusion (that internal rate constants are linearly proportional to solid/aqueous ratio and that internal rate constants are independent of solid/aqueous ratio) has been made for anion exchange resin and zirconium phosphate under both batch and column conditions. Statistical analysis of data from the batch experiments shows that the numerical simulation method operated using the assumption that the rate of internal diffusion is independent of solid/aqueous ratio fitted the experimental data less well than the model based on the assumption that internal rate constants are linearly proportional to solid/aqueous ratio (Table 5.3. and Figures 5.9.-5.11.). It should, however, be noted that all three experimental datasets had large uncertainties associated with the distribution constant measurements (average for dataset >20 %) with the low sorption of uranium on anion exchange resin being particularly hard to accurately quantify (uncertainty average for dataset = 163 %). In addition, one data point for the sorption of thorium on 0.01 g of anion exchange resin appeared to be anomalously low. Repetition of this data point may help discriminate between the two models for this material.

Table 5.3.
Goodness of fit between experimental data and results of numerical simulation method using different models of intraparticle diffusion.
Comparison has been made using normalised standard deviation (Δq(%)) analysis (Equation 4.12.).
The batch sorption/desorption numerical simulation method used input parameters based on an aqueous volume of 10 mL for each experiment. No external mass transfer was included.
Forward and reverse rate constants for each analyte-sorption material system are kept the same between the two models of internal diffusion. Values for internal rate constants are either equal to ($k_{internal}$ independent of solid/aqueous ratio) or calculated from ($k_{internal}$ proportional to solid/aqueous ratio) those determined from 0.1 g solid batch sorption/desorption experiments.

Sorptive material	Analyte	Solid mass (g)	Number of internal fractions	Δq(%)	
				$k_{internal}$ linearly proportional to solid/aqueous ratio	$k_{internal}$ independent of solid/aqueous ratio
Anion exchange resin	Uranium	0.01	2	78	69
	Thorium	0.01	2	45	95
Zirconium phosphate	Barium	1	3	38	49
			5	22	57

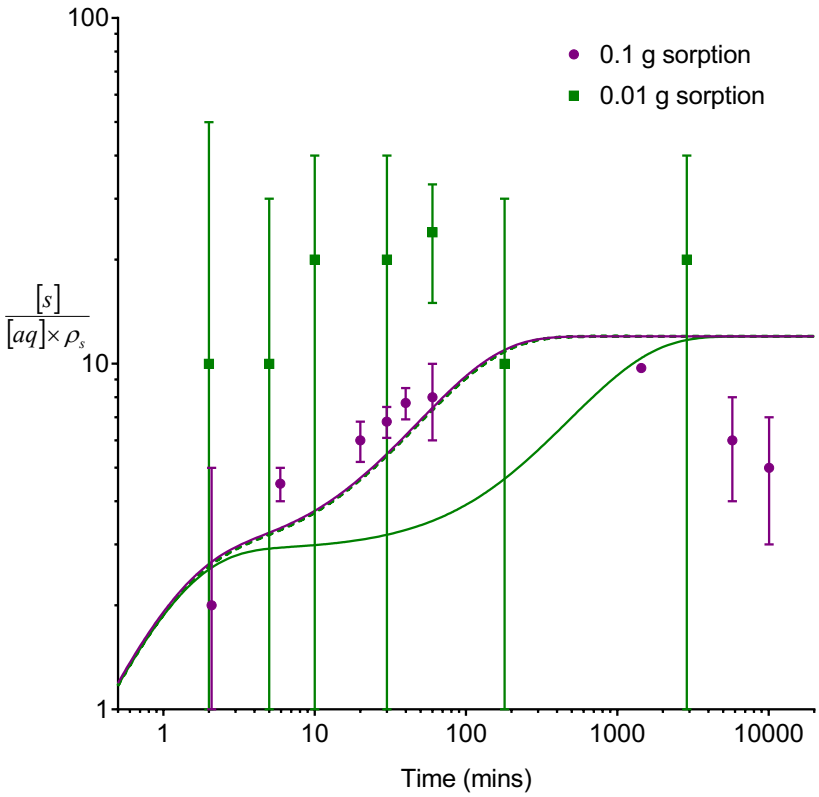

Figure 5.9.
Comparison between experimental data and numerical simulation of sorption of uranium between 8M HNO_3 and anion exchange resin using different models of intraparticle diffusion.
Two internal fractions based on a radial penetration of 5 µm were included.
The value for the internal rate constant is either equal to (dashed line) or calculated from (solid line) that determined from 0.1 g solid batch sorption/desorption experiments.
The numerical simulation method used input parameters based on an aqueous volume of 10 mL for each experiment. No external mass transfer was included.

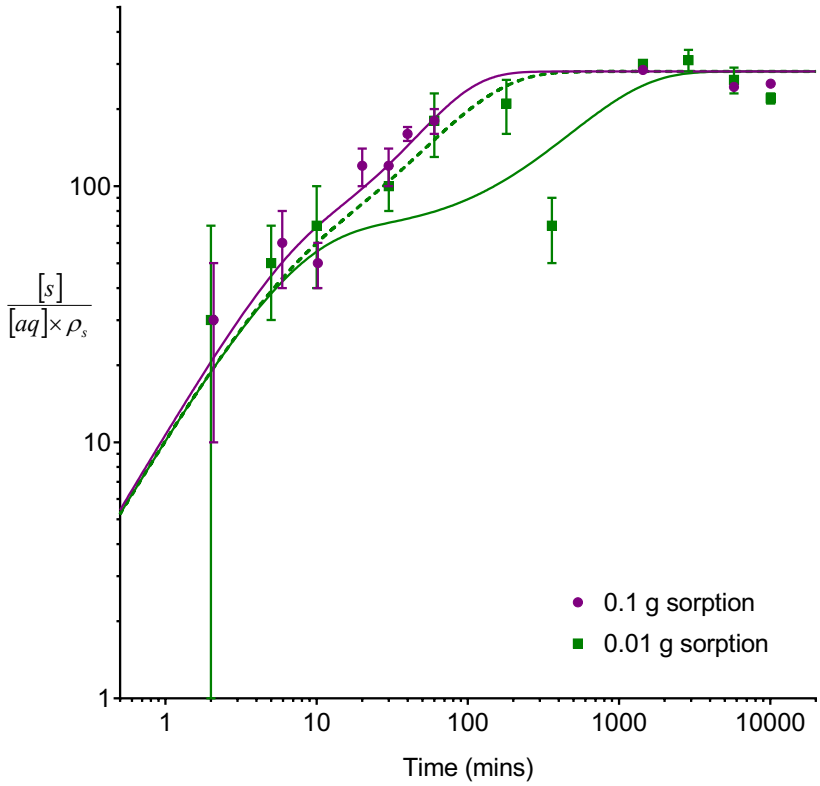

Figure 5.10.
Comparison between experimental data and numerical simulation of sorption of thorium between 8M HNO_3 and anion exchange resin using different models of intraparticle diffusion.
Two internal fractions based on a radial penetration of 5 µm were included.
The value for the internal rate constant is either equal to (dashed line) or calculated from (solid line) that determined from 0.1 g solid batch sorption/desorption experiments.
The numerical simulation method used input parameters based on an aqueous volume of 10 mL for each experiment. No external mass transfer was included.

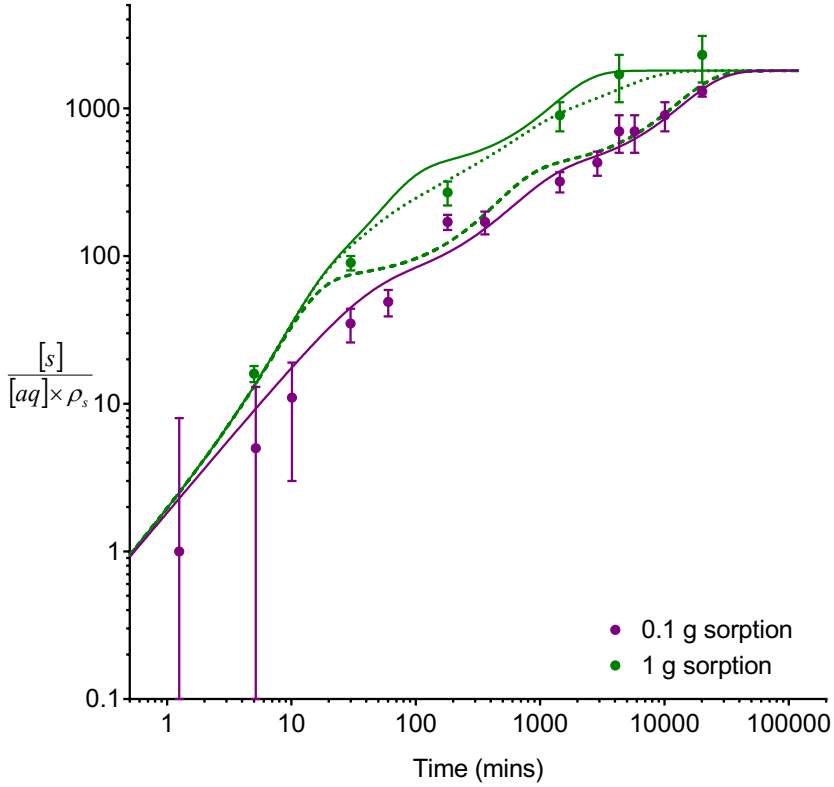

Figure 5.11.
Comparison between experimental data and numerical simulation of sorption of barium between seawater and zirconium phosphate using different models of intraparticle diffusion.
The numerical simulation method using three internal fractions assumes values for the internal rate constants are either equal to (dashed line) or calculated from (solid line) those determined from 0.1 g solid batch sorption/desorption experiments.
The numerical simulation method using five internal fractions assumes values for the internal rate constants are calculated from (dotted line) those determined from 0.1 g solid batch sorption/desorption experiments.
The numerical simulation method used input parameters based on an aqueous volume of 10 mL for each experiment. No external mass transfer was included.

Comparing chromatographic breakthrough profiles generated by the numerical simulation method indicated that the assumption that the rate of internal diffusion is independent of solid/aqueous ratio gave a better description of the experimental data in general (Table 5.4.). Two internal fractions have been used for the numerical simulation of anion exchange resin and three internal fractions have been used for zirconium phosphate. The numerical simulation method did not, however, include any description of aqueous phase diffusion and used a set axial division length of 0.1 cm. As previously discussed, these processes have a greater impact at slower flow rates.

Table 5.4.
Linear regression analysis for comparison of experimental data to simulated breakthrough profiles using different models of intraparticle diffusion.
Experimental data (x-axis) is plotted against simulated data (y-axis) to generate R^2 and slope values.
The numerical simulation method uses rate constant and solid volume fractions calculated from batch sorption/desorption experimental data. The experimental data and numerical simulation method input parameters correspond to experiments 8-20 (Table 5.1.).
Values for internal rate constants are either equal to ($k_{internal}$ independent of solid/aqueous ratio) or calculated from ($k_{internal}$ proportional to solid/aqueous ratio) those determined from 0.1 g solid batch sorption/desorption experiments.
Figures for all the experiments and simulations summarised in this table are shown in Appendix A.

Expt	Sorptive material	Analyte	$k_{internal}$ linearly proportional to solid/aqueous ratio		$k_{internal}$ independent of solid/aqueous ratio	
			Slope	R^2	Slope	R^2
8	Anion exchange resin	Uranium	0.2282	0.9016	0.4107	0.9833
		Thorium	0.2080	-0.6483	0.5800	0.7943
9	Anion exchange resin	Uranium	0.5548	-0.0110	1.0427	0.5354
		Thorium	0.1583	-2.0435	0.8732	0.3984
10	Anion exchange resin	Uranium	0.8160	0.4924	1.2114	0.4090
		Thorium	0.0546	0.5348	0.7552	0.9334
11	Anion exchange resin	Uranium	0.8038	0.5264	1.2006	0.3827
		Thorium	0.0835	0.7173	0.8637	0.9913
12	Anion exchange resin	Uranium	0.5326	0.5430	0.9042	0.6272
		Thorium	0.3961	-4.9171	1.1081	-1.8196
13	Anion exchange resin	Uranium	0.1426	0.8790	0.2235	0.9392
		Thorium	0.1834	-1.2835	0.4855	0.6415
14	Anion exchange resin	Uranium	1.0715	0.9040	0.7340	0.0431
		Thorium	1.4777	0.3451	1.2868	0.7120
15	Anion exchange resin	Uranium	2.4847	0.4161	2.7832	0.4865
		Thorium	0.2525	-0.1738	0.7847	-0.3324
16	Zirconium phosphate	Barium	2.1677	0.5707	2.1774	0.5733
17	Zirconium phosphate	Barium	1.0424	0.4666	1.0812	0.4854
18	Zirconium phosphate	Barium	0.1372	0.8567	0.3507	-1.0925
19	Zirconium phosphate	Barium	2×10^{-5}	-0.3328	0.6608	-0.8957
20	Zirconium phosphate*	Barium	3×10^{-7}	-0.0896	0.0879	-0.1438

*This experiment was based on a particle size of 125-250 µm. All other zirconium phosphate experiments used a particle size of 125-1000 µm.

As previously discussed, thorium showed a strong interaction with anion exchange resin in 8M HNO_3 under batch conditions and generated highly asymmetrical breakthrough profiles. The numerical simulation method using the assumption that the rate of internal diffusion is independent of solid/aqueous ratio managed to estimate the rough position of the breakthrough profile peak in all but the experiments with the fastest flow rate (Experiment 13) and the shortest bed length (Experiment 8). This is in contrast to simulated datasets using the assumption that the rate of internal diffusion is proportional to solid/aqueous ratio which only managed a rough

estimation of peak position for the experiment at the slowest flow rate (Experiment 14), but greatly over-estimated the position of peak breakthrough under most of the other conditions tested (for an example see Figure 5.12.).

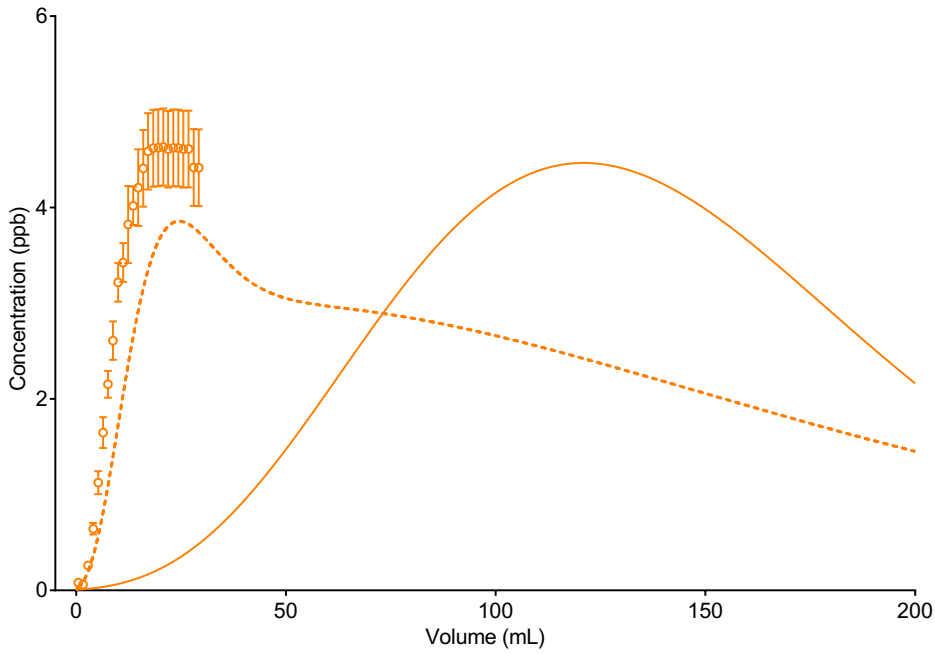

Figure 5.12.
Comparison between experimental data and numerical simulation of thorium breakthrough profiles from anion exchange resin in 8M HNO_3 under conditions corresponding to experiment 10 (Table 5.1.).
The two analytes (uranium and thorium) have been simulated separately. Axial division length = 0.1 cm. Aqueous phase diffusion has not been included in the simulations.
The value for the internal rate constant is either equal to (dashed line) or calculated from (solid line) that determined from 0.1 g solid batch sorption/desorption experiments.

In the case of the two experiments (8 and 13) where the independent model did not describe the breakthrough peak, it gave a superior description of the tailing slope than the proportional model. For these two experiments and others with flow rates greater than 3 mL/min (or >1 mL/min for the shorter bed lengths tested) an initial spike was also generated by both models which was not seen in the experimental data even if corrections were made for differences in resolution. As with the spike seen in the simulations of breakthrough profiles for UTEVA resin, the magnitude was greater for simulations with faster flow rates or shorter bed lengths with the largest spikes accompanied by poor description of the leading slope.

One explanation for the presence of these spikes in the simulated datasets is that the delay between pipetting the discrete loading solution (0.025 mL) on to the top of the upper frit, re-connecting the lid and commencing pumping was not included in the numerical simulation method. In order to accurately simulate this process, a better understanding of aqueous phase

diffusion as well as some knowledge of the interaction of the solution with the frit must be gained. A spike was also observed in both simulated datasets for the experiment where a larger discrete loading solution (~1 mL) was directly pumped on to the upper frit (Experiment 15). A possible explanation in this case is that the first collected fraction was of a significantly lower mass than all subsequent fractions indicating that the flow rate was not immediately at the average rate for that experiment. Both of these explanations for the appearance of concentration spikes will be discussed in more detail with regards to the numerical simulation of chromatographic breakthrough experiments using UTEVA resin.

In order to improve the numerical simulation method for the description of the breakthrough of thorium from anion exchange resin under 8M HNO_3 conditions, further investigations into internal diffusion processes must be made. These investigations could include more batch sorption/desorption experiments using a range of solid/aqueous ratios as well as additional packed bed experiments with a longer period of fraction collection in order to cover the shape of the tailing slope. Once more evidence in support of either the independent or proportional models has been gathered, additional slow flow rate column experiments could help quantify aqueous phase diffusion and eddy dispersion.

As with the batch sorption data, the breakthrough profiles for uranium from anion exchange resin in 8M HNO_3 gave less evidence for either model. Some experimental datasets seemed to switch between favouring the independent model, the proportional model and back to the independent model over the course of the tailing slope (for an example see Figure 5.13.).

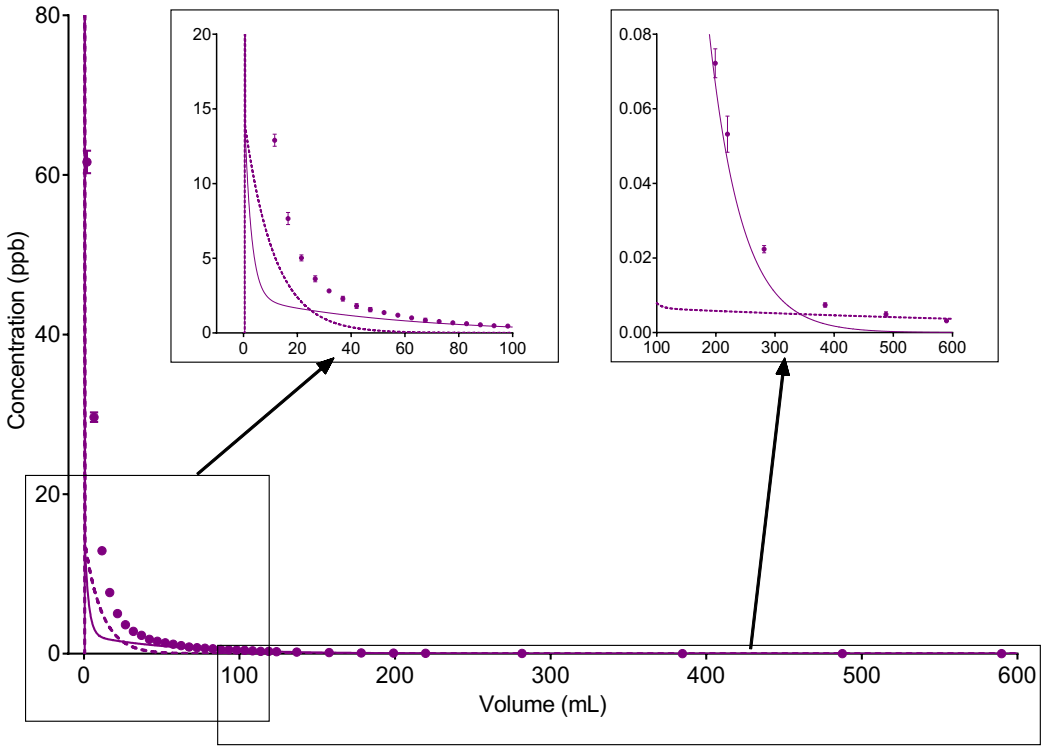

Figure 5.13.
Comparison between experimental data and numerical simulation of uranium breakthrough profiles from anion exchange resin in 8M HNO_3 under conditions corresponding to experiment 13 (Table 5.1.).
The two analytes (uranium and thorium) have been simulated separately. Axial division length = 0.1 cm. Aqueous phase diffusion has not been included in the simulations.
The value for the internal rate constant is either equal to (dashed line) or calculated from (solid line) that determined from 0.1 g solid batch sorption/desorption experiments.

As previously mentioned, a more accurate estimation of the distribution constant could be made by using a larger solid/aqueous ratio in the batch sorption experiments. This would improve the numerical simulation of the position of the breakthrough peak for this weakly interacting species. This additional investigation could also help improve the understanding of internal diffusion processes.

For the two zirconium phosphate chromatographic experiments using a flow rate of 1.82 mL/min (Experiments 16 and 17), the numerical simulation method using either assumption gave similar results; both assumptions simulated the early breakthrough peak and low levels of Ba-133 still measureable after lengthy washing but failed to accurately describe the shape of the tailing slope. At the slowest flow rates (Experiments 19 and 20) the independent model generated earlier peaks than the proportional model. For experiment 20, the simulated peak was still later than that seen in the experimental dataset whereas the simulated profile for experiment 19 more closely matched the position of the experimental breakthrough peak but also exhibited a shoulder

(Figure 5.14.). The numerical simulation method assuming that the rate of internal diffusion is independent of solid/aqueous ratio also generated a peak in the incorrect position when using the experiment 18 input parameters.

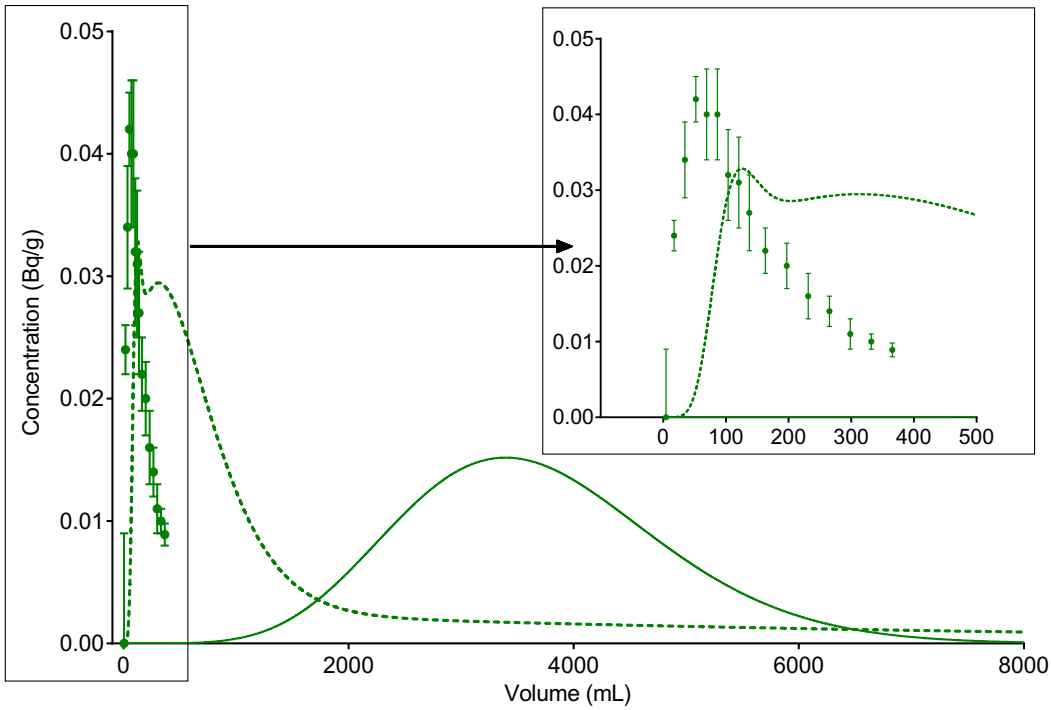

Figure 5.14.
Comparison between experimental data and numerical simulation of barium breakthrough profiles from zirconium phosphate in seawater under conditions corresponding to experiment 19 (Table 5.1.).
Axial division length = 0.1 cm. Aqueous phase diffusion has not been included in the simulations.
The value for the internal rate constant is either equal to (dashed line) or calculated from (solid line) that determined from 0.1 g solid batch sorption/desorption experiments.

Taking into account the experimental data from the extended loading/wash investigation as well as the discrete volume chromatographic breakthrough tests it appears that the independent model better describes internal diffusion within zirconium phosphate. Using three internal fractions and an assumption of a homogeneous rate of surface diffusion throughout the solid particle is an oversimplification and does not fully describe the experimental profiles. This lack of consistency between the simulated and experimental data is particularly significant at faster flow rates in the shape of the breakthrough peak and the initial response to changes in inlet concentration (Figure 5.8. inset plot). This seems to indicate that either the rate of internal diffusion is greater at the outer radius of the particle or that pore diffusion plays a significant role in overall sorption/desorption kinetics. A greater number of internal fractions than three may be needed to describe these processes. For an even more accurate description, a PDE solver can be employed. This solves a set of partial differential equations calculating concentration change with

respect to time and radial coordinate within the solid particles. A more complex model of diffusion than Fickian diffusion might be required; for example, the Maxwell-Stefan model takes into account frictional forces due to the presence of solvent molecules as well as other dissolved species[42]. Further batch experiments at a range of solid/aqueous ratios would help assess these possibilities.

5.2.3. Tolerance of numerical simulation method to errors in input parameters

It was shown that the numerical simulation method should be able to describe the breakthrough of uranium and thorium from a packed bed of UTEVA resin in 8M HNO_3 at fast flow rates (>1 mL/min) without the inclusion of aqueous phase diffusion and using an estimated axial division length of 0.1 cm. The accuracy of this method was proven using experiment 4 (Figure 5.3.). Reasons for the drop in accuracy seen in the simulation of other experimental datasets could be explained by differences in the experimental conditions between them leading to errors in input parameters. This possibility has been explored by altering the packed bed dimensions, flow rate, solution density and position of equilibrium to obtain a good fit for experiment 3 (Table 5.5.).

Table 5.5.
Linear regression analysis for comparison of experimental data to simulated breakthrough profiles using different input parameters.
Experimental data (x-axis) is plotted against simulated data (y-axis) to generate R^2 and slope values.
The experimental data corresponds to experiment 3 (Table 5.1.).
The listed inputs for the numerical simulation method have been chosen to fit the position of the concentration peak in the experimental data. The axial division length is set at 0.1 cm except for the simulation using a bed length of 1.75 cm where it is 1.75/18 cm. Aqueous phase diffusion has not been included in the simulations.

Bed length (cm)	V_{aq}	Column radius (cm)	Flow rate (mL/min)	Density (g/mL)	$\vec{k}$	$\overleftarrow{k}$	Analyte	Slope	R^2
2	0.655	0.35	1.89	1.25	2.263	4.483×10^{-3}	Uranium	0.8374	0.7746
					1.73	2.656×10^{-3}	Thorium	0.8160	0.9640
1.75	0.655	0.35	1.89	1.25	2.263	4.483×10^{-3}	Uranium	0.9531	0.9893
					1.73	2.656×10^{-3}	Thorium	1.0105	0.9521
2	**0.7**	0.35	1.89	1.25	2.263	4.483×10^{-3}	Uranium	0.9592	0.9897
					1.73	2.656×10^{-3}	Thorium	1.0184	0.9485
2	0.655	**0.327**	1.89	1.25	2.263	4.483×10^{-3}	Uranium	0.9573	0.9904
					1.73	2.656×10^{-3}	Thorium	1.0144	0.9526
2	0.655	0.35	**4.8**	1.25	2.263	4.483×10^{-3}	Uranium	0.6660	-0.3269
					1.73	2.656×10^{-3}	Thorium	0.6985	-2.6070
2	0.655	0.35	**2.15**	**1.1**	2.263	4.483×10^{-3}	Uranium	0.9524	0.9908
					1.73	2.656×10^{-3}	Thorium	1.0042	0.9614
2	0.655	0.35	1.89	1.25	**2**	4.483×10^{-3}	Uranium	0.9498	0.9901
					1.5	2.656×10^{-3}	Thorium	1.0222	0.9442
2	0.655	0.35	1.89	1.25	2.263	**5.1×10^{-3}**	Uranium	0.9836	0.9927
					1.73	**3.1×10^{-3}**	Thorium	1.0746	0.9872

Experiment 3 was chosen as all these input parameters were recorded or assumed to be identical to those for experiment 4. The experimental results, however, showed earlier breakthrough peaks for both uranium and thorium for experiment 3 in comparison to both experiment 4 and the simulated breakthrough profile. Fitting input parameters to account for the difference in the breakthrough shape and peak position will therefore offer guidance on the sensitivity of the numerical simulation method to changes in input parameters and the level of accuracy needed when measuring or estimating these values.

The percentage reduction in bed length required to achieve a good fit to both sets of experimental data is greater than the percentage reduction in column radius required. This is due to the contribution of each of these factors to the duration of solution residence time in the column (Equation 5.9.). As the column radius is squared, a smaller percentage error makes a larger difference to the volume of the total aqueous phase than a similar error in the bed length.

$$duration\ (s) = \frac{V_{aq} \times \pi \times r^2 \times 60 \times L_{col}}{flow\ rate\ (mL\ min^{-1})} \qquad \text{Equation 5.9.}$$

The bed length was measured to the nearest 0.05 cm so it is unlikely that an error of 0.25 cm could have been made in the measurement. The internal diameter of the column is less easily measured; dissection of a column and the use of calipers gave a diameter of 0.683 cm at the bottom of the column, 0.713 cm around the middle and 0.760 cm at the top of the available packed bed region (before the column broadens to accommodate a reservoir of solution). These measurements indicate that the columns used in these experiments taper and the single column radius input may be an oversimplification. Shorter bed lengths would also have a smaller average column radius than longer beds. The column radius of 0.327 cm needed to fit the experimental data is, however, even smaller than that measured at the lower region of the column. As the internal dimensions of only one column were measured, there could be some variation between experiments.

A reduction in aqueous volume fraction would also reduce the solution residence time in the column giving less time for transfer onto/from the solid phase. The associated increase in solid volume fraction would, however, increase the interphase area allowing for a greater flux between the two phases. The effect of errors in the solid/aqueous ratio is therefore more complex. Under these conditions, a drop from 0.345/0.655 to 0.3/0.7 is needed to achieve a good fit to the experimental data. The original ratio was calculated from volumetric displacement

measurements where dry particles were added to MQ water and allowed to settle into a bed. This calculated ratio is closer to the published free column volume (V_{aq}) of 0.65 mL/mL[70].

It is also possible that both the bed length and packing density may change over the course of an experiment. Depending on the flow rate, fluid pressures may compress the packed bed. This would decrease the bed length and increase the solid/aqueous ratio. As these two changes appeared to have opposing effects it is hard to estimate the net effect on the breakthrough profile. Another possible physical change is the swelling or shrinking of the particles. If the electrostatic forces keeping the UTEVA resin particles in their loosely packed structure were unaffected, this could change both the available interphase area and bed length without altering the solid/aqueous ratio. Swelling or shrinking is normally seen after changes to the aqueous environment such as pH or acid strength changes. In the experiments conducted in this study, a reduction in the bed length was observed for anion exchange resin when changing from MQ water to 8M HNO_3. To minimise physical changes due to bed compression, shrinking or swelling, the packed bed was always preconditioned by pumping the same matrix as the loading solution through the column at a moderate flow rate (~2 mL/min) for 5 minutes. The bed length measurement was made after this procedure.

Another phenomenon that is unaccounted for in column dimension and phase fraction inputs is the presence of air bubbles. Although the practice of slurry packing (for UTEVA resin and anion exchange resin) and capping of the column during set-up to avoid the bed drying out both help avoid the formation of bubbles, some may still be present. The presence of air bubbles would impact on the available aqueous phase volume without affecting the other measured dimensions.

Flow rate has an inverse relationship with the duration of solution residence time in the column. In order to accurately simulate the position of the experimental breakthrough peak, the flow rate had to be increased from 1.89 mL/min to 4.8 mL/min. This change also significantly affected the shape of the breakthrough profile for both species. Much broader peaks were generated as quantified by the negative R^2 values. This poor description of the breakthrough profile shape and calculated standard deviation of 0.01 mL/min associated with the average flow rate value makes this large error in flow rate a very unlikely cause of the earlier uranium and thorium breakthrough peak positions seen for experiment 3 in comparison to experiment 4. The flow rate input value was calculated from the average of the collected fractions. The flow rate in each of these fractions was calculated by dividing the mass collected by the collection time. Another factor causing a change in the average volumetric flow rate would therefore be the assumed density of the solution. A density of 8M HNO_3 at room temperature of 1.25 g/mL[55] was used in both the

calculation of the flow rate input value and the volume of each collected fraction. A better fit between the experimental and simulated datasets was achieved by using a density of 1.1 g/mL; this altered the volumetric position of the breakthrough peak in both sets of data. This would correspond to a molarity of ~3M which is far outside the expected uncertainty range on the laboratory prepared solution.

The final set of input parameters that impact the simulation of chromatographic breakthrough of uranium and thorium from UTEVA resin in 8M HNO_3 are the forward and reverse rate constants. These were determined empirically from the initial slope of sorption using a solid/aqueous ratio of 0.01 g/10 mL and the average distribution constant (sorption value at equilibrium) based on all the data collected under batch conditions. The distribution constant is calculated from knowledge of the initial aqueous concentration of the species ($[aq]_0$) and the aqueous concentration at equilibrium ($[aq]_{eq}$) as well as the volume of the aqueous phase (V_{aq}) and the mass of the solid phase (W_s). This can be used to calculate the concentration in the solid phase at equilibrium ($[s]_{eq}$) if the density of the solid phase (ρ_s) is known (Equation 5.10.). As the numerical simulation method for UTEVA resin uses a single pair of differential equations to describe sorption/desorption kinetics the ratio of solid phase concentration to aqueous phase concentration at equilibrium is equal to the ratio of the forward rate constant to the reverse rate constant (Equation 5.11.).

$$k_D = \frac{([aq]_0 - [aq]_{eq}) \times V_{aq}}{[aq]_{eq} \times W_s} = \frac{[s]_{eq}}{[aq]_{eq} \times \rho_s} \qquad \text{Equation 5.10.}$$

$$k_D \rho_s = \frac{[s]_{eq}}{[aq]_{eq}} = \frac{\vec{k}}{\overleftarrow{k}} \qquad \text{Equation 5.11.}$$

The rate constants for UTEVA resin used thus far have been based on k_D values of 459 for uranium and 592 for thorium (in 8M HNO_3). The range of both of these values measured over all batch experiments conducted was quite large however, with a standard deviation of 25 for uranium and 61 for thorium.

In order for the numerical simulation method to generate a breakthrough profile with the peak in an earlier position, $\vec{k}/\overleftarrow{k}$ must be smaller. This was achieved by either reducing the forward rate constant or increasing the reverse rate constant. The precision of the fitted rate constant value was only given to two significant figures but corresponded to approximate k_D values of 405 for uranium and 510 for thorium. It was also observed that the breakthrough profiles simulated when the reverse rate constant was increased gave a better description of the experimental

datasets for both uranium and thorium with the best R^2 values of any of the fitted parameter tests. Using the same approximate $\vec{k}/\overleftarrow{k}$ ratio, a larger magnitude of both values produced a narrower breakthrough profile than that generated using smaller values (Figures 5.15. and 5.16.). Although the fitted rate constants are out of the range seen in the batch sorption/desorption experiments, it is possible that a difference in $\vec{k}/\overleftarrow{k}$ due to either a different batch of UTEVA resin or 8M HNO_3, a variation in temperature or a different length of time stored in slurry form could explain the difference between the breakthrough profiles observed for experiments 3 and 4.

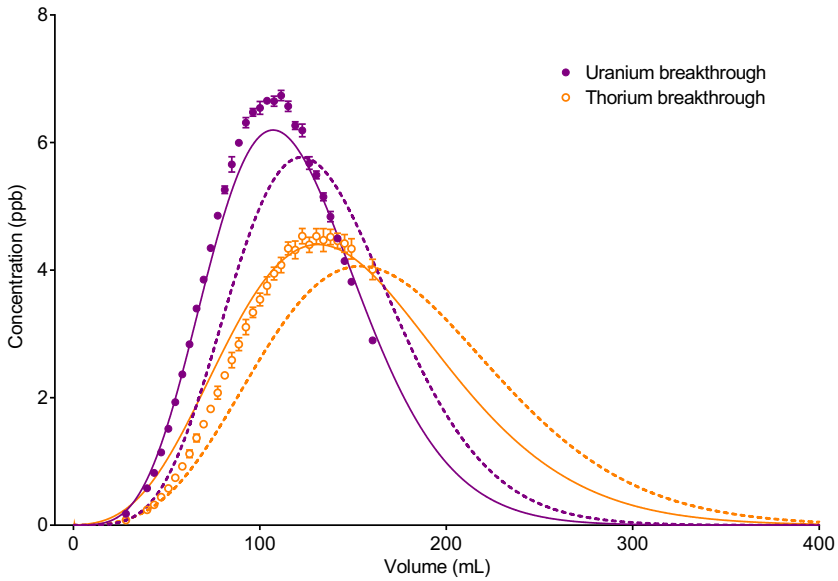

Figure 5.15.
Comparison between experimental data and numerical simulation of uranium and thorium breakthrough profiles from UTEVA resin in 8M HNO_3 under conditions corresponding to experiment 3 (Table 5.1.) – Simulations with and without an amendment to the forward rate constant.
The two analytes (uranium and thorium) have been simulated separately. Axial division length = 0.1 cm. Aqueous phase diffusion has not been included in the simulations.
The numerical simulation uses either $\vec{k}$ and $\overleftarrow{k}$ determined from batch sorption/desorption data (dashed lines) or fitted values (solid lines) of $\vec{k}$ = 2 (uranium) and $\vec{k}$ = 1.5 (thorium).

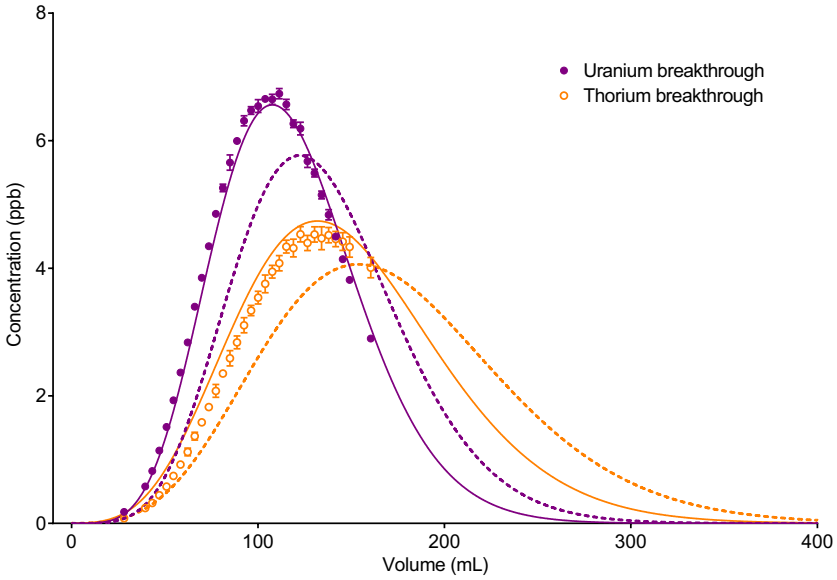

Figure 5.16.
Comparison between experimental data and numerical simulation of uranium and thorium breakthrough profiles from UTEVA resin in 8M HNO_3 under conditions corresponding to experiment 3 (Table 5.1.) – Simulations with and without an amendment to the reverse rate constant.
The two analytes (uranium and thorium) have been simulated separately. Axial division length = 0.1 cm. Aqueous phase diffusion has not been included in the simulations.
The numerical simulation uses either $\vec{k}$ and $\overleftarrow{k}$ determined from batch sorption/desorption data (dashed lines) or a fitted values (solid lines) of $\overleftarrow{k}$ = 5.1 x 10^{-3} (uranium) and $\overleftarrow{k}$ = 3.1 x 10^{-3} (thorium).

As mentioned earlier, an initial spike was seen in the simulated datasets for UTEVA resin column experiments with flow rates >2 mL/min (Experiments 1, 2, 5 and 6). This spike could be due to an improper representation of flow rates at the beginning of the experiment. The delay between pipetting the solution (0.025 mL) on to the top of the upper frit, reattaching the lid and commencing pumping was not included in the numerical simulation method. During this time, the dissolved species may be able to pass through the frit to interact with the sorptive material. There are two ways that this may happen; the solution could flow through the frit or the species could diffuse through it. Although there is no pumping pressure, solution would continue flowing due to gravity although surface tension forces would slow this process if the reservoir above the column was empty. Flow through the frit could be possible if it was already dry and could be helped by the increased pressure associated with the attachment of the lid. Additionally, the tapered column dimensions mean that the upper frit does not sit as tightly in the column as the lower frit; solution could therefore flow around the edge of the frit. The rate of diffusion through the frit is dependent upon the porosity and thickness of the frit. If the dissolved species were able to enter the aqueous phase in the top division of the column before the pumping was commenced they could transfer into the solid phase or the next aqueous phase due to diffusion.

As the flow rate was ~0 mL/min for up to a minute before pumping was commenced, the latter process could be significant.

The length of this delay was not recorded; whether or not species did pass through the frit during this time and the process by which they might have are not known. A low estimate of ~10 seconds delay in the uppermost division was simulated for the four chromatographic experiments with flow rates >2 mL/min (Experiments 1, 2, 5 and 6) without the inclusion of any aqueous phase diffusion. This was achieved by programming a flow rate of 0.15 mL/min for the iteration after addition of the discrete loading volume before returning to the average flow rate for that experiment. This modification greatly reduced the size of the initial spike for both uranium and thorium breakthrough profiles (Figures 5.17.-5.19.), completely removing it in the slower flowing experiments (Experiments 1 and 2). In addition to this change, the delay modification caused a shift in the position of the peak to a later volume fraction. This could be due to not including diffusion in the numerical simulation method or by errors in the input parameters such as a different batch of resin having lower distribution constants.

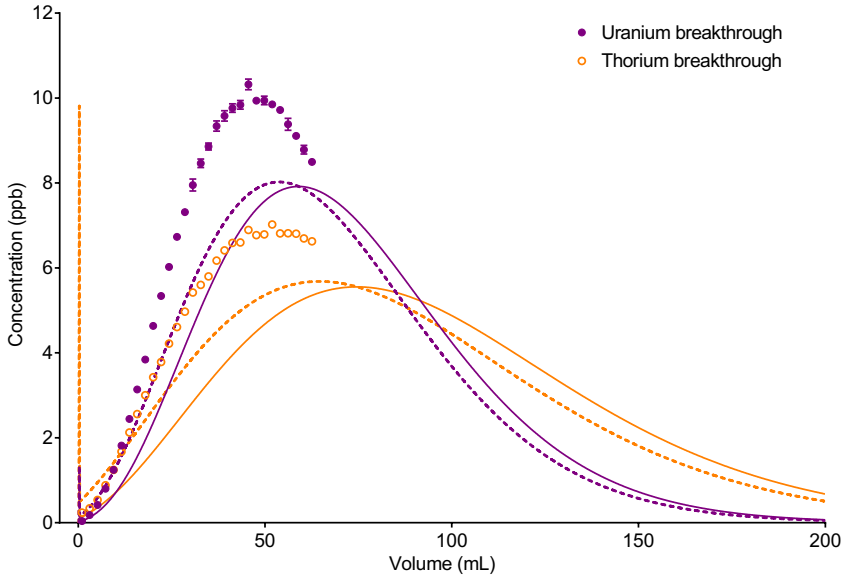

Figure 5.17.
Comparison between experimental data and numerical simulation of uranium and thorium breakthrough profiles from UTEVA resin in 8M HNO_3 under conditions corresponding to experiment 1 (Table 5.1.) – Simulations with and without a delay after loading.
The two analytes have been simulated separately. Axial division length = 0.1 cm. Aqueous phase diffusion has not been included in the simulations.
The numerical simulation has been run either with (solid lines) or without (dashed lines) a slower flow rate (0.15 mL/min) for the iteration after the addition of the discrete loading volume.

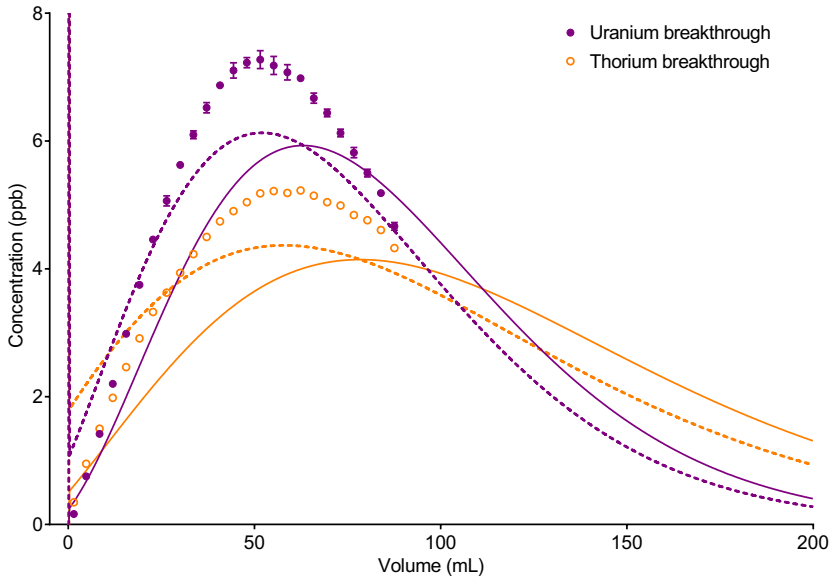

Figure 5.18.
Comparison between experimental data and numerical simulation of uranium and thorium breakthrough profiles from UTEVA resin in 8M HNO_3 under conditions corresponding to experiment 2 (Table 5.1.) – Simulations with and without a delay after loading.
The two analytes have been simulated separately. Axial division length = 0.1 cm. Aqueous phase diffusion has not been included in the simulations.
The numerical simulation has been run either with (solid lines) or without (dashed lines) a slower flow rate (0.15 mL/min) for the iteration after the addition of the discrete loading volume.

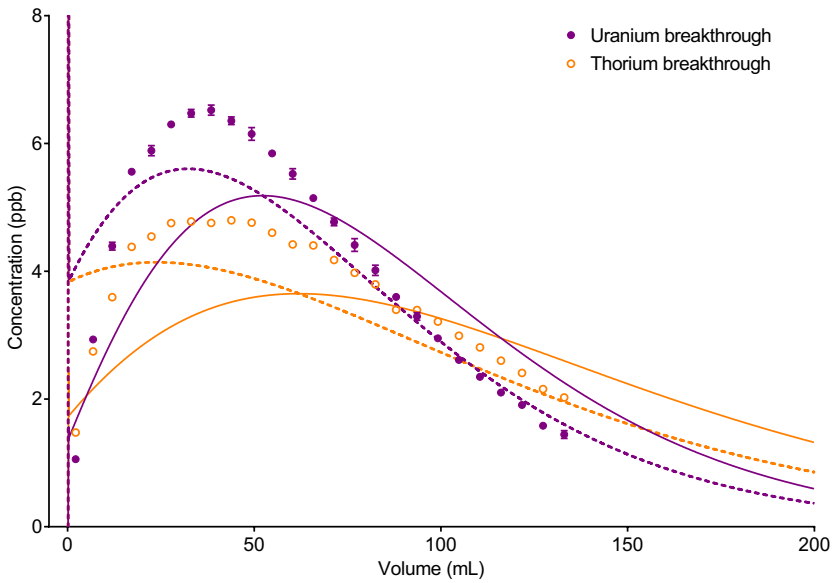

Figure 5.19.
Comparison between experimental data and numerical simulation of uranium and thorium breakthrough profiles from UTEVA resin in 8M HNO_3 under conditions corresponding to experiment 5 (Table 5.1.) – Simulations with and without a delay after loading.
The two analytes (uranium and thorium) have been simulated separately. Axial division length = 0.1 cm. Aqueous phase diffusion has not been included in the simulations.
The numerical simulation has been run either with (solid line) or without (dashed line) a slower flow rate (0.15 mL/min) for the iteration after the addition of the discrete loading volume.

It was also observed that the flow rate in the first collected fraction for these four experiments was lower than the average flow rate through the rest of the experiment (Figure 5.20.). This gradual build-up of flow rate could be due to the competing processes of backpressure and compression of the air in the volume above the column. An accumulation of solution in this headspace volume was visible at the highest flow rates. The length of time taken to build-up flow appeared to be related to the final flow rate.

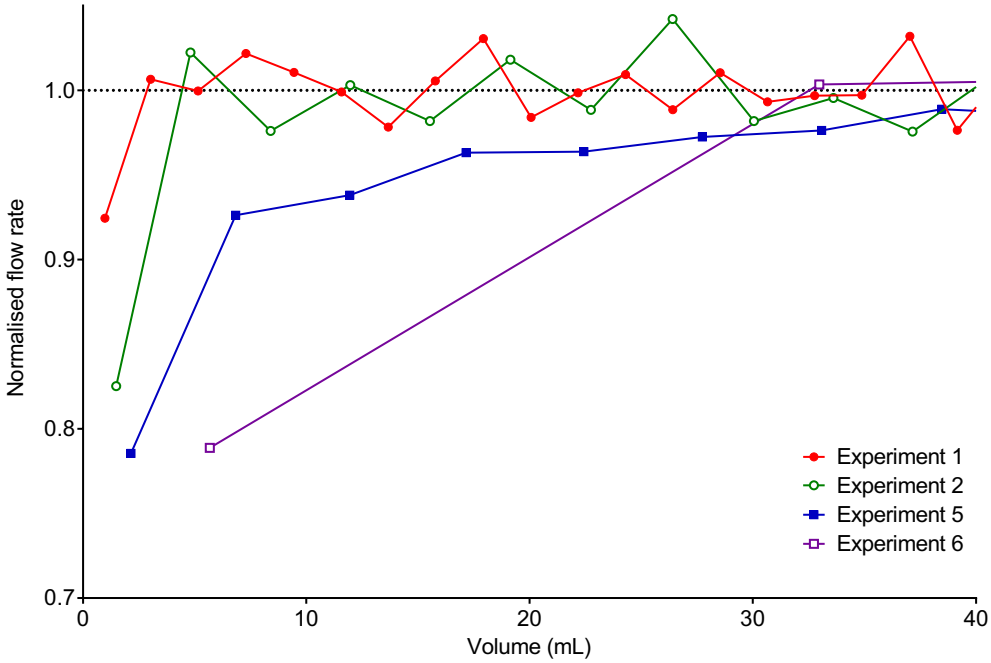

Figure 5.20.
Graph to show gradual build-up of flow rate at the start of the experiment.
The flow rate in each collected fraction is normalised by dividing by the average flow rate across the entire experiment.
The volumetric mid-point of each collected fraction has been used to plot the x-coordinate.

An estimation of the gradual build-up of flow rate was made for the experiment ran at the fastest flow rate (Experiment 6.). The LabVIEW code was modified to include this estimation by programmatically setting 6 lower flow rates for a set number of iterations prior to the final average flow rate of 28.8 mL/min. This modification generated simulated breakthrough profiles without an initial spike for both uranium and thorium (Figures 5.21. and 5.22.). The programmed step changes in flow rate are seen in the shape of the leading slope. The position of the simulated breakthrough peak and shape of the tailing slope were later than the experimental data and very similar to those simulated when applying the ~10s delay modification (Table 5.6.).

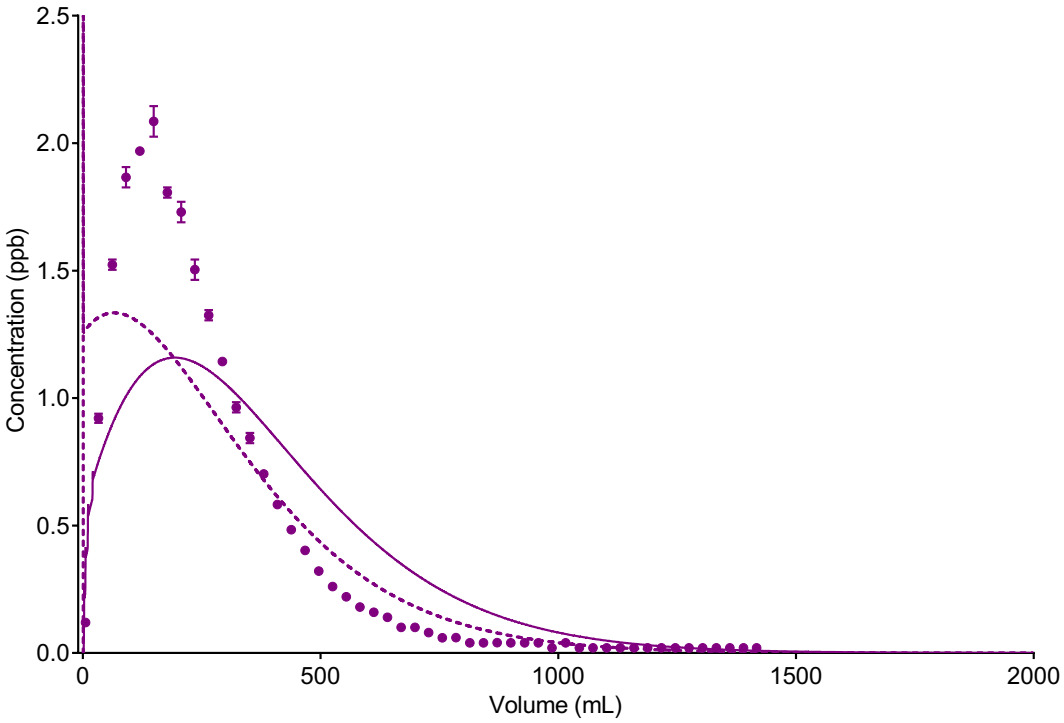

Figure 5.21.
Comparison between experimental data and numerical simulation of uranium breakthrough profiles from UTEVA resin in 8M HNO_3 under conditions corresponding to experiment 6 (Table 5.1.) – Simulations with either a gradual build-up of flow rate or a delay after loading.
The two analytes (uranium and thorium) have been simulated separately. Axial division length = 0.1 cm. Aqueous phase diffusion has not been included in the simulations.
The numerical simulation has been run either with a gradual build-up of flow rate (solid line) or with a slower flow rate (0.15 mL/min) for the iteration after the addition of the discrete loading volume (dashed line).

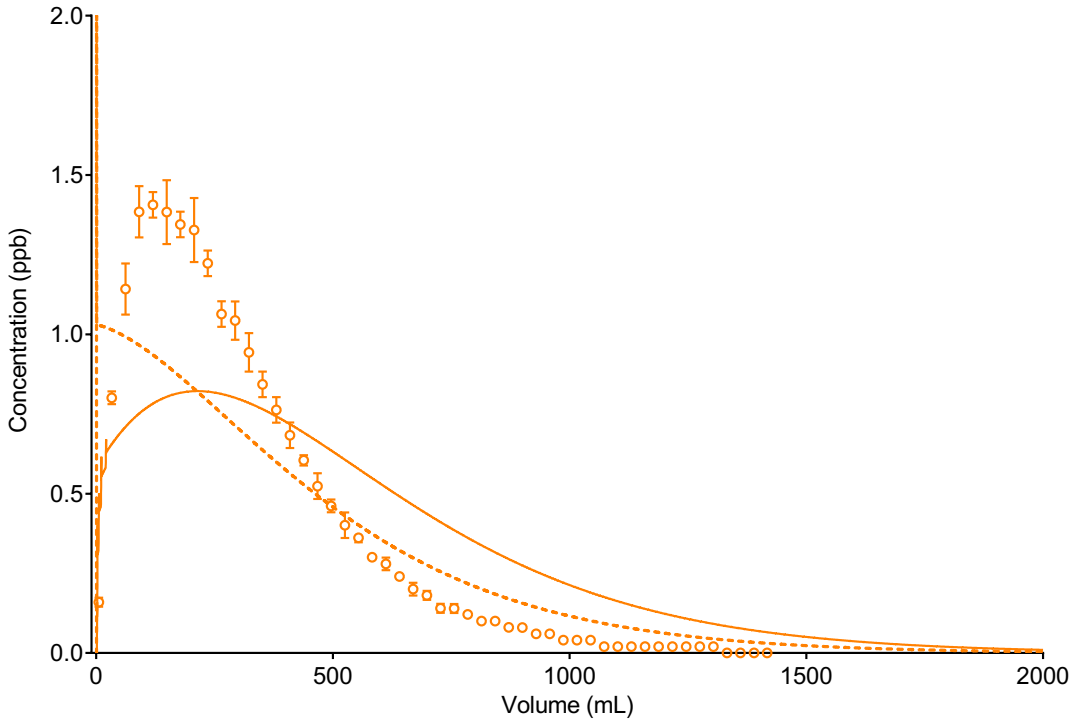

Figure 5.22.
Comparison between experimental data and numerical simulation of thorium breakthrough profiles from UTEVA resin in 8M HNO_3 under conditions corresponding to experiment 6 (Table 5.1.) – Simulations with either a gradual build-up of flow rate or a delay after loading.
The two analytes (uranium and thorium) have been simulated separately. Axial division length = 0.1 cm. Aqueous phase diffusion has not been included in the simulations.
The numerical simulation has been run either with a gradual build-up of flow rate (solid line) or with a slower flow rate (0.15 mL/min) for the iteration after the addition of the discrete loading volume (dashed line).

Table 5.6.
Linear regression analysis for comparison of experimental data to simulated breakthrough profiles using different descriptions of the initial flow rate.
Experimental data (x-axis) is plotted against simulated data (y-axis) to generate R^2 and slope values.
The experimental data corresponds to experiment 6 (Table 5.1.).
The numerical simulation method has been modified to include a ~10s delay by including a single iteration at 0.15 mL/min or a gradual build-up using iterations of 0.15, 6, 12, 18, 22 and 26 mL/min.
The axial division length is set at 0.1 cm. Aqueous phase diffusion has not been included in the simulations.

Amendments to initial flow rate	$\vec{k}$	$\overleftarrow{k}$	Analyte	Slope	R^2
None	2.263	4.483×10^{-3}	Uranium	0.7498	0.7745
	1.73	2.656×10^{-3}	Thorium	0.7535	0.7181
~10s delay	2.263	4.483×10^{-3}	Uranium	0.7134	0.6548
	1.73	2.656×10^{-3}	Thorium	0.7444	0.3248
Gradual build-up	2.263	4.483×10^{-3}	Uranium	0.7206	0.6854
	1.73	2.656×10^{-3}	Thorium	0.7503	0.3728
	1.4	4.483×10^{-3}	Uranium	0.8692	0.8405
	0.92	2.656×10^{-3}	Thorium	0.9533	0.7405
	2.263	7.0×10^{-3}	Uranium	0.9681	0.9703
	1.73	5.0×10^{-3}	Thorium	1.1167	0.9430

As differences in the distribution constant at equilibrium and associated forward and reverse rate constants between experiments was seen as a possible cause of peaks in experimental breakthrough profiles appearing earlier than simulated, the input values of $\vec{k}$ and $\overleftarrow{k}$ were changed to fit the experimental data. By increasing the value of the reverse rate constant, an improved fit to the position of the peak of the breakthrough profile and the shape of the tailing slope could be achieved (Figures 5.23. and 5.24.).

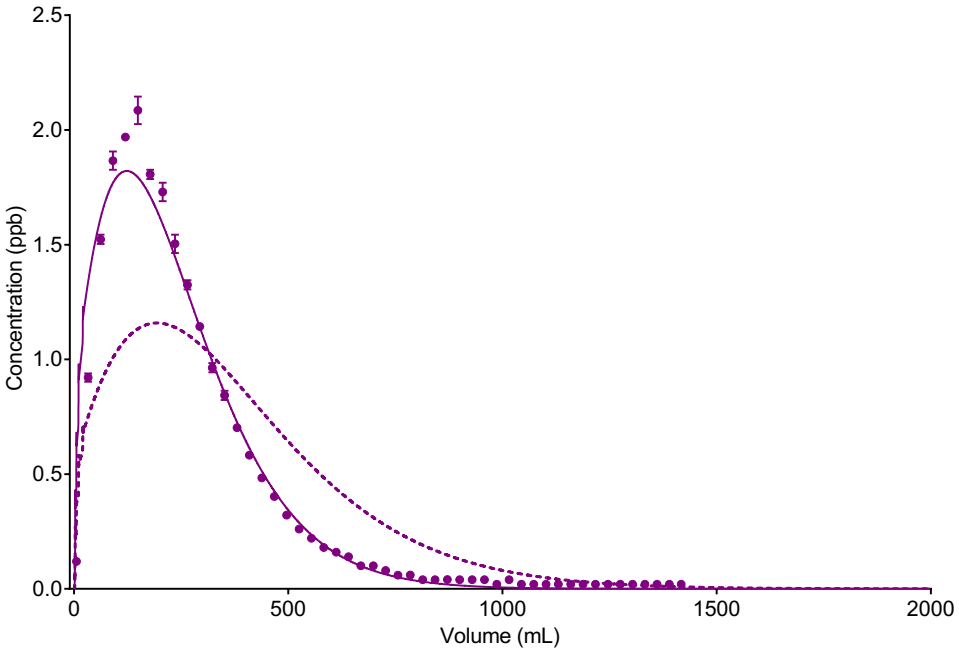

Figure 5.23.
Comparison between experimental data and numerical simulation of uranium breakthrough profiles from UTEVA resin in 8M HNO_3 under conditions corresponding to experiment 6 (Table 5.1.) – Simulations with and without an amendment to the reverse rate constant.
The two analytes (uranium and thorium) have been simulated separately. Axial division length = 0.1 cm. Aqueous phase diffusion has not been included in the simulations.
A gradual build-up of flow rate has been programmatically simulated using either $\vec{k}$ and $\overleftarrow{k}$ determined from batch sorption/desorption data (dashed line) or using a fitted value of $\overleftarrow{k}$ = 0.007 (solid line).

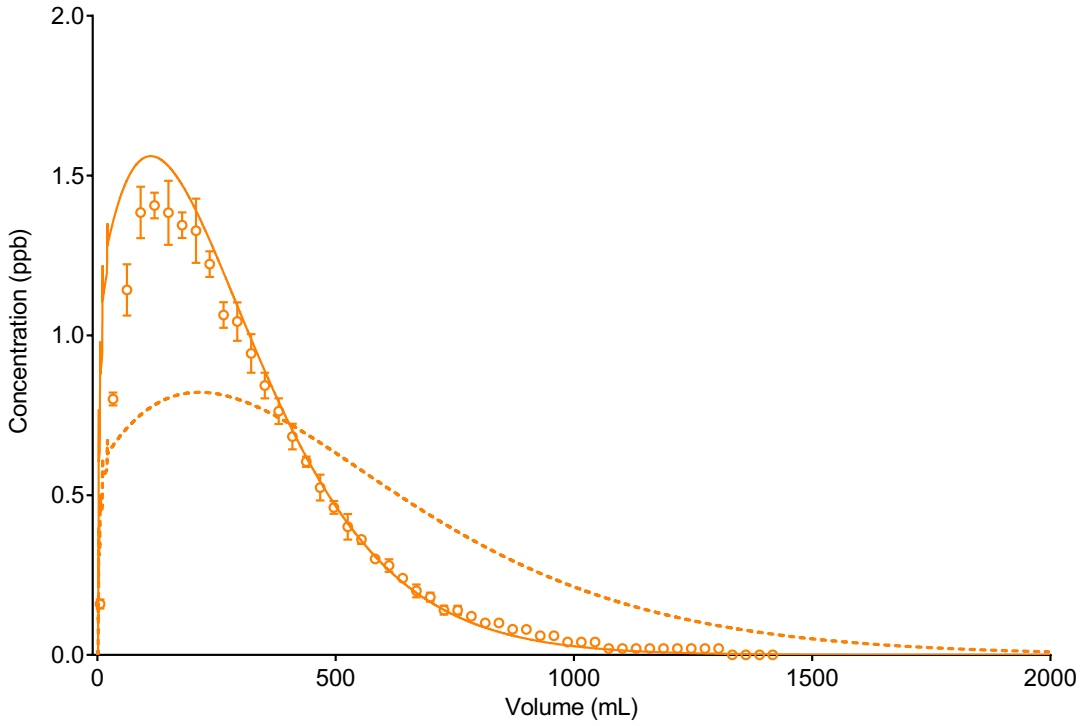

Figure 5.24.
Comparison between experimental data and numerical simulation of thorium breakthrough profiles from UTEVA resin in 8M HNO_3 under conditions corresponding to experiment 6 (Table 5.1.) – Simulations with and without an amendment to the reverse rate constant.
The two analytes (uranium and thorium) have been simulated separately. Axial division length = 0.1 cm. Aqueous phase diffusion has not been included in the simulations.
A gradual build-up of flow rate has been programmatically simulated using either $\vec{k}$ and $\overleftarrow{k}$ determined from batch sorption/desorption data (dashed line) or using a fitted value of $\overleftarrow{k}$ = 0.005 (solid line).

The alternative approach of decreasing the value of the forward rate constant failed to generate a simulated dataset that described the experimental data. Using a similar ratio of $\vec{k}/\overleftarrow{k}$, the simulated breakthrough profile using smaller rate constant inputs gave a worse description of both the position of the peak and shape of the profile. The fitted rate constant values corresponded to a decrease in k_D from 459 to 294 for uranium and from 592 to 315 for thorium. These amended distribution constants are far outside the range observed under the batch conditions.

The much larger reverse rate constants could be due to increased leaching of the solvent extractant under the high fluid pressure. Evidence for this phenomenon has been observed for other extraction chromatographic resins either directly through measurement of organic species in the effluent[72] or indirectly through loss of efficiency on repeated use of the same resin bed[135]. The extent of leaching was also suggested to be related to flow rate[134] and could be reduced by saturating the chromatographic reagents with the organic phase solvent[69]. An evaluation of

extractant loss was also carried out by Horwitz et al. in their initial characterisation of UTEVA resin[70]. After washing a column with ~100 free column volumes of 2M HNO_3, analysis of the effluent for phosphorus indicated a total extractant loss of 5.8 %. The loss of extractant would provide an additional mechanism for transfer of the complexed species from the lumped solid phase into the aqueous phase. The relationship between flow rate and the mobilisation of the organic solvent from UTEVA resin could be explored by measuring total organic content present in collected fractions. The extent of extractant loss is also important when considering regeneration and reusability of the sorptive material.

5.3. Conclusions

A LabVIEW based numerical simulation method developed for the description of batch sorption/desorption kinetics has shown the potential to accurately simulate chromatographic breakthrough profiles. Due to the mechanistic and modular nature of numerical simulation, the accuracy of the method depends on the level of the descriptive detail regarding the experimental and kinetic parameters.

The transfer of uranium and thorium between an 8M HNO_3 solution and UTEVA resin was simulated using a single pair of differential equations and associated rate constants. This was found to be suitable for describing kinetics within the closed system providing the mixture was constantly tumbling. This model was also able to accurately simulate chromatographic breakthrough of these species under moderate flow rates without a detailed understanding of aqueous phase diffusion or additional dispersion processes. Further investigations into breakthrough profiles produced under slow flow rate conditions would help to quantify these processes. This could also help to define the conditions under which diffusion becomes a significant contributor to the shape of breakthrough profiles and should be included in the numerical simulation method. At faster flow rates, physical forces such as competition between backpressure and compression of the air in the headspace above the column and leaching of solvent extractant become significant. Measurements of total organic content in the column output solution could help to confirm and quantify the latter process. The gradual build-up of flow rate at the start of the experiment would be hard to accurately simulate. It could instead be reduced by employing an alternative column configuration with less dead volume such as pre-packed cartridges.

The kinetics of sorption/desorption for anion exchange resin and zirconium phosphate are more complex and require knowledge of the rate of internal diffusion within the solid particles. Division of the solid phase into two fractions (inner and outer) was sufficient to describe the kinetics of the

transfer of uranium and thorium between an 8M HNO_3 solution and anion exchange resin under batch conditions with a solid/aqueous ratio of 0.1 g / 10 mL. Three fractions (inner, mid and outer) were needed to describe the transfer of barium between seawater and zirconium phosphate with the same ratio. The batch experiments also suggested that the rate of internal surface diffusion between the solid fractions was dependent on the solid/aqueous ratio and that more fractions were required to accurately describe the kinetics of transfer at higher solid/aqueous ratios. Numerical simulation of the chromatographic breakthrough experiments was not very accurate. The experimental results under column conditions suggest that the relationship between solid/aqueous ratio and the rate of internal diffusion is more complex. The chromatographic breakthrough profiles of tritiated water from these two materials indicate that physical diffusion within the solid pores is also possible and may need to be included in the numerical simulation method. Further batch investigations into sorption/desorption at different solid/aqueous ratios would help improve the accuracy of the numerical simulation method in describing chromatographic breakthrough. It might, however, be concluded that an ODE solver is not sufficient and the change in concentration with respect to both time and radial position in porous particles must be solved using a partial differential equation (PDE) solver. Once internal diffusion has been accurately described, the additional processes of aqueous phase diffusion and eddy dispersion can be better quantified.

As this mechanistic method is able to produce temporal data on the concentration of species within the solid and aqueous phases in all the axial divisions, complex loading and elution sequences involving multiple species, changes in flow rate or input matrix, volume or concentration can easily be simulated. This is an advantage of the numerical simulation method over simpler models of chromatographic breakthrough.

Chapter 6: Implementation of Numerical Simulation as a Radiochemical Tool for Routine Analysis and Method Development

Abstract

A numerical method for simulating the breakthrough profiles of discrete volumes of uranium or thorium in 8M HNO_3 from a bed of UTEVA resin has previously been developed using LabVIEW visual programming software. This method involves representing the chromatographic column as an array of solid and aqueous concentration values. The temporal change in concentration in each division is determined by the solution of two simultaneous differential equations. The aqueous concentration values progress according to the flow rate and column dimensions with the aqueous concentration in the bottom array position generating the column output. This chapter extends the application of the method to include simultaneous simulation of two analytes from varying loading volumes and at different loading concentrations. In addition, the effect of changing eluent has been explored. These developments indicate that the prediction of elution profiles from typical radiochemical separation sequences is possible. The mechanistic nature of the numerical simulation method is also shown to be superior to single equation models. Finally, the potential to develop the LabVIEW coding into user friendly software is discussed. Although access to the coding would be restricted, the database of kinetic data could be added to and the application of the software extended. This software will be a useful tool to radiochemists particularly in the development of new analytical methods using automated separation systems.

6.1. Introduction

The large workload of radioanalytical laboratories and the need to improve emergency preparedness have led to the development of rapid, semi-automated and automated chromatographic separation techniques. The introduction of new sorptive materials, advances in measurement instrumentation such as the ICP-QQQ that is capable of a much higher degree of online interferent filtering as well as the economic and environmental desire to reduce reagent use and waste volumes (both radioactive and not) have all led to previously established elution sequences are being reassessed and new sequences developed. Method development can be an extensive process even if experimental optimisation techniques are followed; this process is complicated if vacuum box or pump technology is available to vary the flow rate through the column. A software tool capable of simulating elution profiles under a range of flow rates, bed

dimensions, sample volumes and matrices would therefore be very useful in method development as well as optimising routine analysis to cover any sample type.

A numerical method for simulating the breakthrough profiles of inorganic species from chromatographic columns has previously been developed using LabVIEW visual programming software. This method built upon earlier work simulating the transfer between aqueous and solid phases in a closed batch system. The differential equations and kinetic rate constants determined for the three sorptive materials under these conditions were directly applied to a simulated flow-through column by considering the resin bed as a series of discrete vertically stacked sections. Analyte transfer between the solid and aqueous phases was simulated within each section to produce an array of solid and aqueous concentration values; this was followed by advancement of the aqueous phase values by one array position. This process was repeated in an iterative manner with the aqueous concentration value in the final array position generating the simulation of column output.

From comparison of the simulated profiles with experimental datasets, it was concluded that further investigations into internal mass transfer were needed before the numerical simulation method could be applied to porous materials. The potential complexity required and associated computational demand restricts the current use of this method for accurately describing and predicting chromatographic processes for these materials. Radiochemical extraction chromatographic resins such as UTEVA resin, however, consist of a solvent extractant immobilised on a solid support meaning that internal diffusion is not a rate determining step in the sorption/desorption process. This allows for the concentration in the solid particles to be represented by an average value and transfer of a single analyte between the aqueous and solid phases to be described by only two differential equations. At moderate flow rates, the numerical simulation method was shown to accurately describe breakthrough profiles for uranium and thorium in 8M HNO_3 from UTEVA resin without detailed knowledge of axial dispersion processes or the physical impacts of high fluid pressures.

The experimental data successfully simulated in the previous work related to the loading of a discrete volume (0.025 mL) of 8M HNO_3 containing low concentrations of uranium and thorium followed by washing with 8M HNO_3. This is not however, indicative of typical radioanalytical procedures where samples of various volumes and complex matrices are loaded onto the sorptive material and the analytes eluted separately using a sequence of different reagents. This chapter develops the numerical simulation method for UTEVA resin in a packed bed geometry to simulate multiple analytes simultaneously as well as accounting for the effect of concentration and loading volume. The numerical simulation method is compared to the Gaussian theoretical plate model

of chromatographic breakthrough as well as the Bohart-Adams model, demonstrating the limits that single equation models have in predicting breakthrough profiles. Finally, the potential to refine the coding to produce a software tool with a graphical user interface and an expandable database of rate constants for any extraction chromatography resin, dissolved species, sample matrix composition and eluting reagent is discussed. Guidance on determination of the necessary parameters is given, along with an example of a complex elution sequence.

6.2. Results and discussion

6.2.1. Simulating chromatographic breakthrough profiles of multiple analytes simultaneously

In Chapter 5, a numerical simulation method for the description of chromatographic breakthrough profiles was developed and successfully applied to uranium and thorium breakthrough from UTEVA resin in 8M HNO_3. This method was based upon axial division of the chromatographic column into equal length sections; each containing the lumped solid phase and the aqueous phase in a known ratio. Each section is thought of as a temporarily closed system, wherein species can transfer between the two phases for a set duration before the aqueous phase progresses onto the next section. This model of a packed bed of UTEVA resin was represented in LabVIEW visual programming language as a 2D array of solid $[s]$ and aqueous $[aq]$ concentration values. As the numerical simulation method only simulated the breakthrough of a single analyte at once, the size of the array was 2 x n (number of axial divisions). The temporal change in concentration for each array value was determined by the solution of two simultaneous differential equations (Equations 4.8. and 4.9. – reproduced below for clarity) using an *ODE solver VI*.

$$\frac{d[s]}{dt} = \vec{k}[aq] - \overleftarrow{k}[s] \qquad \text{Equation 4.8.}$$

$$\frac{d[aq]}{dt} = \left(\overleftarrow{k}[s] - \vec{k}[aq]\right) \times \left(\frac{V_s}{V_{aq}}\right) \qquad \text{Equation 4.9.}$$

The *model constants* for the *ODE solver* were the forward ($\vec{k}$) and reverse ($\overleftarrow{k}$) rate constants for the system being simulated and the volume fractions of the aqueous (V_{aq}) and solid (V_s) phases. The rate constants were determined from batch sorption/desorption data and are unique to the analyte, sorptive material and solution composition. The volume fractions for a packed bed of UTEVA resin were calculated from volumetric displacement measurements to be 0.655 for the aqueous phase and 0.345 for the lumped solid phase. The *input variables* were the array values which were initially set to zero. The *simulation parameters* include a final time value which is

equal to the duration of solution residence time in each axial division. After the ODE solver has run, the final time and concentration output values are extracted and processed; the aqueous concentration value in the bottom array position becomes the column output, all other aqueous concentration values are passed along one array position and a new concentration value is input into the top array position according to the solution being delivered to the top of the column. The amended array is passed through the *while loop shift register* to become the new input variable for the next iteration while the column output is displayed on an *XY-graph* and saved to file. The length of time simulated in each iteration is programmatically calculated (Equation 5.1. – reproduced below for clarity) from the effective cross sectional area, the flow rate in mL/min (u) and the length of each axial division (L_{ax}). For the experiments simulated in the previous chapter and the current study, the same batch of columns with an assumed average internal radius (r) of 0.35 cm was used.

$$duration\ (s) = \frac{V_{aq} \times \pi \times r^2 \times 60 \times L_{ax}}{u} \qquad \text{Equation 5.1.}$$

The axial division length relates to eddy dispersion within the column and can be calculated by subtracting the effects of molecular diffusion in the aqueous phase at slow flow rates. Not enough experimental data for breakthrough profiles from UTEVA resin using slow flow rates has been gathered to separate these two axial dispersion processes. An estimated axial division length of 0.1 cm was therefore used in the numerical simulation method along with no inclusion of aqueous phase diffusion. This simplified model of chromatographic breakthrough was able to describe experimental data using a flow rate of ~2 mL/min. The accuracy of the method was, however, sensitive to input parameters, particularly the distribution constant of the batch of resin used. At faster flow rates, additional physical complications were observed including a gradual build-up of flow rate at the start of the experiment due to backpressure and possible elevated leaching of the solvent extractant.

It is hypothesised that the numerical simulation method for describing the chromatographic breakthrough of single analytes detailed above was able to accurately simulate breakthrough profiles of uranium and thorium from a discrete volume of 8M HNO_3 containing a mixture of both analytes without accounting for competition between the analytes due to the small volume (0.025 mL) and low analyte concentration (~25 ppm for each species) of the loading solution. This hypothesis is based on experimental data collected from batch sorption of uranium and thorium from 8M HNO_3 onto UTEVA resin at a range of initial aqueous concentrations. This data helped

develop a modified numerical simulation method for the simultaneous transfer of both species in the closed batch system.

The concentration of complexant molecules and their stoichiometric relationship with the analytes was determined from isotherm experiments measuring the change in sorption of a single analyte with concentration. The results suggested an extractant concentration of 1.5 mol/dm^3, a stoichiometric reaction of uranyl nitrate with the extractant of 1:2 (Equation 4.21. – reproduced below for clarity) and a 1:4 stoichiometric reaction for thorium nitrate (Equation 4.22. – reproduced below for clarity); this corresponds to one extractant molecule per nitrate ligand. The proposed reaction mechanisms are assumed to be single step reactions with no intermediate products meaning that the rate order with respect to the extractant is 2 in the case of uranium sorption and 4 in the case of thorium sorption.

$$UO_2(NO_3)_2 + 2E \leftrightarrow UO_2(NO_3)_2E_2 \qquad \text{Equation 4.21.}$$

$$Th(NO_3)_4 + 4E \leftrightarrow Th(NO_3)_4E_4 \qquad \text{Equation 4.22.}$$

The numerical simulation method for single analyte sorption/desorption under batch conditions was therefore modified to include both species and their relationship with the extractant. This involved an expansion from two differential equations to four (Equations 4.23.-4.26.). In these equations, the temporal change in analyte concentration in the solid phase ($\frac{d[s]_i}{dt}$) is equal to the forward rate constant ($\vec{k}_i$) multiplied by the analyte concentration in the aqueous phase ($[aq]_i$) as well as the concentration of available extractant sites (taking into account the respective rate order) minus the reverse rate constant ($\overleftarrow{k}_i$) multiplied by the analyte concentration in the solid phase ($[s]_i$). The temporal change in analyte concentration in the aqueous phase ($\frac{d[aq]_i}{dt}$) is equal to $-\frac{d[s]_i}{dt}$ multiplied by the ratio of the volume fractions of the aqueous (V_{aq}) and solid (V_s) phases. The concentration of available extractant sites includes a lumped solid extractant concentration model constant ($[s]_E$).

$$\frac{d[s]_U}{dt} = \vec{k}_U[aq]_U([s]_E - 4[s]_{Th} - 2[s]_U)^2 - \overleftarrow{k}_U[s]_U \qquad \text{Equation 4.23.}$$

$$\frac{d[aq]_U}{dt} = \left[\overleftarrow{k}_U[s]_U - \vec{k}_U[aq]_U([s]_E - 4[s]_{Th} - 2[s]_U)^2\right] \times \left(\frac{V_s}{V_{aq}}\right) \qquad \text{Equation 4.24.}$$

$$\frac{d[s]_{Th}}{dt} = \vec{k}_{Th}[aq]_{Th}([s]_E - 4[s]_{Th} - 2[s]_U)^4 - \overleftarrow{k}_{Th}[s]_{Th} \qquad \text{Equation 4.25.}$$

$$\frac{d[aq]_{Th}}{dt} = \left[\overleftarrow{k}_{Th}[s]_{Th} - \vec{k}_{Th}[aq]_{Th}([s]_E - 4[s]_{Th} - 2[s]_U)^4\right] \times \left(\frac{V_s}{V_{aq}}\right) \qquad \text{Equation 4.26.}$$

For the numerical simulation of multiple analytes method, the reverse rate constants for uranium/thorium and initial aqueous/solid concentration input variables were set to the same values as those used for single analyte simulation whereas the forward rate constants were corrected to account for $[s]_E$. The multiple analyte numerical simulation method was able to accurately describe the reduction in equilibrium position due to an increase in initial aqueous concentration for sets of experimental isotherm data for uranium and thorium (single analyte 8M HNO_3 solutions). This supported the proposed stoichiometric relationships with the extractant (Equations 4.21. and 4.22.). When the initial aqueous concentrations of both analytes were low (<300 ppb), both the single and multiple analyte numerical simulation methods generated accurate descriptions of the batch experimental kinetic datasets. For sorption from an 8M HNO_3 solution containing a high concentration of uranium (470 ppm) and a low concentration of thorium (240 ppb), the multiple analyte method was also able to accurately describe the change in kinetics and equilibrium position for both analytes (in comparison to the low concentration conditions). This supported the competitive relationship between uranium and thorium described in the differential equations (Equations 4.23.-4.26.).

Modification of the numerical simulation method for chromatographic breakthrough to include the combined uranium and thorium differential equations is also possible. This is expected to have an impact on the shape and peak position of the breakthrough profiles generated when the loading concentration of one or both of the analytes is high.

6.2.1.1. Comparison of multiple analyte numerical simulation method with experimental data

The LabVIEW coding for simulation of breakthrough profiles was therefore modified in order to accommodate the four differential equations including both species (Equations 4.23.-4.26.); the input variable array was increased in size to 4 x n, two separate analyte loading concentrations were included, the forward rate constants were amended and the lumped solid extractant concentration model constant determined from the batch sorption/desorption experimental data was also included. This improved numerical simulation method generated temporal column output data for both uranium and thorium simultaneously.

The single analyte and multiple analyte numerical simulation methods were compared to experimental datasets for the breakthrough of mixed solutions of uranium and thorium in 8M

HNO_3 from UTEVA resin at a range of loading volumes and loading concentrations (Table 6.1.). The experimental conditions of bed length (~2 cm) and flow rate (~2 mL/min) were kept to approximately the same as those that were known to produce breakthrough profiles that could be simulated without inclusion of aqueous phase diffusion or gradual build-up of flow rate. In each of these experiments, after the loading solution had been totally delivered to the top of the column, the feedstock was switched to an 8M HNO_3 wash solution.

For experiments with either a low loading concentration of both analytes or a small loading volume (Experiments 21-24), both numerical simulation methods showed accurate descriptions of the position of the breakthrough peak of both species (indicated by the closeness of the slope of experimental against simulated datasets to 1) and the shape of the profiles (indicated by the R^2 value). The slight differences in goodness of fit between the two methods could be due to the precision of forward rate constants without inclusion of a lumped solid extractant concentration model constant and the corrected forward rate constants; both were given to 4 significant figures so some differences in kinetics due to rounding may have been present. Alternatively, the slight difference may be due to the loading concentrations approaching values where a change in breakthrough profile between the single and multiple analyte methods is observed. For the experiment with a higher loading concentration of uranium and a moderately large loading volume (Experiment 25), the single analyte method failed to describe either the shape or peak position of the experimental breakthrough profiles for both uranium and thorium. The multiple analyte method, on the other hand, generated breakthrough profiles with a much better fit to the experimental data.

A change in the shape of the breakthrough profiles (both experimental and simulated) can be seen when comparing small loading volumes of 0.025 mL (Experiment 21) and 1.004 mL (Experiment 22) to a large loading volume of 258.59 mL (Experiment 23) whilst keeping the concentrations of both analytes low (Figure 6.1.).

Table 6.1.

Linear regression analysis for comparison of experimental data to simulated breakthrough profiles using either the single analyte or multiple analyte numerical simulation method.

Experimental data (x-axis) is plotted against simulated data (y-axis) to generate R^2 and slope values.

Both numerical simulation methods use rate constants calculated from batch sorption/desorption experimental data. For the single analyte simulation of uranium and thorium breakthrough profiles, a lumped solid extractant concentration model constant is not included. For the multiple analyte simulation of uranium and thorium breakthrough profiles, a lumped solid extractant concentration model constant is included along with stoichiometric relationships with the extractant of 1:2 for uranyl nitrate and 1:4 for thorium nitrate.

In addition to the variable input parameters listed for each experiment, values of column radius = 0.35 cm and V_{aq} = 0.655 are assumed. The axial division length is set to 0.1 cm except for experiments 22 and 24 where it is 1.95/20 cm. Aqueous phase diffusion has not been included in the simulations.

Experiment	Bed length (cm)	Flow rate (mL/min)	Loading volume (mL)	Analyte	Loading concentration (ppm)	Total amount loaded (mg)	Single analyte		Multiple analyte	
							Slope	R^2	Slope	R^2
21*	2	1.89	0.025	Uranium	25.3	7.90×10^{-4}	0.9791	0.9985	0.9791	0.9985
				Thorium	25.7	8.04×10^{-4}	1.1003	0.9782	1.1004	0.9778
22	1.95	1.59	1.004	Uranium	25.0	3.14×10^{-2}	0.9563	0.9897	0.9600	0.9936
				Thorium	25.2	3.17×10^{-2}	0.9515	0.9454	0.9603	0.9644
23	2	1.82	258.59	Uranium	0.0963	3.11×10^{-2}	0.9569	0.9892	0.9573	0.9899
				Thorium	0.0970	3.14×10^{-2}	0.9369	0.9681	0.9386	0.9713
24	1.95	1.56	0.025	Uranium	514	1.61×10^{-2}	1.0410	0.9920	1.0413	0.9914
				Thorium	25.2	7.89×10^{-4}	1.0105	0.9969	1.0120	0.9963
25	2.1	1.86	24.64	Uranium	479	14.7	0.1466	-0.5164	0.9380	0.9568
				Thorium	28.9	0.890	0.0178	-0.8942	0.8016	0.8822

*The experimental data for experiment 21 is equivalent to experiment 4 (Table 5.1.).

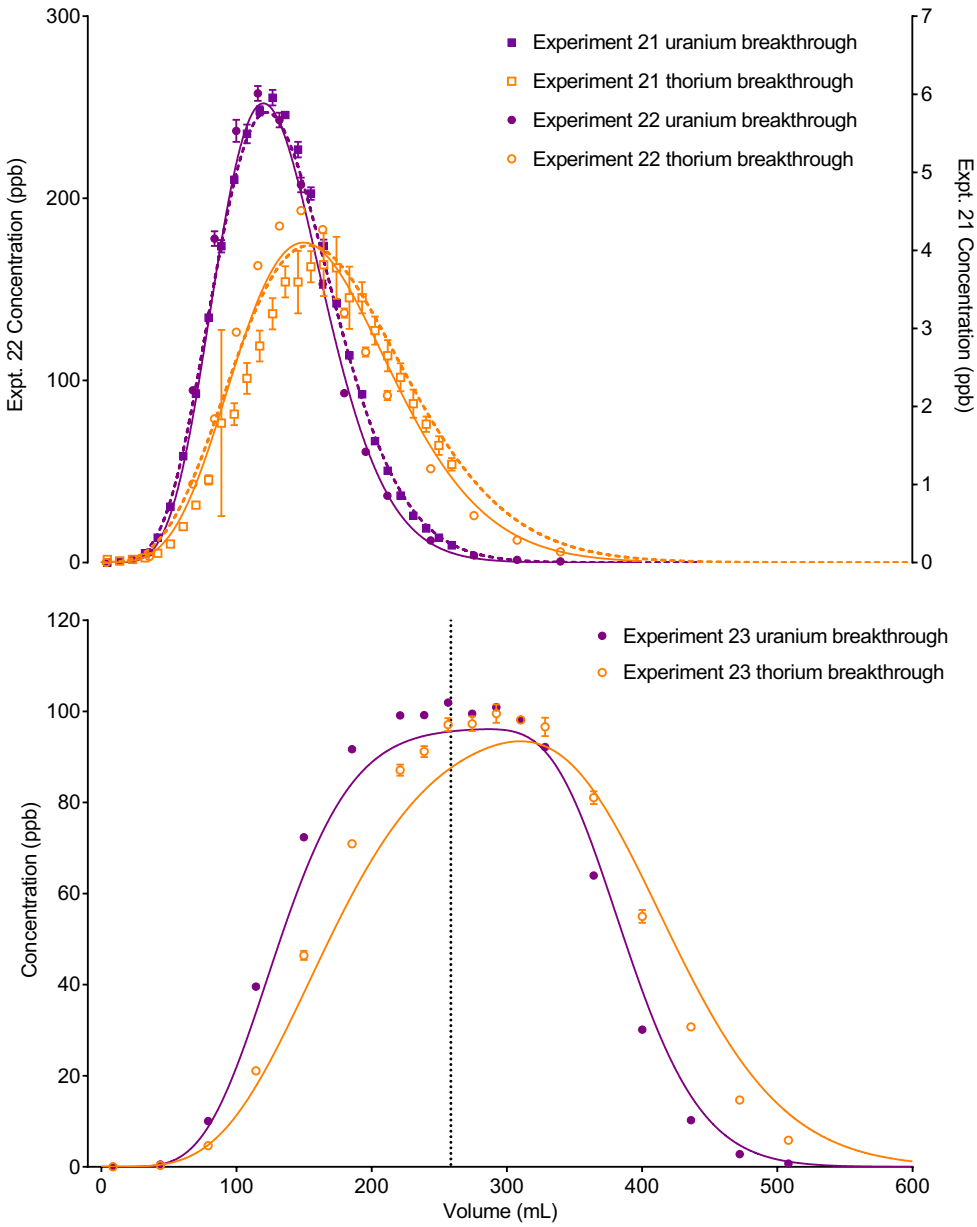

Figure 6.1.
Comparison between experimental data and multiple analyte numerical simulation of uranium and thorium breakthrough profiles from UTEVA resin in 8M HNO_3 under low concentration conditions whilst varying the loading volume.
The top plot shows experimental conditions corresponding to experiments 21 and 22 (Table 6.1.). Experiment 21 (square points, dashed line) is plotted on the right hand axis and experiment 22 (circular points, solid line) is plotted on the left hand axis.
The lower plot shows experimental conditions corresponding to experiment 23 (Table 6.1.). The vertical dotted line shows the volume at which the column input was switched from the loading solution to the wash solution.

The increase in loading volume from 0.025 mL to 1.004 mL caused an increase in the height of the breakthrough profiles but not a significant change in the position or shape of the peak. The slight

differences in the position and width of the simulated breakthrough peaks are due to the small differences in bed length, flow rate and loading concentrations between the two experiments. At the large loading volume of 258.59 mL, however, the concentration of both uranium and thorium in the column outlet fractions keeps rising beyond the peak position seen for the smaller loading volumes. The breakthrough profiles for both species are wider and more asymmetrical with the peak for uranium showing a plateau in concentration. These shapes are depicted in the experimental and numerically simulated datasets although the simulated profiles are shifted to slightly later positions. This could be due to errors in the assumed distribution constant due to the properties of the batch of resin used in this experiment. As all three experiments use different bed lengths, flow rates and loading concentrations a direct analysis of the effect of loading volume on the shape of the breakthrough profile cannot be made. A set of simulations where these parameters have been constrained and only the loading volume varied has, however, been carried out and will be discussed in the context of comparison of the numerical simulation method with single equation models.

An increase in the concentration of uranium in the loading solution of approximately 20 fold did not significantly change the position or shape of the experimental breakthrough profiles for either uranium or thorium when the loading volume was small (0.025 mL, Experiments 21 and 24). Again, the slight differences in the position and width of the simulated breakthrough peaks are due to the small differences in bed length, flow rate and loading concentrations between the two experiments. Using a much larger loading volume of 24.64 mL (Experiment 25), however, this elevated uranium concentration did have an impact on the peak position and shape of the breakthrough profiles for the experimental datasets for both analytes (Figure 6.2.). The peak positions are earlier than would be expected if no relationship between concentration and sorption kinetics was considered; i.e. the single analyte numerical simulation method. In addition, the experimental datasets for both species are more asymmetrical than the single analyte simulations with a longer tailing slope and a shorter leading slope. These observations indicate that concentration of complexant molecules in the extractant is a limiting factor under these experimental conditions and provides evidence for the competing relationship between the two analytes as described in the differential equations (Equations 4.23.-4.26.). The peak positions and shapes of the breakthrough profiles are accurately described using the multiple analyte numerical simulation method. The slightly lower height of the simulated thorium peak in comparison to the experimental data could be due to uncertainty in the thorium loading concentration or variation in distribution constants between different batches of resin.

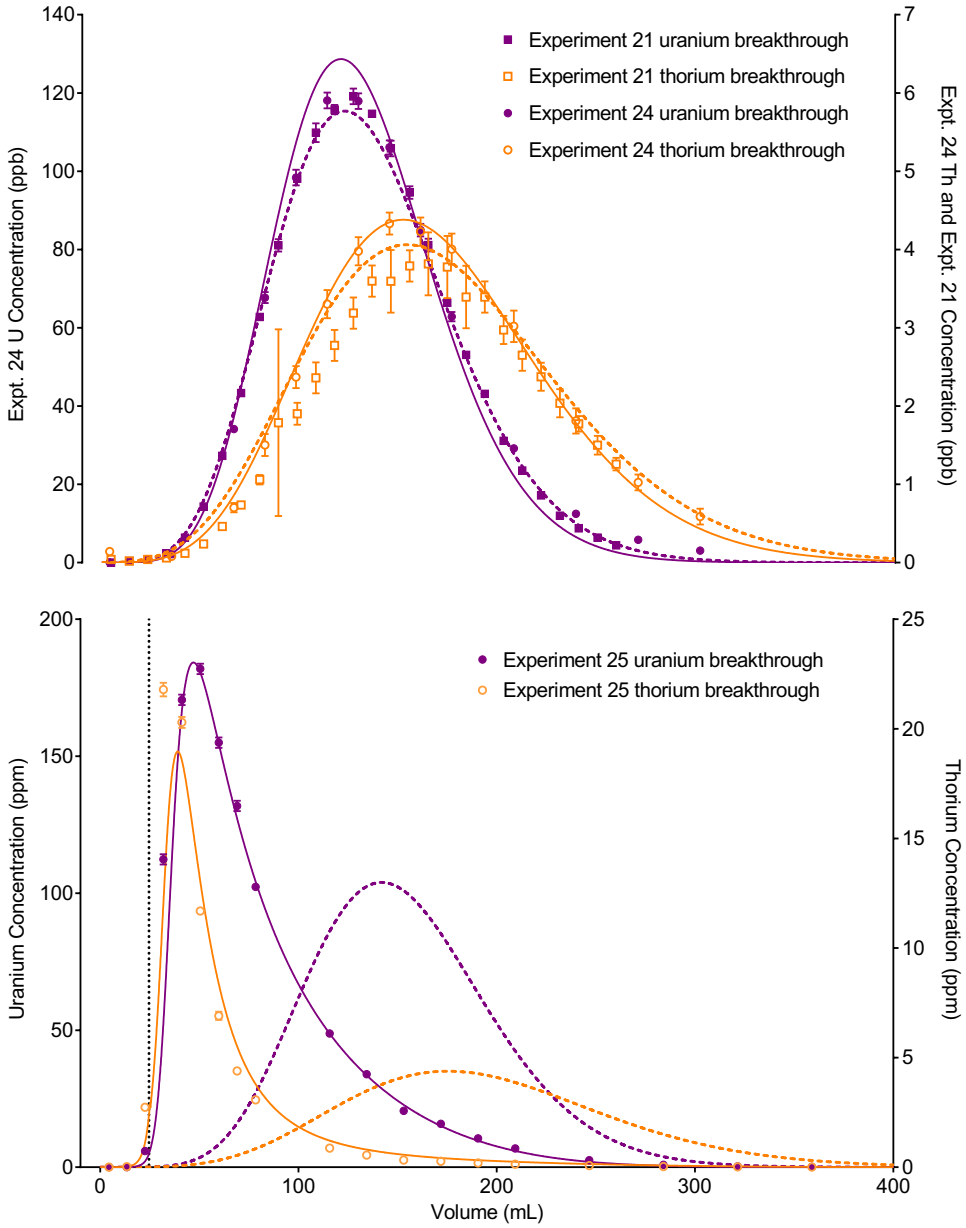

Figure 6.2.
Comparison between experimental data and multiple analyte numerical simulation of uranium and thorium breakthrough profiles from UTEVA resin in 8M HNO_3 under conditions varying both the loading concentration and volume.
The top plot shows experimental conditions corresponding to experiments 21 and 24 (Table 6.1.). Experiment 21 (square points, dashed line) and experiment 24 thorium concentration (open circular points, solid line) are plotted on the right hand axis and experiment 24 uranium concentration (closed circular points, solid line) is plotted on the left hand axis. Only simulated data using the multiple analyte method is shown on this plot.
The lower plot shows experimental conditions corresponding to experiment 25 (Table 6.1.). The vertical dotted line shows the volume at which the column input was switched from the loading solution to the wash solution. Both sets of simulated data from the single analyte method (dashed lines) and multiple analyte method (solid lines) are shown on this plot.

From the experimental breakthrough data generated by varying the loading concentration and volume, qualitative relationships have been proposed (Table 6.2.). At sufficiently slow flow rates and low loading concentration, equilibrium is obtained down the whole length of the column. The breakthrough profile is Gaussian for discrete loading volumes and increases to a plateau for continuous loading. Under these conditions, the total amount of analyte loaded is not a useful parameter in predicting the shape of the breakthrough profile.

If the loading concentration is high enough for concentration of sorption sites to become a rate limiting factor, the position of equilibrium shifts and the k_D value is reduced. If the loading volume is small in relation to the length of the column, the reduced k_D value only applies to the top of the column where the elevated concentration is introduced and equilibrium is quickly re-established throughout the column. Under these conditions, the total amount of analyte loaded as a percentage of the total capacity of the column may be a useful measure to predict the extent of peak position shift and distortion away from a Gaussian shaped peak. A concentration of uranium of ~500 ppm was previously shown to cause a significant (50 %) reduction in k_D (Figure 4.13.) whilst complete saturation of the solid material was only observed for uranium concentrations above 2,500 ppm (0.25 %).

Two of the column experiments conducted (Experiments 24 and 25) could therefore be considered to have a moderate loading concentration of uranium. For a small loading volume (0.025 mL, Experiment 24), the total amount of uranium loaded (1.61×10^{-2} mg) is significantly below the amount required to saturate a 2 cm long column. The total column capacity has been calculated to be 28.5 mg of uranium if using the reference capacity (37 mg/mL bed) from the original UTEVA resin characterisation data by Horwitz et al[70] or 47.3 mg if using the lumped solid extractant concentration model constant ($[s]_E$) of 1.5 mol/dm^3. For the moderate loading volume (24.64 mL, Experiment 25), however, the total amount of uranium loaded is 14.7 mg. Whilst this is below either estimation of the total column capacity, it is above the recommended loading amount of 20 % total capacity.

Table 6.2.
Qualitative description of the effect of loading concentration and volume on the position and shape of breakthrough peaks for a column operated under a slow flow rate.

Loading concentration	Ratio of loading volume to column length	Column saturated or equilibrated?	Position of peak breakthrough	Symmetry of breakthrough profile
Low (within linear part of sorption isotherm)	Small	Equilibrated: k_D applies down whole length of column	Constant value	Gaussian shaped
	Moderate		Increased	Gaussian shaped
	Large		Plateau rather than peak	Symmetrical with plateau
Moderate (above linear part of sorption isotherm but below maximum sorption capacity)	Small	Reduced k_D at top of column, equilibrium re-established by bottom of column	Insignificant effect on peak shape	
	Moderate	Reduced k_D down whole length of column	Reduced	Higher degree of asymmetry
High (above maximum sorption capacity)	Very small	Saturation at top of column, equilibrium re-established by bottom of column	Insignificant effect on peak shape	
	Small	Saturation at top of column, reduced kD at bottom of column	Reduced	Higher degree of asymmetry
	Moderate	Saturation down whole length of column	Immediate breakthrough	Highly asymmetrical

Another factor that can cause deviation from equilibrium conditions is flow rate. If solution is flowing through the column sufficiently fast that equilibrium is not obtained, k_D is reduced down the whole length of the column and experiments with low loading concentrations (within the linear part of the sorption isotherm) can exhibit non-Gaussian breakthrough profiles. As all of these column parameters (loading concentration, loading volume, column length and flow rate) can affect the position and shape of the breakthrough profiles, a large amount of experiments would need to be conducted to assess the values at which each parameter becomes a significant contributor. This assessment is more easily achieved using a numerical simulation method based on robust knowledge of sorption kinetics. This will be carried out in the context of comparison with single equation models.

6.2.1.2. Comparison of multiple analyte numerical simulation method with the Gaussian model

Numerical simulation methods for the description of chromatographic breakthrough profiles use a computational tool (the *ODE solver*) to solve an array of ordinary differential equations via a numerical method based on iterative comparison and readjustment of values until the equations

are met to a specified level of accuracy. Under certain conditions, the differential equations can also be solved algebraically. This can only be achieved if a number of simplifications and assumptions are applied.

The lumped kinetic model of chromatography operates under the assumption that transfer of species between the aqueous and lumped solid phases can be modelled using a linear driving force (LDF) approximation[39,42,43,47]. This approximation models the contribution of mass transfer processes (film diffusion and/or intraparticle diffusion) to sorptive kinetics as a first-order rate equation. The driving force is for the concentration gradient between two neighbouring regions to be zero; i.e. to achieve local equilibrium. Although following a less mechanistic approach to modelling sorptive processes, equations based on the LDF approximation have been shown to generate comparable breakthrough profiles to more complex equations based on the Fick model of diffusion[64]. The algebraic solution of the lumped kinetic model using the assumptions of a linear sorption isotherm, an infinitely narrow rectangular pulse injection and sufficiently high column efficiency, allows the concentration profile of a chromatographic column output to be described using a single equation[39]. As this equation generates symmetrical breakthrough profiles with a Gaussian distribution, it can be referred to as the Gaussian model. Although often used to plot output concentration as a function of time, the equation for plotting output concentration as a function of volume ($C_{out,V}$) has been provided (Equation 6.1.) for consistency with the previous plots of simulated and experimental breakthrough profiles (Figures 6.1. and 6.2.). The analyte concentration (C_{in}) and volume (V_{in}) of the loading solution are input into the Gaussian model equation along with the calculated retention volume (V_R) for the analyte of interest and the standard deviation (σ)[47].

$$C_{out,V} = C_{in}V_{in}f(V) = \frac{C_{in}V_{in}}{\sigma\sqrt{2\pi}}e^{-\left(\frac{V-V_R}{\sigma\sqrt{2}}\right)^2} \qquad \text{Equation 6.1.}$$

The retention volume is equal to the volume at which the peak of the breakthrough profile is observed whilst the value of the standard deviation dictates the width of the symmetrically shaped profile; the peak width at half the maximum concentration is equal to 2.355σ (Figure 6.3.). The standard deviation value is calculated from the retention volume and a kinetic term, N (Equation 6.2.) whereas the retention volume is calculated from the volume of the mobile phase (v_m) and a thermodynamic term, k' (Equation 6.3.)[26,35].

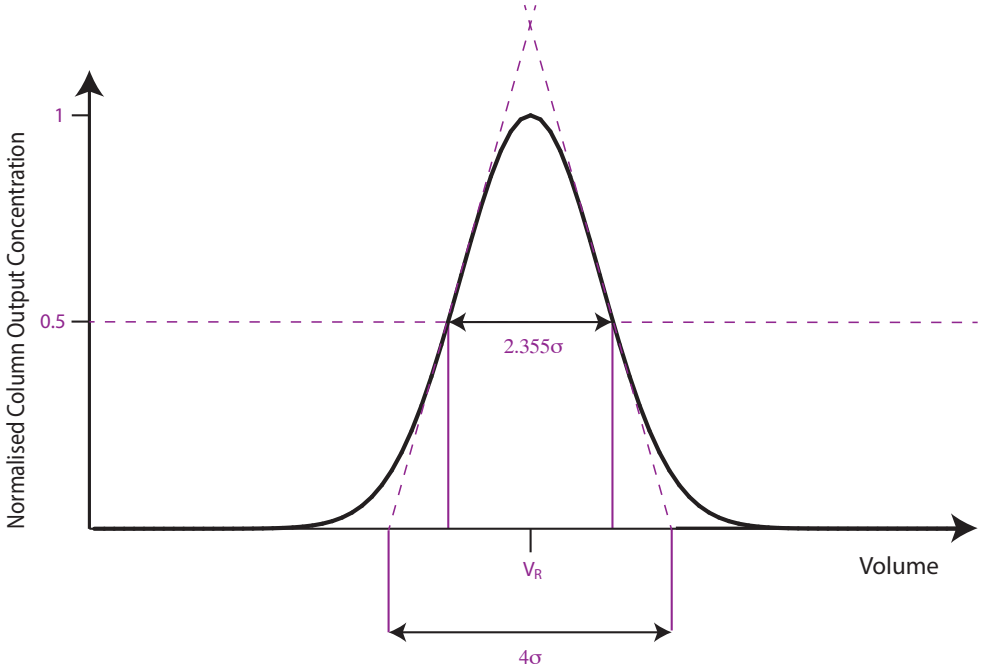

Figure 6.3. (Reproduction of Figure 1.2.)
Diagram depicting the Gaussian distribution.

$$\sigma = \frac{V_R}{\sqrt{N}} \qquad \text{Equation 6.2.}$$

$$V_R = v_m(1 + k') \qquad \text{Equation 6.3.}$$

In relation to the input parameters used in the numerical simulation method, the volume of the mobile phase is the volume fraction of the aqueous phase (V_{aq}) multiplied by the total bed volume. It is therefore a measure of the total volume of the aqueous phase in volumetric units (mL). The thermodynamic term, k' is known as the retention factor (or number of free column volumes to peak maximum[19,20]) and is a measure of the partitioning of analyte between the mobile and stationary phases at equilibrium. The retention factor can be calculated from analyte uptake experiments conducted under batch conditions. These thermodynamic batch experiments involve contacting a known mass of sorptive material in grams (W_s) with a known volume of solution in mL (V_{aq}) containing a known initial concentration of analyte ($[aq]_0$). The closed system is left to reach equilibrium and the concentration remaining in the aqueous phase ($[aq]_{eq}$) is determined. This value, along with the experimental conditions can be used to calculate (Equation 6.4.) the distribution constant (k_D) for the analyte-sorptive material system

investigated. The distribution constant is a measure of uptake per gram of sorptive material and can be converted to the retention factor (k') by knowledge of the ratio of solid material (g) to mobile phase volume (mL) in the packed bed (Equation 6.5.). The packing density of a column is related to the composition of the sorptive material and the packing method (e.g. dry or slurry packing).

$$k_D = \frac{([aq]_0 - [aq]_{eq}) \times V_{aq}}{[aq]_{eq} \times W_s} \qquad \text{Equation 6.4.}$$

$$k' = k_D \left(\frac{W_s}{v_m}\right) \qquad \text{Equation 6.5.}$$

The kinetic term, N is the number of theoretical plates in the column. A theoretical plate is a vertical column division within which equilibrium between the aqueous and solid phases is reached. The height equivalent of a theoretical plate (HETP) is calculated from the column length divided by the number of theoretical plates (Equation 6.6.).

$$HETP = L/N \qquad \text{Equation 6.6.}$$

Quantification of HETP is a common method for evaluating the efficiency of a column and optimising the operating conditions. A more efficient column has a higher number of theoretical plates which leads to narrower analyte/interferent breakthrough peaks and better separation between them. Both the kinetics of sorption/desorption and axial dispersion contribute to HETP with sorptive processes dominating at faster flow rates and molecular diffusion becoming the controlling factor at slower flow rates. HETP values can be calculated from the width of breakthrough profiles (using Equations 6.2. and 6.3.). This method has been used to compare the efficiency of Ln resin in terms of particle size, HDEHP loading, flow rate, temperature, packing method, column diameter and bed length[19,20]. Like UTEVA resin, Ln resin is an extraction chromatographic resin developed by Eichrom (distributed in Europe by TrisKem). In addition, a large amount of the literature[20,28,70–72,74] related to characterisation of this range of sorptive materials describes analyte sorption using k'. This indicates that breakthrough profiles from chromatographic columns using extraction chromatographic resins could be described using the Gaussian model[26]. Direct application of the Gaussian model to describe a chromatographic system for determination of radionuclides has also been made[31]. The system investigated used a composite column of anion exchange resin and plastic scintillating beads for on-column detection of Tc-99. The equilibrium-based preconcentrating technique used continuous sample loading

until the concentration at the column output becomes equal to that being loaded; at this point the system has reached equilibrium and the on-column activity is now constant. Under the continuous loading condition, the breakthrough profile can be described by the integral of the Gaussian distribution. This continuous loading Gaussian model was shown to provide a good fit to the experimental data for the longer length column tested (2.9 cm) but not for a shorter column (0.6 cm). It was concluded that an alternative low plate number model was needed if there were less than (or equal to) 5 theoretical plates.

Another single equation model for describing the breakthrough profile from a continuous loading experiment is the Bohart-Adams model. This model is often applied to organic sorptive materials such as activated carbon and operates under the assumptions of a (highly favourable) rectangular sorption isotherm, a quasi-chemical rate equation and negligible axial dispersion[46]. The assumption of a rectangular isotherm means that the time/volume of breakthrough is directly correlated to the loading concentration. Generally, a rectangular isotherm can only be applied to very high analyte concentrations, limiting the applicability of the Bohart-Adams model. It has, however, been suggested that the constant value for analyte concentration on the solid phase at equilibrium can be substituted for an equation describing sorption using the more realistic Langmuir isotherm[46]. This correction could extend the application to a larger concentration range. A further modification of the Bohart-Adams model to enable description of discrete loading experiments may also be possible (see Section 6.2.1.3.). Whilst the Bohart-Adams model is not commonly used to describe discrete volume breakthrough profiles under low loading concentrations so may not be applicable to radioanalytical procedures, it will also be included in the following discussion.

An assessment of the ability of the Gaussian model to describe radioanalytical chromatographic breakthrough profiles can be made by comparison with the developed multiple analyte numerical simulation method. Narrow and highly symmetrical peaks are often seen in high performance liquid chromatography (HPLC)[35]. HPLC columns use small particle sizes (2-20 μm) in order to maximise column efficiency. This means that a relatively short column (10 cm) can be capable of achieving plate numbers in excess of 5000 and the assumption of all peaks fitting a Gaussian distribution is valid. The typical particle size used for radioanalytical separations is significantly larger than for HPLC columns. For example, the UTEVA resin particle size used in this investigation had a distribution of 100-150 μm. A simulated column length of 20 cm was chosen to fit the Gaussian model parameters as it was hoped this would generate sufficiently symmetrical breakthrough profiles without an excessively long simulation time. The multiple analyte simulation method was operated as previously described using the forward and reverse rate

constants determined for uranium and thorium transfer between 8M HNO_3 and UTEVA resin as well as the lumped solid extractant concentration value and solid and aqueous volume fractions for UTEVA resin. The axial division length was set to 0.1 cm and aqueous phase diffusion was included using estimated aqueous diffusion rate constants corresponding to the quoted diffusion coefficients of 0.426 x 10^{-5} cm^2/s for $^1/_2UO_2^{2+}$ and 0.620 x 10^{-5} cm^2/s for $^1/_3Ce^{3+}$ (as a proxy for Th^{4+}) in water at 25°C[55]. No correction for tortuosity has been applied. A small loading volume (0.1 mL) containing a low concentration of uranium and thorium (1 x 10^{-8} mol/L; ~2 ppb of each analyte) was employed along with a moderate flow rate (2 mL/min) and the previously used column radius (0.35 cm).

The retention volume (V_R) and standard deviation (σ) terms in the Gaussian equation for plotting output concentration as a function of volume (Equation 6.1) were calculated for uranium and thorium using the simulated datasets corresponding to a 20 cm length column (Figure 6.4.). The V_R values were taken from the volume at which the column output concentration of the simulated datasets reaches a maximum; these values were 1333.2 mL and 1714.3 mL for uranium and thorium respectively. The retention factor (k') for each analyte can then be calculated using the volume of the mobile phase (Equation 6.3.). For uranium, k' was therefore determined to be 263 whereas a value of 339 was calculated for thorium. These values are of a similar order of magnitude to the values quoted in the literature[70] but in a different order regarding the affinity of UTEVA resin for the two analytes in 8M HNO_3 (quoted k' for U(VI) in 8 M HNO_3 ~300; quoted k' for Th(IV) in 8 M HNO_3 ~200; assuming $k_D/k' = 1.7$). Using the distribution constants previously measured under batch conditions and the packing and solid material densities calculated via volumetric and gravimetric displacement measurements (Chapter 4), predicted retention factors are much closer to those determined using the Gaussian model analysis (calculated k' for U(VI) in 8M HNO_3 = 266; calculated k' for Th(IV) in 8M HNO_3 = 343; assuming $k_D/k' = 1.726$).

The width of the simulated peak at half the maximum concentration was divided by 2.355 to calculate σ for each analyte and hence the number of theoretical plates (Equation 6.2.). Under the stated conditions, the breakthrough of uranium from the 20 cm column was calculated to have an efficiency corresponding to 84 theoretical plates whereas the thorium breakthrough profile corresponded to 66 plates. Whilst these plate numbers are over an order of magnitude lower than those seen in HPLC columns, they are not so low that the Gaussian model would fail to accurately predict column parameters as observed by Egorov et al. in the case of short columns ($N \leq 5$)[31]. The measured plate numbers can further be used to calculate the height equivalent of a theoretical plate (HETP) for each analyte (Equation 6.6.). These values were determined to be 0.24 cm for uranium and 0.31 cm for thorium.

a

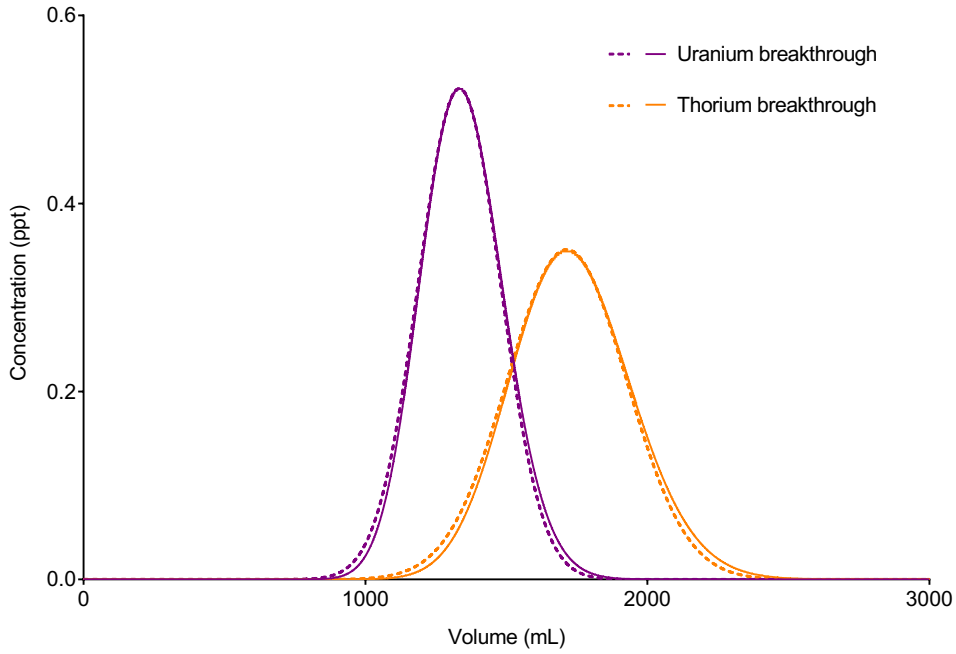

b

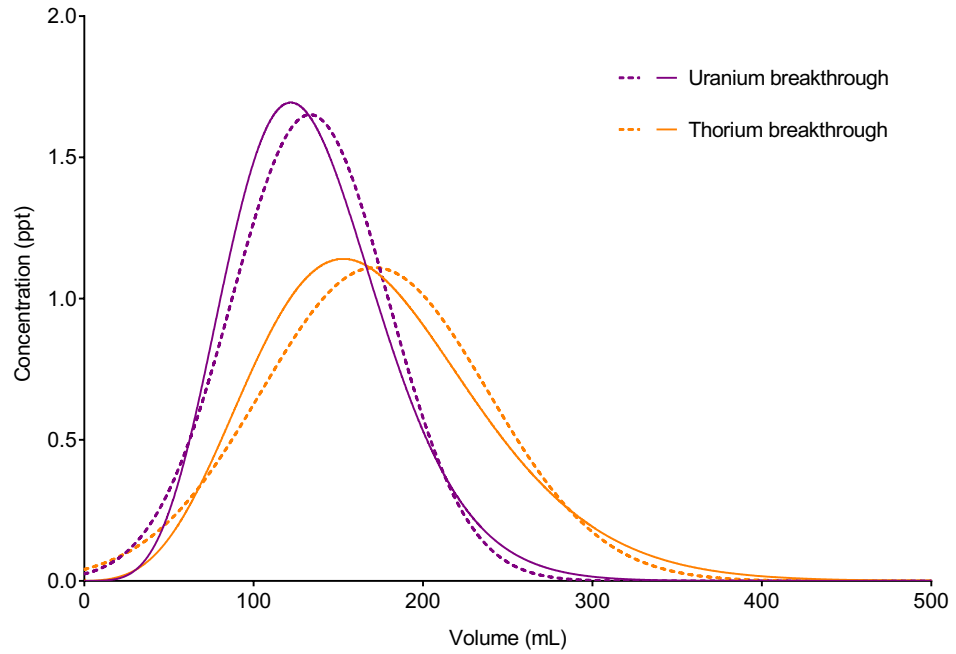

Figure 6.4.
Comparison between the Gaussian model and multiple analyte numerical simulation of breakthrough profiles for different bed lengths.
Both the Gaussian model (dashed lines) and numerical simulation method (solid lines) use the following common parameters: loading volume = 0.1 mL; loading concentration of uranium and thorium = 1 x 10^{-8} mol/L (~2 ppb); flow rate = 2 mL/min; column radius = 0.35 cm; V_{aq} = 0.655.
The multiple analyte numerical simulation method uses rate constants calculated from batch sorption/desorption experimental data. An axial division length of 0.1 cm was input along with estimated aqueous phase diffusion rate constants. A lumped solid extractant concentration model constant and stoichiometric relationships with the extractant of 1:2 for uranyl nitrate and 1:4 for thorium nitrate are also included.
The Gaussian model parameters of k' and HETP for each analyte have been calculated from the simulated datasets for a 20 cm length column (a) and applied to a 2 cm length column (b).

The retention factors and HETP values for each analyte as determined from the simulated data for a 20 cm length column can be used to generate a Gaussian model prediction of breakthrough curves from any length column. By keeping all other column operating parameters (loading volume, analyte concentration, flow rate and column radius) constant, a change in bed length would have an impact on plate number (N) and retention volume (V_R) via a linear relationship (Equations 6.3. and 6.6.). For example, the Gaussian model predicts the uranium breakthrough profile from a 2 cm length column to have a concentration maximum at 133.3 mL and 8.4 theoretical plates. Comparison of the Gaussian model prediction to breakthrough curves generated using the numerical simulation method for a 2 cm length column (other input parameters same as for 20 cm column simulation), however, indicates that the Gaussian model overestimates the volume at which the breakthrough maximum occurs (Figure 6.4.). Applying the Gaussian model analysis to the simulated uranium breakthrough profile for the 2 cm column gives a V_R value of 121.9 and a plate number of 7.4 (using the width of the simulated peak at half the maximum concentration). A similar discrepancy between the predicted profile characteristics using the single equation Gaussian model and the numerical simulation method is seen for the breakthrough of thorium.

The discrepancy between the Gaussian model predictions and the simulated datasets is due to simulated breakthrough profiles from shorter column lengths exhibiting shapes that correlate less with the Gaussian distribution. The extent of deviation from the Gaussian distribution can be quantified by calculating an asymmetry factor. This factor is determined by dividing the width (in mL) from the centre of the peak to the tailing edge by the width from the centre of the peak to the leading edge at 10 % of the maximum concentration[47]. As the Gaussian distribution is perfectly symmetrical, profiles exhibiting Gaussian shaped breakthrough/elution peaks would have an asymmetry factor of 1. Asymmetry factors >1 are indicative of tailing, whilst factors <1 indicate fronting peaks.

The simulated breakthrough profiles for the 2 cm length column were significantly more asymmetrical than those for the 20 cm length column with asymmetry factors of 1.51 for uranium and 1.59 for thorium. The asymmetry of the simulated breakthrough profiles of both uranium and thorium was observed to increase with decreasing bed length (Figure 6.5.). The asymmetrical breakthrough profiles generated using the numerical simulation method are likely to be a more accurate representation of experimental results as the symmetrical profiles predicted by the Gaussian model show an immediate analyte breakthrough as evidenced by the positive column output concentration at V=0. This is a physical impossibility unless the flow rate is very slow and aqueous phase diffusion occurs faster than linear flow. In addition, the continuation of the

leading edge of the Gaussian distribution to negative volumes creates a mass imbalance between the total amount of analyte loaded and the total amount in the column output solution as determined by calculation of the area under the breakthrough peak.

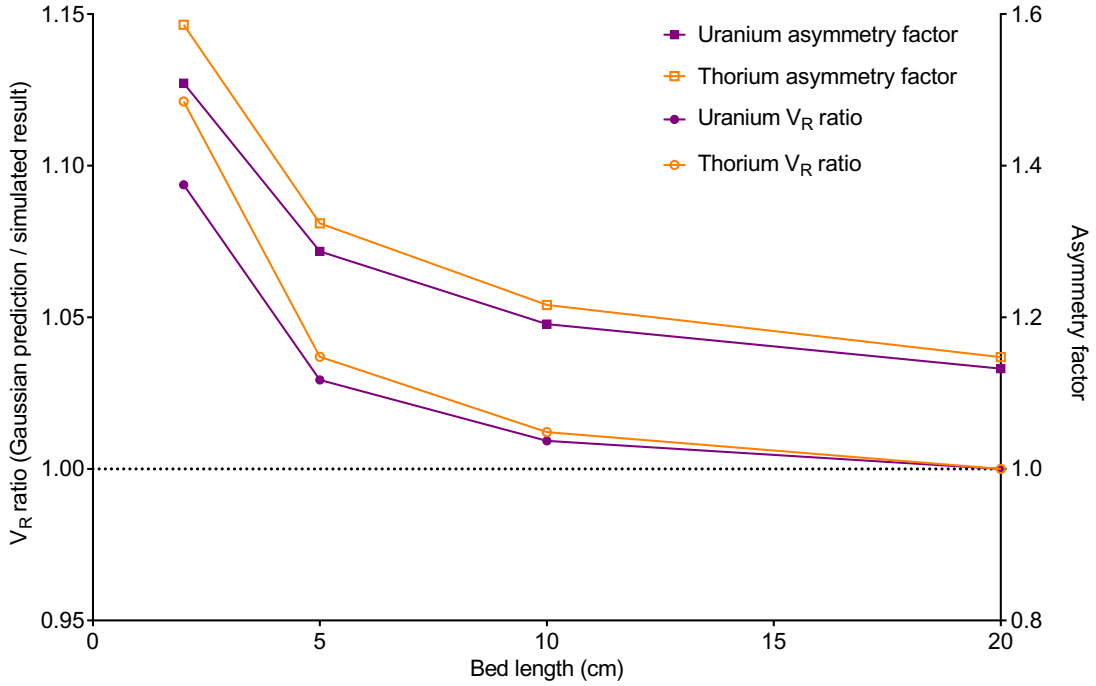

Figure 6.5.
Bed length plotted against V_R ratio and asymmetry factor.
The left hand axis displays the ratio of the volume of maximum column output concentration as predicted by the Gaussian model divided by the volume of maximum concentration resulting from the multiple analyte numerical simulation method.
The right hand axis displays the asymmetry of the simulated breakthrough profiles.
The horizontal dotted line simultaneously represents an agreement between the Gaussian model and numerical simulation method in terms of the retention volume and a perfectly symmetrical simulated profile.
Both the Gaussian model and numerical simulation method use the following common parameters: loading volume = 0.1 mL; loading concentration of uranium and thorium = 1 x 10^{-8} mol/L (~2 ppb); flow rate = 2 mL/min; column radius = 0.35 cm; V_{aq} = 0.655.
The multiple analyte numerical simulation method uses rate constants calculated from batch sorption/desorption experimental data. An axial division length of 0.1 cm was input along with estimated aqueous phase diffusion rate constants. A lumped solid extractant concentration model constant and stoichiometric relationships with the extractant of 1:2 for uranyl nitrate and 1:4 for thorium nitrate are also included.
The Gaussian model parameters of k' and HETP for each analyte have been calculated from the simulated datasets for a 20 cm length column and applied to all other length columns.

The relationship between bed length and asymmetry indicates that the Gaussian model is not suitable for describing experimental breakthrough/elution profiles from short columns. The asymmetry factor is also shown to correlate with the level of discrepancy between the volume at which the breakthrough maximum is predicted to occur and the resulting maximum concentration value as generated by the numerical simulation method. It should be noted

however, that the simulated breakthrough profiles for the 20 cm length column were also not perfectly symmetrical with asymmetry factors of 1.13 for uranium and 1.15 for thorium. This may mean that the retention factor and HETP values determined by Gaussian model analysis are slightly inaccurate. It is predicted that a much longer length column would be needed to generate simulated breakthrough profiles with an exactly Gaussian shaped distribution.

Generally, use of the Gaussian model for describing chromatographic systems assumes the retention factor to be a constant whilst the HETP value is given as a function of the interstitial velocity (u_e). This function has been assessed for the multiple analyte numerical simulation method by applying the Gaussian model analysis to breakthrough curves simulated using a range of input flow rates. HETP values were calculated from the width of the simulated peak at half the maximum concentration and the resulting HETP vs interstitial velocity plot compared to the Van Deemter equation (Equation 6.7.).

$$HETP = A + \frac{B}{u_e} + Cu_e \qquad \text{Equation 6.7.}$$

The first term in the Van Deemter equation relates to eddy dispersion so was set to 0.1 in line with the axial division length of 0.1 cm used in the numerical simulation method. The second term relates to molecular diffusion; B was therefore set to the aqueous phase diffusion rate constant (0.0008 for uranium and 0.002 for thorium). The final term is related to sorption/desorption kinetics and was determined by linear regression analysis of the data points above the interstitial velocity at which HETP is at a minimum. Comparing the relationship between interstitial velocity and HETP as predicted by the Van Deemter equation and that derived from the Gaussian model analysis of breakthrough profiles generated by the multiple analyte numerical simulation method (Figure 6.6.), shows an imperfect fit.

Although the HETP minimum for both analytes in both the Van Deemter prediction and the Gaussian model analysis of the simulated datasets is approximately equal to the axial division length (0.1 cm), the exact position of the minima are not in agreement. As seen with the shorter length columns, the reason for this discrepancy could be due to the increase in asymmetry with decreasing number of theoretical plates. At flow rates away from the HETP minimum, the efficiency of the column decreases due to either molecular diffusion or kinetic sorption/desorption limitations; this causes breakthrough profiles to become broader and more asymmetrical, reducing the validity of quantifying parameters according to an analysis method based on the assumption of a Gaussian distribution. As the bed length chosen for the assessment

of the relationship between interstitial velocity and HETP was 10 cm, the asymmetry factor for the simulated breakthrough profiles of both analytes was >1.15, even for the flow rates at which the narrowest peaks were generated.

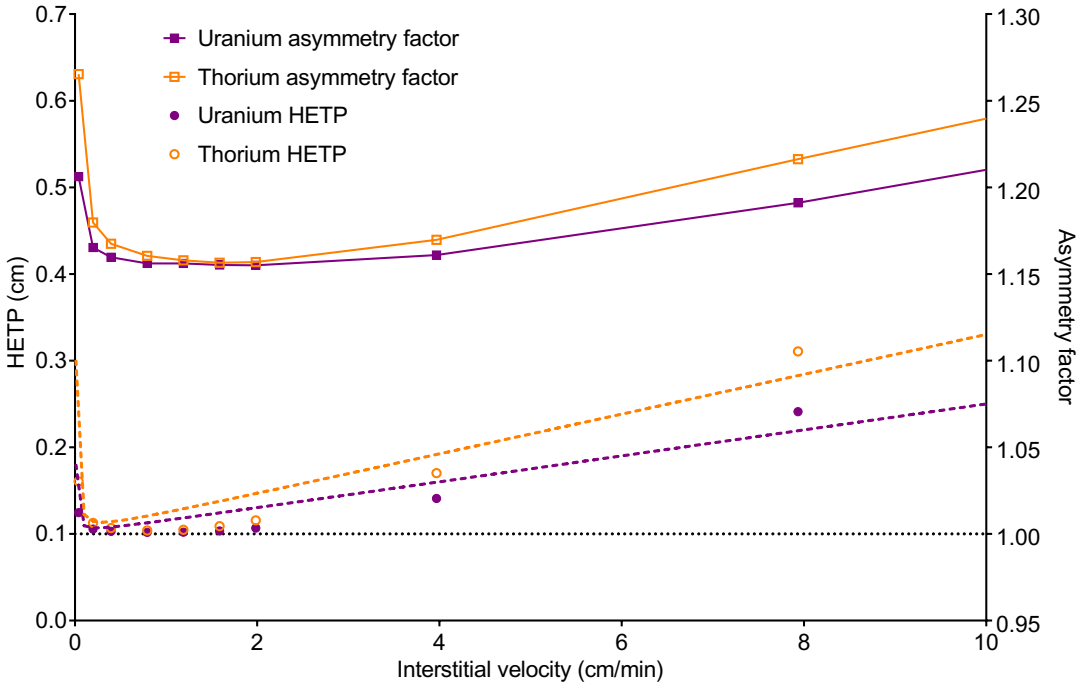

Figure 6.6.
Interstitial velocity plotted against HETP and asymmetry factor.
The left hand axis displays the height equivalent of a theoretical plate (HETP). The data points represent the values determined by Gaussian model analysis of breakthrough profiles generated by the multiple analyte numerical simulation method. The dashed lines represent the relationship between interstitial velocity and HETP as predicted by the Van Deemter equation (Equation 6.7.).
The right hand axis displays the asymmetry of the simulated breakthrough profiles.
The horizontal dotted line simultaneously represents HETP if the second and third terms of the Van Deemter equation (Equation 6.7.) were neglected and a perfectly symmetrical simulated profile.
The multiple analyte numerical simulation method uses the following parameters: loading volume = 0.1 mL; loading concentration of uranium and thorium = 1 x 10^{-8} mol/L (~2 ppb); bed length = 10 cm; column radius = 0.35 cm; V_{aq} = 0.655; axial division length = 0.1 cm; aqueous phase diffusion rate constant for uranium = 0.0008; aqueous phase diffusion rate constant for thorium = 0.002.
Rate constants were calculated from batch sorption/desorption experimental data. A lumped solid extractant concentration model constant and stoichiometric relationships with the extractant of 1:2 for uranyl nitrate and 1:4 for thorium nitrate are also included.

As a linear sorption isotherm is assumed in the Gaussian model, both k' and HETP are independent of concentration. Increasing either the input concentration or the loading volume increases the value of maximum concentration predicted by the Gaussian single equation model (Equation 6.1.) but not the volume at which the maximum occurs or the width of the peak. For UTEVA resin, it has already been shown that under discrete loading conditions, the shape and position of a breakthrough profile is related to both analyte concentration and volume of the loading solution. To further demonstrate this, a series of numerical simulations have been run

using a range of sample loading conditions whilst maintaining a set bed length (2 cm) and flow rate (2 mL/min) likely to be used in an automated radioanalytical procedure.

At sufficiently low analyte concentration, the shape and position of maximum output concentration for simulated breakthrough profiles from small loading volumes (0.1 mL, 1 mL or 10 mL) does not vary significantly (Figure 6.7.).

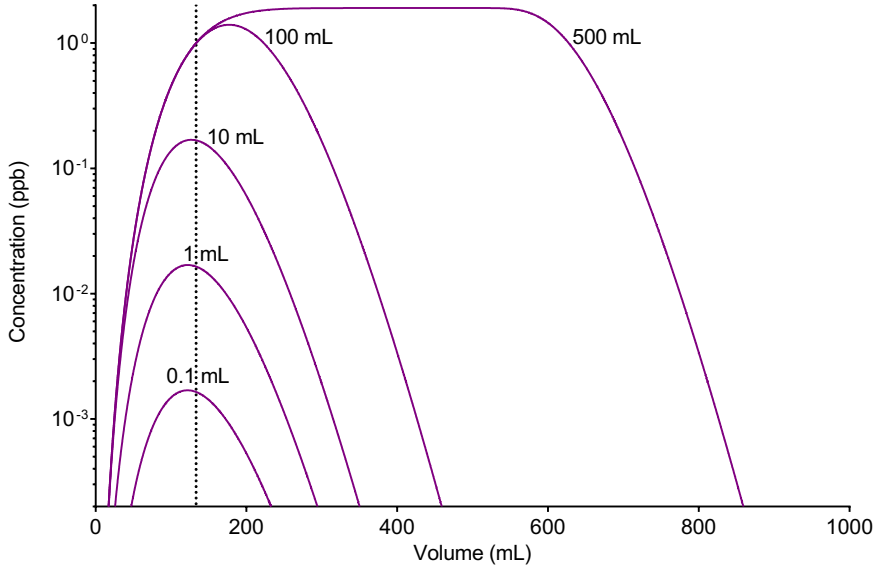

Figure 6.7.
Multiple analyte numerical simulation of uranium breakthrough profiles using different loading volume inputs.
The vertical dotted line represents V_R as predicted by the Gaussian model using k' calculated from the simulated dataset for uranium breakthrough from a 20 cm length column (Figure 6.4.).
The multiple analyte numerical simulation method uses the following parameters: flow rate = 2 mL/min; loading concentration of uranium and thorium = 1 x 10^{-8} mol/L (~2 ppb); bed length = 2 cm; column radius = 0.35 cm; V_{aq} = 0.655; axial division length = 0.1 cm; aqueous phase diffusion rate constant for uranium = 0.0008; aqueous phase diffusion rate constant for thorium = 0.002.
Rate constants were calculated from batch sorption/desorption experimental data. A lumped solid extractant concentration model constant and stoichiometric relationships with the extractant of 1:2 for uranyl nitrate and 1:4 for thorium nitrate are also included.

At a loading volume of 500 mL, however, a plateau of maximum concentration is reached. This is equivalent to continuous loading followed by a step change in analyte concentration (to 0 ppb). For a loading volume of 100 mL, the shape of the breakthrough profile approaches that of continuous loading with the volume at which maximum concentration occurs shifting from that of the small volume loading simulations. The observed relationship between loading volume and breakthrough profile shape could not be predicted by the single equation Gaussian model.

At higher analyte loading concentrations, the shape and position of maximum output concentration for simulated breakthrough profiles can change significantly from that predicted by

the Gaussian model. The volume at which column output concentration reaches a maximum reduces at higher loading concentrations due to the limited capacity of the sorptive material (Figure 6.8.). The analyte concentration at which this reduction becomes significant is related to the volume of the loading solution. For example, at a loading concentration of 1×10^{-3} mol/L (~200 ppm) of both uranium and thorium, the position of peak breakthrough for both analytes drops to <20 mL for a 10 mL loading volume whereas little change from the breakthrough profiles generated using a 1×10^{-8} mol/L (~2 ppb) loading solution is seen for a 0.1 mL loading volume. In addition, the bed length was also observed to have an impact on the extent of the drop in the position of peak breakthrough. For example, using the same loading conditions (concentration = 1×10^{-2} mol/L (~2000 ppm) for both uranium and thorium; volume = 1 mL) the reduction in the volume at which the maximum concentration in the breakthrough profile occurs at is 16 % for uranium and 29 % for thorium when simulating a 20 cm length column whilst it is 47 % for uranium and 68 % for thorium when simulating a 2 cm length column. The simulated maximum breakthrough volume is therefore related to the difference between the total amount of analyte loaded and the total amount of available sorption sites. The loading volume is also important, as the shape of the breakthrough profile is not identical for the same total amount of analyte loaded in varying volumes. Comparing the results of the multiple analyte numerical simulation method for 2.38 mg of uranium loaded in either 0.1 mL, 1 mL or 10 mL of nitric acid, the volume at which the maximum concentration in the breakthrough profile occurs is 64.8 mL, 65.4 mL and 71.5 mL respectively (for a 2 cm length column).

For simulations run under overloaded conditions, the difference in kinetics and stoichiometric relationship with the extractant between the two analytes also causes a difference in the position of maximum output concentration. This can be observed in the breakthrough profiles of uranium and thorium using a 10 mL loading volume and a high concentration (0.1 mol/L; ~20,000 ppm) of both analytes. The shape of the breakthrough profiles suggests that uranium is initially transferred into the solid phase in preference to thorium followed by a replacement of 2 uranyl nitrate molecules with 1 thorium nitrate molecule. Further experiments could be conducted in order to compare this simulated result with empirical data.

a

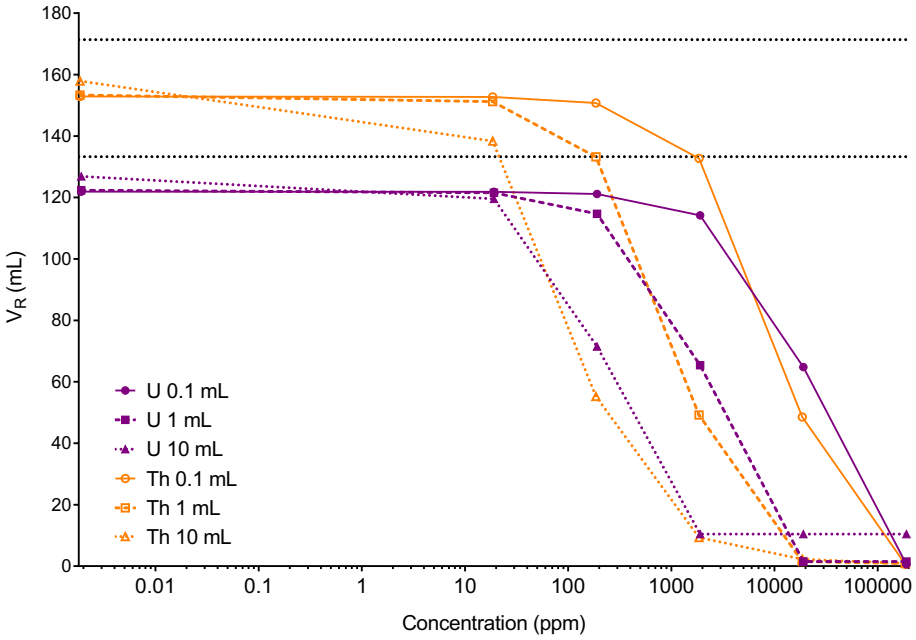

b

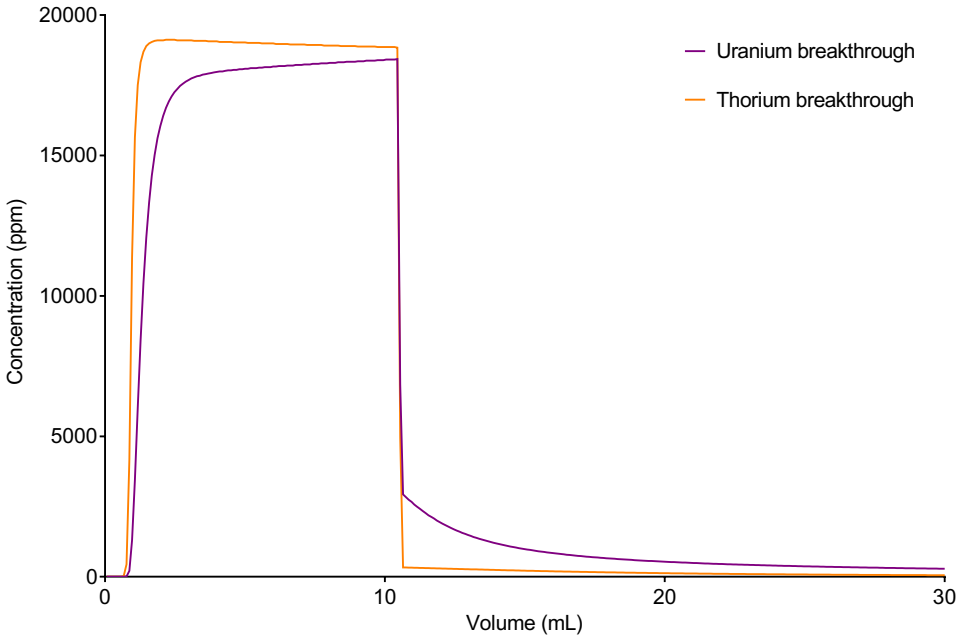

Figure 6.8.
Impact of analyte concentration and loading volume on breakthrough profiles generated by the multiple analyte numerical simulation method.
(a) Comparison of volume at which column output concentration reaches a maximum for different analyte concentration and loading volume inputs.
The horizontal dotted lines (upper = thorium, lower = uranium) represent V_R as predicted by the Gaussian model using k' calculated from the simulated dataset for breakthrough from a 20 cm length column (Figure 6.4.).
(b) The shape the breakthrough profiles generated using a loading concentration of 1 x 10^{-1} mol/L (~20,000 ppm for both uranium and thorium) and a loading volume of 10 mL.
The multiple analyte numerical simulation method uses the following parameters: flow rate = 2 mL/min; bed length = 2 cm; column radius = 0.35 cm; V_{aq} = 0.655; axial division length = 0.1 cm; aqueous phase diffusion rate constant for uranium = 0.0008; aqueous phase diffusion rate constant for thorium = 0.002. Rate constants were calculated from batch sorption/desorption experimental data. A lumped solid extractant concentration model constant and stoichiometric relationships with the extractant of 1:2 for uranyl nitrate and 1:4 for thorium nitrate are also included.

6.2.1.3. Comparison of multiple analyte numerical simulation method with the Bohart-Adams model

The Bohart-Adams model has been employed for describing the breakthrough profile from columns run under a continuous loading condition using the assumptions of a (highly favourable) rectangular sorption isotherm, a quasi-chemical rate equation and negligible axial dispersion[46]. As the integral of the Gaussian equation for discrete sample loading could be used to describe continuous sample loading, it is hypothesised that differentiating the continuous loading Bohart-Adams equation could lead to an equation for describing breakthrough profiles observed under discrete loading conditions. The proposed discrete loading Bohart-Adams equation (Equation 6.8.) as a function of volume (V) includes the flow rate through the column (u in mL/min), the analyte concentration in the loading solution (C_{in}), the volume of the loading solution (V_{in}) and the total volume of the solid phase (v_s) as well as a term describing the analyte concentration on the solid phase at equilibrium (q_e) and the Bohart-Adams constant (k_{BA}) for each analyte. The total volume of the solid phase is calculated from the volume fraction of the solid phase (V_s) multiplied by the total bed volume. As the concentration is given in mol/L, v_s, V and V_{in} must be input in L.

$$C_{out,V} = C_{in}V_{in}f(V) = \frac{(C_{in})^2 V_{in} k_{BA} e^{\frac{k_{BA}}{u}(q_e v_s - C_{in}V)}}{u\left(e^{\frac{k_{BA}}{u}(q_e v_s - C_{in}V)} + 1\right)^2} \qquad \text{Equation 6.8.}$$

It has also been suggested by Chu[46] that the constant q_e value could be replaced by an equation describing the Langmuir isotherm (Equation 6.9.) where q_e is expressed in terms of the maximum analyte concentration on the solid phase (q_{max}), the analyte concentration in the aqueous phase at equilibrium (C_e) and a constant (b) related to the ratio of the forward and reverse rate constants for sorption following Langmuir kinetics.

$$q_e = \frac{q_{max} b C_e}{1 + bC_e} \qquad \text{Equation 6.9.}$$

At low concentrations the Langmuir isotherm (Figure 6.9.) tends to the linear isotherm with the analyte concentration on the solid phase a function of the analyte concentration in the aqueous phase ($q_e = q_{max}bC_e$) whilst at high concentrations it tends towards the rectangular isotherm with the analyte concentration on the solid phase independent of the analyte concentration in the aqueous phase ($q_e = q_{max}$). The Bohart-Adams model with a Langmuir correction may therefore behave similarly to the Gaussian model (linear isotherm assumed) at low concentrations and

similarly to the Bohart-Adams model without a Langmuir correction (rectangular isotherm assumed) at high concentrations; thereby extending the application of the Bohart-Adams model to a larger concentration range.

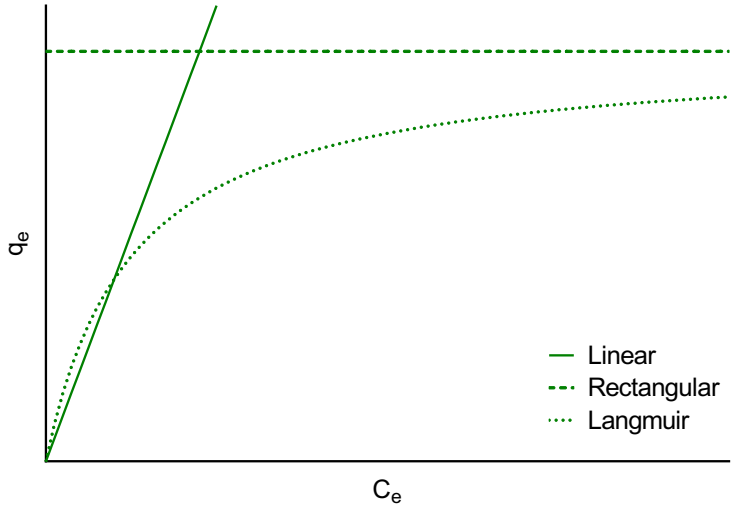

Figure 6.9.
Diagram depicting the difference between linear, rectangular and Langmuir isotherms.

As with the Gaussian model, an assessment of the ability of the Bohart-Adams model to describe radioanalytical chromatographic breakthrough profiles can be made by comparison with the developed multiple analyte numerical simulation method. The model parameters were initially fitted using the same pair of simulated datasets used for fitting the Gaussian model parameters (i.e. uranium and thorium breakthrough from a 20 cm bed length – Figure 6.10.). The total volume of the solid phase (v_s) was calculated using the same volume fraction of the solid phase value as input into the numerical simulation method. It was discovered that analogous to the V_R term in the Gaussian model, varying q_e changed the position of the volume at which maximum column output concentration occurred and that a good fit was achieved using the distribution constant in terms of volume ($k_D \times \rho_s$) previously measured via batch experiments multiplied by the loading concentration in mol/L (i.e. 5.05×10^{-6} mol/L for uranium and 6.51×10^{-6} mol/L for thorium). These values are also equivalent to the ratio of $\vec{k}/\overleftarrow{k}$ used in the single analyte numerical simulation method (ratio calculated without adjustment of the forward rate constant to account for the lumped solid extractant concentration value). Using these q_e values, the Bohart-Adams constant (k_{BA}) for each analyte was then fitted to a precision of 2 significant figures using a trial and error method. The resulting breakthrough profiles as predicted by the Bohart-Adams model were similar to both the simulated datasets and the profiles predicted by the Gaussian model. The profiles predicted by both the single equation models were perfectly

symmetrical with the breakthrough profiles predicted by the Bohart-Adams model having a slightly narrower peak and wider base than those predicted by the Gaussian model.

If all other simulation input parameters were kept the same and only the bed length altered, it was hypothesised that the Bohart-Adams model could predict the change in the simulated breakthrough profiles in a similar way to the Gaussian model. As the bed length is used in calculation of v_s, it was thought the change in this value would alter the position and width of the breakthrough profiles predicted by the Bohart-Adams model. As the analyte concentration in the loading solution was not altered, q_e was not changed and the same prediction would be made whether either the rectangular isotherm or Langmuir isotherm was applied to the Bohart-Adams model.

Comparison of the Bohart-Adams model prediction to breakthrough curves generated using the numerical simulation method for a 2 cm length column, however, showed that whilst the volume at which the breakthrough maximum occurs was quite accurately estimated, the width of the predicted profiles were much larger than the simulated datasets (Figure 6.10.). Alternative values of k_{BA} were therefore fitted using the trial and error method. As observed with the profiles predicted by the Gaussian model, the fitted breakthrough profiles for a 2 cm length column also overestimated the maximum breakthrough concentration volume. This overestimation could also be due to the increase in asymmetry of the simulated profiles at shorter column lengths. In addition, the Bohart-Adams model also predicted the impossible result of immediate analyte breakthrough for the 2 cm length column leading to a mass imbalance between the total amount of analyte loaded and the total amount in the column output solution as determined by calculation of the area under the breakthrough peak. The Bohart-Adams model is therefore shown to have a similarly low level of suitability to the Gaussian model for describing experimental breakthrough/elution profiles from short columns.

a

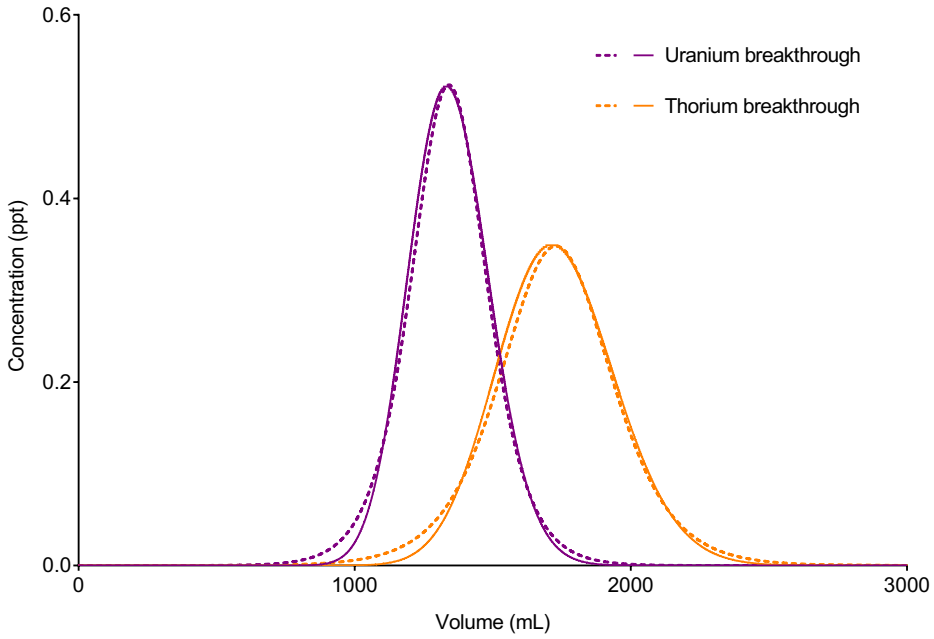

b

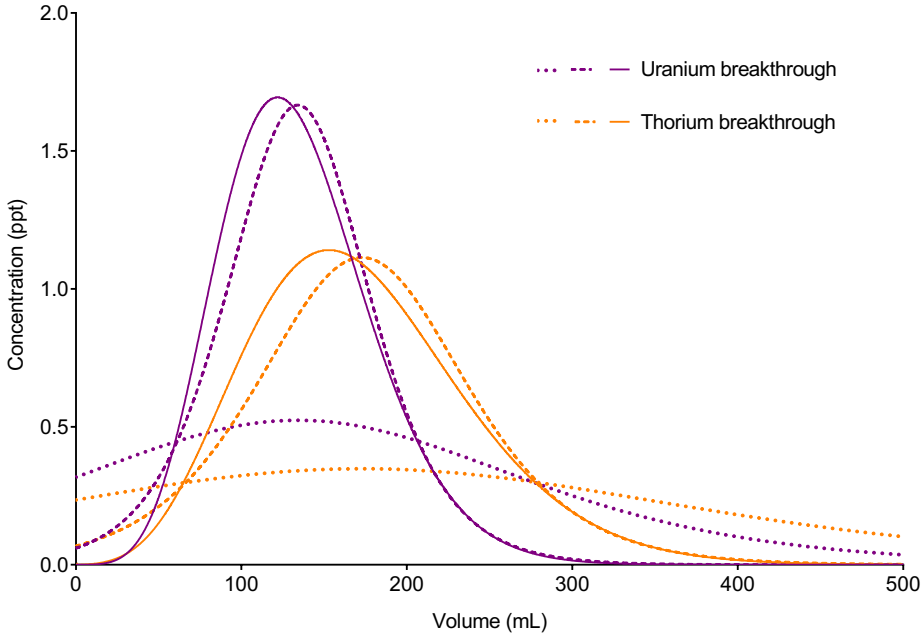

Figure 6.10.
Comparison between the Bohart-Adams model and multiple analyte numerical simulation of breakthrough profiles for different bed lengths.
Both the Bohart-Adams model (dashed/dotted lines) and numerical simulation method (solid lines) use the following common parameters: loading volume = 0.1 mL; loading concentration of uranium and thorium = 1 x 10^{-8} mol/L (~2 ppb); flow rate = 2 mL/min; column radius = 0.35 cm; V_{aq} = 0.655.
The multiple analyte numerical simulation method uses rate constants calculated from batch sorption/desorption experimental data. An axial division length of 0.1 cm was input along with estimated aqueous phase diffusion rate constants. A lumped solid extractant concentration model constant and stoichiometric relationships with the extractant of 1:2 for uranyl nitrate and 1:4 for thorium nitrate are also included.
The Bohart-Adams model parameter of q_e for each analyte has been calculated from the simulated datasets for a 20 cm length column (a) and applied to a 2 cm length column (b). The Bohart-Adams parameter of k_{BA} is either the same as the value used in the 20 cm length column (dotted lines) or fitted (dashed lines).

The relationship between bed length and k_{BA} was further investigated by running a set of simulations varying the bed length whilst keeping all other column operating parameters constant. The fitted k_{BA} values needed to produce as close an agreement as possible between the Bohart-Adams predictions and the simulated datasets were found to be directly related to the bed length being simulated (Figure 6.11.). This relationship included the square root of the bed length (Equation 6.10.).

$$k_{BA} = \frac{A}{\sqrt{L}} \qquad \text{Equation 6.10.}$$

The dependence of k_{BA} on bed length is an interesting finding as k_{BA} was expected to be a constant for the analyte-resin sorption system being modelled.

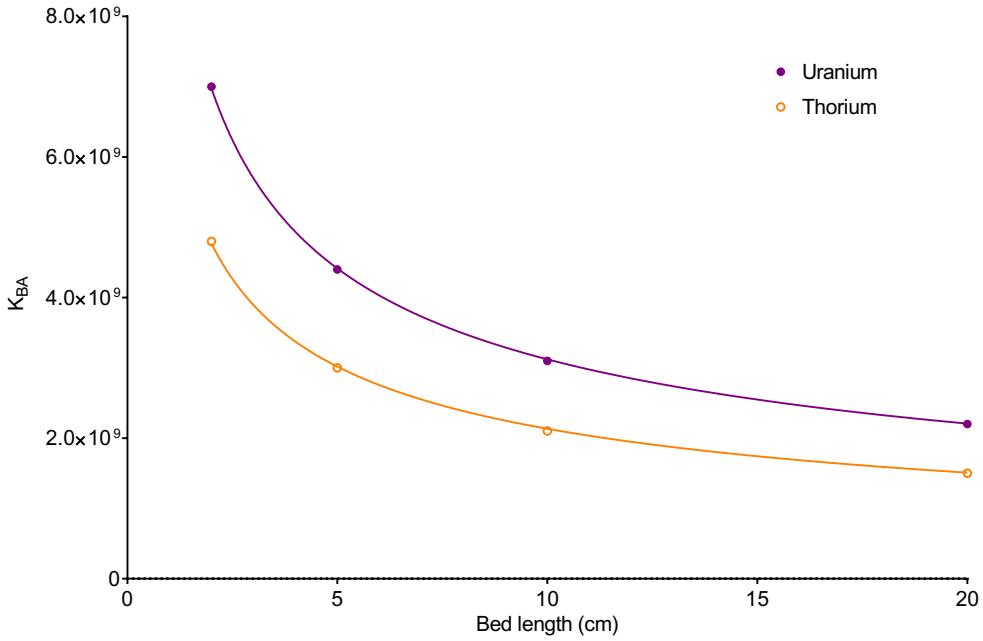

Figure 6.11.
Bed length plotted against fitted k_{BA} parameter.
Both the Bohart-Adams model and numerical simulation method use the following common parameters: loading volume = 0.1 mL; loading concentration of uranium and thorium = 1 x 10^{-8} mol/L (~2 ppb); flow rate = 2 mL/min; column radius = 0.35 cm; V_{aq} = 0.655.
The multiple analyte numerical simulation method uses rate constants calculated from batch sorption/desorption experimental data. An axial division length of 0.1 cm was input along with estimated aqueous phase diffusion rate constants. A lumped solid extractant concentration model constant and stoichiometric relationships with the extractant of 1:2 for uranyl nitrate and 1:4 for thorium nitrate are also included.
The Bohart-Adams model parameter of q_e for each analyte has been calculated from the simulated datasets for a 20 cm length column (Figure 6.10.) and applied to all other length columns. The Bohart-Adams parameter of k_{BA} has been fitted in all instances.
Non-linear regression analysis has been applied to the data points to produce fitted curves (solid lines) with the formula y = A*x^-0.5 where A = 9.870 x 10^9 for uranium and A = 9.747 x 10^9 for thorium.

The relationship between flow rate and k_{BA} was also investigated. As with the retention factor term (k') in the Gaussian model, q_e was also assumed to be independent of flow rate. The discrepancy between the maximum breakthrough concentration volume as predicted by Bohart-Adams model and the result of the numerical simulation method therefore also increased with asymmetry for flow rates slower or faster than the HETP minimum. Nevertheless, the k_{BA} values that gave the best fit of the Bohart-Adams model to the simulated datasets were plotted against interstitial velocity (Figure 6.12.) and non-linear regression analysis applied using a polynomial equation (Equation 6.11.).

$$k_{BA} = B_1 u_e^3 + B_2 u_e^2 + B_3 u_e + B_4 \qquad \text{Equation 6.11.}$$

The results indicated a positive value for B_1 and B_3 and a negative value for B_2 and B_4 for both analytes.

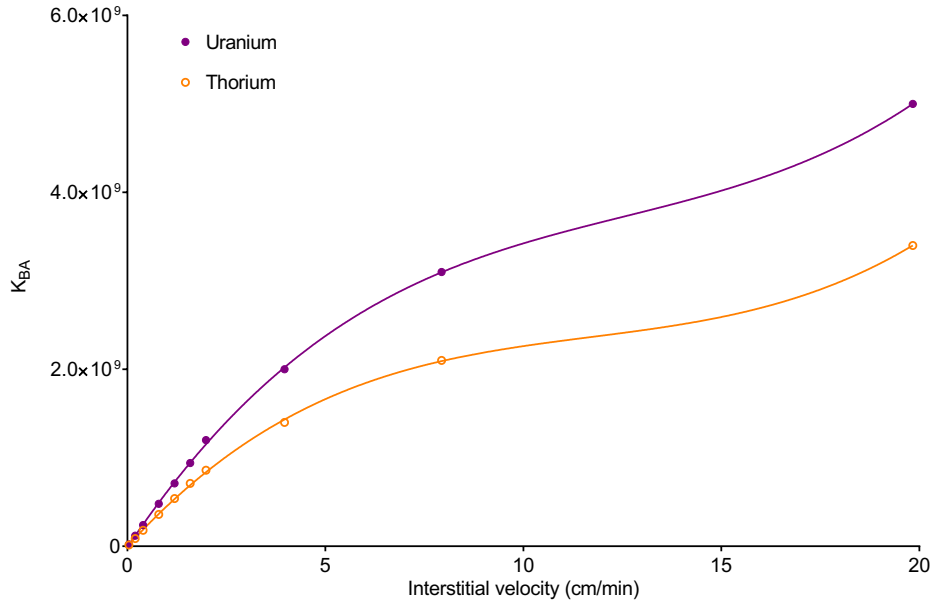

Figure 6.12.
Interstitial velocity plotted against fitted k_{BA} parameter.
Both the Bohart-Adams model and numerical simulation method use the following common parameters: loading volume = 0.1 mL; loading concentration of uranium and thorium = 1 x 10^{-8} mol/L (~2 ppb); bed length = 10 cm; column radius = 0.35 cm; V_{aq} = 0.655.
The multiple analyte numerical simulation method uses rate constants calculated from batch sorption/desorption experimental data. An axial division length of 0.1 cm was input along with estimated aqueous phase diffusion rate constants. A lumped solid extractant concentration model constant and stoichiometric relationships with the extractant of 1:2 for uranyl nitrate and 1:4 for thorium nitrate are also included.
The Bohart-Adams model parameter of q_e for each analyte has been calculated from the simulated datasets for a 20 cm length column (Figure 6.10.). The Bohart-Adams parameter of k_{BA} has been fitted in all instances.
Non-linear regression analysis has been applied to the data points to produce fitted curves (solid lines) using a third order polynomial (cubic) equation.

The observed relationships between k_{BA} and both bed length and flow rate could be mathematical artefacts from the differentiation of the Bohart-Adams equation for describing breakthrough under the continuous sample loading condition. In addition, the Bohart-Adams model was not developed for use at low analyte concentrations where the sorptive material is undergoing equilibration with the analyte concentration in the aqueous phase rather than saturation. In general, the Bohart-Adams has not been found to be superior to the Gaussian model in describing the simulated breakthrough profiles thus far; it suffers from the same decreasing accuracy when higher levels of asymmetry are observed and has an additional level of complexity regarding the variation of k_{BA} with bed length and flow rate. The Bohart-Adams model, however, does include concentration in the calculation of predicted breakthrough profiles. Conversely, increasing either the input concentration or the loading volume in the Gaussian equation had no effect on the volume at which the maximum output concentration occurs or the width of the peak.

The volume of maximum breakthrough concentration predicted by the Bohart-Adams model using a constant value of q_e (rectangular isotherm assumption) has a direct correlation to the analyte concentration in the loading solution; increasing the concentration by a factor of 2, halves the maximum breakthrough volume. This is unrealistic for radioanalytical separation procedures where the analyte concentration in the sample is likely to be low. Under these conditions, the simulated maximum breakthrough volume was shown to be independent of loading concentration. Even at higher analyte concentrations, the reduction in simulated maximum breakthrough volume was shown to be more complex than the function of 1/concentration suggested by the Bohart-Adams model (see Figure 6.8.).

The Bohart-Adams model with a Langmuir correction may provide a more realistic estimation of the relationship between analyte concentration in the loading solution and the volume at which maximum concentration occurs in simulated breakthrough datasets. This has been assessed by running a series of simulations where the loading concentration is varied (Figure 6.13.). These simulations use a column length of 10 cm and a loading volume of 0.1 mL. As the inability of the Bohart-Adams model to produce asymmetrical breakthrough profiles has already been discussed, the difference in maximum breakthrough volume between the prediction and simulated breakthrough profiles is focussed upon. It should however be noted that simulated breakthrough profiles using high analyte concentrations become significantly asymmetrical and in some cases the uncertainty involved with the assessment of asymmetry using the width at 10 % of the maximum output concentration can be very large.

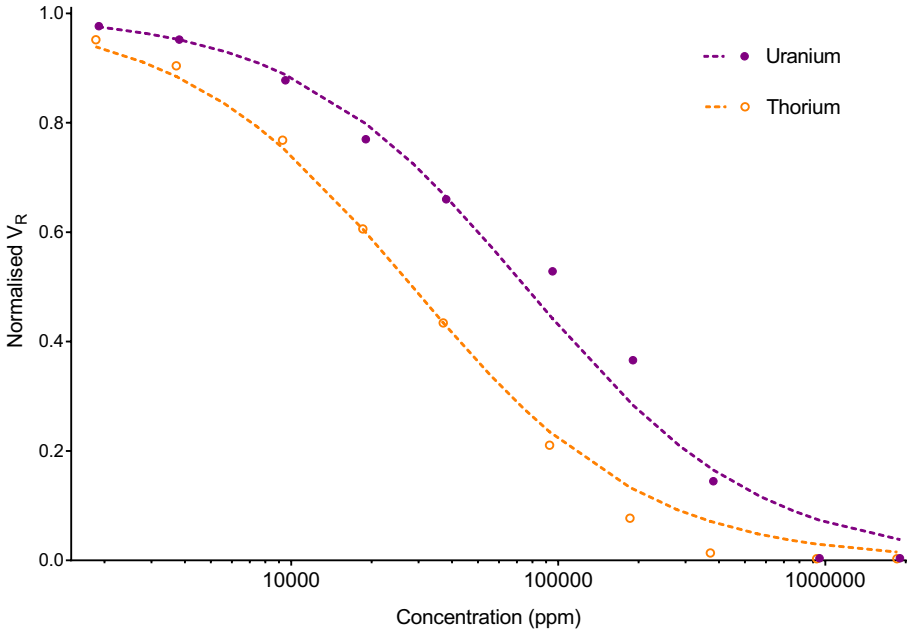

Figure 6.13.
Plot of normalized V_R against analyte concentration in the loading solution as predicted by the Bohart-Adams model with a Langmuir correction and the result generated using the multiple analyte numerical simulation method.
V_R is normalised by dividing the volume at which maximum breakthrough concentration occurs for a particular analyte concentration (same concentration for both analytes) by the volume at which maximum breakthrough occurs for the low analyte condition (loading concentration of uranium and thorium = 1 x 10^{-8} mol/L or ~2 ppb).
The Bohart-Adams model (dashed lines) and numerical simulation method (data points) use the following common parameters: flow rate = 2 mL/min; bed length = 10 cm; loading volume = 0.1 mL; column radius = 0.35 cm; V_{aq} = 0.655.
The multiple analyte numerical simulation method uses rate constants calculated from batch sorption/desorption experimental data. An axial division length of 0.1 cm was input along with estimated aqueous phase diffusion rate constants. A lumped solid extractant concentration model constant and stoichiometric relationships with the extractant of 1:2 for uranyl nitrate and 1:4 for thorium nitrate are also included.
The Bohart-Adams model uses values of b = 2.525 and q_{max} = 200 for uranium and b = 6.51 and q_{max} = 100 for thorium.

The values of the Langmuir parameters (b and q_{max} – see Equation 6.9.) in the modified Bohart-Adams model were fitted using trial and error to provide an estimated agreement of the maximum breakthrough volume relationship with analyte concentration observed in the simulated datasets. The predicted relationship has been compared to the simulated results by normalising both sets of data to the maximum breakthrough volume values for low analyte concentration in the loading solution (~2 ppb). Whilst the Bohart-Adams model does show the general trend observed in the simulated data, the relationship between analyte concentration and position of peak breakthrough generated using the numerical simulation method is more complex, particularly at high concentrations.

Additional factors that the Bohart-Adams model fails to include are bed length and loading volume. Varying either of these input parameters changes the volume at which maximum breakthrough concentration occurs in profiles generated by the multiple analyte numerical simulation method (Figure 6.14.). This change is not reflected in the Bohart-Adams model as the Langmuir parameters (b and q_{max}) are assumed to be constant for each analyte.

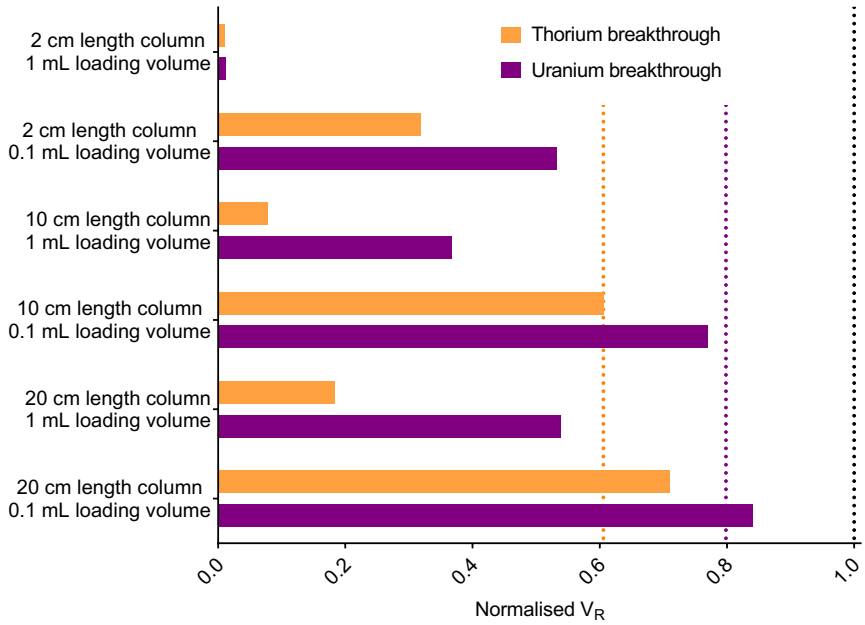

Figure 6.14.
Comparison of normalized V_R results for breakthrough profiles simulated under different column operating conditions (bed length and loading volume).
V_R is normalised by dividing the volume at which maximum breakthrough concentration occurs for an analyte concentration of 1 x 10^{-1} mol/L (~20,000 ppm uranium and thorium) by the volume at which maximum breakthrough occurs for the low analyte condition (loading concentration of uranium and thorium = 1 x 10^{-8} mol/L or ~2 ppb).
The Bohart-Adams model (coloured vertical lines) and numerical simulation method (horizontal bars) use the following common parameters: flow rate = 2 mL/min; loading concentration of uranium and thorium = 1 x 10^{-1} mol/L (~20,000 ppm); column radius = 0.35 cm; V_{aq} = 0.655.
The multiple analyte numerical simulation method uses rate constants calculated from batch sorption/desorption experimental data. An axial division length of 0.1 cm was input along with estimated aqueous phase diffusion rate constants. A lumped solid extractant concentration model constant and stoichiometric relationships with the extractant of 1:2 for uranyl nitrate and 1:4 for thorium nitrate are also included.
The Bohart-Adams model uses values of b = 2.525 and q_{max} = 200 for uranium and b = 6.51 and q_{max} = 100 for thorium.
The Gaussian model prediction (black vertical line) where V_R is independent of analyte concentration is included for comparison.

As discussed in regard to the Gaussian model, the simulated maximum breakthrough volume is a function of the difference between the total amount of analyte loaded and the total amount of available sorption sites. Changing the value of the loading volume (V_{in}) in the Bohart-Adams equation (Equation 6.8.) only changes the magnitude of the predicted breakthrough peak and not

the position. Replacing the input concentration term (C_{in}) with a term for total amount of analyte loaded (C_{in} multiplied by V_{in}) could account for the difference in breakthrough position for different loading volumes. This has not yet been tested. It is also uncertain as to whether the relationship between bed length and position of maximum breakthrough concentration could be included in the Bohart-Adams model for discrete breakthrough from high loading concentrations. The lack of change in the predicted volume of peak breakthrough for different bed lengths could be due to the incorrect application of the model to discrete sample loading by differentiation of the original equation for describing breakthrough profiles from continuous loading experiments.

Finally, larger loading volumes caused the shape of the simulated breakthrough profile to change from that of the discrete sample loading condition towards the continuous loading condition (see Figure 6.7.). As with the Gaussian model, this change in the shape of breakthrough profiles could not be predicted by the Bohart-Adams model. Overall, the numerical simulation method is shown to be superior to both of the single equation models investigated.

6.2.2. Potential to develop numerical simulation method into a user-friendly software tool

The flexibility of the numerical simulation method to predict breakthrough profiles under a large range of column operating conditions has been shown to be a great advantage over simpler single equation models. The ability to vary the column dimensions (bed length and column radius), flow rate and sample loading conditions (analyte concentration and volume) and observe the impact on breakthrough profiles would help to streamline the radioanalytical method development process and reduce the amount of experiments required. Another aspect of chromatographic separations for radioanalytical purposes has not yet, however, been discussed. This is the use of step changes in reagent. A typical radioanalytical chromatographic procedure consists of a sample loading step, a rinse step to remove interferents and one or more selective elution steps to isolate the analyte(s) of interest. A final regeneration step may also be carried out if the column is to be reused. The rinse step is usually carried out using the same reagent that the sample was introduced in whilst subsequent elution steps involve changes in the on-column environment to promote desorption of the analyte from the sorptive material. The recent development of automated radioanalytical techniques means that precise delivery of a sequence of reagents to a column can be made using software control of pumps and valves. The volume and flow rate of each solution can be regulated and the column output either collected or diverted to waste. As the numerical simulation method stores data on the axial distribution of analyte concentration in both the aqueous and solid phases after each iteration of the *ODE solver*, a change in the column input solution after any specified volume of sample loading and rinse

solution could be simulated. The ability to describe more complex elution sequences is another potential advantage of the numerical simulation method over single equation models.

The multiple analyte numerical simulation method has been modified to include step changes in eluent and tested using a procedure for the sequential elution of thorium and uranium from UTEVA resin. The experimental sequence consisted of loading a discrete volume of both analytes in 8M HNO_3 followed by an 8M HNO_3 rinse step, the elution of thorium using 6M HCl and finally the elution of uranium using 0.3M HNO_3. The switch between reagent solutions was manually achieved by quickly moving the tubing into the next container once the previous had been emptied; this produced a small air bubble between the two solutions. This experimental sequence was represented using the numerical simulation method by addition of a *case structure* to the LabVIEW coding. The flow rate and forward ($\vec{k}$) and reverse ($\overleftarrow{k}$) rate constant values for each solution were written into separate cases which were selected using the output of a *subVI* that assessed the *while loop* iteration and assigned a case input value (Table 6.3.). For example, the rinse volume of ~20 mL was loaded on to the column from iterations 2≤i≥807 during which time a case outputting a flow rate of 1.83 mL/min and the forward and reverse rate constant values determined for uranium and thorium (onto UTEVA resin) from 8M HNO_3 was selected.

Table 6.3.
Experimental conditions for the sequential elution of thorium and uranium from UTEVA resin with corresponding numerical simulation inputs.
The following constant values are also used: bed length = 1.95 cm; column radius = 0.35 cm; V_{aq} = 0.655; axial division length = 1.95/20 cm; lumped solid extractant concentration = 1.5 mol/dm^3.
Aqueous phase diffusion has not been included in the simulations.

Step		**Sample loading**	**Rinse**	**Thorium elution**	**Uranium elution**
Solution		8M HNO_3	8M HNO_3	6M HCl	0.3M HNO_3
Flow rate (mL/min)		0.15	1.83	1.83	1.83
Volume (mL)		0.025	19.82752	34.57969	34.67384
Iterations		0 - 1	2 - 807	808 - 2214	2215 - end
Concentration (ppm)	**Uranium**	25.0	0	0	0
	Thorium	25.2	0	0	0
$\vec{k}$	**Uranium**	1.006	1.006	0.58	0.053
	Thorium	0.3417	0.3417	1.8×10^{-3}	2.0×10^{-3}
$\overleftarrow{k}$	**Uranium**	4.483×10^{-3}	4.483×10^{-3}	1.7×10^{-3}	6.9×10^{-3}
	Thorium	2.656×10^{-3}	2.656×10^{-3}	9.0×10^{-3}	1.0×10^{-2}
k_D	**Uranium**	459	459	700	16
	Thorium	592	592	1*	1*

*Estimated values.

The values of $\vec{k}$ and $\overleftarrow{k}$ were calculated from batch sorption/desorption experiments, with the forward rate constants corrected to account for the lumped solid extractant concentration ($[s]_E$).

For 8M HNO_3 solutions these values were the same as those used in the previous multiple analyte numerical simulations (Table 6.1.) whilst the rate constants for 6M HCl and 0.3M HNO_3 solutions were estimated from two sets of batch desorption experiments. In these experiments, an 8M HNO_3 solution containing both uranium and thorium was equilibrated with UTEVA resin for 24 hours before separation of the aqueous and solid phases. After the solid phase had been left to air dry, a set mass was taken and mixed with either 6M HCl or 0.3M HNO_3. The calculated distribution constant (k_D) for thorium in both 6M HCl and 0.3M HNO_3 were <0 as the measured concentration in the aqueous phase after 24 hours was greater than the maximum expected concentration assuming total desorption. This impossible result could be due to uncertainties with the calculated solid concentration or the applied volume correction factor. An estimated k_D value of 1 was therefore chosen for thorium sorption in both of these solutions. This estimate is similar to the value quoted in the literature[70] for 6M HCl but a little low for 0.3M HNO_3 (k' for Th(IV) in 6 M HCl ~0.9; k' for Th(IV) in 0.3M HNO_3 ~5; assuming $k_D/k' = 1.7$). The calculated distribution constants for uranium in 6M HCl and 0.3M HNO_3 were both positive values with UTEVA resin having a strong affinity for uranium in 6M HCl and a weak affinity in 0.3M HNO_3. The calculated k_D value for 0.3M HNO_3 was similar to the literature[70] value whereas the 6M HCl value was slightly higher (k' for U(VI) in 6 M HCl ~200; k' for U(VI) in 0.3M HNO_3 ~20; assuming $k_D/k' = 1.7$). For uranium and thorium in both solutions, equations involving the initial rate of desorption, distribution constant and lumped solid extractant concentration were used to calculate the forward and reverse rate constants. These input parameters were only estimated to two significant figures and are likely to be of low accuracy due to the small amount of experimental data used and large uncertainties in the multi-step desorption procedure.

The multiple analyte numerical simulation method using the described input parameters (Table 6.3.) gave a moderately accurate description of the experimental dataset for the sequential thorium and uranium elution procedure (Figure 6.15.). The greater width of the uranium elution peak (in comparison to the thorium elution peak) was reflected in the simulated data due to the difference in estimated distribution constants on UTEVA resin between thorium in 6M HCl ($k_D = 1$) and uranium in 0.3M HNO_3 ($k_D = 16$).

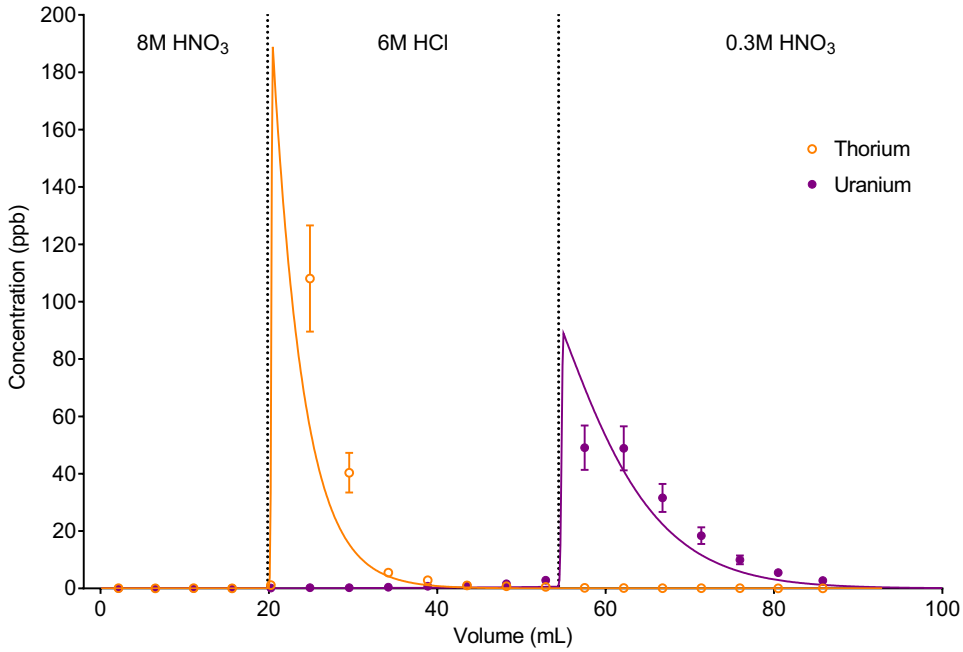

Figure 6.15.
Comparison between experimental data and numerical simulation of uranium and thorium elution profiles from UTEVA resin using a programmatically input elution sequence (Table 6.3.).
Both analytes were simulated simultaneously. The vertical dotted lines show the volumes at which the step changes in reagent were made.

The accuracy of the numerical simulation method could be improved by gaining a better estimate of the forward and reverse rate constants for uranium and thorium during the two elution steps. For conditions where an analyte is weakly retained on the sorptive material, the $\vec{k}/\overleftarrow{k}$ ratio could be more accurately determined by conducting batch sorption experiments using an increased solid/aqueous ratio (> 0.1 g / 10 mL). Using a larger solid/aqueous ratio would, however, make it harder to measure the initial rate of sorption due to equilibrium being obtained in a shorter amount of time. Nevertheless, a better estimate of the $\vec{k}/\overleftarrow{k}$ ratio could allow for the magnitude of the two values to be fitted using data obtained by column experiments.

Another factor reducing the accuracy of the modified numerical simulation method described is the use of a single pair of rate constants for each analyte. This 1D set of parameters is input into the differential equations describing the transfer of analyte between the aqueous and solid phases in each axial division. Upon a step change in reagent, the 1D set of parameters are replaced with new values according to the new reagent. This implies an immediate change in environment (or acid concentration) over the whole column length. This is incorrect as the new reagent is added to the top of column. Whilst this simplification may produce reasonable results for short columns, the deviation between experimental and simulation datasets is expected to be larger for longer bed lengths. The LabVIEW coding could therefore be modified to better simulate

a step change in reagent by replacing the 1D set of rate constants with a 2D array allowing for the new parameters to be introduced at the top axial division and progress down the column. A further complication is that the change in environment (or acid concentration) in each axial division may not be a step change; instead a gradient may form between the existing and new reagents. This effect would be further increased if mixing between reagents occurred in the tubing prior to delivery to the top of the column. Intermediate rate constants could be included to simulate this phenomenon. Once better estimates of forward and reverse rate constants for uranium and thorium sorption/desorption between UTEVA resin and 6M HCl / 0.3M HNO_3 have been calculated via batch experiments with a lower degree of uncertainty, the impact of replacing the 1D set of parameters with a 2D array using either step changes or gradient changes in values can be investigated.

Some further research is needed to improve the numerical simulation method for the description of radioanalytical separations on UTEVA resin. This includes gaining a better understanding of step changes in reagent as well as conducting more investigations into processes occurring at very slow and very fast flow rates. Separation of axial dispersion and molecular diffusion can be made by investigating the relationship between flow rate and the shape of breakthrough profiles at slow flow rates. This would improve the selection of axial division length and aqueous phase diffusion rate constants. The gradual build of flow rate due to backpressure could be reduced by employing an alternative column configuration with less dead volume such as pre-packed cartridges. Minimisation of this physical process and measurement of organic species in the column output solution would allow for a better estimation of the extent of organic solvent leaching at fast flow rates. This could be included in the numerical simulation method by modification of the backward rate constant. Once these processes are better understood, the LabVIEW coding could be published as user-friendly software.

Publication of a LabVIEW project as software removes access to the *block diagram*, leaving only the *front panel* of the main *VI* for the user to interact with. This means that coding for the numerical simulation method that has been developed including the *ODE solver* with model constants, differential equations and simulation parameters (see Chapter 4) along with *while loops*, *case structures*, *subVI*s, functions for storing and outputting data and all other necessary functions would be fixed. The end-user would be able to control a selection of input variables and view the results of the simulation either on a graph within the software and/or as an exported dataset accessible using common spreadsheet applications (e.g. Microsoft Excel).

The specifications of the published software would need to match the requirements of the end-user. These requirements could be gathered through discussions with radiochemical analysts and researchers working in radioanalytical method development. It may be that two versions of the software should be produced; one version with the full range of functionality including aqueous phase diffusion, organic solvent leaching and the ability to select the concentration of analytes and interfering species in the sample for use as a method development tool and another version with a restricted range of flow rate inputs and set sample composition to support routine analysis.

Radiochemical analysis of samples from nuclear decommissioning, NORM industries or environmental surveys is carried out in order to determine the concentration of radionuclides. The analyte concentration in the sample undergoing chromatographic separation is therefore unknown. The concentration of radionuclides is typically low in relation to stable isotopes even after preconcentration and initial separation steps for removal of bulk matrix elements. An expected sample composition for each matrix could therefore be used provided the unknown radionuclide concentration is sufficiently low (within the linear part of the sorption isotherm). Development of a database of matrix compositions could be used to tailor the same chromatographic procedure to multiple different sample types. Sample matrix selection could be achieved in published numerical simulation software using a drop-down menu (*ring* or *enum control* function) with a link to an editable spreadsheet file. This database could then be extended to include additional matrix types with expected composition determined by published data or stable isotope characterisation.

Restricting the range of flow rate inputs to values where aqueous phase diffusion and organic solvent leaching are negligible would allow for simpler differential equations and hence quicker simulation time. As one of the main advantages of automated radioanalytical separation systems is the reduced time taken to carry out chromatographic procedures, it is likely that the flow rate through the column would be increased above the rate of gravity flow and therefore sufficiently high enough that aqueous phase diffusion could be ignored. The exception to this situation is if flow through the column is stopped to allow for kinetically slow processes to occur. For example, a pause of at least 7 minutes was required for the complete reduction of Np(IV) to Np(III) in a method for the separation of actinides using TEVA and DGA resins[68]. Additionally, very fast flow rates leading to loss of the immobilised solvent extractant would be avoided particularly if the sorptive material was to be reused. This could mean that inclusion of leaching rate in the numerical simulation method would be unnecessary. Conversely, if a packed bed was to be reused multiple times using moderate to slow flow rates, the small drop in capacity between uses may need to be included in the coding.

The different motivations for conducting simulations of radioanalytical chromatographic separations dictate the desired data output format. A more qualitative and temporary format such as an on-screen graph or value indicator may be required to support a routine analysis whereas a full quantitative dataset may need to be saved for comparison between different column operating conditions for optimisation of a new method. Different options for the export of numerical data are available in LabVIEW including automatic generation of sequentially numbered spreadsheet files or the use of a user prompt to specify the output destination and file name. The most important data output (by display or saved data) is likely to be the concentration profile in the column output solution for all chosen analytes. This output could also be used to programmatically determine the fraction volume needed to collect a specified percentage of the total analyte amount and/or achieve a specified decontamination factor. Another possible output value of interest is the total activity remaining on the column. This may be important in single use columns for effective waste management or for carryover calculation in multiple use columns. Storage of information between simulations for multiple use columns such as remaining on-column activity or capacity reduction is possible through the use of *while loops* and *shift registers* and even after closing and reopening the application through the use of externally saved data files. All of these potential data output considerations depend on the intended use of the numerical simulation software. One potential application is the use of simulation prior to bespoke chromatographic separation using an automated radioanalytical system. As control software written in LabVIEW is already in use for automated systems[29,51–54], it is possible that the elution sequence could be optimised using a numerical simulation method and the resulting sample/reagent volumes and flow rates fed directly in to the linked or integrated control software.

The numerical simulation method has been shown to accurately describe breakthrough profiles of uranium and thorium from 8M HNO_3. The further research needed to improve the simulation of elution profiles using step changes to either 6M HCl or 0.3M HNO_3 has also been discussed. It is proposed, however, that the numerical simulation method could be easily extended to other extraction chromatographic resins covering a wide range of analyte separation procedures using various reagents. Providing the kinetics of sorption/desorption can be described using a single pair of differential equations, the equation parameters (forward and reverse rate constants, lumped solid extractant concentration, stoichiometric relationship and ratio of solid to aqueous phases) could be programmatically input using a drop-down menu in a similar way to the suggested method for typical sample matrix compositions. By using a ring or enumerated control function, selection of an option could programmatically retrieve data from a particular row of an

external spreadsheet file relating to that choice. The list of choices would be set by reading from the external file. Using this method the database of analyte-sorptive material kinetics could be expanded upon without modification of the LabVIEW coding. Consideration into the design of software using drop-down menu functionality would have to be taken to reduce the amount of times the application has to open and close files in order to minimise computation time. This could be achieved by a simulation set up step prior to execution of the numerical simulation method.

Unfortunately, understanding of the differential equations needed to fully describe more complex porous materials such as anion exchange resin is not yet sufficient to be included in numerical simulation software (see Chapter 5). For materials exhibiting similar kinetic behaviour to UTEVA resin, the appropriate input parameters can be readily determined by a series of batch experiments. The forward rate constant ($\vec{k}$) can be calculated by dividing the initial slope of concentration change in the lumped solid phase by the initial concentration in the aqueous phase. It is recommended that as short a mixing time as practically possible with a low solid/aqueous ratio (0.01 g / 10 mL) is used to improve the accuracy of this measurement. The reverse rate constant ($\overleftarrow{k}$) is then calculated by dividing the concentration ratio (solid/aqueous) at equilibrium by the forward rate constant. It is recommended that a moderate solid/aqueous ratio (0.1 g / 10 mL) is used if the analyte is strongly retained on the resin under the conditions investigated and a higher solid/aqueous ratio (1 g / 10 mL) if the analyte is weakly retained. Accurate measurement of low k_D values is important as a difference between a distribution constant of 1 or 10 can have a large impact on the width of the elution profile (Figure 6.15.). The lumped solid extractant concentration and stoichiometric relationships are harder to determine. The method carried out previously (Chapter 4) used a combination of distribution constant measurements at a range of initial analyte concentrations and knowledge of the structure of the complexed species to propose differential equations for the simultaneous sorption of two species. These equations were tested using the numerical simulation method for batch sorption/desorption and a binary analyte experiment where the effect of high concentration was observed on both species. The forward rate constant must also be modified to account for the $[s]_E$ term. Finally, the ratio of aqueous to lumped solid phase in the packed bed geometry can be measured by volumetric displacement measurements. Data gathered using this series of lab based measurements should be sufficient to generate all the parameters necessary to add a new system to the proposed numerical simulation software external database.

Regardless of the exact nature of a potential chromatographic simulation tool for radiochemical analysts, a few features are likely to be required (Table 6.4.). These features include input of column dimensions, selection of an elution sequence including sample introduction, a rinse step and one or more elution steps and output of the simulated dataset either via an on-screen display or exportation to an external file. As LabVIEW is a visual programming language, it is easy to display these controls and indicators in an intuitive graphical interface. A combination of versatility and accessibility will make the proposed numerical simulation software a useful tool for research scientists and radiochemical analysts.

Table 6.4.
List of software features likely to be required in any potential numerical simulation software.

Software feature	Possible formats
Column radius control	Typed numerical input
Bed length control	Typed numerical input (rounded to multiple of axial division length)
Resin selection	Drop-down menu
Elution sequence control	Input of solution, volume and flow rate in specified order
Sample composition	Drop-down menu or numerical input of concentrations
Sample and reagent solution selection	Drop-down menu
Sample and reagent volume control	Typed numerical input
Sample and reagent flow rate control	Typed numerical input (possible upper and lower limit restrictions)
Data output	On-screen graph, on-screen value, exported dataset

6.3. Conclusions

A LabVIEW based numerical simulation method developed for the description of chromatographic breakthrough profiles has been successfully extended to allow for the simultaneous simulation of multiple analytes with the ability to control a large range of column operating parameters including analyte concentration and sample loading volume. This method also has the flexibility to simulate complete elution sequences typical of radioanalytical separation procedures.

Using the interaction of uranium and thorium with UTEVA resin as a case study, the numerical simulation method was shown to predict the relationship between sample loading conditions (volume and analyte concentration) and the shape of breakthrough profiles. This relationship is not included in the Gaussian single equation model for predicting column output behaviour. The Gaussian model is therefore limited to low concentration and small volume loading conditions. The modified Bohart-Adams model for use with discrete loading volumes, whilst able to predict the change in peak position due to loading concentration, was unable to account for loading volume. In addition, the Bohart-Adams constant was shown to not be a constant value when applying the equation in the differentiated form with a complex relationship to bed length, flow

rate and loading concentration. Both single equation models failed to describe the increased asymmetry of breakthrough profiles under short bed length conditions and for flow rates that are slower or faster than the optimum value. The multiple different combinations of column operating parameters (analyte concentration, loading volume, bed length, column radius and flow rate) restricts the application of single equation models to a small range of experimental conditions. The mechanistic nature of the numerical simulation method is able to overcome these restrictions and generate any shape of breakthrough profile. The main reason for a difference between experimental and simulated datasets is the introduction of additional chemical or physical processes previously unaccounted for. These processes are likely to impact under extreme conditions; for example, significant leaching of extractant at very fast flow rates. These processes could either be introduced into the numerical simulation method or the range of the input parameter restricted.

Another advantage of the numerical simulation method is the ability to simulate complex elution sequences. Although further work is needed to improve the estimation of rate constants for eluting reagents and better validate the method, the potential to programmatically introduce step changes in reagent has been demonstrated. Guidance on the experimental techniques required to improve rate constant estimations and calculate rate constants for a larger range of analytes, reagents and sorptive materials has also been given. Following this guidance would allow for the creation of an expandable database of elution sequences that could be programmatically selected in order to simulate any radioanalytical chromatographic separation procedure. The described numerical simulation method therefore shows potential for publication as a user-friendly software tool for assisting in method development or routine radiochemical analysis.

Chapter 7: Overall Conclusions and Future Work

This thesis describes the development of a numerical simulation method for the description of radioanalytical chromatographic separations using LabVIEW visual programming language. The method, based on numerical solution of ordinary differential equations, was optimised using experimental batch sorption/desorption data (Chapter 4) before being applied to the breakthrough of analytes from a packed bed geometry (Chapter 5). The numerical simulation method was shown to have clear advantages over single equation models and great potential for development into a user friendly software tool (Chapter 6).

The numerical simulation method was shown to be suitable for describing systems using extraction chromatography resins as demonstrated by simulations of the interaction of dissolved uranium and thorium species with UTEVA resin. Under conditions of constant mixing, the batch sorption/desorption of either analyte could be accurately described using a single pair of differential equations indicating that internal diffusion was not a significant contributor to kinetics. An initial investigation into aqueous phase diffusion was carried out by conducting stationary batch experiments. It was found that division of the aqueous phase into two sections was required to accurately simulate the empirical data. The ratio of these sections was related to the volume of settled material. These findings could be further investigated by conducting additional stationary batch experiments using a range of container geometries and solid/aqueous ratios.

The differential equations developed for describing the interaction of uranium and thorium with UTEVA resin under batch conditions were successfully applied to chromatographic breakthrough conditions by division of the column into equally sized vertical sections. Further experiments at slow flow rates are needed to improve the estimate of both eddy dispersion and molecular diffusion and better inform the selection of axial division length. At faster flow rates, physical processes such as backpressure and extractant leaching were hypothesised to occur. This is another area for future research via investigation of flow rates produced under different column geometries and the measurement of organic species in the column output solution.

The numerical simulation method was also applied to two porous ion exchangers (anion exchange resin and zirconium phosphate). The method was able to describe the kinetics of sorption/desorption under batch conditions through the inclusion of additional differential equations describing internal diffusion. Transferring the equations to the packed bed geometry,

however, failed to accurately describe the experimental breakthrough results. In addition, an investigation into the breakthrough of Ba-133 from a zirconium phosphate column under continuous loading conditions over an extended period of time indicated that the previous assumption that the internal diffusion constant parameter was linearly related to the solid/aqueous ratio was incorrect. Additional batch experiments using a range of solid/aqueous ratios are therefore needed to better understand the process of internal diffusion in both of the porous materials.

It is possible that the numerical simulation method may require the inclusion of both pore diffusion and surface diffusion to accurately simulate chromatographic breakthrough profiles for porous materials. Pore diffusion was suggested as a reason for differences in the width of the breakthrough profile of an inert tracer (tritiated water) between the porous and non-porous materials. Other possible explanations for the lack of agreement between the simulated and experimental breakthrough profiles include oversimplification of internal diffusion through the assumption of Fickian kinetics and a homogeneous pore structure or an insufficient amount of radial divisions. A more accurate numerical simulation method for porous materials may require the use of partial differential equations describing concentration change in terms of both time and radial position.

Extension of the numerical simulation method from discrete volume chromatographic breakthrough conditions to more complex radioanalytical separation sequences was also discussed. Addition of a parameter quantifying the concentration of extractant in the lumped solid phase as well as modification of the differential equations to include the stoichiometric relationships of both uranium and thorium with the extractant allowed for the simultaneous simulation of the interaction of both analytes with UTEVA resin. Unlike the single analyte numerical simulation method, the modified method for multiple analytes was shown to generate accurate results for batch experiments using a high initial analyte concentration in the aqueous phase. The impact of higher loading concentrations on the shape of chromatographic breakthrough profiles was dependent on the loading volume and the bed length; this relationship was observed in both experimental data and the multiple analyte numerical simulation method.

The numerical simulation method was demonstrated to be more flexible than single equation models for prediction of either batch sorption/desorption or chromatographic breakthrough. The mechanistic nature of the method should allow for the simulation of any separation sequence providing sufficient estimations of the input parameters are made. Most of these parameters can be determined by simple batch experiments. Future work could therefore involve adding more materials, analytes and reagents to a database of input parameters. The direct application of

equations developed to describe batch sorption processes to the column geometry is novel and increases our understanding of the kinetics and thermodynamics of radiochemical separations.

The LabVIEW developed coding has potential for publication as user friendly software. This would be achieved by gathering information on the desired specifications and making decisions on which chromatographic processes to include based on the level of accuracy required and the computational demands. The database of input parameters could be added to without further amendment of the software through the use of an offline spreadsheet from which data would be programmatically extracted. This would make the numerical simulation software a useful tool in radiochemical method development. The researcher or analyst would have the ability to control a large variety of column operating parameters including bed length, column radius, sorptive material, sample loading conditions and elution sequence (reagent volume and flow rate) and obtain data on predicted breakthrough/elution profiles much faster than by conducting lab-based experiments. This is particularly important for supporting the development of rapid and automated radioanalytical techniques where flow through a chromatographic column is increased above the rate at which the separation procedure was originally characterised. Rapid and automated radioanalytical techniques for radioactive waste characterisation will lead to considerable economic savings for the UK's nuclear decommissioning industry through lower analyst input, faster turnaround, optimisation of reagent use and an increased quality of results.

Appendix A: Additional Figures for Chapter 5

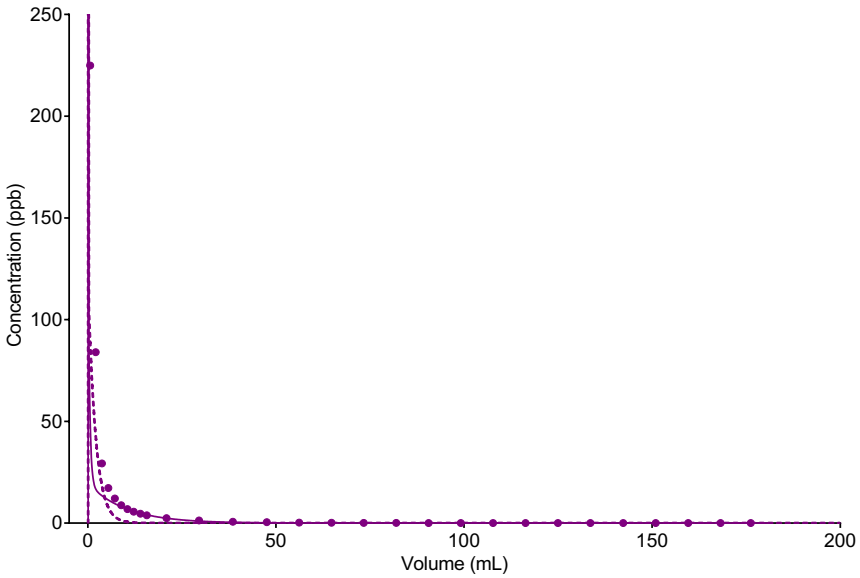

Figure A.1.
Comparison between experimental data and numerical simulation of uranium breakthrough profiles from anion exchange resin in 8M HNO_3 under conditions corresponding to experiment 8 (Table 5.1.).
The two analytes (uranium and thorium) have been simulated separately. Axial division length = 0.95/10 cm. Aqueous phase diffusion has not been included in the simulations.
The value for the internal rate constant is either equal to (dashed line) or calculated from (solid line) that determined from 0.1 g solid batch sorption/desorption experiments.

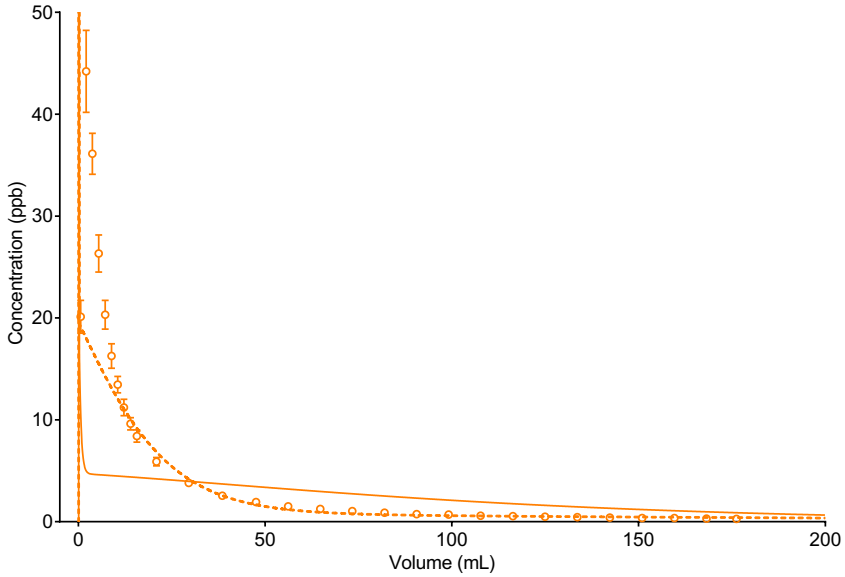

Figure A.2.
Comparison between experimental data and numerical simulation of thorium breakthrough profiles from anion exchange resin in 8M HNO_3 under conditions corresponding to experiment 8 (Table 5.1.).
The two analytes (uranium and thorium) have been simulated separately. Axial division length = 0.95/10 cm. Aqueous phase diffusion has not been included in the simulations.
The value for the internal rate constant is either equal to (dashed line) or calculated from (solid line) that determined from 0.1 g solid batch sorption/desorption experiments.

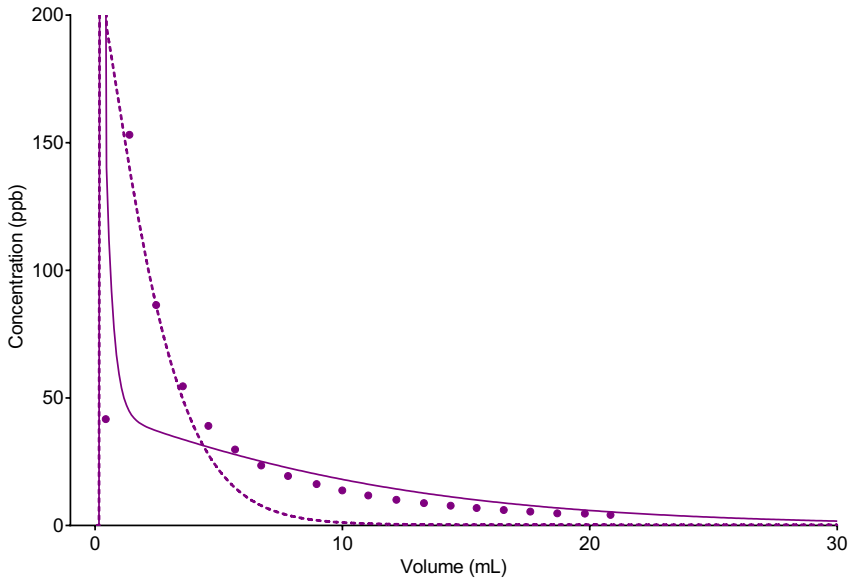

Figure A.3.
Comparison between experimental data and numerical simulation of uranium breakthrough profiles from anion exchange resin in 8M HNO_3 under conditions corresponding to experiment 9 (Table 5.1.).
The two analytes (uranium and thorium) have been simulated separately. Axial division length = 0.1 cm. Aqueous phase diffusion has not been included in the simulations.
The value for the internal rate constant is either equal to (dashed line) or calculated from (solid line) that determined from 0.1 g solid batch sorption/desorption experiments.

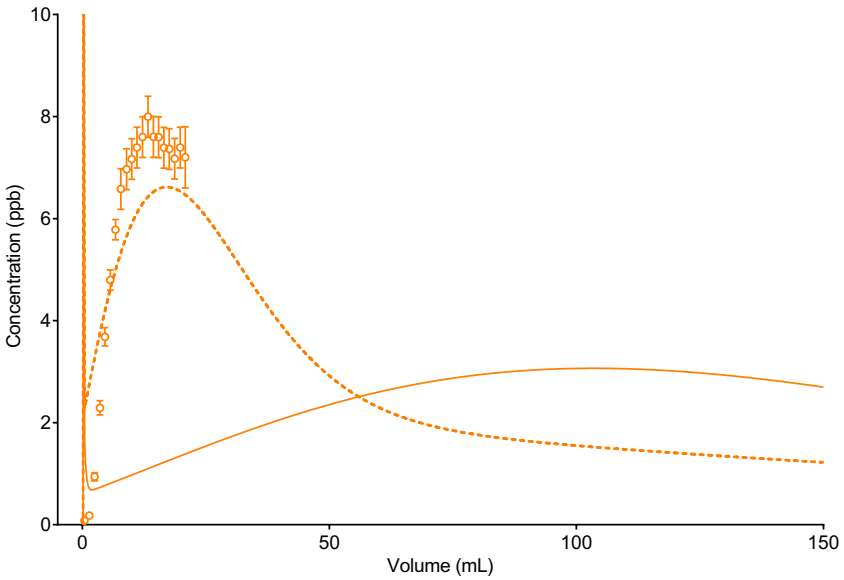

Figure A.4.
Comparison between experimental data and numerical simulation of thorium breakthrough profiles from anion exchange resin in 8M HNO_3 under conditions corresponding to experiment 9 (Table 5.1.).
The two analytes (uranium and thorium) have been simulated separately. Axial division length = 0.1 cm. Aqueous phase diffusion has not been included in the simulations.
The value for the internal rate constant is either equal to (dashed line) or calculated from (solid line) that determined from 0.1 g solid batch sorption/desorption experiments.

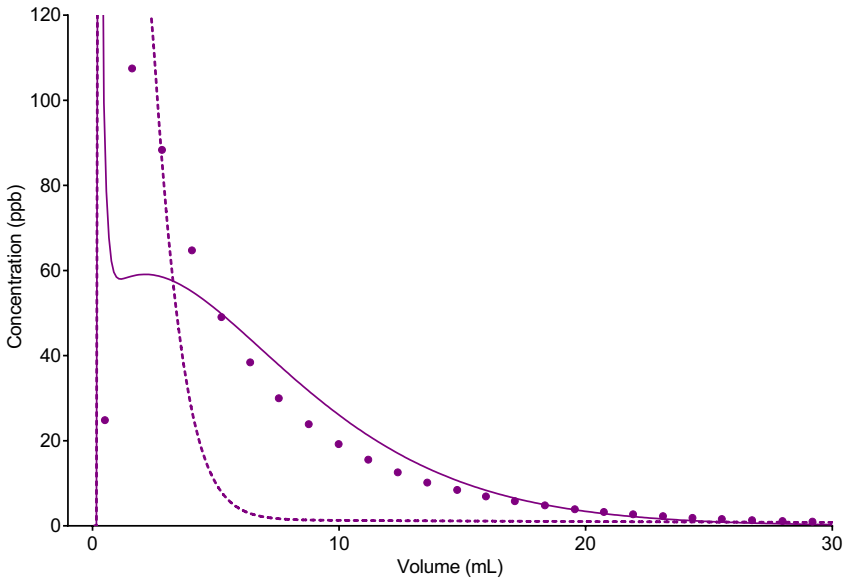

Figure A.5.
Comparison between experimental data and numerical simulation of uranium breakthrough profiles from anion exchange resin in 8M HNO_3 under conditions corresponding to experiment 10 (Table 5.1.).
The two analytes (uranium and thorium) have been simulated separately. Axial division length = 0.1 cm. Aqueous phase diffusion has not been included in the simulations.
The value for the internal rate constant is either equal to (dashed line) or calculated from (solid line) that determined from 0.1 g solid batch sorption/desorption experiments.

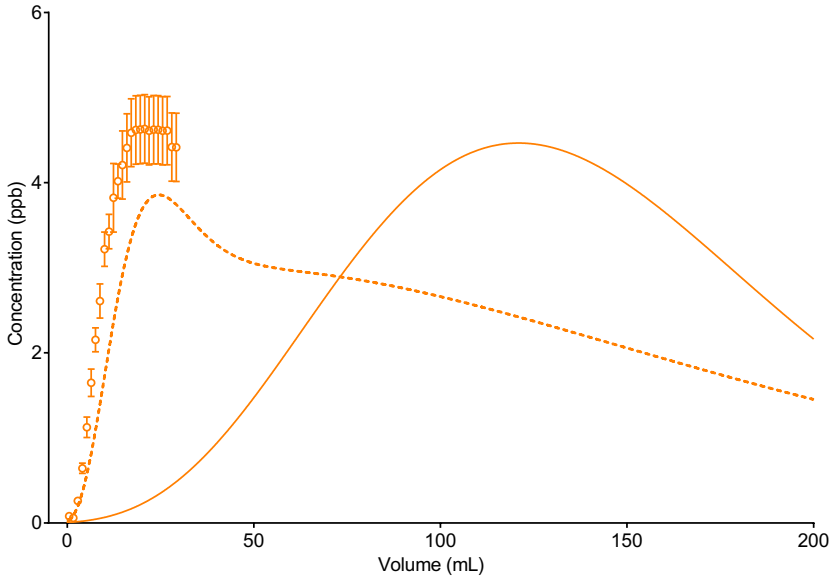

Figure A.6. (Reproduction of Figure 5.12.)
Comparison between experimental data and numerical simulation of thorium breakthrough profiles from anion exchange resin in 8M HNO_3 under conditions corresponding to experiment 10 (Table 5.1.).
The two analytes (uranium and thorium) have been simulated separately. Axial division length = 0.1 cm. Aqueous phase diffusion has not been included in the simulations.
The value for the internal rate constant is either equal to (dashed line) or calculated from (solid line) that determined from 0.1 g solid batch sorption/desorption experiments.

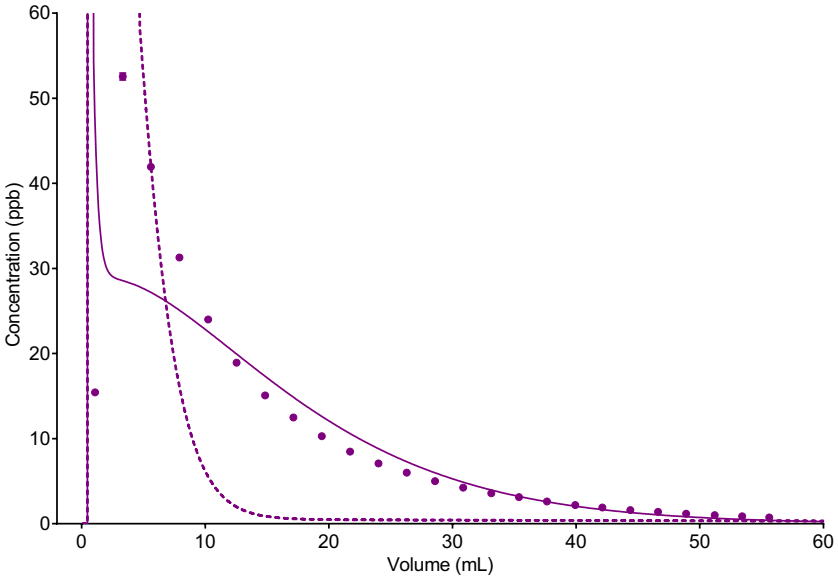

Figure A.7.
Comparison between experimental data and numerical simulation of uranium breakthrough profiles from anion exchange resin in 8M HNO_3 under conditions corresponding to experiment 11 (Table 5.1.).
The two analytes (uranium and thorium) have been simulated separately. Axial division length = 0.1 cm. Aqueous phase diffusion has not been included in the simulations.
The value for the internal rate constant is either equal to (dashed line) or calculated from (solid line) that determined from 0.1 g solid batch sorption/desorption experiments.

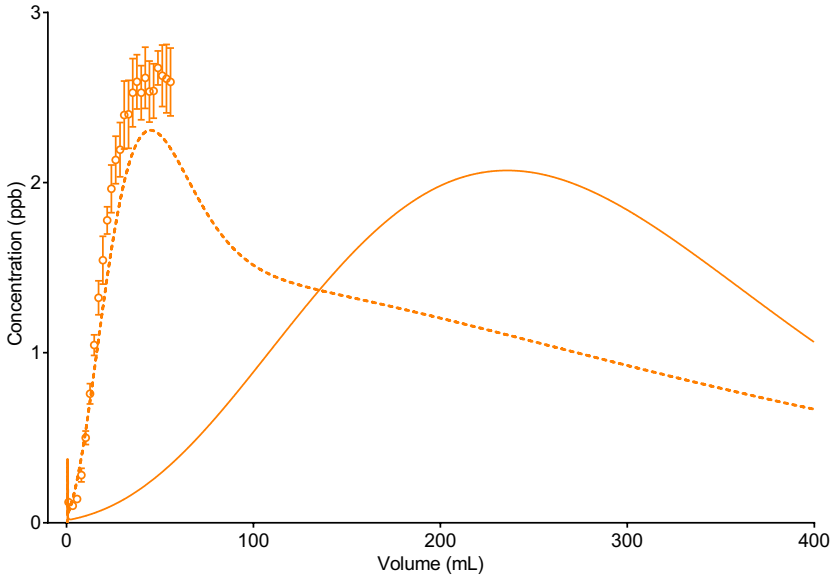

Figure A.8.
Comparison between experimental data and numerical simulation of thorium breakthrough profiles from anion exchange resin in 8M HNO_3 under conditions corresponding to experiment 11 (Table 5.1.).
The two analytes (uranium and thorium) have been simulated separately. Axial division length = 0.1 cm. Aqueous phase diffusion has not been included in the simulations.
The value for the internal rate constant is either equal to (dashed line) or calculated from (solid line) that determined from 0.1 g solid batch sorption/desorption experiments.

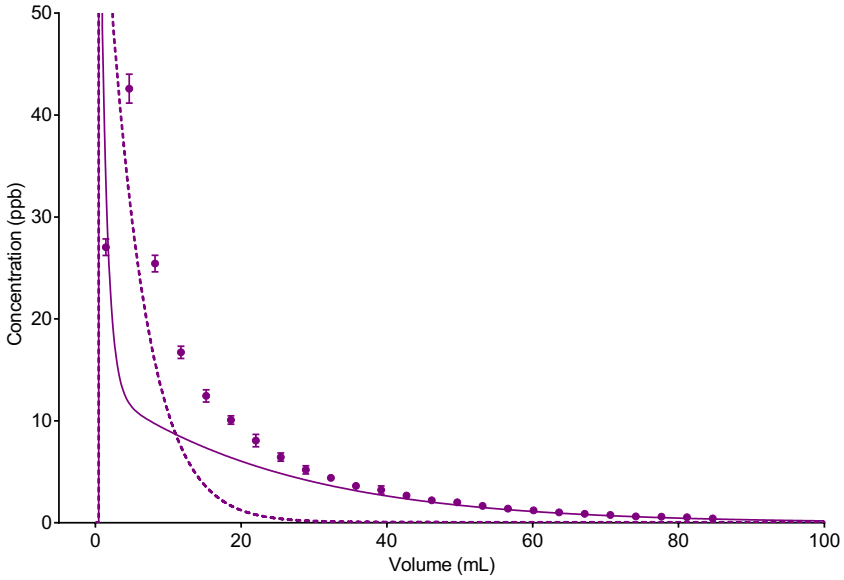

Figure A.9.
Comparison between experimental data and numerical simulation of uranium breakthrough profiles from anion exchange resin in 8M HNO_3 under conditions corresponding to experiment 12 (Table 5.1.).
The two analytes (uranium and thorium) have been simulated separately. Axial division length = 0.1 cm. Aqueous phase diffusion has not been included in the simulations.
The value for the internal rate constant is either equal to (dashed line) or calculated from (solid line) that determined from 0.1 g solid batch sorption/desorption experiments.

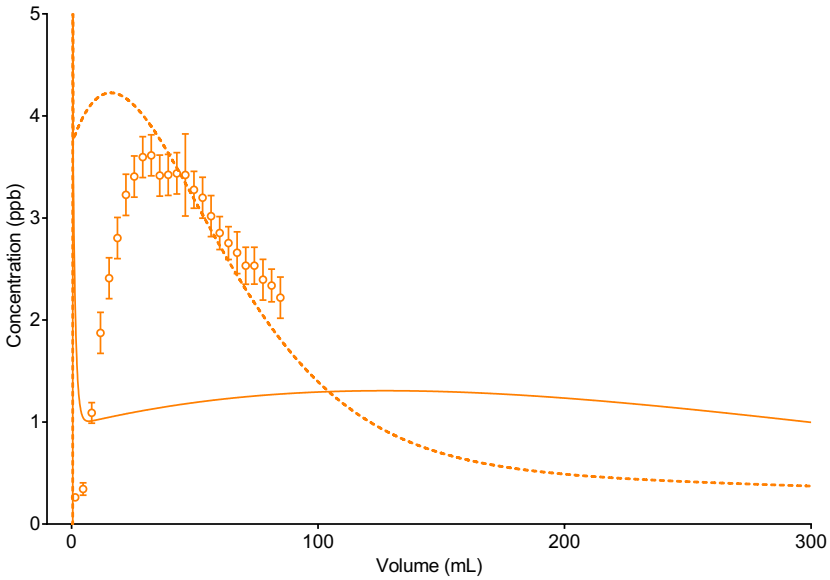

Figure A.10.
Comparison between experimental data and numerical simulation of thorium breakthrough profiles from anion exchange resin in 8M HNO_3 under conditions corresponding to experiment 12 (Table 5.1.).
The two analytes (uranium and thorium) have been simulated separately. Axial division length = 0.1 cm. Aqueous phase diffusion has not been included in the simulations.
The value for the internal rate constant is either equal to (dashed line) or calculated from (solid line) that determined from 0.1 g solid batch sorption/desorption experiments.

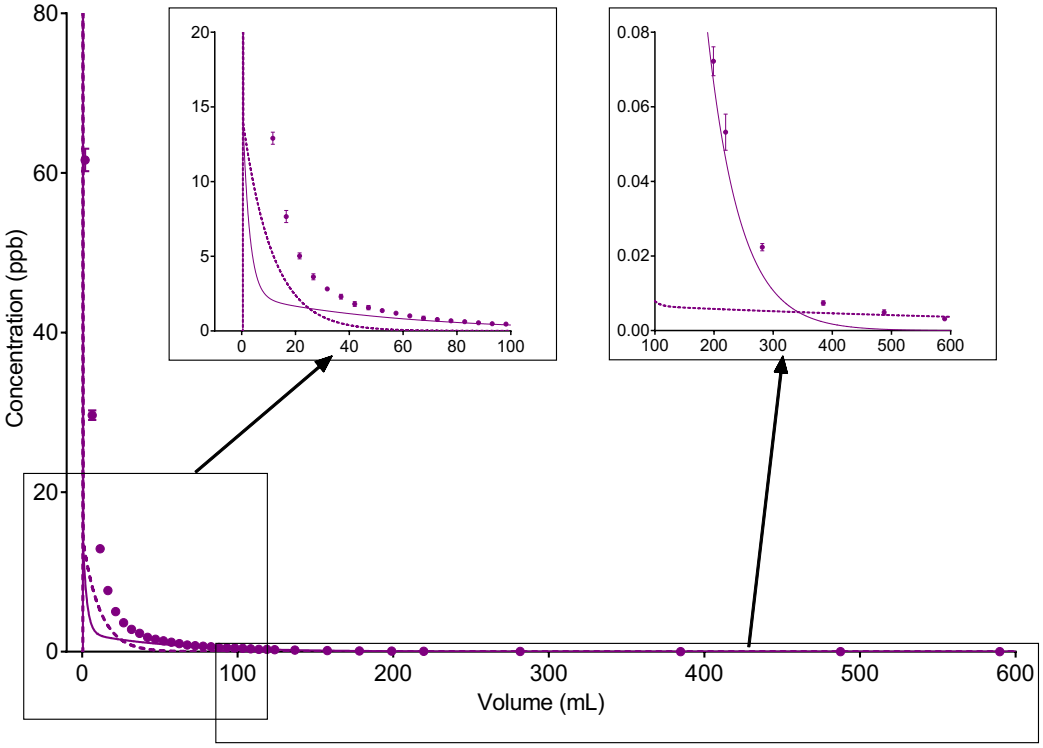

Figure A.11. (Reproduction of Figure 5.13.)
Comparison between experimental data and numerical simulation of uranium breakthrough profiles from anion exchange resin in 8M HNO_3 under conditions corresponding to experiment 13 (Table 5.1.).
The two analytes (uranium and thorium) have been simulated separately. Axial division length = 0.1 cm. Aqueous phase diffusion has not been included in the simulations.
The value for the internal rate constant is either equal to (dashed line) or calculated from (solid line) that determined from 0.1 g solid batch sorption/desorption experiments.

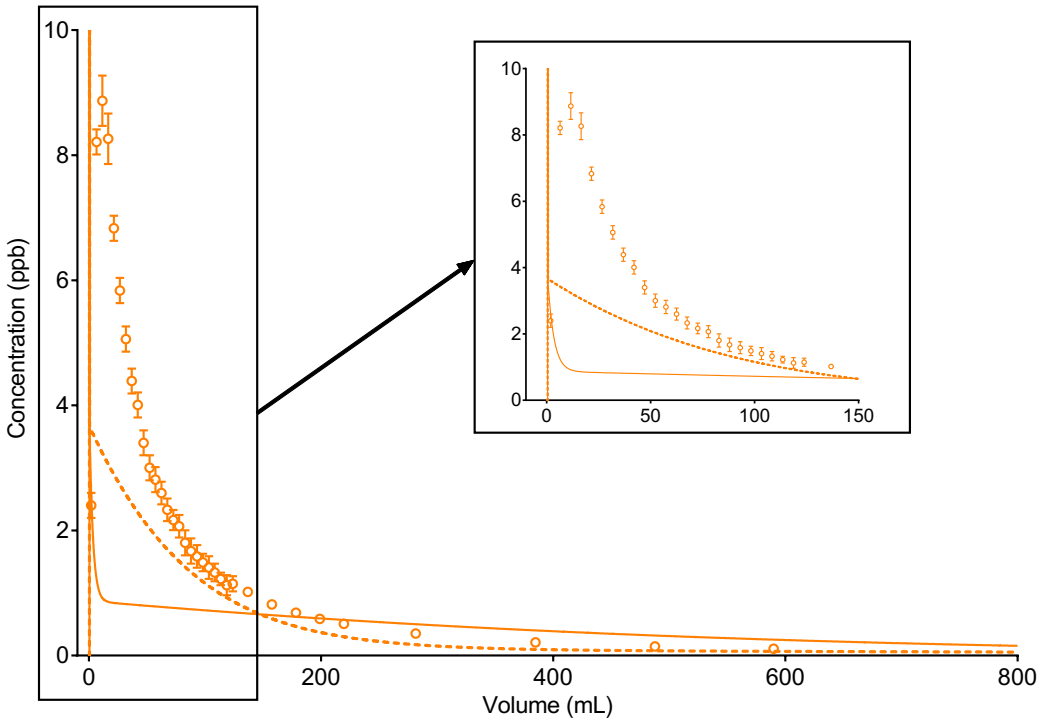

Figure A.12.
Comparison between experimental data and numerical simulation of thorium breakthrough profiles from anion exchange resin in 8M HNO_3 under conditions corresponding to experiment 13 (Table 5.1.).
The two analytes (uranium and thorium) have been simulated separately. Axial division length = 0.1 cm. Aqueous phase diffusion has not been included in the simulations.
The value for the internal rate constant is either equal to (dashed line) or calculated from (solid line) that determined from 0.1 g solid batch sorption/desorption experiments.

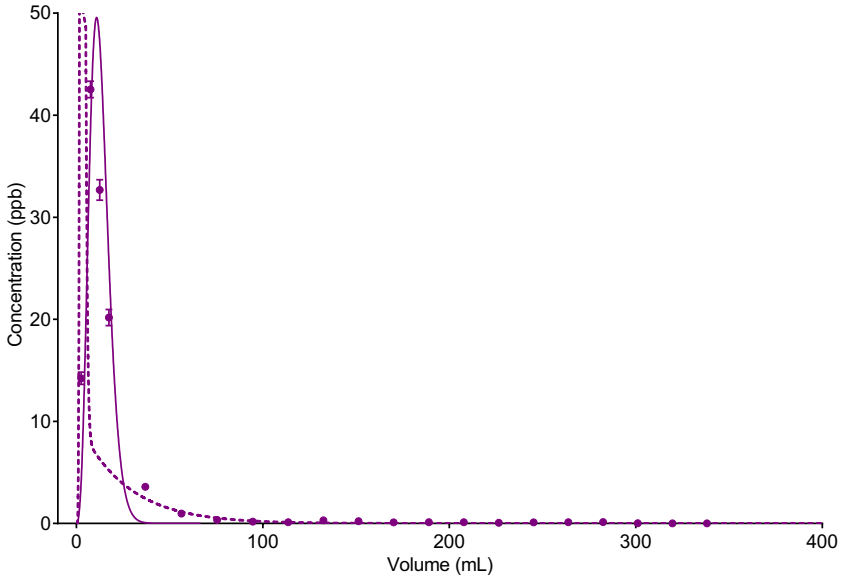

Figure A.13.
Comparison between experimental data and numerical simulation of uranium breakthrough profiles from anion exchange resin in 8M HNO_3 under conditions corresponding to experiment 14 (Table 5.1.).
The two analytes (uranium and thorium) have been simulated separately. Axial division length = 0.1 cm. Aqueous phase diffusion has not been included in the simulations.
The value for the internal rate constant is either equal to (dashed line) or calculated from (solid line) that determined from 0.1 g solid batch sorption/desorption experiments.

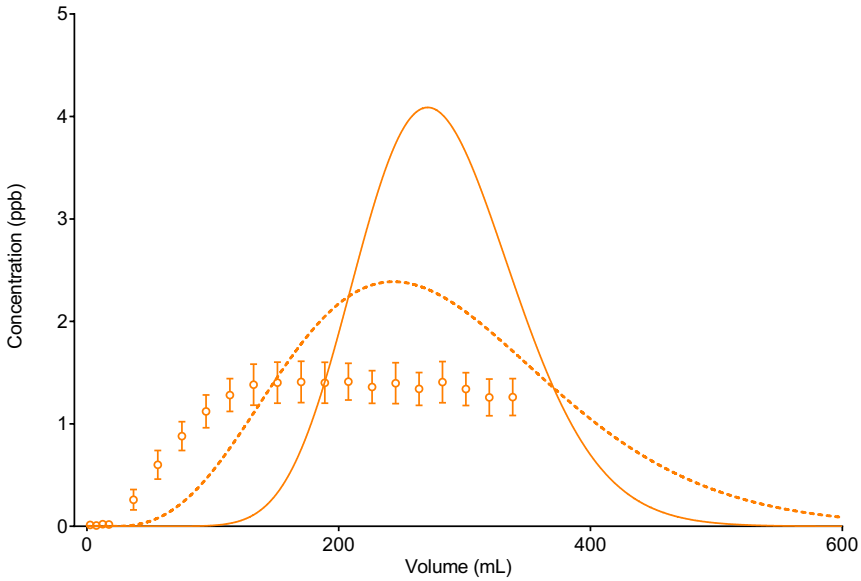

Figure A.14.
Comparison between experimental data and numerical simulation of thorium breakthrough profiles from anion exchange resin in 8M HNO_3 under conditions corresponding to experiment 14 (Table 5.1.).
The two analytes (uranium and thorium) have been simulated separately. Axial division length = 0.1 cm. Aqueous phase diffusion has not been included in the simulations.
The value for the internal rate constant is either equal to (dashed line) or calculated from (solid line) that determined from 0.1 g solid batch sorption/desorption experiments.

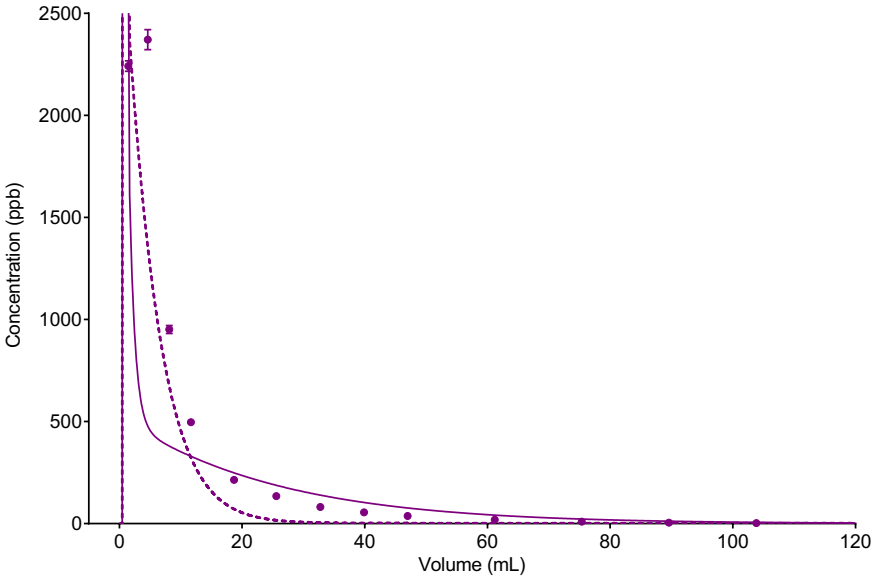

Figure A.15.
Comparison between experimental data and numerical simulation of uranium breakthrough profiles from anion exchange resin in 8M HNO_3 under conditions corresponding to experiment 15 (Table 5.1.).
The two analytes (uranium and thorium) have been simulated separately. Axial division length = 0.1 cm. Aqueous phase diffusion has not been included in the simulations.
The value for the internal rate constant is either equal to (dashed line) or calculated from (solid line) that determined from 0.1 g solid batch sorption/desorption experiments.

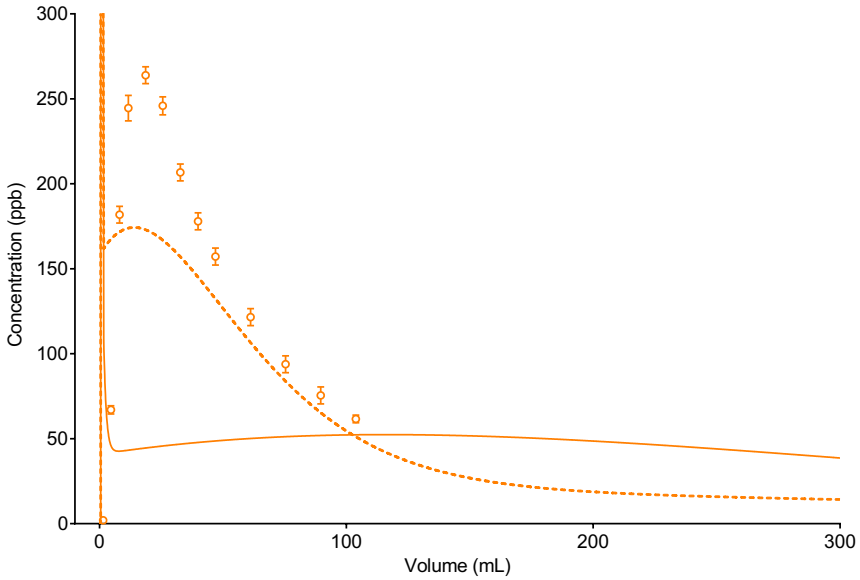

Figure A.16.
Comparison between experimental data and numerical simulation of thorium breakthrough profiles from anion exchange resin in 8M HNO_3 under conditions corresponding to experiment 15 (Table 5.1.).
The two analytes (uranium and thorium) have been simulated separately. Axial division length = 0.1 cm. Aqueous phase diffusion has not been included in the simulations.
The value for the internal rate constant is either equal to (dashed line) or calculated from (solid line) that determined from 0.1 g solid batch sorption/desorption experiments.

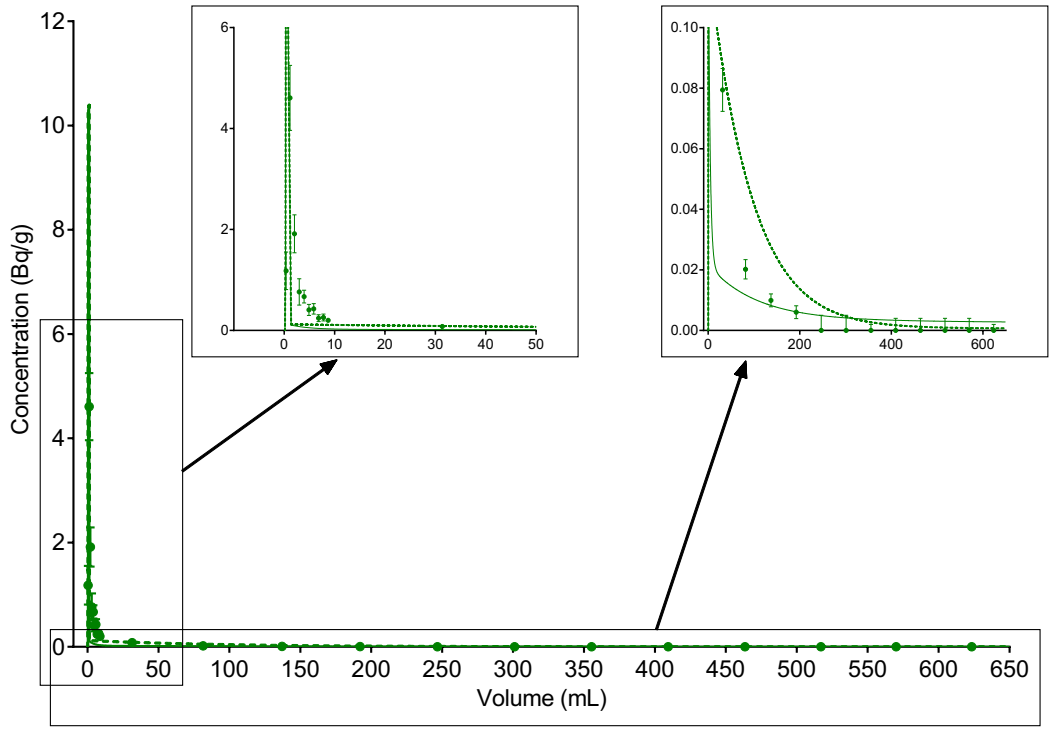

Figure A.17.
Comparison between experimental data and numerical simulation of barium breakthrough profiles from zirconium phosphate in seawater under conditions corresponding to experiment 16 (Table 5.1.).
Axial division length = 0.1 cm. Aqueous phase diffusion has not been included in the simulations.
The value for the internal rate constant is either equal to (dashed line) or calculated from (solid line) that determined from 0.1 g solid batch sorption/desorption experiments.

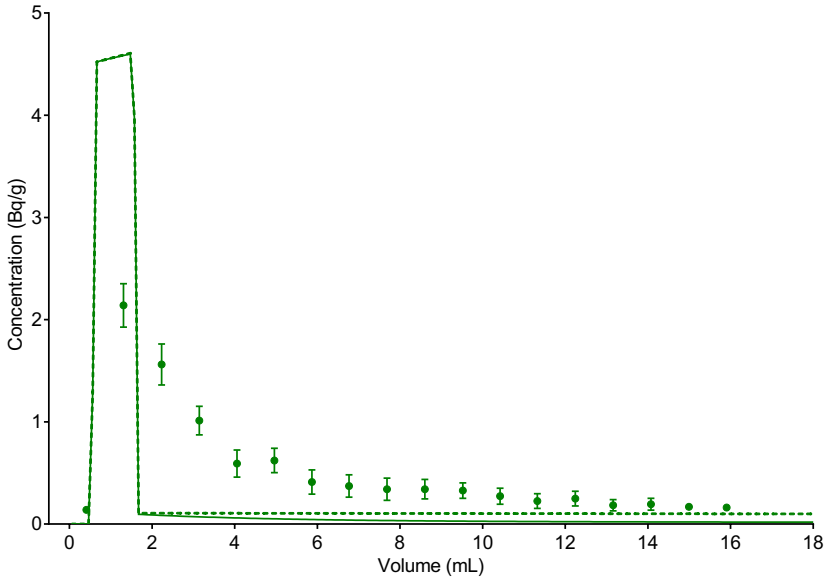

Figure A.18.
Comparison between experimental data and numerical simulation of barium breakthrough profiles from zirconium phosphate in seawater under conditions corresponding to experiment 17 (Table 5.1.).
Axial division length = 0.1 cm. Aqueous phase diffusion has not been included in the simulations.
The value for the internal rate constant is either equal to (dashed line) or calculated from (solid line) that determined from 0.1 g solid batch sorption/desorption experiments.

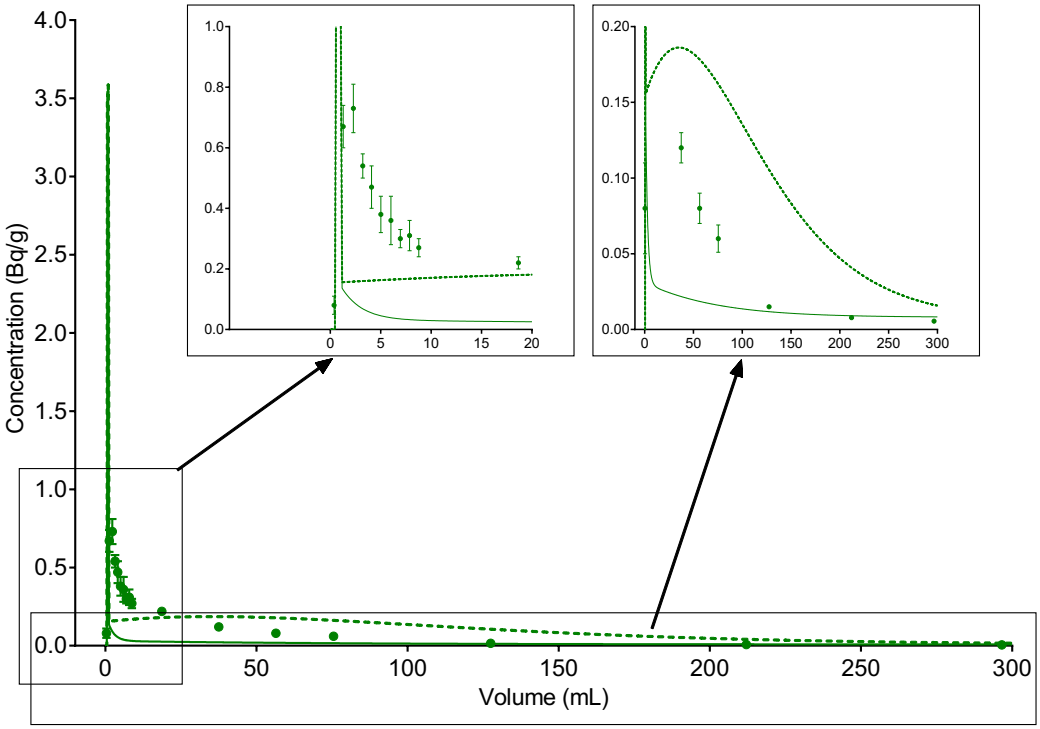

Figure A.19.
Comparison between experimental data and numerical simulation of barium breakthrough profiles from zirconium phosphate in seawater under conditions corresponding to experiment 18 (Table 5.1.).
Axial division length = 0.1 cm. Aqueous phase diffusion has not been included in the simulations.
The value for the internal rate constant is either equal to (dashed line) or calculated from (solid line) that determined from 0.1 g solid batch sorption/desorption experiments.

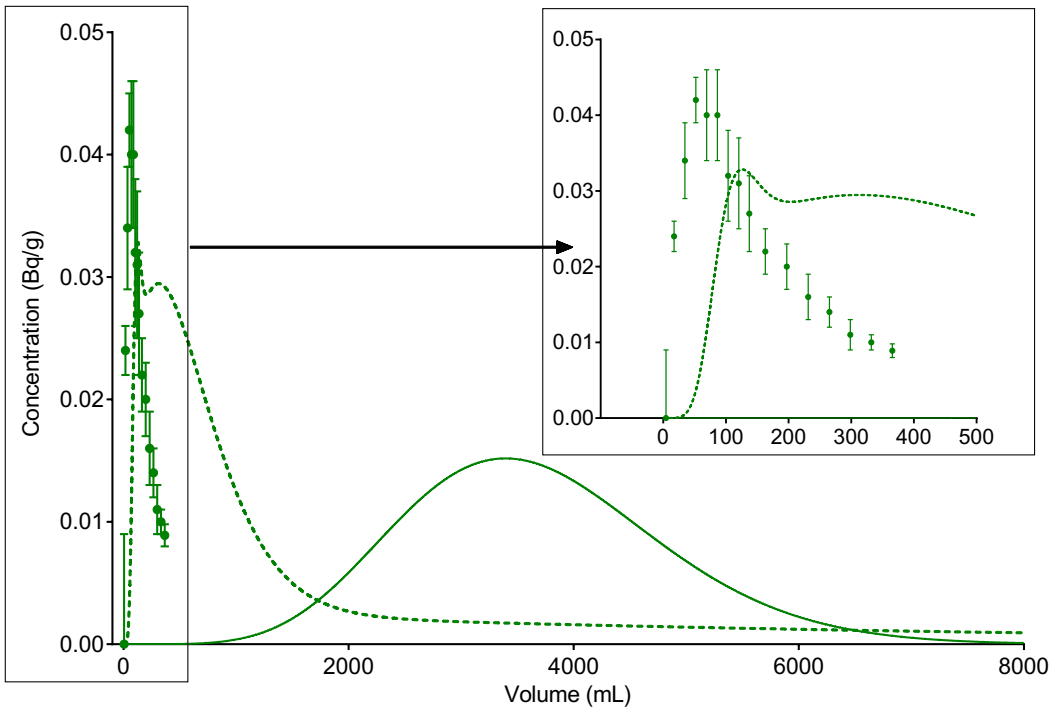

Figure A.20. (Reproduction of Figure 5.14.)
Comparison between experimental data and numerical simulation of barium breakthrough profiles from zirconium phosphate in seawater under conditions corresponding to experiment 19 (Table 5.1.).
Axial division length = 0.1 cm. Aqueous phase diffusion has not been included in the simulations.
The value for the internal rate constant is either equal to (dashed line) or calculated from (solid line) that determined from 0.1 g solid batch sorption/desorption experiments.

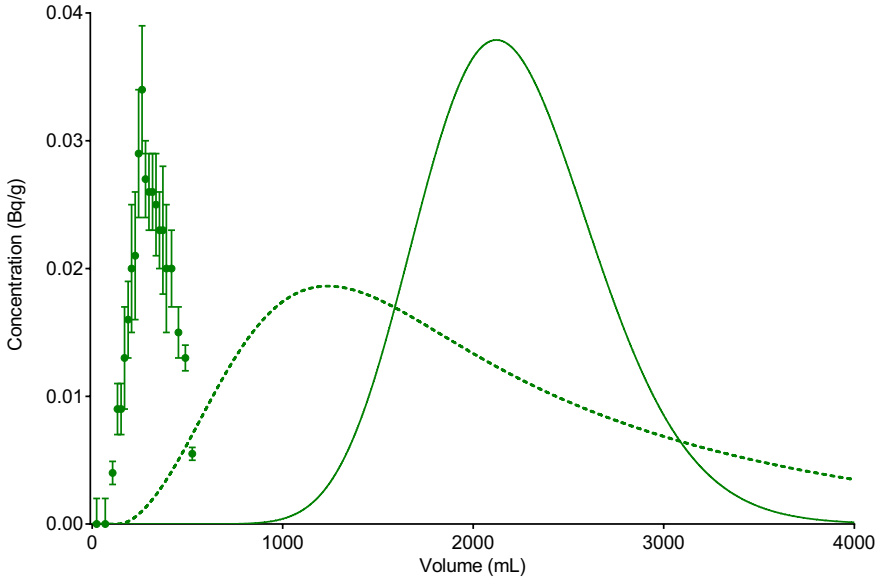

Figure A.21.
Comparison between experimental data and numerical simulation of barium breakthrough profiles from zirconium phosphate in seawater under conditions corresponding to experiment 20 (Table 5.1.).
Axial division length = 0.1 cm. Aqueous phase diffusion has not been included in the simulations.
The value for the internal rate constant is either equal to (dashed line) or calculated from (solid line) that determined from 0.1 g solid batch sorption/desorption experiments.

References

1. Nuclear Decommissioning Authority. *Strategy - effective from April 2016*. (2016).

2. International Atomic Energy Agency. *Managing Low Radioactivity Material from the Decommissioning of Nuclear Facilities*. (2008).

3. Emptage, M., Loudon, D., Mcleod, R., Milburn, H. & Row, N. Characterisation : Challenges and Opportunities – A UK Perspective. in *PREDEC International Symposium on Preparation for Decommissioning* (2016).

4. Nuclear Energy Agency. *Radiological Characterisation for Decommissioning of Nuclear Installations*. (2013).

5. International Atomic Energy Agency. *Strategy and methodology for radioactive waste characterization*. (2007).

6. Kashiwagi, M., Masui, H., Denda, Y., James, D., Lantès, B., Müller, W., Garamszeghy, M., Leganes, J. L., Maxeiner, H. & van Velzen, L. ISO Standardization of the Scaling Factor Method for Low- and Intermediate Level Radioactive Wastes Generated at Nuclear Power Plants. *11th Int. Conf. Environ. Remediat. Radioact. Waste Manag. Parts A B* 625–629 (2007). doi:10.1115/ICEM2007-7015

7. International Atomic Energy Agency. *Determination and Use of Scaling Factors for Waste Characterization in Nuclear Power Plants*. (2009).

8. Sellafield Ltd. *Technical challenges, needs and opportunities in decommissioning of the Sellafield Site*. (2013).

9. Robotics and AI: apply in the Industrial Strategy Challenge Fund. (2017). Available at: https://www.gov.uk/government/news/robotics-and-ai-apply-in-the-industrial-strategy-challenge-fund. (Accessed: 14th July 2017)

10. Liezers, M., Lehn, S. A., Olsen, K. B., Farmer, O. T. & Duckworth, D. C. Determination of plutonium isotope ratios at very low levels by ICP-MS using on-line electrochemically modulated separations. *J. Radioanal. Nucl. Chem.* **282,** 299–304 (2009).

11. Bliznyuk, V. N., Seliman, A. F., Ishchenko, A. A., Derevyanko, N. A. & Devol, T. A. New

Efficient Organic Scintillators Derived from Pyrazoline. *ACS Appl. Mater. Interfaces* **8,** 12843–12851 (2016).

12. Kossert, K. & Mougeot, X. The importance of the beta spectrum calculation for accurate activity determination of 63Ni by means of liquid scintillation counting. *Appl. Radiat. Isot.* **101,** 40–43 (2015).

13. Aggarwal, S. K. Analytical Methods Alpha-particle spectrometry for the determination of alpha emitting isotopes in nuclear environmental and biological samples: past, present and future. *Anal. Methods* **8,** 5353–5371 (2016).

14. Russell, B., García-Miranda, M., Ivanov, P., Garcia-Miranda, M. & Ivanov, P. Development of an optimised method for analysis of 90Sr in decommissioning wastes by triple quadrupole inductively coupled plasma mass spectrometry. *Appl. Radiat. Isot.* **126,** 35–39 (2016).

15. Brennetot, R., Pierry, L., Atamyan, T., Favre, G. & Vailhen, D. Optimisation of the operating conditions of a quadrupole ICP-MS with hexapole collision/reaction cell for the analysis of selenium-79 in spent nuclear fuel using experimental designs. *J. Anal. At. Spectrom.* **23,** 1350–1358 (2008).

16. Comte, J., Bienvenu, P., Brochard, E., Fernandez, J.-M. & Andreoletti, G. Determination of selenium-79 in solutions of fission products after pre-treatment by ion exchange chromatography and ETV-ICP-MS. *J. Anal. At. Spectrom.* **18,** 702–707 (2003).

17. Chartier, F., Isnard, H., Degros, J. P., Faure, A. L. & Fréchou, C. Application of the isotope dilution technique for 93Zr determination in an irradiated cladding material by multiple collector-inductively coupled plasma mass spectrometry. *Int. J. Mass Spectrom.* **270,** 127–133 (2008).

18. Parry, S. J. Quality assurance in the nuclear sector. *Radiochim. Acta* **100,** 495–501 (2012).

19. Horwitz, E. P., Bloomquist, C. A. A. & Henderson, D. J. The Extraction Chromatography of Californium, Einsteinium, and Fermium with di(2-ethylhexyl)orthophosphoric acid. *J. Inorg. Nucl. Chem.* **31,** 1149–1166 (1969).

20. Horwitz, E. P. & Bloomquist, C. A. A. The preparation, performance and factors affecting band spreading of high efficiency extraction chromatographic columns for actinide separations. *J. Inorg. Nucl. Chem.* **34,** 3851–3871 (1972).

21. Peters, W. A. The Efficiency and Capacity of Fractionating Columns. *J. Ind. Eng. Chem.* **14,** 476–479 (1922).

22. Ney, W. O. & Lochte, H. L. Columns for Liquid-Liquid Extraction. *J. Ind. Eng. Chem.* **33,** 825–827 (1941).

23. Craig, L. C. Identification of small amounts of organic compounds by distribution studies II. Separation by counter-current distribution. *J. Biol. Chem.* **155,** 519–534 (1944).

24. Martin, A. J. P. & Synge, R. L. M. A new form of chromatogram employing two liquid phases. *Biochem. J.* **35,** 1358–1368 (1941).

25. Glueckauf, E. Theory of chromatography Part 9. The 'theoretical plate' concept in column separations. *Trans. Faraday Soc.* **51,** 34–44 (1955).

26. Braun, T. & Ghersini, G. *Extraction Chromatography*. (Elsevier, 1975).

27. Ettre, L. S. Nomenclature for chromatography. *Pure Appl. Chem.* **65,** 819–872 (1993).

28. Horwitz, E. P., Chiarizia, R., Dietz, M. L., Diamond, H. & Nelson, D. M. Separation and preconcentration of actinides from acidic media by extraction chromatography. *Anal. Chim. Acta* **281,** 361–372 (1993).

29. Miyamoto, Y., Yasuda, K. & Magara, M. Sequential separation of ultra-trace U, Th, Pb, and lanthanides using a simple automatic system. *Analyst* **140,** 4482–4488 (2015).

30. Egorov, O. B., Fiskum, S. K., O'Hara, M. J. & Grate, J. W. Radionuclide sensors based on chemically selective scintillating microspheres: renewable column sensor for analysis of (99)Tc in water. *Anal. Chem.* **71,** 5420–5429 (1999).

31. Egorov, O. B., O'Hara, M. J. & Grate, J. W. Equilibration-based preconcentrating minicolumn sensors for trace level monitoring of radionuclides and metal ions in water without consumable reagents. *Anal. Chem.* **78,** 5480–5490 (2006).

32. Lövkvist, P. & Jönsson, J. A. Capacity of sampling and preconcentration columns with a low number of theoretical plates. *Anal. Chem.* **59,** 818–821 (1987).

33. Yamamura, T., Miyakoshi, T., Shiokawa, Y. & Mitsugashira, T. Experimental and theoretical study of anion-exchange preparative chromatography for neptunium: the first application to thorium(IV) and its equilibrium and kinetics. *J. Chromatogr. A* **1169,** 95–102 (2007).

34. Owens, S., Higgins-Bos, M., Bankhead, M. & Austin, J. Using Chemical and Process Modelling to Design, Understand and Improve an Effluent Treatment Plant. *NNL Science* (2015).

35. Guiochon, G. Optimization in Liquid Chromatography. in *High-Performance Liquid Chromatography Advances and Perspectives Volume 2* (ed. Horvath, C.) 1–56 (Academic Press, Inc, 1980).

36. Swartz, M. E. & Swartz, M. E. UPLC: An Introduction and Review. *J. Liq. Chromatogr. Relat. Technol.* **28,** 1253–1263 (2005).

37. Boswell, P. G., Stoll, D. R., Carr, P. W., Nagel, M. L., Vitha, M. F. & Mabbott, G. A. An Advanced, Interactive, High-Performance Liquid Chromatography Simulator and Instructor Resources. *J. Chem. Educ.* **90,** 198–202 (2013).

38. Jönsson, J. A. Nomenclature for non-linear chromatography. *Pure Appl Chem* **68,** 1591–1595 (1996).

39. Guiochon, G. Preparative liquid chromatography. *J. Chromatogr. A* **965,** 129–161 (2002).

40. Alberti, G., Amendola, V., Pesavento, M. & Biesuz, R. Beyond the synthesis of novel solid phases: Review on modelling of sorption phenomena. *Coord. Chem. Rev.* **256,** 28–45 (2012).

41. Dunnebier, G. & Klatt, K. U. Modelling and simulation of nonlinear chromatographic separation processes: A comparison of different modelling approaches. *Chem. Eng. Sci.* **55,** 373–380 (2000).

42. Nicoud, R.-M. *Chromatographic Processes: Modeling, Simulation, and Design*. (Cambridge University Press, 2015).

43. Xu, Z., Cai, J.-G. & Pan, B.-C. Mathematically modeling fixed-bed adsorption in aqueous systems. *J. Zhejiang Univ. A (Applied Phys. Eng.* **14,** 155–176 (2013).

44. Foo, K. Y. & Hameed, B. H. Insights into the modelling of adsorption isotherm systems. *Chem. Eng. J.* **156,** 2–10 (2010).

45. Morbidelli, M., Servida, A., Storti, G. & Carra, S. Simulation of Multicomponent Adsorption Beds. Model Analysis and Numerical Solution. *Ind. Eng. Chem. Fundam.* **21,** 123–131 (1982).

46. Chu, K. H. Fixed bed sorption: Setting the record straight on the Bohart-Adams and Thomas models. *J. Hazard. Mater.* **177,** 1006–1012 (2010).

47. LeVan, M. D. & Carta, G. Adsorption and Ion Exchange. in *Perry's Chemical Engineer's Handbook* (eds. Green, D. W. & Perry, R. H.) 16-1-16–69 (McGraw-Hill Education, 2008).

48. Jensen, O. & Finlayson, B. Solution of the transport equations using a moving coordinate system. *Adv. Water Resour.* **3,** 9–18 (1980).

49. Lim, Y. I., Chang, S. C. & Jørgensen, S. B. A novel partial differential algebraic equation (PDAE) solver: Iterative space-time conservation element/solution element (CE/SE) method. *Comput. Chem. Eng.* **28,** 1309–1324 (2004).

50. von Lieres, E. & Andersson, J. A fast and accurate solver for the general rate model of column liquid chromatography. *Comput. Chem. Eng.* **34,** 1180–1191 (2010).

51. Barbesi, D., Vicente Vilas, V., Millet, S., Sandow, M., Colle, J.-Y. & Aldave de las Heras, L. A LabVIEW-based software for the control of the AUTORAD platform: a fully automated multisequential flow injection analysis Lab-on-Valve (MSFIA-LOV) system for radiochemical analysis. *J. Radioanal. Nucl. Chem.* **313,** 217–227 (2017).

52. Chung, K. H., Choi, S. Do, Choi, G. S. & Kang, M. J. Design and performance of an automated radionuclide separator: Its application on the determination of 99Tc in groundwater. *Appl. Radiat. Isot.* **81,** 57–61 (2013).

53. Chung, K. H., Kim, H., Lim, J. M., Ji, Y.-Y., Choi, G.-S. & Kang, M. J. Rapid determination of radiostrontium in milk using automated radionuclides separator and liquid scintillation counter. *J. Radioanal. Nucl. Chem.* **304,** 293–300 (2015).

54. Yoon, S., Ha, W.-H., Park, S., Lee, S.-S. & Jin, Y.-W. Development and optimization of an on-site sequential extraction system for radiobioassay in radiation emergency. *J. Radioanal. Nucl. Chem.* **311,** 1053–1057 (2016).

55. Lide, D. R. *CRC Handbook of Chemistry and Physics*. (CRC Press, 2003).

56. Liu, Y. & Liu, Y. J. Biosorption isotherms, kinetics and thermodynamics. *Sep. Purif. Technol.* **61,** 229–242 (2008).

57. Lagergren, S. About the Theory of So-Called Adsorption of Soluble Substances. *K. Sven. Vetenskapsakademiens Handl.* **24,** 1–39 (1898).

58. Blanchard, G., Maunaye, M. & Martin, G. Removal of heavy metals from waters by means of natural zeolites. *Water Res.* **18,** 1501–1507 (1984).

59. Ho, Y. S., Wase, D. a. J. & Forster, C. F. Kinetic Studies of Competitive Heavy Metal Adsorption by Sphagnum Moss Peat. *Environ. Technol.* **17,** 71–77 (1996).

60. Largitte, L. & Pasquier, R. A review of the kinetics adsorption models and their application to the adsorption of lead by an activated carbon. *Chem. Eng. Res. Des.* **109,** 495–504 (2016).

61. Sen Gupta, S. & Bhattacharyya, K. G. Kinetics of adsorption of metal ions on inorganic materials: A review. *Adv. Colloid Interface Sci.* **162,** 39–58 (2011).

62. Duval, C. E. Uranium-selective adsorbent materials for environmental radiation sensing. (2017).

63. Paxton, W. F., O'Hara, M. J., Peper, S. M., Petersen, S. L. & Grate, J. W. Accelerated analyte uptake on single beads in microliter-scale batch separations using acoustic streaming: plutonium uptake by anion exchange for analysis by mass spectrometry. *Anal. Chem.* **80,** 4070–4077 (2008).

64. Sircar, S. & Hufton, J. R. Why does the linear driving force model for adsorption kinetics work? *Adsorption* **6,** 137–147 (2000).

65. Astrath, D.-U., Lottes, F., Vu, D. T., Arlt, W. & Stenby, E. H. Experimental investigation of liquid chromatography columns by means of computed tomography. *Adsorption* **13,** 9–19 (2007).

66. Moon, D. S., Burnett, W. C., Nour, S., Horwitz, E. P. & Bond, A. Preconcentration of radium isotopes from natural waters using MnO2 Resin. *Appl. Radiat. Isot.* **59,** 255–262 (2003).

67. Roman, A. Characterization and Optimization of Extraction Chromatography Resins for Rapid Separations for Safeguard and Nuclear Forensics Purposes. (2014).

68. Guérin, N., Nadeau, K., Potvin, S., Hardy, J.-M. & Larivière, D. Automated pressurized injection system for the separation of actinides by extraction chromatography. *J. Radioanal. Nucl. Chem.* **295,** 1803–1811 (2012).

69. Grate, J. W., Fadeff, S. & Egorov, O. B. Separation-optimized sequential injection method for rapid automated analytical separation of 90Sr in nuclear waste. *Analyst* **124,** 203–210

(1999).

70. Horwitz, E. P., Dietz, M. L., Chiarizia, R. & Diamond, H. Separation and preconcentration of uranium from acidic media by extraction chromatography. *Anal. Chim. Acta* **266,** 25–37 (1992).

71. Horwitz, E. P., Dietz, M. L., Chiarizia, R., Diamond, H., Maxwell, S. L. & Nelson, M. R. Separation and preconcentration of actinides by extraction chromatography using a supported liquid anion exchanger: application to the characterization of high-level nuclear waste solutions. *Anal. Chim. Acta* **310,** 63–78 (1995).

72. Horwitz, E. P., McAlister, D. R., Bond, A. H. & Barrans, R. E. Novel extraction of chromatographic resins based on tetraalkyldiglycolamides: Characterization and potential applications. *Solvent Extr. Ion Exch.* **23,** 319–344 (2005).

73. Despotopulos, J. D., Gostic, J. M., Bennett, M. E., Gharibyan, N., Henderson, R. A., Moody, K. J., Sudowe, R. & Shaughnessy, D. A. Characterization of Group 5 dubnium homologs on diglycolamide extraction chromatography resins from nitric and hydrofluoric acid matrices. *J. Radioanal. Nucl. Chem.* **303,** 485–494 (2015).

74. Dietz, M. L., Horwitz, E. P., Sajdak, L. R. & Chiarizia, R. An improved extraction chromatographic resin for the separation of uranium from acidic nitrate media. *Talanta* **54,** 1173–1184 (2001).

75. Rahmani-Sani, A., Hosseini-Bandegharaei, A., Hosseini, S.-H., Kharghani, K., Zarei, H. & Rastegar, A. Kinetic, equilibrium and thermodynamic studies on sorption of uranium and thorium from aqueous solutions by a selective impregnated resin containing carminic acid. *J. Hazard. Mater.* **286,** 152–163 (2015).

76. Faris, J. P. & Buchanan, R. F. *Anion exchange characteristics of the elements in nitric acid and nitrate solutions and application in trace element analysis*. (1964).

77. Saito, N. Selected Data on Ion Exchange Separations in Radioanalytical Chemistry. *Pure Appl. Chem.* **56,** 523–539 (1984).

78. Kumaresan, R., Sabharwal, K. N., Srinivasan, T. G., Rao, P. R. V. & Dhekane, G. Evaluation of New Anion Exchange Resins for Plutonium Processing. *Solvent Extr. Ion Exch.* **24,** 589–602 (2006).

79. Chiarizia, R., Horwitz, E. P., Alexandratos, S. D. & Gula, M. J. Diphonix® Resin: A Review of

Its Properties and Applications. *Sep. Sci. Technol.* **32,** 1–35 (1997).

80. Fernandes, S. & Gando-Ferreira, L. M. Kinetic modeling analysis for the removal of Cr(III) by Diphonix resin. *Chem. Eng. J.* **172,** 623–633 (2011).

81. Phelps, D. & Ruthven, D. The Kinetics of Uptake of Cu++ Ions in Ionac SR-5 Cation Exchange Resin. *Adsorption* **7,** 221–229 (2001).

82. Kullberg, L. & Clearfield, A. Mechanism of ion exchange in zirconium phosphates. 32. Thermodynamics of alkali metal ion exchange on crystalline α-ZrP. *J. Phys. Chem.* **85,** 1585–1589 (1981).

83. Veliscek-Carolan, J., Rawal, A., Luca, V. & Hanley, T. L. Zirconium phosphonate sorbents with tunable structure and function. *Microporous Mesoporous Mater.* **252,** 90–104 (2017).

84. Komarneni, S. & Roy, R. Use of γ-zirconium phosphate for Cs removal from radioactive waste. *Nature* **299,** 707–708 (1982).

85. Pet'kov, V., Asabina, E., Loshkarev, V. & Sukhanov, M. Systematic investigation of the strontium zirconium phosphate ceramic form for nuclear waste immobilization. *J. Nucl. Mater.* **471,** 122–128 (2016).

86. Scheetz, B. E., Agrawal, D. K., Breval, E. & Roy, R. Sodium zirconium phosphate (NZP) as a host structure for nuclear waste immobilization: A review. *Waste Manag.* **14,** 489–505 (1994).

87. Jayswal, A. & Chudasama, U. Sorption and ion exchange behavior of Pb (II), Bi (III) and Th (IV) in aqueous solutions towards zirconium phosphate. *J. Sci. Ind. Res.* **66,** 945–951 (2007).

88. Pan, B., Zhang, Q., Du, W., Zhang, W., Pan, B., Zhang, Q., Xu, Z. & Zhang, Q. Selective heavy metals removal from waters by amorphous zirconium phosphate: Behavior and mechanism. *Water Res.* **41,** 3103–3111 (2007).

89. Nancollas, G. H. & Paterson, R. The kinetics of ion exchange on zirconium phosphate and hydrated thoria. *J. Inorg. Nucl. Chem.* **22,** 259–268 (1961).

90. Harvie, S. J. & Nancollas, G. H. The kinetics of ion exchange on crystalline zirconium phosphate. *J. Inorg. Nucl. Chem.* **30,** 273–276 (1968).

91. Kotov, V. Y., Stenina, I. A. & Yaroslavtsev, A. B. Kinetics of hydrogen-sodium ion exchange in acid zirconium phosphate. *Solid State Ionics* **125,** 55–60 (1999).

92. Izatt, R. M. Solid phase extraction of ions using molecular recognition technology. **67,** 1069–1074 (1995).

93. Miura, T. & Minai, Y. Radiometric analysis of 90Sr in fish bone ash samples by liquid scintillation counting after separation by extraction chromatographic resin. *J. Radioanal. Nucl. Chem.* **313,** 343–351 (2017).

94. Remenec, B. The Selective Separation of 90 Sr and 99 Tc in Nuclear Waste Using Molecular Recognition Technology. *Czechoslov. J. Phys.* **56,** 645–651 (2006).

95. Grate, J. W., Egorov, O. B., O'Hara, M. J. & DeVol, T. A. Radionuclide sensors for environmental monitoring: from flow injection solid-phase absorptiometry to equilibration-based preconcentrating minicolumn sensors with radiometric detection. *Chem. Rev.* **108,** 543–562 (2008).

96. Alfonso, M. C., Bennett, M. E. & Folden, C. M. Extraction chromatography of the Rf homologs, Zr and Hf, using TEVA and UTEVA resins in HCl, HNO3, and H2SO4 media. *J. Radioanal. Nucl. Chem.* **307,** 1529–1536 (2015).

97. Pourmand, A. & Dauphas, N. Distribution coefficients of 60 elements on TODGA resin: application to Ca, Lu, Hf, U and Th isotope geochemistry. *Talanta* **81,** 741–53 (2010).

98. Sadi, B. B., Fontaine, A., McAlister, D. & Li, C. Emergency Radiobioassay Method for Determination of 90 Sr and 226 Ra in a Spot Urine Sample. *Anal. Chem.* **87,** 7931–7937 (2015).

99. Wang, Z., Zheng, J., Tagami, K. & Uchida, S. Extraction behaviors of interfering elements on TRU and DGA resins for 241Am determination by mass spectrometry. *J. Radioanal. Nucl. Chem.* **312,** 151–160 (2017).

100. Gostic, J. M. Evaluation of extraction chromatography resins for rapid actinide analysis. (2009).

101. Janda, J., Sas, D. & Tokárová, A. Characterization of the extraction properties of the selected extraction sorbents TRU, TEVA, UTEVA and DIPHONIX. *J. Radioanal. Nucl. Chem.* **304,** 301–312 (2015).

102. Guérin, N., Nadeau, K. & Larivire, D. Neptunium(III) application in extraction chromatography. *Talanta* **87,** 8–14 (2011).

103. Sommers, J., Cummings, D., Giglio, J. & Carney, K. 'age' determination of irradiated materials utilizing inductively coupled plasma mass spectrometric (ICP-MS) detection. *J. Radioanal. Nucl. Chem.* **282,** 591–595 (2009).

104. Zhang, A., Wang, W., Chai, Z. & Kumagai, M. Separation of strontium ions from a simulated highly active liquid waste using a composite of silica-crown ether in a polymer. *J. Sep. Sci.* **31,** 3148–3155 (2008).

105. Zhang, A., Hu, Q. & Chai, Z. SPEC: A New Process for Strontium and Cesium Partitioning Utilizing Two Macroporous Silica-Based Supramolecular Recognition Agents Impregnated Polymeric Composites. *Sep. Sci. Technol.* **44,** 2146–2168 (2009).

106. Ruzicka, J. & Hansen, E. H. Flow injection analyses: Part I. A new concept of fast continuous flow analysis. *Anal. Chim. Acta* **78,** 145–157 (1975).

107. Kołacińska, K. & Trojanowicz, M. Application of flow analysis in determination of selected radionuclides. *Talanta* **125,** 131–145 (2014).

108. Trojanowicz, M. & Kołacińska, K. Recent Advances in Flow Injection Analysis. *Analyst* **141,** 2085–2139 (2016).

109. Miró, M., Cerdà, V. & Estela, J. M. Multisyringe flow injection analysis: characterization and applications. *TrAC Trends Anal. Chem.* **21,** 199–210 (2002).

110. Horstkotte, B., Elsholz, O. & Cerdà, V. Review on automation using multisyringe flow injection analysis. *J. Flow Inject. Anal.* **22,** 99–109 (2005).

111. Ivaska, A. & Ruzicka, J. From flow injection to sequential injection: comparison of methodologies and selection of liquid drives. *Analyst* **118,** 885–889 (1993).

112. Fajardo, Y., Avivar, J., Ferrer, L., Gómez, E., Cerdà, V. & Casas, M. Automation of radiochemical analysis by applying flow techniques to environmental samples. *TrAC Trends Anal. Chem.* **29,** 1399–1408 (2010).

113. Grate, J. W. & Egorov, O. B. Automating Analytical Separations in Radiochemistry. *Anal. Chem.* **70,** 779–788 (1998).

114. Miró, M. & Hansen, E. H. Solid reactors in sequential injection analysis: recent trends in the environmental field. *TrAC Trends Anal. Chem.* **25,** 267–281 (2006).

115. Rodríguez, R., Avivar, J., Leal, L. O., Cerdà, V. & Ferrer, L. Strategies for automating solid-

phase extraction and liquid-liquid extraction in radiochemical analysis. *TrAC Trends Anal. Chem.* **76,** 145–152 (2016).

116. Aldstadt, J. H., Kuo, J. M., Smith, L. L. & Erickson, M. D. Determination of uranium by flow injection inductively coupled plasma mass spectrometry. *Anal. Chim. Acta* **319,** 135–143 (1996).

117. Egorov, O. B., Grate, J. W. & Ruzicka, J. Automation of radiochemical analysis by flow injection techniques: Am-Pu separation using TRU-resin™ sorbent extraction column. *J. Radioanal. Nucl. Chem.* **234,** 231–235 (1998).

118. Grate, J. W. & Egorov, O. B. Investigation and optimization of on-column redox reactions in the sorbent extraction separation of americium and plutonium using flow injection analysis. *Anal. Chem.* **70,** 3920–3929 (1998).

119. Hosseini, S.-H., Rahmani-Sani, A., Jalalabadi, Y., Karimzadeh, M., Hosseini-Bandegharaei, A., Kharghani, K. & Allahabadi, A. Preconcentration and determination of ultra-trace amounts of U(VI) and Th(IV) using titan yellow-impregnated Amberlite XAD-7 resin. *Int. J. Environ. Anal. Chem.* **95,** 277–290 (2015).

120. Charlton, J. J., Sepaniak, M. J., Sides, A. K., Schaaff, T. G., Mann, D. K. & Bradshaw, J. A. The automation and optimization of solid phase extraction inductively coupled plasma mass spectrometry analysis for the high throughput determination of aqueous levels of U, Th, Np, Pu, and Am. *J. Anal. At. Spectrom.* **28,** 711–718 (2013).

121. DeVol, T. A., Clements, J. P., Farawila, A., O'Hara, M. J., Egorov, O. B. & Grate, J. W. Characterization and application of SuperLig® 620 solid phase extraction resin for automated process monitoring of 90Sr. *J. Radioanal. Nucl. Chem.* **282,** 623–628 (2009).

122. Egorov, O. B., O'Hara, M. J., Ruzicka, J. & Grate, J. W. Sequential injection separation system with stopped-flow radiometric detection for automated analysis of 99Tc in nuclear waste. *Anal. Chem.* **70,** 977–984 (1998).

123. Egorov, O. B., O'Hara, M. J. & Grate, J. W. Sequential Injection Renewable Separation Column Instrument for Automated Sorbent Extraction Separations of Radionuclides. *Anal. Chem.* **71,** 345–352 (1999).

124. Egorov, O. B., Grate, J. W., O'Hara, M. J. & Farmer III, O. T. Extraction chromatographic separations and analysis of actinides using sequential injection techniques with on-line

inductively coupled plasma mass spectrometry (ICP MS) detection. *Analyst* **126,** 1594–1601 (2001).

125. Egorov, O. B., O'Hara, M. J. & Grate, J. W. Automated Radioanalytical System Incorporating Microwave-Assisted Sample Preparation, Chemical Separation, and Online Radiometric Detection for the Monitoring of Total 99Tc in Nuclear Waste Processing Streams. *Anal. Chem.* **84,** 3090–3098 (2012).

126. Grate, J. W., Egorov, O. B. & Fiskum, S. K. Automated extraction chromatographic separations of actinides using separation-optimized sequential injection techniques. *Analyst* **124,** 1143–1150 (1999).

127. Qiao, J., Hou, X., Steier, P. & Golser, R. Sequential Injection Method for Rapid and Simultaneous Determination of 236 U, 237 Np, and Pu Isotopes in Seawater. *Anal. Chem.* **85,** 11026–11033 (2013).

128. Taguchi, S., Yamamoto, M. & Surugaya, N. Determination of neptunium in a reprocessing plant by an on-line solid-phase extraction/electrochemical detection system. *J. Radioanal. Nucl. Chem.* **299,** 1539–1545 (2014).

129. Avivar, J., Ferrer, L., Casas, M. & Cerdà, V. Lab on valve-multisyringe flow injection system (LOV-MSFIA) for fully automated uranium determination in environmental samples. *Talanta* **84,** 1221–1227 (2011).

130. Avivar, J., Ferrer, L., Casas, M. & Cerdà, V. Smart thorium and uranium determination exploiting renewable solid-phase extraction applied to environmental samples in a wide concentration range. *Anal. Bioanal. Chem.* **400,** 3585–3594 (2011).

131. Avivar, J., Ferrer, L., Casas, M. & Cerdà, V. Fully automated lab-on-valve-multisyringe flow injection analysis-ICP-MS system: an effective tool for fast, sensitive and selective determination of thorium and uranium at environmental levels exploiting solid phase extraction. *J. Anal. At. Spectrom.* **27,** 327–334 (2012).

132. Ceballos, M. R., Borràs, A., García-Tenorio, R., Rodríguez, R., Estela, J. M., Cerdà, V. & Ferrer, L. 226Ra dynamic lixiviation from phosphogypsum samples by an automatic flow-through system with integrated renewable solid-phase extraction. *Talanta* **167,** 398–403 (2017).

133. Fajardo, Y., Gómez, E., Mas, F., Garcias, F., Cerdà, V. & Casas, M. Multisyringe flow

injection analysis of stable and radioactive strontium in samples of environmental interest. *Appl. Radiat. Isot.* **61,** 273–277 (2004).

134. Fajardo, Y., Gómez, E., Garcias, F., Cerdà, V. & Casas, M. Multisyringe flow injection analysis of stable and radioactive yttrium in water and biological samples. *Anal. Chim. Acta* **539,** 189–194 (2005).

135. Kołacińska, K., Chajduk, E., Dudek, J., Samczyński, Z., Łokas, E., Bojanowska-Czajka, A. & Trojanowicz, M. Automation of sample processing for ICP-MS determination of 90Sr radionuclide at ppq level for nuclear technology and environmental purposes. *Talanta* **169,** 216–226 (2017).

136. Mola, M., Avivar, J., Nieto, A., Peñalver, A., Aguilar, C., Ferrer, L., Cerdà, V. & Borrull, F. Determination of 90Sr and 210Pb in Sludge Samples using a LOV-MSFIA System and Liquid Scintillation Counting. *Appl. Radiat. Isot.* **86,** 28–35 (2014).

137. Mola, M., Nieto, A., Peñalver, A., Borrull, F. & Aguilar, C. Uranium and thorium sequential separation from norm samples by using a SIA system. *J. Environ. Radioact.* **127,** 82–87 (2014).

138. Qiao, J., Hou, X., Roos, P. & Miró, M. Bead injection extraction chromatography using high-capacity lab-on-valve as a front end to inductively coupled plasma mass spectrometry for urine radiobioassay. *Anal. Chem.* **85,** 2853–2859 (2013).

139. Rodríguez, R., Avivar, J., Ferrer, L., Leal, L. O. & Cerdà, V. Automated total and radioactive strontium separation and preconcentration in samples of environmental interest exploiting a lab-on-valve system. *Talanta* **96,** 96–101 (2012).

140. Rodríguez, R., Leal, L., Miranda, S., Ferrer, L., Avivar, J., García, A. & Cerdà, V. Automation of 99Tc extraction by LOV prior ICP-MS detection: Application to environmental samples. *Talanta* **133,** 88–93 (2014).

141. Villar, M., Avivar, J., Ferrer, L., Galmés, M., Vega, F. & Cerdà, V. Automatic and simple method for ^{99}Tc determination using a selective resin and liquid scintillation detection applied to urine samples. *Anal. Chem.* **85,** 5491–5498 (2013).

142. Avivar, J., Ferrer, L., Casas, M. & Cerdà, V. Automated determination of uranium(VI) at ultra trace levels exploiting flow techniques and spectrophotometric detection using a liquid waveguide capillary cell. *Anal. Bioanal. Chem.* **397,** 871–878 (2010).

143. Fajardo, Y., Ferrer, L. & Gómez, E. Development of an automatic method for americium and plutonium separation and preconcentration using an multisyringe flow injection analysis-multipumping flow. *Anal. …* **80,** 195–202 (2008).

144. Egorov, O. B., O'Hara, M. J. & Grate, J. W. Microwave-assisted sample treatment in a fully automated flow-based instrument: oxidation of reduced technetium species in the analysis of total technetium-99 in caustic aged nuclear waste samples. *Anal. Chem.* **76,** 3869–77 (2004).

145. Alexovič, M., Horstkotte, B., Solich, P. & Sabo, J. Automation of static and dynamic non-dispersive liquid phase microextraction. Part 1: Approaches based on extractant drop-, plug-, film- and microflow-formation. *Anal. Chim. Acta* **906,** 22–40 (2016).

146. Rodríguez, R., Avivar, J., Ferrer, L., Leal, L. O. & Cerdà, V. Uranium monitoring tool for rapid analysis of environmental samples based on automated liquid-liquid microextraction. *Talanta* **134,** 674–680 (2015).

147. Villar, M., Avivar, J., Ferrer, L., Borràs, A., Vega, F. & Cerdà, V. Automatic in-syringe dispersive liquid–liquid microextraction of 99Tc from biological samples and hospital residues prior to liquid scintillation counting. *Anal. Bioanal. Chem.* **407,** 5571–5578 (2015).

148. Hellé, G., Mariet, C. & Cote, G. Liquid–liquid microflow patterns and mass transfer of radionuclides in the systems Eu (III)/HNO3/DMDBTDMA and U (VI)/HCl/Aliquat® 336. *Microfluid. Nanofluidics* **17,** 1113–1128 (2014).

149. Hellé, G., Mariet, C. & Cote, G. Liquid–liquid extraction of uranium(VI) with Aliquat® 336 from HCl media in microfluidic devices: Combination of micro-unit operations and online ICP-MS determination. *Talanta* **139,** 123–131 (2015).

150. Launiere, C. A. & Gelis, A. V. High Precision Droplet-Based Microfluidic Determination of Americium(III) and Lanthanide(III) Solvent Extraction Separation Kinetics. *Ind. Eng. Chem. Res.* **55,** 2272–2276 (2016).

151. Zhang, J., Qin, Z., Deng, D., Liao, J., Wei, X. & Zhang, N. A novel method for the online measurement of impurities in uranium by coupling microfluidics with ICP-MS. *J. Anal. At. Spectrom.* **31,** 934–939 (2016).

152. Hellé, G., Roberston, S., Cavadias, S. & Mariet, C. Toward numerical prototyping of labs - on - chip : modeling for liquid – liquid microfluidic devices for radionuclide extraction.

Microfluid. Nanofluidics **19,** 1245–1257 (2015).

153. Buda, R., Balsley, S. D. V., Emblico, L. & Schachinger, A. Semi-Automatic Separation Unit for Actinides at JRC-ITU and IAEA. in *37th ESARDA Symposium on Safeguards and Nuclear Non-Proliferation* 19–21 (2015).

154. Grate, J. W. & O'Hara, M. Automation of column-based radiochemical separations: a comparison of fluidic, robotic, and hybrid architectures. *APSORC09. Proc. Radiochem. A Suppl. to Radiochim. Acta* **19,** 13–19 (2011).

155. Grate, J. W., O'Hara, M. J., Farawila, A. F., Douglas, M., Haney, M. M., Petersen, S. L., Maiti, T. C. & Aardahl, C. L. Extraction chromatographic methods in the sample preparation sequence for thermal ionization mass spectrometric analysis of plutonium isotopes. *Anal. Chem.* **83,** 9086–91 (2011).

156. Zapata-García, D. & Wershofen, H. Development of radiochemical analysis strategies for decommissioning activities. *Appl. Radiat. Isot.* **126,** 204–207 (2017).

157. Guérin, N., Calmette, R., Johnson, T. & Larivière, D. Multi-dimensional extraction chromatography of actinides for alpha and mass spectrometry. *Anal. Methods* **3,** 1560–1567 (2011).

158. Miyamoto, Y., Yasuda, K. & Magara, M. Automatic sequential separation with an anion-exchange column for ultra-trace analysis of Pu, U, Th, Pb, and lanthanides in environmental samples. *J. Radioanal. Nucl. Chem.* **309,** 303–308 (2016).

159. Duval, C. E., DeVol, T. A. & Husson, S. M. Extractive scintillating polymer sensors for trace-level detection of uranium in contaminated ground water. *Anal. Chim. Acta* **947,** 1–8 (2016).

160. Fan, J., Lu, J., Zhang, L., Yu, G., Huang, P., Shi, Q., Liu, Z., Li, X. & Bai, T. Automated separation of short-lived 72Ga from fresh fission products based on tandem column chromatography. *J. Radioanal. Nucl. Chem.* **309,** 467–476 (2015).

161. Grate, J. W., Strebin, R. & Janata, J. Automated Analysis of Radionuclides in Nuclear Waste : Rapid Determination of 90 Sr by Sequential Injection Analysis. *Anal. Chem.* **68,** 333–340 (1996).

162. Habibi, A., Vivien, C., Boulet, B., Cossonnet, C., Gurriaran, R., Gleizes, M., Cote, G. & Larivière, D. A rapid sequential separation of actinides and radiostrontium coupled to ICP-

MS and gas proportional counting. *J. Radioanal. Nucl. Chem.* **310,** 217–227 (2016).

163. Hollenbach, M., Grohs, J., Mamich, S., Kroft, M. & Denoyer, E. Determination of technetium-99, thorium-230 and uranium-234 in soils by inductively coupled plasma mass spectrometry using flow injection preconcentration. *J. Anal. At. Spectrom.* **9,** 927–933 (1994).

164. Kim, C., Kim, C., Rho, B. & Lee, J. Rapid determination of 99 Tc in environmental samples by high resolution ICP-MS coupled with on-line flow injection system. *J. Radioanal. Nucl. Chem.* **252,** 421–427 (2002).

165. Kim, C. S., Kim, C. K. & Lee, K. J. Simultaneous analysis of 237Np and Pu isotopes in environmental samples by ICP-SF-MS coupled with automated sequential injection system. *J. Anal. At. Spectrom.* **19,** 743–750 (2004).

166. St-Amant, N. & Whyte, J. Radiostrontium and radium analysis in low-level environmental samples following a multi-stage semi-automated chromatographic sequential separation. *Appl. Radiat. Isot.* **69,** 8–17 (2011).

167. Qiao, J., Shi, K., Hou, X., Nielsen, S. & Roos, P. Rapid multisample analysis for simultaneous determination of anthropogenic radionuclides in marine environment. *Environ. Sci. Technol.* **48,** 3935–3942 (2014).

168. Zhang, Z., Zhang, L., Zhang, J. & Ma, Y. An improved procedure for determining 90Sr in groundwater based on cation-exchange enrichment and solid-phase extraction. *J. Radioanal. Nucl. Chem.* **308,** 1–5 (2015).

169. Lin, J. & Wang, L. Comparison between linear and non-linear forms of pseudo-first-order and pseudo-second-order adsorption kinetic models for the removal of methylene blue by activated carbon. *Front. Environ. Sci. Eng. China* **3,** 320–324 (2009).

170. Ho, Y. S. Review of second-order models for adsorption systems. *J. Hazard. Mater.* **136,** 681–689 (2006).

171. Azizian, S. Kinetic models of sorption: A theoretical analysis. *J. Colloid Interface Sci.* **276,** 47–52 (2004).

172. Liu, Y. & Shen, L. From Langmuir kinetics to first- and second-order rate equations for adsorption. *Langmuir* **24,** 11625–11630 (2008).

173. Plazinski, W., Rudzinski, W. & Plazinska, A. Theoretical models of sorption kinetics including a surface reaction mechanism: A review. *Adv. Colloid Interface Sci.* **152,** 2–13 (2009).

174. Rudzinski, W. & Plazinski, W. Theoretical description of the kinetics of solute adsorption at heterogeneous solid/solution interfaces - On the possibility of distinguishing between the diffusional and the surface kinetics models. *Appl. Surf. Sci.* **253,** 5827–5840 (2007).

175. Rexwinkel, G., Heesink, A. B. M. & Swaaij, W. P. M. Van. Mass transfer in packed beds at low Peclet numbers - wrong experiments or wrong interpretations? *Chem. Eng. Sci.* **52,** 3995–4003 (1997).

176. Ward, C. A. The rate of gas absorption at a liquid interface. *J. Chem. Phys.* **67,** 229–235 (1977).

177. Ward, C. A. Statistical rate theory of interfacial transport. I. Theoretical development. *J. Chem. Phys.* **76,** 5615 (1982).

178. Rudzinski, W. & Plazinski, W. Kinetics of solute adsorption at solid/solution interfaces: A theoretical development of the empirical pseudo-first and pseudo-second order kinetic rate equations, based on applying the statistical rate theory of interfacial transport. *J. Phys. Chem. B* **110,** 16514–16525 (2006).

179. Azizian, S., Bashiri, H. & Iloukhani, H. Statistical Rate Theory Approach to Kinetics of Competitive Adsorption at the Solid/ Solution Interface. *J. Phys. Chem. C* **112,** 10251–10255 (2008).

180. Azizian, S., Haerifar, M. & Basiri-Parsa, J. Extended geometric method: A simple approach to derive adsorption rate constants of Langmuir-Freundlich kinetics. *Chemosphere* **68,** 2040–2046 (2007).

181. Haerifar, M. & Azizian, S. Mixed Surface Reaction and Diffusion-Controlled Kinetic Model for Adsorption at the Solid / Solution Interface. *J. Phys. Chem. C* **8317,** 8310–8317 (2013).

182. Holz, M., Heil, S. R. & Sacco, A. Temperature-dependent self-diffusion coefficients of water and six selected molecular liquids for calibration in accurate 1H NMR PFG measurements. *Phys. Chem. Chem. Phys.* **2,** 4740–4742 (2000).

183. TrisKem International. Available at: www.triskem-international.com.